DOCTORAL THESIS

High-Frequency Modeling and Diagnostics of Winding Insulation Degradation in Induction Machines

Muhammad Usman Sardar

TALLINNA TEHNIKAÜLIKOOL
TALLINN UNIVERSITY OF TECHNOLOGY
TALLINN 2026

TALLINN UNIVERSITY OF TECHNOLOGY
DOCTORAL THESIS
87/2026

High-Frequency Modeling and Diagnostics of Winding Insulation Degradation in Induction Machines

MUHAMMAD USMAN SARDAR

TAL TECH PRESS

TALLINN UNIVERSITY OF TECHNOLOGY
School of Engineering
Department of Electrical Power Engineering and Mechatronics
This dissertation was accepted for the defence of the degree 06/11/2026.

Supervisor: Dr. Toomas Vaimann
School of Engineering
Tallinn University of Technology
Tallinn, Estonia

Co-supervisor: Dr. Lauri Kütt
School of Engineering
Tallinn University of Technology
Tallinn, Estonia

Opponents: Prof. Ing. Michael Galea
Electrical Engineering
Faculty of Engineering
University of Malta
Msida, Malta

Dr. Levon Gevorkov
Power Systems Group
Catalonia Institute for Energy Research (IREC)
Barcelona, Spain

Defence of the thesis: 16/12/2026, Tallinn

Declaration:
I hereby declare that this doctoral thesis, my original investigation and achievement, submitted for the doctoral degree at Tallinn University of Technology has not been submitted for doctoral or equivalent academic degree.

Muhammad Usman Sardar _____
signature



Copyright: Muhammad Usman Sardar, 2026
ISSN 2585-6901 (PDF)
ISBN 978-9916-80-609-8 (PDF)
https://doi.org/10.23658/taltech.87/2026

Sardar, M. U. (2026). *High-Frequency Modeling and Diagnostics of Winding Insulation Degradation in Induction Machines* [TalTech Press]. https://doi.org/10.23658/taltech.87/2026

TALLINN UNIVERSITY OF TECHNOLOGY
DOCTORAL THESIS
87/2026

Asünkroonmasinate mähiste isolatsiooni degradeerumise kõrgsageduslik modelleerimine ja diagnostika

MUHAMMAD USMAN SARDAR

TAL TECH
KIRJASTUS

Contents

List of Publications 8
Author's Contribution to the Publications 9
1 Introduction 10
1.1 Reliability Challenges in Inverter-Fed Induction Machines 10
1.2 Research Motivation: Insulation Diagnostics Across a Wide Frequency Range 11
1.3 Research Problem 12
1.4 Hypothesis 12
1.5 Research Tasks 12
1.6 Contribution and Dissemination 13
1.6.1 Scientific Novelties: 13
1.6.2 Practical Novelties: 13
1.7 Organization of the Thesis 14
Abbreviations 15
Symbols 17
2 State-of-the-Art Techniques for Machine Insulation Monitoring, Diagnosis, and Useful Life Estimation 21
2.1 Overview of Multiple Faults in Induction Machines 21
2.2 PWM Inverter-Related Stresses 22
2.2.1 Common Mode Voltage 23
2.2.2 Terminal Transient Overvoltage 23
2.2.3 Resonance Occurrence Phenomena in Machine's Winding 24
2.3 Insulation Degradation Monitoring and Diagnosis 25
2.3.1 Insulation Condition Monitoring Techniques 26
2.3.2 Role of GBM in Characterization of Electric Machines 29
2.4 Estimations of Useful Life and Prognostics 30
3 High-Frequency Modeling of Cable-Fed Motor Drives 31
3.1 Cable-Fed Drive Systems 31
3.2 Impedance Measurement Setup and Results 31
3.2.1 Setup for Measuring Machine Impedance 31
3.3 Impedance Parameter Characterization of GBM 33
3.3.1 Proposed GBM Modeling Approach 33
3.3.2 Optimal Characterization of Machine GBM Parameters 33
3.3.3 Proposed Machine GBM 34
3.3.4 Grey-Box Model of Cable 39
3.3.5 Identification of Cable Model Parameters 40
3.3.6 Cable's GBM Validation 40
3.3.7 Error Analysis of Motor and Cable Modeling 40
3.4 Time Domain Analysis 41
3.4.1 Practical Test-bench Details and Model Simulation 41
3.4.2 Time Domain Analysis of TOV and CMV 42
3.4.3 Frequency Domain Analysis of TOV and CMV 43
3.5 Motor Winding TOV Stress Analysis 43
3.5.1 Motor Winding HF TOV Estimation 43
3.5.2 Motor Winding Terminal ARO Estimation 44

3.6 Parametric Sensitivity Analysis 45
3.6.1 ROA Criteria 45
3.7 Discussion 47
3.8 Chapter Summary 47
4 Signal Processing-Based Approach for Insulation Degradation Estimation 48
4.1 Proposed Signal Processing-Based Diagnostic Framework 48
4.1.1 Limitations of Conventional Spectral Analysis 48
4.1.2 Parametric GBM Model of IM 49
4.2 Natural PWM Switching Transients for Insulation Diagnosis 50
4.3 Fractional Fourier Transform-Based Diagnostics 54
4.3.1 Fractional Fourier Transform and Mel Filter Bank 54
4.3.2 Design of Resonance-Centered Mel Filter Bank 56
4.3.3 Methodology for Insulation State Estimation and Implementation 56
4.3.4 Validation of FRFT-RMFB with Variable-Frequency Signal Source 58
4.3.5 Validation of Proposed Methodology with Inverter-Fed Supply 61
4.4 Implementation of FRFT-RMFB on Thermally Aged Machine Stator 63
4.4.1 Accelerated Thermal Aging and Measurement 63
4.4.2 Evolution of Fractional-Domain Features 64
4.4.3 Incipient Degradation Detection Performance 66
4.5 Discussion 67
4.6 Chapter Summary 67
5 Model-Based Insulation Aging State and Lifetime Evaluation 68
5.1 Thermal Degradation Phenomena and Parameter Tracking 68
5.1.1 Induction Machine Stator as a Sample 68
5.1.2 Machine RLC Parameter-Based GBM 68
5.1.3 Optimal GBM Parameter Through Optimization 70
5.2 Experimental Degradation Measurements and Evaluation of GBM Parameters 70
5.2.1 Heat Cycle and Exposure Time 71
5.2.2 Insulation breakdown and End-of-life Criterion 71
5.2.3 GBM Parameter Identification and Model-Fit Assessment 72
5.3 Evolution of Multiple IDPs and Life Estimation 73
5.3.1 Lifetime Estimation Model for Samples 74
5.3.2 Health Index and Lifetime Estimations 77
5.4 Discussion 79
5.5 Chapter Summary 79
6 Thesis Conclusion and Future Work 80
6.1 Conclusion 80
6.2 Limitations in the Thesis Work 80
6.3 Future Work 81
List of Figures 82
List of Tables 85
References 86
Acknowledgements 91
Abstract 92
Lühikokkuvõte 93

Appendix 1 95
Appendix 2 139
Appendix 3 149
Appendix 4 167
Appendix 5 177
Appendix 6 197
Curriculum Vitae 207
Elulookirjeldus 208

List of Publications

The list of the author's publications, on the basis of which the thesis has been prepared:

I M. U. Sardar et al., "Inverter-fed motor drive system: A systematic analysis of condition monitoring and practical diagnostic techniques," *Energies*, vol. 16, no. 15, Jul. 2023, Art. no. 5628, doi: 10.3390/en16155628.

II M. U. Sardar, T. Vaimann, L. Kütt, B. Asad, A. Kallaste and K. Kudelina, "Characterization of High-Frequency Impedance-Based Models for Transient Terminal Overvoltage Estimation in Cable-Fed Motor Drive Systems," *2024 International Conference on Electrical Machines (ICEM)*, Torino, Italy, 2024, pp. 1-7, doi: 10.1109/ICEM60801.2024.10700495.

III M. U. Sardar, T. Vaimann, L. Kütt, B. Asad, A. Kallaste and A. Rassõlkin, "Modeling Cable-Fed Induction Motor Drives with Optimized Impedance Characterization Across a Low to High-Frequency Spectrum," in *IEEE Transactions on Energy Conversion*, vol. 41, no. 2, pp. 1055-1069, June 2026, doi: 10.1109/TEC.2025.3630465.

IV M. U. Sardar, T. Vaimann, L. Kütt, B. Asad, A. Kallaste and H. A. Raja, "Wideband Frequency Diagnosis for High-Sensitivity Turn-Insulation Degradation Estimation in Inverter-Fed Machines," *2025 IEEE Symposium on Diagnostics for Electric Machines, Power Electronics and Drives (SDEMPED)*, Dallas, TX, USA, 2025, pp. 1-7, doi: 10.1109/SDEMPED53223.2025.11154298.

V M. U. Sardar, T. Vaimann, L. Kütt, B. Asad, and A. Kallaste, "Switching oscillation-based fractional-domain high-sensitive diagnosis of machine turn insulation degradation," *Engineering Science and Technology, an International Journal*, vol. 72, Dec. 2025, doi: 10.1016/j.jestch.2025.102224.

VI M. U. Sardar *et al*., "High-Frequency Impedance Parametric Modeling and Partial Discharge Validation for RUL Estimation of Thermally Aged Stator Insulation," *2026 International Conference on Electrical Machines (ICEM)*, Funchal (Madeira), Portugal, 2026, pp. 1-7, doi: 10.1109/ICEM68283.2026.11757493.

Author's Contribution to the Publications

Contribution to the papers in this thesis are:

I M. U. Sardar is the primary author of this article. He conducted the literature review on condition monitoring and practical diagnostic techniques for inverter-fed motor drive systems, structured the content, analyzed the existing approaches, and wrote the initial draft.

II M. U. Sardar is the primary author of this article. He developed the high-frequency impedance-based parametric models for cable-fed motor drive systems, performed impedance characterization and transient terminal overvoltage analysis, validated the models experimentally, and prepared the conference paper.

III M. U. Sardar is the primary author of this article. He developed the optimized low-to-high-frequency grey-box modeling approach, performed impedance characterization and parameter identification, validated the cable-motor models, and investigated transient terminal overvoltage, common-mode voltage, cable–motor interactions and generated resonances, and insulation-stress assessment.

IV M. U. Sardar is the primary author of this article. He developed the high-sensitivity frequency-based diagnostic approach for turn-insulation degradation in inverter-fed machines, performed the experimental investigation and diagnostic analysis, and wrote the initial draft.

V M. U. Sardar is the primary author of this article. He developed the switching-oscillation-based fractional-domain diagnostic method, performed the signal processing, experimental validation, and comparative analysis, and led the writing of the article.

VI M. U. Sardar is the primary author of this article. He developed the high-frequency impedance parametric modeling approach for thermally aged machine stator insulation, performed aging and impedance characterization, incorporated partial-discharge measurements, and investigated parameters for RUL estimation.

1 Introduction

Electrical machines share an important role in the transition towards more efficient and sustainable energy systems. Electric motors account for approximately 51% of global electricity consumption, making their efficiency and reliability important for reducing energy demand and associated emissions [1].

The European Union (EU) has established targets for climate neutrality and energy efficiency through the European Green Deal and the Fit for 55 framework, including a reduction of at least 55% in net greenhouse-gas emissions by 2030 and climate neutrality by 2050 [2]. The revised Energy Efficiency Directive 2023/1791 further requires an additional 11.7% reduction in energy consumption by 2030 [3]. Within this framework, EU ecodesign requirements establish minimum efficiency classes for electric motors and variable-speed drives, supporting the adoption of energy-efficient drive systems.

Because of their efficiency, controllability, and power density, inverter-fed machines are primarily used in modern industrial and energy-conversion applications. However, inverter operation introduces repetitive electrical stresses that can accelerate degradation of the electrical insulation system (EIS) and adversely affect machine reliability [4]. With more optimal insulation material usage, given volume, mass and material types, the stress levels imposed by modern inverters could lead to faster insulation degradation. This requires more attention to insulation design, as well as timely detection of insulation faults.

Winding insulation is one of the most failure-prone components of electrical machines. Previous studies report that stator winding faults account for 40–50% of machine failures, and insulation degradation can eventually lead to inter-turn, phase-to-phase, or ground-wall short circuits [5], [6]. Still, the successful methods to estimate insulation deterioration and aging margins before breakdown are scarce. Thus, insulation faults can occur with little warning; with added modern converter-induced stresses, the likelihood of insulation faults becomes even more critical. Incipient inter-turn insulation degradation is particularly important because localized deterioration can develop before a measurable short-circuit occurs. Although conventional electrical insulation tests and partial-discharge (PD) monitoring provide valuable information about insulation condition, offline testing often requires machine shutdown, while online PD measurements can be affected by electromagnetic interference and may have limited sensitivity to early-stage inter-turn insulation degradation [7].

1.1 Reliability Challenges in Inverter-Fed Induction Machines

Induction machines (IMs) are widely used in industrial and energy-conversion applications because of their efficiency, controllability, and operational reliability. However, their winding insulation remains vulnerable to progressive degradation under electrical, thermal, and mechanical stresses [5], [8]. These challenges become particularly pronounced in inverter-fed applications, where pulse-width modulation (PWM) converters generate repetitive high-frequency (HF) switching transients.

The interaction among the inverter, cable, and machine produces higher-frequency-range proprietary transient electrical phenomena, including steep voltage gradients (dv/dt), common-mode voltages (CMVs), and transient terminal overvoltages (TOVs). Furthermore, the impedance–frequency response of machine windings exhibits multi-resonant characteristics, including multiple series and parallel resonance configurations. These resonance phenomena influence the propagation and amplification of transient

voltage components within the winding system. When a dominant frequency component of a TOV coincides with a winding series resonance (SR) frequency, an anti-resonance occurrence (ARO) phenomenon may increase electrical stress on the winding insulation. Repeated ARO exposure to these electrical stresses accelerates insulation aging and increases the risk of premature failure.

IM winding insulation remains vulnerable to degradation during operation, as the practical challenges above act as additional catalysts. This is compounded by classic material degradation related to heating and chemical decomposition due to aging.

Insulation degradation is particularly challenging because local damage can develop before conventional measurements detect an electrical fault. An example can be found in a recent survey covering 3,934 grid-fed drives and 286 variable-speed inverter drives, which reported a substantially higher failure rate for inverter-fed IM drives [9]. This evidence highlights the importance of understanding the factors affecting insulation reliability and developing effective approaches for assessing its condition throughout the machine's remaining useful life.

1.2 Research Motivation: Insulation Diagnostics Across a Wide Frequency Range

Reliable assessment of winding-insulation degradation requires methods that capture EIS characteristics that vary with frequency and insulation condition. Conventional low-frequency (LF) machine models do not fully represent the parasitic elements and frequency-dependent impedance characteristics relevant to high-frequency (HF) phenomena. Similarly, conventional diagnostic techniques, including insulation resistance (IR) measurement and partial discharge (PD) monitoring, may have limited sensitivity to incipient turn-insulation degradation under certain operating conditions. In addition, these methods require the IM to be fully disconnected during testing.

Frequency response analysis (FRA), particularly impedance spectroscopy analysis (ISA), characterizes machine impedance over a wide frequency band up to 100 MHz. The measured response can reveal changes in inter-turn and ground-wall capacitances, dielectric losses, and resonance characteristics, offering physically interpretable indicators of insulation condition [10], [11]. In operation, inherent PWM switching transients provide an opportunity to extract degradation-sensitive information during inverter-fed operation without introducing a separate high-frequency excitation source. Fractional-domain signal processing can further enhance the identification of subtle changes in these transient responses.

To address these research needs, this thesis investigates three complementary aspects of winding-insulation assessment. First, HF grey-box modeling (GBM) characterizes cable–machine impedance interactions, resonance phenomena, and terminal transient overvoltages. Second, fractional-domain signal processing of machine-fed current is investigated to extract sensitive features for incipient turn-insulation diagnosis. Third, impedance-derived parameters are examined as indicators of insulation aging and combined with Arrhenius-based thermal-aging calculations to support sample-specific lifetime estimation under the investigated laboratory conditions. These contributions are investigated through their respective modeling and experimental studies; their integration into a single diagnostic and prognostic system remains a subject for future research.

1.3 Research Problem

Conventional electrical machine models are primarily developed for LF electromagnetic analysis and therefore do not accurately represent the frequency-dependent behavior at HF ranges. These limitations hinder the development of reliable, physics-informed diagnostic methodologies for modern inverter-fed drive systems. Consequently, this thesis addresses the following research problems:

- How can the frequency-dependent electrical and dielectric insulation behavior of IM be accurately represented using low-to-HF parametric models while preserving their physical interpretation?
- How can the coupled HF interactions between the inverter, cable, and machine be characterized to accurately identify key resonant frequency items, including series and parallel resonance modes, terminal overvoltage phenomena that provide indices for insulation reliability?
- How can degradation-sensitive information be extracted from non-stationary HF switching oscillations generated by inverter pulse-width modulation to improve the sensitivity and robustness of early-stage insulation fault diagnosis?
- How can physics-informed winding impedance parameters be correlated with insulation aging as a PoF model to establish reliable health assessment and lifetime evaluation until end of life (EoL)?

1.4 Hypothesis

This thesis investigates whether HF modeling, switching-transient signal processing, and insulation-parameter analysis can improve the characterization, diagnosis, and lifetime assessment of winding insulation degradation in induction machines. The following hypotheses are formulated:

- A low-to-high-frequency parametric induction-motor model enables efficient drive-system characterization by capturing impedance, resonances, cable–motor interactions, and transient terminal overvoltages for insulation-stress assessment and high-frequency switching transient analysis.
- Fractional-domain analysis of high-frequency switching transients extracts highly relevant diagnostic features for estimating winding inter-turn insulation degradation, enabling earlier and more reliable pre-emptive insulation wear-out detection.
- A physics-informed parametric model captures various insulation-degradation-sensitive electrical parameter variations, providing a basis for comprehensive state-of-health reporting, including insulation condition assessment, aging-state estimation, health-index mapping, and remaining useful life evaluation.

1.5 Research Tasks

To validate the proposed hypotheses, targeted research tasks focus on wider-frequency-bandwidth (BW) machine modeling, insulation-degradation characterization, and physics-informed parameter tracking. The specific research tasks are outlined as follows:

- Develop a low-to-HF parametric GBM of the IM and power cable.
- Incorporate inverter–cable–machine interactions as a drive-system model.
- Analyze HF impedance characteristics, including multiple resonance cases.

- Quantify multiple terminal overvoltage stress mechanisms, resonance analysis, and machine-cable impedance interactions.
- Develop a *time-frequency* signal-processing framework that exploits inverter-induced switching oscillations without external excitation.
- Enhance diagnostic sensitivity to incipient insulation degradation by operating in an optimized fractional time–frequency domain.
- Design a resonance-centered feature extraction strategy aligned with machine HF common-mode impedance characteristics to detect degradation-sensitive signatures.
- Establish a state-estimation factor (SEF) for insulation condition assessment under various experimental conditions.
- Use the proposed GBM to track insulation dielectric parameter variations, particularly inter-turn and ground-wall capacitances, loss components, impedance, resonance, and phase characteristics during controlled accelerated thermal-aging cycles.
- Correlate the evolution of insulation-related parameters with lifetime estimations.

1.6 Contribution and Dissemination

The research findings and results have been disseminated through presentations at international conferences, scientific seminars and peer-reviewed journals. This thesis is based on 6 research papers, including 3 journal papers and 3 conference papers.

1.6.1 Scientific Novelties:

- Presented a physically interpretable low-to-HF machine model for identifying multiple electrical and insulation-related parameters, extending conventional analysis beyond a single dominant resonance.
- Developed a resonance-guided fractional-domain diagnostic approach using optimal FRFT and precise filtering to enhance weak interturn-insulation degradation signatures.
- Established a multi-parameter insulation-aging characterization framework using inter-turn and ground-wall capacitances, loss components, impedance, resonance, and phase characteristics to track progressive degradation.

1.6.2 Practical Novelties:

- Wider-frequency-band impedance measurements enable practical extraction of electrical and insulation-sensitive machine parameters without an additional HF voltage sensor and signal post-processing.
- Inverter PWM switching transients are utilized as inherently sensitive initiators of high-frequency transients, providing excitation for inter-turn degradation diagnosis, which is demonstrated under varying switching frequencies and reduced data-acquisition bandwidth, supporting practical implementation.
- Measured frequency response parameters are translated into a practical degradation-sensitive data set through controlled insulation-aging experiments.

1.7 Organization of the Thesis

The thesis structure is as follows:

- Chapter 2 reviews the state of the art in inverter-fed induction machine reliability, insulation degradation mechanisms, HF phenomena, existing diagnostic techniques, and frequency-dependent modeling approaches, and identifies the research gaps addressed in this thesis.
- Chapter 3 presents the proposed physics-informed HF modeling framework for cable-fed induction machine drive systems, including system description, grey-box modeling, parameter identification, model validation, and HF characterization of the electrical behavior.
- Chapter 4 describes the proposed high-sensitivity signal-based diagnostic methodology based on HF switching oscillations, fractional-domain signal processing, feature extraction, and comparative performance evaluation for early-stage insulation degradation detection.
- Chapter 5 presents the physics-informed parameter-based insulation health assessments using thermal aging experiments, thermal damage estimations and insulation lifetime evaluation.
- Chapter 6 summarizes the main scientific contributions and key findings of the thesis, discusses their industrial significance, limitations and presents recommendations for future research.

Abbreviations

AAF	Aging acceleration factor
AC	Alternating current
DC	Direct current
AI	Artificial intelligence
ANN	Artificial neural network
ASD	Adjustable-speed drive
BBM	Black-box model
BW	Bandwidth
CBM	RLC circuit-based model
CM	Common mode
CMV	Common-mode voltage (V_{CM})
CWT	Continuous wavelet transform
DF	Dissipation factor (also defined as $tan\ \delta$)
DM	Differential mode
EIM	Electrical insulation material
EIS	Electrical insulation system
EMI	Electromagnetic interference
EoL	End of life
EPRI	Electric Power Research Institute
EUT/DUT	Equipment/device under test
FEA/FEM	Finite element analysis/finite element method
FT/FFT	Fourier transform/Fast Fourier transform
FRA	Frequency response analysis
FRFT	Fractional Fourier transform
GaN	Gallium nitride
GBM	Grey-box model
HC	Heat cycle(s)
HF	High-frequency
HFCT	High-frequency current transformer
HSCT	High-sensitivity current transformer
HV	High-voltage
IDP	Insulation dielectric parameter(s)
IEC	International Electrotechnical Commission
IEEE	Institute of Electrical and Electronics Engineers
IAS	Industry Applications Society
IFRA	Impulse frequency response analysis
IGBT	Insulated-gate bipolar transistor
IM	Induction machine
IR	Insulation resistance

ISA	Impedance spectroscopy analysis
LF	Low-frequency
LGFB	Log-Gaussian filter bank
LV	Low voltage
MAE	Mean absolute error
MAPE	Mean absolute percentage error
MF	Medium-frequency
MFCC	Mel-frequency cepstral coefficient
ML	Machine learning
N	Neutral point
PSO	Modified particle swarm optimization
MSE	Mean squared error
OA	Optimization algorithm
PAI	Polyamide-imide
PD	Partial discharge(s)
PDIV	Partial discharge inception voltage
PE	Polyester
PEI	Polyester-imide
PoF	Physics of failure
PR	Parallel resonance(s)
PRPD	Phase-resolved partial discharge pattern
PWM	Pulse-width modulation
RLC	Resistance-inductance-capacitance (equivalent circuit)
RMFB	Resonance-centered Mel filter bank
RMSE	Root mean square error
RO	Resonance occurrence
ROA	Reliable operating area
RUL	Remaining useful life
SEF	State estimation factor
SFRA	Sweep frequency response analysis
SiC	Silicon carbide
SR	Series resonance
ARO	Anti-resonance occurrence
SWO	Transient switching oscillation
TLM	Transmission-line modeling
TOV	Line-to-line transient terminal overvoltage (V_{ab})
VFD	Variable-frequency drive
WBG	Wide-bandgap
WBM	White-box model
WT	Wavelet transform

Symbols

A	Scale factor in the Arrhenius thermal-endurance relationship.
a	Phase a of the three-phase induction machine.
A'_1	Intercept coefficient in the linearized Arrhenius relationship.
AAF	Aging acceleration factor relative to the reference temperature.
AAF_{eq}	Equivalent aging acceleration factor for a variable thermal profile.
AAF_i	Aging acceleration factor for temperature interval i.
B	Temperature-sensitivity constant in the Arrhenius thermal-endurance relationship.
B'_1	Slope coefficient in the linearized Arrhenius relationship.
C	Equivalent capacitance in the resonant-circuit expression, where specified.
C_{eq}	Equivalent capacitance for a branch.
C_{G1}	Terminal-side ground-wall insulation capacitance in the grey-box model.
C_{G2}	Additional ground-wall insulation capacitance in the grey-box model.
C_{gr1}	First ground-conductor parasitic capacitance in the cable model.
C_{gr2}	Second ground-conductor parasitic capacitance in the cable model.
C_{HF}	Equivalent capacitance associated with the HF common-mode response.
C_{Ph}	Phase-to-phase capacitance.
C_P	Phase-to-ground wall capacitance.
C_{p1}	First parallel parasitic capacitance in the cable model.
C_{p2}	Second parallel parasitic capacitance in the cable model.
C_{ph}	Phase-to-phase parasitic capacitance in the machine model.
C_{SUM}	Total low-frequency common-mode capacitance.
C_T	Inter-turn insulation capacitance.
D	Cumulative insulation damage.
$dD(t)$	Incremental insulation damage over time.
DF / $\tan\delta$	Dielectric dissipation factor.
$E_{0,m}$	*m-th* feature value for the healthy/reference condition.
E_q	Feature vector extracted for degradation condition q.
$E_{q,m}$	*m-th* feature value for degradation condition q.
f	Frequency.
f_o	Centre frequency
f_p	Parallel-resonance frequency.
f_r	Resonance frequency.
f_s	Series resonance frequency.
f_{sw}	Inverter switching frequency.
$\bar{h}$	Mean of the measured values in the model-fit assessment.
h_i	Measured value at sample i in the model-fit assessment.
$\hat{h}_i$	Model-estimated value corresponding to h_i.
I_a	Stator phase-a current.

I_{CM}	Stator common-mode current.
i_{CM}	Instantaneous common-mode current.
i_{CM-1}	Common-mode switching-transient current component associated with the first return path.
i_{CM-2}	Common-mode switching-transient current component associated with the internal winding/ground path.
i_{DM-1}	Differential-mode switching-transient current component.
$i_f(t)$	Fundamental component of the phase current.
$i_p(t)$	Instantaneous phase current, represented as the sum of fundamental, ripple, and switching components.
$R_{INS,br}$	Insulation resistance measured immediately before the final breakdown measurement.
$IR_{degraded}$	Insulation resistance measured under degraded conditions.
$IR_{healthy}$	Insulation resistance measured in the healthy reference condition.
$i_r(t)$	Ripple-current component of the phase current.
$i_{sw}(t)$	High-frequency switching-current component.
K	Number of frequency bins used in the filter-bank computational-cost expression.
k_{cycle}	Number of thermal-aging cycles used in the exposure-time calculation.
$K_\alpha(t,t')$	Kernel of the fractional Fourier transform.
t_{LIFE}	Total insulation lifetime in the Arrhenius model.
L_a, L_b, L_c	Self-inductances associated with phases *a*, *b*, and *c*.
L_C	Equivalent connector/internal-feed connector inductance.
L_{eq}	Equivalent inductance.
L_g	Ground-conductor inductance in the cable model.
L_{mag}	Magnetizing inductance.
L_r	Rotor per-phase inductance referred to the stator side.
L_{ref}	Nominal insulation lifetime at the reference temperature.
L_s	Stator inductance; subscripts identify the relevant winding or cable branch.
L_{s1}	First series inductance in the cable model.
L_{s2}	Additional series inductance representing frequency-dependent cable effects.
L_T	Inductance of the inter-turn branch in the grey-box model.
M	Number of filter-bank features in the feature-vector expressions.
M_{ab}	Mutual inductance between phases *a* and *b*.
MAE	Mean absolute error.
MAE_q	Mean absolute error of the features for degradation condition *q*.
$MAPE$	Mean absolute percentage error used to summarize model deviation.
M_{bc}	Mutual inductance between phases *b* and *c*.
M_{ca}	Mutual inductance between phases *c* and *a*.
$M_{C,ab}/M_{C,bc}/M_{C,ca}$	Mutual inductances associated with the cable connectors/internal conductors.
MSE	Mean square error.

N	Number of observations or sampled temperature intervals.
n	Number of distributed sections.
p	Fractional Fourier transform order.
$P_{initial}$	Initial parameter set of the proposed grey-box model.
P_{varied}	Parameter set after applying the prescribed variation to the initial parameters.
q	Index identifying a degradation or heat-cycle condition.
R	Equivalent resistance in the resonant-circuit expression, where specified.
K_{R^2}	Coefficient of determination used to assess model-fit quality.
R_E	Eddy-current/iron-loss resistance in the machine grey-box model.
R_{eq}	Equivalent resistance.
R_g	Ground-conductor resistance in the cable model.
R_{G1}	Ground-wall leakage resistance associated with branch G_1.
R_{G2}	Ground-wall leakage resistance associated with branch G_2.
R_{gr1}	First ground-conductor loss resistance in the cable model.
R_{gr2}	Second ground-conductor loss resistance in the cable model.
$RMSE$	Root-mean-square-error.
R_{p1}	First parallel loss resistance.
R_{p2}	Second parallel loss resistance.
R_r	Rotor resistance.
R_s	Stator resistance.
R_{s1}	Series resistance.
R_{s2}	Additional series resistance.
R_T	Resistance of the inter-turn branch in GBM.
s	Slip of IM.
T	Absolute temperature in the Arrhenius relationship.
t	Time variable.
T_{eq}	Damage-equivalent temperature for a variable thermal profile.
$t_{exposure}$	Thermal exposure duration per aging cycle.
T_F	Thermal index temperature.
T_i	Temperature at sampled interval *i*.
t_i	Student-t coefficient for the selected confidence level and degrees of freedom.
T_{ref}	Reference temperature.
u	Fractional-frequency variable in *FRFT*.
V_a	Instantaneous phase-*a* voltage with machine ground.
V_{ab}	Line-to-line terminal voltage or terminal voltage to access *TOV*.
V_b	Instantaneous phase-*b* voltage with machine ground.
V_c	Instantaneous phase-*c* voltage with machine ground.
V_{CM}	Stator common-mode voltage.
V_i	Incident travelling-wave voltage.

V_T	Terminal voltage.
X	Equal to $1/T$, or reciprocal absolute temperature in the linearized Arrhenius relationship.
$\bar{x}$	Mean EoL capacitance.
X_C	Capacitive reactance.
x^*_i	Reference/healthy feature or data value for sample i.
x_i	Feature/data value for sample i under the condition being evaluated.
X_L	Inductive reactance.
Y	Equal to $\log_{10}L$, or the Logarithm of insulation lifetime.
Z_c	Cable surge impedance.
Z_{CM}	Common-mode impedance.
Z_{DM}	Differential-mode impedance.
Z_l	Series line impedance in the cable model.
Z_m	Motor input impedance.
Z_p	Parallel impedance branch in the cable model.
α	Fractional-transform angle/order parameter as used in the FRFT kernel notation.
Γ	Voltage reflection coefficient at the cable–machine interface.
$\Delta(f_i)$	Percentage modeling error at frequency point f_i.
$\Delta IR\ (\%)$	Percentage change in insulation resistance relative to the healthy reference.
Δt_i	Duration of temperature interval i.
$\Delta x_q\ (\%)$	Percentage state-estimation factor for degradation condition q.
ϑ	Phase angle of the measured or modeled impedance response.
ϑ_{CM}	Common-mode impedance phase angle.
ϑ_{DM}	Differential-mode impedance phase angle.
κ_{ab}, κ_{bc}, κ_{ca}	Magnetic coupling coefficients between the corresponding phases.
σ	Sample standard deviation used for EoL threshold uncertainty.

2 State-of-the-Art Techniques for Machine Insulation Monitoring, Diagnosis, and Useful Life Estimation

Induction machines (IMs) are among the most widely used electric motors in industrial applications, spanning a power range from a few watts to several megawatts, and converting electrical energy into the required mechanical power. IMs are used in about 80 % of industrial applications, including petrochemicals, automotive engineering, mining, drive systems, aerospace, and nuclear power plants. Implementing early fault detection through appropriate condition monitoring and diagnostic techniques is crucial for saving time and resources [12], [13]. Studies [14], [15] discuss condition monitoring and fault diagnosis in IMs operating under grid supply, considering electrical, mechanical, and environmental factors. However, inverter-fed machines face additional challenges due to HF effects. The following sections discuss these challenges and review recent developments in motor modeling, condition monitoring, and fault diagnosis for variable-frequency-drive (VFD) and cable-fed systems.

2.1 Overview of Multiple Faults in Induction Machines

Although IMs are reliable, they remain vulnerable to interconnected electrical, mechanical, thermal, and environmental faults. Major induction-machine faults are typically classified into three categories: stator, rotor, and bearing-related faults. As shown in Figure 2.1, IEEE Industry Applications Society (IEEE-IAS) and Electric Power Research Institute (EPRI) surveys identify bearing faults as dominant (44% and 41%), followed by stator faults (26% and 36%), rotor faults (8% and 9%), and other faults (22% and 14%) [16].

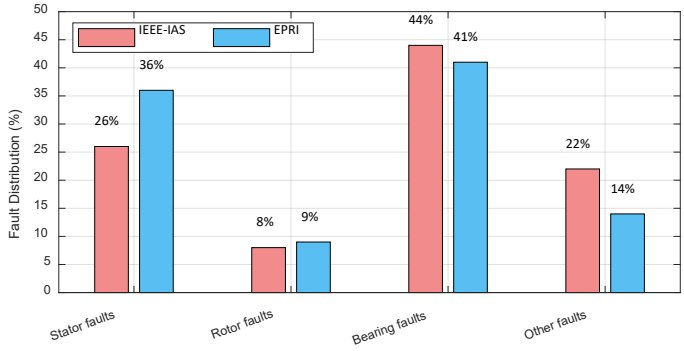


Figure 2.1. Distribution of IM faults according to IEEE-IAS and EPRI reliability surveys.

Literature shows that stator faults comprise one-third of IM faults [17], [18]. Stator insulation faults account for 30–40% of low-voltage (LV) motor failures and 60–70% of high-voltage (HV) motor failures [19], [20]. Insulation deterioration in inter-turn or phase-to-ground-wall (GW) can lead to short-circuit faults [21]. Abrupt motor failure can cause significant downtime and economic losses [22]. Table 2.1 summarizes the main electrical, mechanical, thermal, and magnetic faults in IMs, together with their typical effects on machine operation and reliability. It also highlights inverter-related electrical stresses that can accelerate winding-insulation degradation. Therefore, reliable methods

for monitoring motor insulation conditions are needed to provide early indication of potential failures and support preventive maintenance.

Table 2.1. Classification of IM Faults and Inverter-Related Electrical Stresses.

Fault Category	Typical Faults	Main Effect
Stator electrical faults	Turn-insulation degradation	Progressive deterioration preceding electrical breakdown
	Ground-wall insulation degradation	Leakage or breakdown between winding and grounded core/frame
	Inter-turn short-circuits	Local circulating current, heating, progressive winding damage
	Phase-to-phase short circuit	High fault current between phases
	Phase-to-ground fault	Electrical breakdown between winding and grounded core/frame
	Winding open circuit	Phase imbalance and torque reduction
Rotor electrical faults	Broken bars	Current asymmetry, torque pulsation, and localized heating
	Cracked end rings	Rotor-current imbalance and reduced electromagnetic performance
Mechanical faults	Bearing faults	Increased vibration, friction, and temperature
	Shaft misalignment	Vibration and uneven mechanical loading
	Eccentricity	Uneven air gap and unbalanced magnetic forces
Thermal faults/ stresses	Winding overheating/ localized hotspots	Accelerated insulation aging and reduced insulation lifetime
Magnetic/ core faults	Core or interlaminar insulation faults	Increased core losses and localized heating
Inverter-related stresses	High dv/dt (voltage gradient)	Repetitive electrical stress on turn and ground-wall insulation
	Terminal overvoltage (TOV)	Increased terminal voltage due to cable–machine impedance parameter mismatch, increasing winding insulation stress
	Common mode voltage (CMV/V_{CM})	Common mode currents, bearing voltage, and additional insulation stress
	Resonances (series and parallel)	Amplification or redistribution of HF voltage and current, potentially increasing winding stress

2.2 PWM Inverter-Related Stresses

PWM inverters in modern drives introduce several HF electrical stresses that are not present under grid-fed supply conditions. Fast switching transitions and HV gradients generate transient phenomena that propagate through the cable and machine winding system. These phenomena include multiple TOV characteristic frequencies, CMV, and winding resonances, which may result in non-uniform voltage distribution, insulation overstress, electromagnetic interference (EMI), and accelerated machine aging, as presented in Figure 2.2. Consequently, analyzing inverter-related stresses is essential to improving the reliability and lifetime of inverter-fed electrical machines.

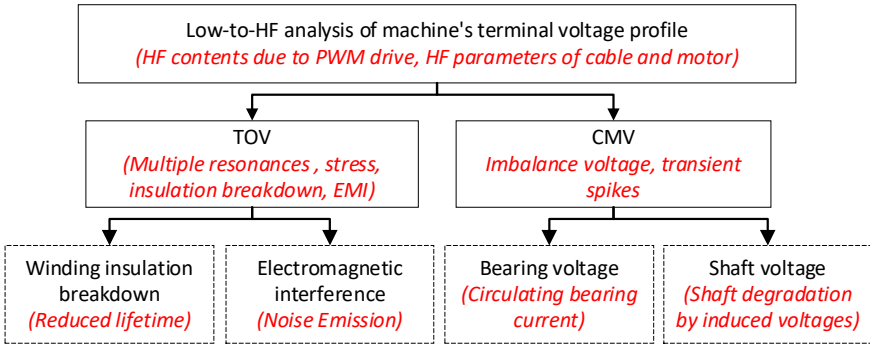


Figure 2.2. Challenges associated with the motor's terminal voltage profile.

2.2.1 Common Mode Voltage

Common mode voltage (CMV, V_{CM}) is defined as the average of the three inverter phase voltage quantities with respect to the direct-current (DC) link midpoint or machine's ground reference, as in (2.1).

$$V_{CM}(t) = \frac{V_a(t) + V_b(t) + V_c(t)}{3} \tag{2.1}$$

where V_a, V_b, and V_c are the instantaneous phase voltages with respect to the machine frame-ground. During PWM operation, rapid switching transitions generate HF CMV components that couple through the parasitic capacitances of the cable, stator winding, rotor, bearings, and machine frame. The resulting common-mode current can be approximated by (2.2).

$$i_{CM}(t) = C_{CM,eq} \frac{dV_{CM}(t)}{dt} \tag{2.2}$$

where $C_{CM,eq}$ represents the drive system's equivalent common-mode capacitance. Consequently, high voltage gradient values in modern switching devices can significantly increase common-mode current, shaft voltage, bearing current, and electromagnetic interference.

2.2.2 Terminal Transient Overvoltage

Transient TOV occurs when inverter-generated voltage pulses propagate through the motor cable and are reflected at the machine terminals due to a mismatch between the cable surge impedance (Z_c) and motor input impedance (Z_m). The voltage reflection coefficient is given by (2.3).

$$\Gamma = \frac{Z_m - Z_c}{Z_m + Z_c} \tag{2.3}$$

Terminal highest voltage due to traveling wave can be expressed as (2.4).

$$V_T = V_i(1 + \Gamma) \tag{2.4}$$

Where V_i is the voltage level of incident traveling wave front. Under severe mismatch conditions between cable and machine parameters, the reflected and incident waves may add constructively, producing terminal voltages approaching twice or higher than the incident voltage. Another way to track multiple TOVs is to identify the RLC equivalent parameters of the cable and machine and analyze their interaction among the inverter, cable and machine. Such repetitive TOV increases electrical stress on the inter-turn and ground-wall insulation systems, thereby accelerating insulation degradation.

2.2.3 Resonance Occurrence Phenomena in Machine's Winding

At low-to-HF, the distributed inductances and capacitances of stator windings form resonant circuits that exhibit frequency-dependent impedance characteristics producing series resonance (SR) and parallel resonances. The resonance frequency (f_r) can be formulated as (2.5).

$$f_r = \frac{1}{2\pi\sqrt{LC}} \tag{2.5}$$

Where L and C are the equivalent inductance and capacitance of the winding system. At SR, the corresponding inductive and capacitive reactance become equal, as in (2.6).

$$X_L = X_C \tag{2.6}$$

An example of RLC circuit representations is illustrated in Figure 2.3. For $R = 10\ \Omega$, $L = 10$ mH, and $C = 1\ \mu$F, the resonant frequency is calculated as $f_r = 1.59$ kHz.

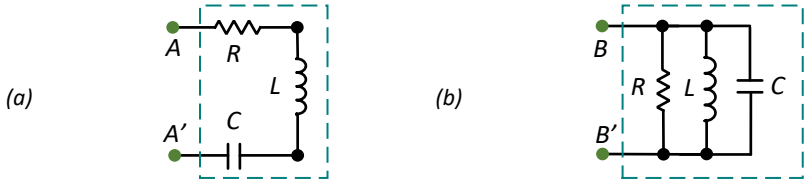


Figure 2.3. RLC circuit representations: (a) series branch and (b) parallel connection.

Figure 2.4 illustrates the impedance–resonance characteristics for the series and parallel circuit representations. Series resonance produces a minimum impedance of approximately 10 Ω, increasing current intensity. Conversely, during parallel resonance, the input impedance reaches its maximum value; this causes localized overvoltage in certain areas of the winding, concentrating electrical stress on the initial winding turns and contributing to premature insulation deterioration in inverter-fed machines.

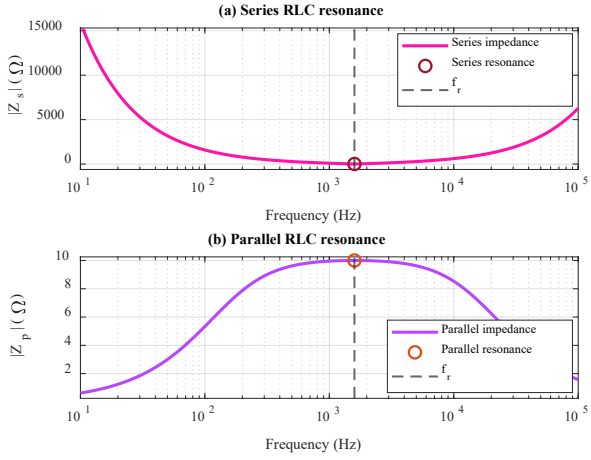


Figure 2.4. Impedance characteristics: (a) series RLC resonance, (b) parallel RLC resonance.

2.3 Insulation Degradation Monitoring and Diagnosis

As illustrated in Figure 2.5, the aging of an EIS is determined by several factors that come into consideration both before and during the machine's operation [23], [24]. Manufacturing and drive-train design parameters define the insulation's initial state, while operational electrical stress, temperature, mechanical loads, and environmental conditions drive progressive degradation. These stress factors are highly interconnected: for instance, switching operations can increase both electrical and thermal stresses, while sudden temperature fluctuations can simultaneously trigger thermal and mechanical aging processes. Consequently, an EIS's remaining useful life cannot be attributed to a single stress mechanism. This necessitates multi-physics approaches to evaluate degradation and estimate useful life, drawing on manufacturer data, accelerated aging tests, statistical models, PoF models, and data-driven prognostic techniques.

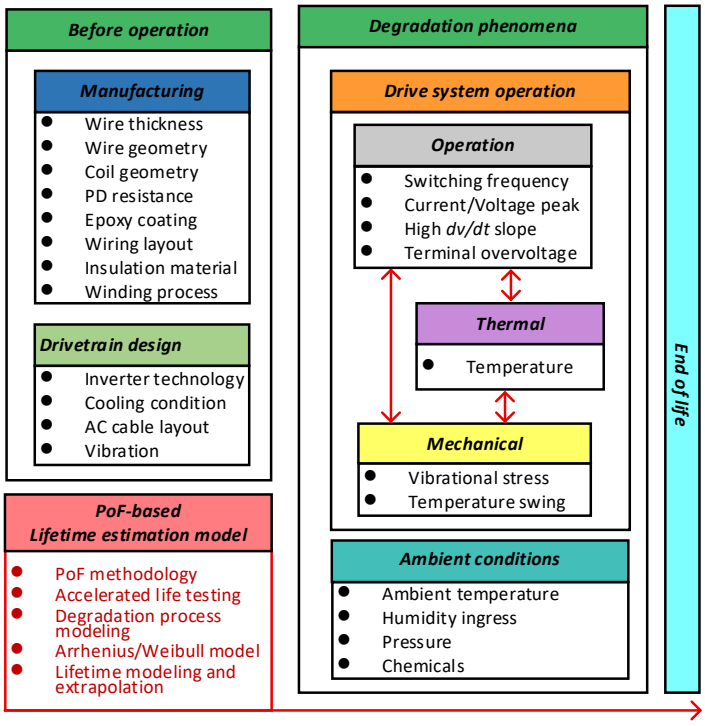


Figure 2.5. Multi-physical factors driving EIS degradation and PoF-based lifetime estimation.

Several IEC and IEEE standards provide established procedures for evaluating individual aspects of EIS condition and aging. IEC 60034-18-21 [25] and IEEE-117 [26] specify thermal aging and functional evaluation procedures for wire-wound insulation systems, including thermal, mechanical, moisture, and diagnostic sub-cycles. IEC 60034-18-41 extends the qualification framework to insulation systems supplied from voltage converters, considering impulse rise time, terminal-voltage overshoot, PD inception, and converter-induced electrical stresses [27]. IEC 60034-27-1 and IEC 60034-27-2 provide complementary diagnostic procedures for offline and online PD measurements, respectively, while IEC 60034-27-3 addresses dielectric dissipation-factor measurements.

IEEE standards additionally provide established practices for insulation-resistance, dielectric, and winding-condition assessment. Collectively, these standards address important individual stress and diagnostic mechanisms; however, integrating them with impedance-frequency-derived degradation markers and multi-physical PoF-based lifetime assessment remains an area for further development.

2.3.1 Insulation Condition Monitoring Techniques

Existing insulation degradation methods include conventional insulation resistance tests, PD measurements, signal feature-based methods using multiple measurement schematics, and impedance-based parametric model-based methods. More recently, researchers have adopted advanced signal processing, physics-based modeling, and artificial intelligence (AI)-driven techniques to improve diagnostic sensitivity and accuracy. Table 2.2 summarizes the major insulation condition monitoring techniques considered in this thesis.

Table 2.2. Summary of Main Techniques for Electrical-Machine Insulation Condition Monitoring.

Category	Technique/ method	Main quantity/signal	Limitations/ challenges	Typical insulation target
Conventional electrical tests	DC insulation resistance	R_{ins}, leakage current	Low sensitivity; offline only	Ground-wall, phase-to-ground
	Polarization index	R_{10min}/ R_{1min}	Slow; environment-dependent	Ground-wall
	Dissipation factor / *tan δ*	*tan δ*, dielectric losses	Low sensitivity; offline-only	Ground-wall / phase-to-ground
PD methods	PD measurements	Charge, PDIV, pulse patterns	Noise-sensitive, setup and interpretation complexity	Ground-wall, inter-turn defects
	HFCT-based PD monitoring	HF discharge-current pulses	Noise, complex interpretation	Ground-wall, surface / internal PD defects
Signal feature-based methods	PWM HF switching-transient current	PWM-switching transient/ringing current	PWM- and noise-dependent	Inter-turn
	CM / DM leakage-current monitoring	CM/DM voltage and leakage current	Weak early-fault signatures	Phase-to-phase/ground-wall
	Impedance monitoring	CM impedance, capacitance and dissipation factor	Sensor BW, operating-condition dependent	Inter-turn/ground-wall
	FT/CWT/ FRFT	Frequency-domain features	Limited early-fault sensitivity and physical interpretability	Inter-turn
	FRFT with filter-bank	**Filtered features**	**Parameter optimization required**	**Incipient inter-turn insulation**
Parametric model-based methods	Frequency response analysis (phase gain/sweep/impulse)	Impedance magnitude and phase, resonance shifts	Requires accurate modeling & parameter identification	Inter-turn / phase-to-phase / ground-wall
	Grey-box RLC parametric modeling	***R, L, C_T, C_G*, resonance parameters**	**Baseline needed; interpretation difficult**	**Inter-turn /phase-to-ground/ ground-wall**
AI / data-driven/ hybrid methods	Machine learning/ ANN, SVM	Learned insulation-sensitive features	Data-dependent; low interpretability	Multiple insulation faults
	Physics-informed hybrid monitoring, digital twin-based diagnostics	Model parameters + measured signals + ML	High implementation complexity	Multiple insulation faults

**Bold marking refers to methods discussed in this thesis.*

2.3.1.1 Conventional Electrical Tests

Well-known tests for the condition of insulation elements in induction machines are carried out offline. Standardized techniques such as surge, polarization index, and offline partial discharge tests can diagnose the condition of several insulation elements [28]. Recently, several offline techniques using the inverter have been reported to detect insulation conditions based on indicators such as insulation capacitance (IC) and dissipation factors (DF) [29].

2.3.1.2 Partial discharge-based methods

Partial discharge (PD) monitoring is a widely adopted technique for the early detection of insulation degradation. PD measurements evaluate parameters such as discharge magnitude, apparent charge, PD inception voltage (PDIV), phase-resolved PD (PRPD) pulse patterns, and HF current transformer (HFCT)-based methods to identify ground-wall and phase-to-phase insulation defects [30], [31]. Several online monitoring methods have also been proposed for stator insulation. PD online measurement, based on the principle of offline PD testing, is commonly used. However, its biggest challenge is interference from noise in the inverter-driven motor operating environment [7].

2.3.1.3 Signal Feature-Based Method

This method assesses electrical machine insulation by measuring voltage and current signals under different connection configurations/schematics. The acquired signals, including phase current, common-mode current, differential-mode current, and common-mode voltage, are processed to extract features associated with insulation condition. Changes in these features can then be used to identify insulation degradation and assess its progression, as represented in Figure 2.6.

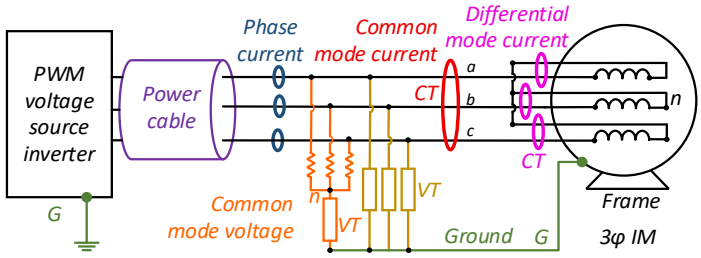


Figure 2.6. Electrical signal measurement for insulation monitoring.

Inverter-based measurements utilize the HF excitation naturally generated by PWM inverters to monitor insulation condition online [32]. Depending on the connection schematics, insulation information can be extracted from PWM switching-transient current ringing, CM or DM leakage currents, or measurements of CM impedance, capacitance, and dissipation factor [33], [34]. These methods have demonstrated sensitivity to inter-turn and ground-wall insulation degradation. However, weak early-fault signatures could be masked by PWM operation modes, sensor BW limitations, and measurement noise, which may affect their performance [34]. The IC and DF were analyzed to assess the insulation degradation trends in high-resistance grounding systems [35] and the leakage current induced by the inverter-generated CMV was measured to evaluate dielectric loss and capacitive behavior under different aging conditions.

Time-frequency analysis of HF switching-transient fed-current responses provides a useful approach for detecting insulation degradation in motor windings [36], [37]. Common signal-processing techniques include the Fourier transform (FT), continuous wavelet transform (CWT), and fractional Fourier transform (FRFT). These methods analyze transient signals in different transform domains to identify insulation degradation.

While conventional frequency-domain methods often show limited sensitivity to incipient faults and are difficult to interpret physically, more advanced approaches such as the fractional Fourier transform (FRFT) combined with filter-bank-based processing can demonstrate degradation-related features and improve detection of early-stage inter-turn insulation faults. However, their performance depends on selecting and optimizing appropriate tuning parameters.

2.3.1.4 Model-Based Methods

Model-based methods assess the condition of a machine's insulation by relating EIS parameter changes in the winding to variations in equivalent electrical RLC model parameters and HF impedance characteristics [38]. These approaches include frequency response analysis (FRA) and HF equivalent-circuit modeling, where insulation degradation is identified through changes in impedance magnitude, phase response, and resonance frequencies. Electric machine models can be classified as white-box models (WBM), black-box models (BBM), and grey-box models (GBM).

1) *White-box model*: A physics-based model that describes a system using its physical laws and parameters, such as FEM/FEA and transmission-line modeling (TLM).
2) *Black-box model:* A data-driven model that learns the relationship between inputs and outputs using measured data, such as machine learning (ML) and artificial neural networks (ANNs), without knowing the actual physical behavior.
3) *Grey-box model:* A hybrid model that combines physical knowledge with experimentally measured data to estimate model parameters, providing a balance between physical accuracy and computational efficiency [39].

2.3.1.5 Artificial Intelligence, Data-Driven and Hybrid Methods

AI- and data-driven methods use machine learning algorithms to identify insulation degradation patterns from measured electrical signals and diagnostic features. Techniques such as artificial neural networks (ANNs), support vector machines (SVMs), and deep-learning architectures can enable automated classification of insulation-degradation patterns. Furthermore, hybrid approaches combine physics-based models with data-driven learning, enabling more reliable and interpretable assessments of insulation degradation, even under varying operating conditions.

2.3.2 Role of GBM in Characterization of Electric Machines

GBMs combine physics-informed knowledge with measurement-based parameter identification. They describe the machine's behavior using practical parameters such as resistance (R), inductance (L), inter-turn capacitance (C_T), and ground capacitance (C_G). These models represent impedance-frequency behavior over wider frequency ranges and support insulation diagnostics, but they require baseline measurements and accurate parameter identification.

2.4 Estimations of Useful Life and Prognostics

Recently, assessing the remaining useful life of insulation in induction machines has shifted from traditional time-to-failure testing to approaches focused on degradation and prognostics. Through accelerated thermal aging, combined with measurements of insulation resistance, capacitance, and dissipation factor, it is possible to detect trends in insulation deterioration well before an actual dielectric failure occurs [40], [41]. Arrhenius-based models relate thermal stress to insulation lifetime, while Weibull analysis captures statistical variability in failure times [29]. Curve-fitting and ML/ANN methods have further demonstrated accelerated lifetime prediction from limited aging data [41]. More advanced approaches use Wiener-process degradation models and Arrhenius-based PoF formulations to describe degradation trajectories and reliability percentiles [29], while recent work incorporates thermal-mechanical stress and temperature cycling for lifetime prediction [23].

However, many existing lifetime models primarily relate applied thermal stress or statistically modeled degradation trajectories to time-to-failure, while giving comparatively less attention to extracting multiple physically interpretable dielectric parameters from machine impedance-frequency measurements and mapping their evolution to insulation health and RUL. Therefore, degradation-sensitive impedance parameters that reflect changes in inter-turn and ground-wall insulation provide an opportunity to bridge physics-based electrical characterization with condition-based insulation prognostics.

3 High-Frequency Modeling of Cable-Fed Motor Drives

Fast-switching inverter-fed drives exhibit complex HF interactions among the inverter, cable, and machine, producing CMV, TOV, and multiple resonances. This chapter develops an optimized low-to-HF GBM over wider frequency ranges, combining impedance-based analytical parameter identification with optimization to more precisely characterize cable–motor interactions, multiple TOV stresses, and AROs.

3.1 Cable-Fed Drive Systems

A cable-fed IM drive comprises a PWM motor drive unit, power cable, and machine as presented in Figure 3.1 whose coupled parametric impedances determine the HF response [18], [42]. Cable transmission-line effects and machine parasitic parameters produce multiple TOV resonances [43]. Consequently, characterizing the combined cable–motor RLC equivalent impedance is required to identify critical resonance frequencies and evaluate terminal voltage stress as TOVs under different cable lengths and drive configurations.

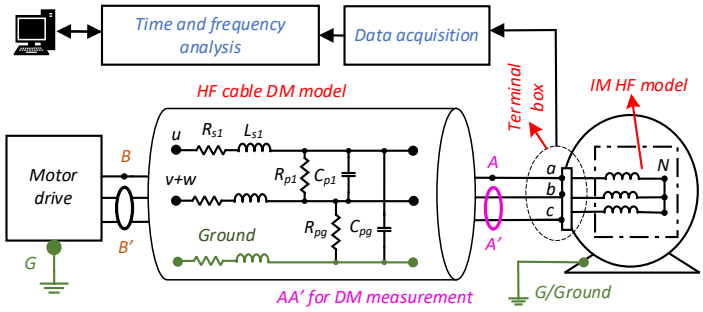


Figure 3.1. Typical configuration of a cable-fed motor drive.

Conventional operating range for different diagnostic IM approaches is limited by the fundamental supply frequency. Beyond this, the machine's impedance becomes highly frequency-dependent, as parasitic capacitances, winding inductances, ohmic losses, and electromagnetic coupling become more significant. The measured common-mode (CM) and differential-mode (DM) impedance response profiles most often demonstrate multiple resonances.

3.2 Impedance Measurement Setup and Results

3.2.1 Setup for Measuring Machine Impedance

The frequency-impedance profile is measured using an impedance analyzer (20 Hz–120 MHz). Variations in impedance amplitude and phase as a function of frequency are recorded for different connection configurations of IM under this study, as detailed in Table 3.1.

Table 3.1. Motor impedance spectrum measurement

Symbol	Configuration	Meaning/ elaboration
a–bc	$Z_{DM.Y}$	Impedance between phase *a* and phase *bc*
abc–G	$Z_{CM.Y}$	Impedance between phase *abc* and *G*
N–G	$Z_{NG.Y}$	Impedance between *N*/neutral point and *G*

Determining the parameters of the GBM model involves measuring CM and DM impedances for analytical calculations, followed by iterative optimization to obtain optimal impedance parameters. An impedance analyzer, covering the range of 20 Hz-120 MHz, is used to experimentally measure the machine in DM, CM, and NG. The machine is tested while stationary, using various motor winding configurations to determine its internal frequency response. A similar procedure is applied to the cable by measuring its differential-mode impedance under both open-circuit and short-circuit conditions. Figure 3.2 demonstrates the setup for measuring low–to–HF impedance spectra of machine and cable separately using an impedance analyzer.

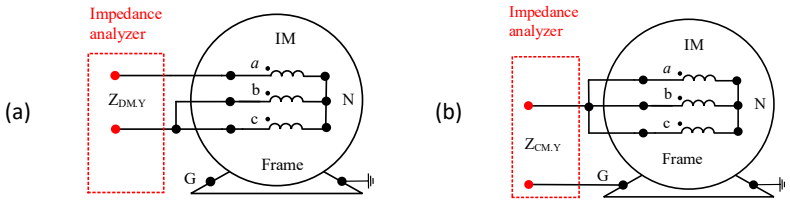


Figure 3.2. IM impedance measurement topologies: (a) DM, (b) CM.

3.2.1.1 Measurement results and Introduction to ARO

Anti-resonance occurrence (ARO) arises when the series resonance (SR) frequency of the machine's DM impedance coincides with the TOV resonance frequencies of V_{ab} voltage, as demonstrated in Figure 3.4. This typically causes a sharp dip in the winding impedance, reaching a minimum of 2 Ω in this IM case.

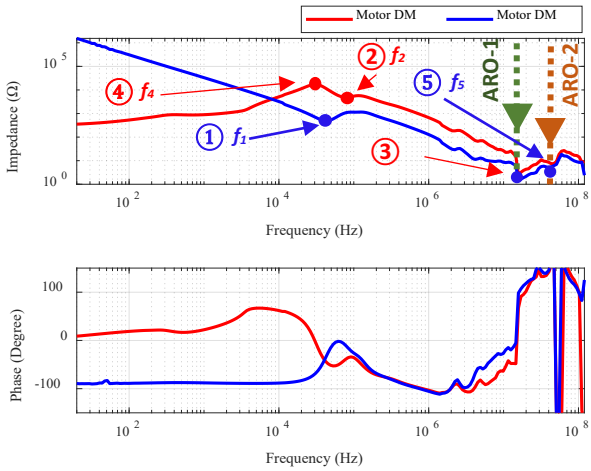


Figure 3.3. Measurement results showing the impedance profile for DM (red) and CM (blue).

Figure 3.4 shows the measured terminal-voltage spectrum V_{ab} (blue) and DM impedance (red), highlighting four TOV resonance peaks and two critical AROs (ARO-1 and ARO-2).

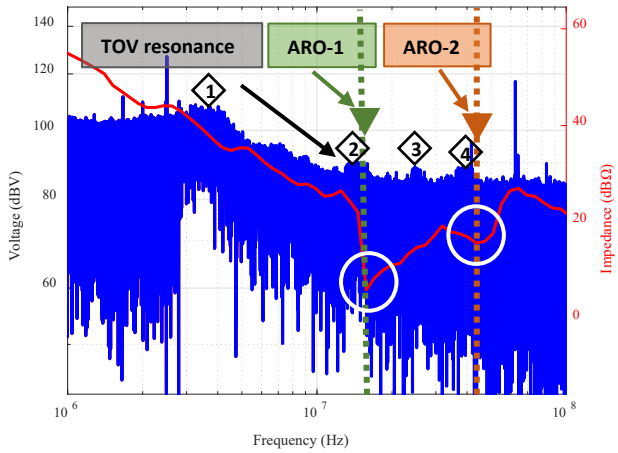


Figure 3.4. Measurement results showing the terminal voltage spectrum V_{ab} (FT; blue, left axis) with DM impedance (red, right axis), showing four TOVs/ resonance frequencies (◊ marker).

3.3 Impedance Parameter Characterization of GBM

The proposed GBM represents the IM using physically relevant self- and mutual inductances, inter-turn branches, parasitic capacitances, and ground-wall parameters. Analytical estimates obtained from CM/DM impedance measurements initialize an optimization-based fitting procedure. The resulting model reproduces impedance behavior up to 100 MHz and supports TOV, CMV, resonance, sensitivity, and insulation-stress analyses.

3.3.1 Proposed GBM Modeling Approach

To accurately characterize the HF electrical behavior of cable-fed IM drive systems, this work proposes a physics-informed GBM approach. Unlike conventional LF equivalent circuits, the proposed model incorporates the frequency-dependent electrical characteristics of both the machine and the connecting cable while preserving the physical interpretation of the model parameters.

3.3.2 Optimal Characterization of Machine GBM Parameters

The modified particle swarm optimization (MPSO) algorithm optimizes the GBM parameters using analytical initial values within a ±20 % search range. Objective functions defined in (3.1) minimizes the mean squared error (MSE) between measured and modeled impedance magnitudes and phase angles, while the optimized parameters remain within a 6 % deviation, demonstrating accurate and robust parameter identification across the investigated frequency range.

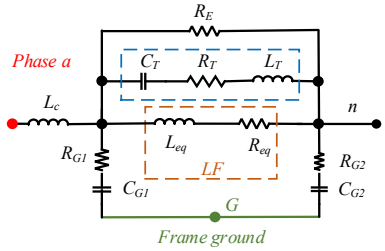
$$Obj_1(x_j) = \frac{1}{n}\sum_{i=1}^{n}[\left|Z_{ini}(f_i,x_j)\right| - \left|Z_{prac}(f_i,x_j)\right|]^2 \text{ and}$$
$$Obj_2(x_j) = \frac{1}{n}\sum_{i=1}^{n}[\left|\theta_{ini}(f_i,x_j)\right| - \left|\theta_{prac}(f_i,x_j)\right|]^2 \quad (3.1)$$

A lower mean squared error (MSE) suggests a better model fit. MPSO algorithm uses an adaptive strategy inspired by bird flocking behavior, enabling it to search for optimal solutions in complex, non-linear, multimodal solution spaces [52]. The low-to-HF characterization comprises analytical parameter identification followed by optimization-based parameter estimation through impedance matching, with time and frequency-domain simulations closely agreeing with measurements.

3.3.3 Proposed Machine GBM

The proposed model (Figure 3.5) combines analytical parameter estimation with optimization-based identification to represent winding resistances, leakage inductances, parasitic capacitances, dielectric losses, and interactions with cable impedance over a wide frequency range. This approach balances computational efficiency and physical accuracy; it enables reliable reproduction of the measured frequency response while maintaining a direct link between the parameters and the machine's physical configuration and insulation system.

(a)



(b)

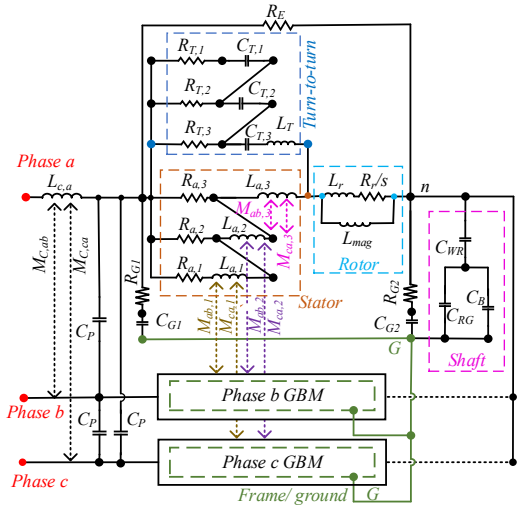


Figure 3.5. RLC circuit-based model of an IM: (a) conventional model, (b) proposed GBM.

The proposed model not only reproduces the HF impedance characteristics of the cable-fed drive system but also establishes the foundation for parameter identification, HF characterization, and the model-based diagnostic methodologies presented in the subsequent chapters. The following sections describe the development of the proposed model, the parameter extraction procedure, and the experimental validation.

3.3.3.1 GBM Parametric Identification of Machine

The proposed low-to-HF GBM uses a hybrid parameter-identification approach that combines analytical estimation and optimization-based fitting. Parameters related to the machine's geometry, including winding resistance and leakage inductance, and others are estimated analytically, while frequency-dependent parasitic elements are optimized using measured impedance data; this ensures physically consistent parameters and an accurate representation of cable-fed drive-system behaviour.

Equations (3.2)-(3.11) are used to calculate the GBM parameters; they are based on asymptotic tracking equations [44], [45]. The stator-winding resistance (R_{eq}) limits the motor phase current; its value is determined using an equivalent circuit diagram for the LF range, as shown in Figure 3.5. C_{HF} represents the total capacitance of the CM model in the HF range; it is calculated as follows (3.2).

$$C_{HF} = \frac{1}{2\pi f_{HF} Z_{HF.CM}} \tag{3.2}$$

Equivalent capacitance C_{SUM} is the total LF-CM capacitance, C_{G1} is the HF terminal-side parasitic ground capacitance, and C_{G2} is the LF neutral-point side parasitic ground capacitance. R_{G1} and R_{G2} are the corresponding insulation loss resistors and are calculated as (3.3)-(3.5).

$$C_{SUM} = \frac{1}{2\pi f_{LF} Z_{LF.CM}} \tag{3.3}$$

$$C_{G1} = \frac{1}{3} C_{HF},\ C_{G2} = \frac{1}{3}(C_{SUM} - C_{HF}) \tag{3.4}$$

$$R_{G1} = \frac{2}{3}|Z_3|,\ R_{G2} \approx \frac{1}{3}|Z_1| \tag{3.5}$$

The HF iron-loss-resistance R_E is estimated from f_4 frequency points as (3.6).

$$R_E = \frac{2}{3}|Z_4| \tag{3.6}$$

The inter-turn branch parameters are evaluated using (3.7)-(3.8).

$$C_T \approx \frac{1}{10}(C_{G1} + C_{G2}),\ L_T \approx \frac{1}{C_T}\left(\frac{1}{2\pi f_2^2}\right)^2 \tag{3.7}$$

$$R_T = |Z_2|\cos(\theta_2) \tag{3.8}$$

The combined stator inductance L_a is obtained from LF winding impedance circuit model using (3.9).

$$L_a \approx \frac{|Z_{DM(LF)}|}{3\pi f_{LF}} \tag{3.9}$$

CM and DM inductance are estimated as in (3.10).

$$L_{CM} = \frac{1}{12\pi^2 C_{G2} f_1^2},\ L_{DM} = \frac{|Z_{DM.LF}|}{2\pi f_{LF}}\sin(\theta_{DM.LF}) \tag{3.10}$$

The connection inductances are determined from the corresponding impedance and resonance characteristics using (3.11).

$$L_C = \frac{3}{16\pi^2 C_{G1} f_3^2} \tag{3.11}$$

In continuation of the proposed GBM, the inter-turn series branch resistance R_T and inductance L_T are represented by a ladder network following (3.12).

$$Z_T(\omega) = \frac{1}{j\omega C_{T,2}} + [\frac{1}{R_{T,2}} + \frac{1}{(\frac{1}{j\omega C_{T,1}} + R_{T,1})}] \tag{3.12}$$

The connector/internal-feed inductance for phase–a , L_c , as in (3.13), together with capacitance C_{G1} , produces the AR at point f_3 in DM impedance:

$$L_C = L_{C,a} - M_{C,ab} \tag{3.13}$$

Here, $L_{C,a}$ and {$M_{C,ab}$, $M_{C,ca}$} denoted the self- and mutual coupling inductances of the connectors and internal feed/line conductors associated with phase–a (Figure 3.6).

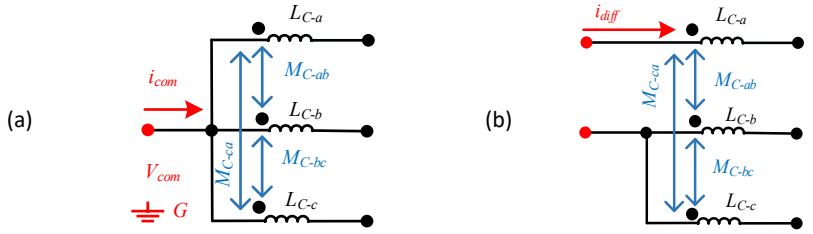


Figure 3.6. The self- and mutual inductances of the connections and internal line conductors schematics in (a) CM, (b) DM.

In the CM connection, the machine's CMV drives a ground current through a parallel path formed by ground-insulation capacitance (C_{G1}). The equivalent CM inductance L_5, which combines the connection-lead inductance L_{lead} and the connector/internal-lead contribution L_c=L_{ca}+2$M_{c,ab}$ (Figure 3.6a), as (3.14).

$$L_5 = L_{lead} + \frac{1}{3}(L_{c,a} + 2M_{c,ab}) = \frac{1}{3}\left(\frac{1}{(2\pi f_5)^2 C_{G1}}\right) \tag{3.14}$$

Accounting explicitly for L_{lead} at f_5 further refines the system's impedance behavior

In DM connection, DM current returns through the equivalent capacitance 2C_{G1}/3 and the equivalent inductance L_3 is (3.15)-(3.16).

$$L_3 = L_{lead} + \frac{3}{2}(L_{c,a} - M_{c,ab}) = L_{lead} + \frac{3}{2}(L_C) \tag{3.15}$$

$$L_3 = \frac{3}{2}\left(\frac{1}{(2\pi f_3)^2 C_{G1}}\right) \tag{3.16}$$

Accounting for the measuring-cable lead inductance L_{lead}, at the AR frequency f_3, further refines the system's impedance behavior.

Using (3.16), first-turn stator inductance L_C is obtained. Solving (3.13)-(3.16) yields the self and mutual inductance terms that define the inductive coupling coefficients $\kappa_{C\text{-}ab}$, $\kappa_{C\text{-}bc}$, $\kappa_{C\text{-}ca}$ for the other connection terminals as given in (3.17).

$$M_{C,ab} = \kappa_{C,ab}\sqrt{L_{C,a}L_{C,b}}, \quad M_{C,bc} = \kappa_{C,bc}\sqrt{L_{C,b}L_{C,c}}\ , \quad M_{C,ca} = \kappa_{C,ca}\sqrt{L_{C,c}L_{C,a}} \tag{3.17}$$

These coefficients enable an accurate, high BW approximation of magnetic coupling in a MATLAB/Simscape implementation. The equivalent inductances of the winding (L_{DM} and L_{CM}) are determined for each DM and CM measurement, as shown in Figure 3.7.

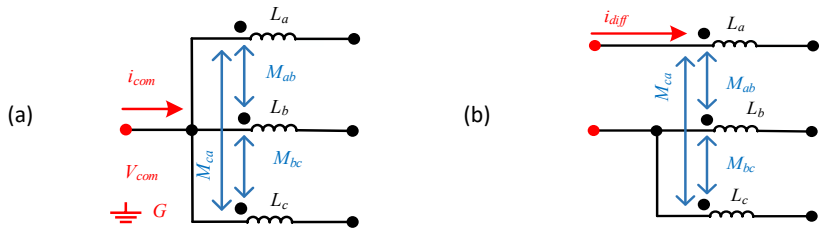


Figure 3.7. Winding self- and mutual inductance representation in (a) CM and (b) DM.

This process identifies the per-phase self and mutual inductances using (3.18)–(3.19).

$$L_{DM}=\frac{3}{2}(L_a-M_{ab})=\frac{|Z_{DM.LF}|}{2\pi f_{LF}}\sin(\theta_{DM.LF}) \tag{3.18}$$

$$L_{CM}=\frac{1}{3}(L_a+2M_{ab})\approx\frac{1}{3(2\pi f_1)^2 C_{G2}} \tag{3.19}$$

The self and mutual inductances are defined in (3.18) and (3.19) are then used to compute phase-to-phase coupling coefficients κ_{ab} , κ_{bc} , κ_{ca}. These coupling coefficients quantify the magnetic interaction between windings and depend on winding configuration and core properties. They are defined in (3.20), which improves the model's representation of machine behavior.

$$M_{ab}=\kappa_{ab}\sqrt{L_aL_b},\ M_{bc}=\kappa_{bc}\sqrt{L_bL_c},\ M_{ca}=\kappa_{ca}\sqrt{L_cL_a} \tag{3.20}$$

The number of mutual inductances incorporated into the model can be adjusted according to the desired level of complexity. Notably, each mutual inductance introduces three additional parameters, as three additional inductive coupling coefficients are needed to represent a three-phase mutual inductor. In this study, the coupling of phase *a* with corresponding three ladder sub-branches {$M_{ab,1}$, $M_{ca,1}$} , {$M_{ab,2}$, $M_{ca,2}$}, and {$M_{ab,3}$, $M_{ca,3}$} is illustrated in Figure 3.5b. These define the corresponding coupling coefficients {$\kappa_{ab,1}$, $\kappa_{ca,1}$}and {$\kappa_{ab,2}$ $\kappa_{ca,2}$}, {$\kappa_{ab,3}$, $\kappa_{ca,3}$} together with other phase sub-branches. The initial values are obtained using (3.20), and the mutual inductances are defined as (3.21).

$$M_{ab,1}=\kappa_{ab,1}\sqrt{L_{a,1}L_{b,1}},\quad M_{bc,1}=\kappa_{bc,1}\sqrt{L_{b,1}L_{c,1}}\ ,\ M_{ca,1}=\kappa_{ca,1}\sqrt{L_{c,1}L_{a,1}} \tag{3.21}$$

These identified elements are utilized in a Simulink-based IM model to parametrize interphase mutual coupling, thereby improving the proposed GBM's accuracy in representing these effects. Figure 3.8 illustrates the equivalent parametric circuit of IM for HF in both CM and DM configurations.

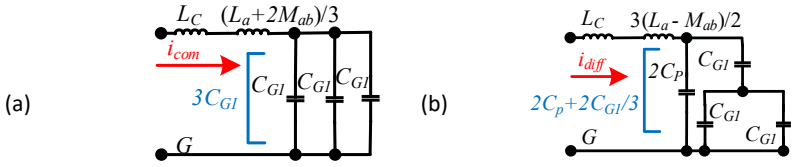


Figure 3.8. Initial HF IM equivalent circuits above 1 MHz: (a) CM and (b) DM configurations.

Also, the parameters C_{CM} and C_{DM} are obtained as in (3.22) [46].

$$C_{CM} = 3C_{G1},\ C_{DM} = 2C_P + \frac{2C_{G1}}{3} = \frac{1}{(2\pi f_4)^2 L_{DM}} \tag{3.22}$$

Similarly, a ladder network for HF modeling represents the stator branch, and the parameters (R_a, L_a) are extended accordingly as (3.23).

$$Z_a(\omega) = j\omega L_{a,2} + \left[\frac{1}{R_{a,2}} + \frac{1}{(j\omega L_{a,1} + R_{a,1})}\right] \tag{3.23}$$

3.3.3.2 IM's GBM Validation

Figure 3.9a and Figure 3.9b, compare the impedance profile showing impedance (Ω) and phase (Degrees) of the GBM, the universal model, and the experimentally measured data. GBM closely matches the measured impedance response across the entire frequency spectrum, demonstrating its effectiveness in frequency-response modeling.

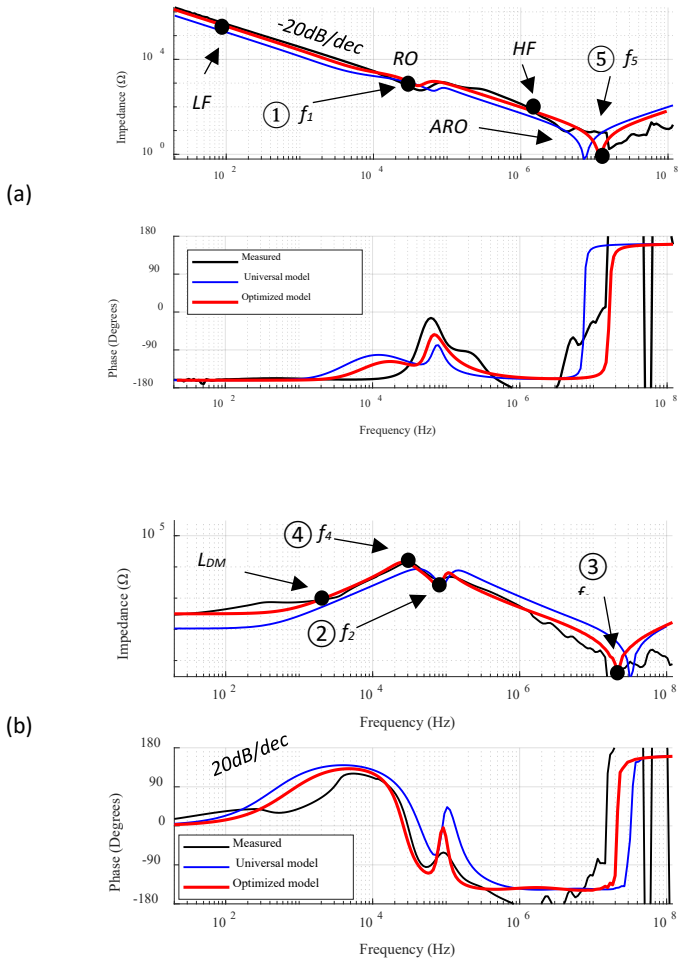


Figure 3.9. Matching of the impedance profile of measured results, the universal machine model, and the proposed optimal GBM for (a) CM and (b) DM typologies.

3.3.4 Grey-Box Model of Cable

For the HF impedance characterization of cables, a GBM is developed using a methodology similar to that employed for electrical machines. The GBM is based on a lumped-parameter equivalent circuit, in which the cable is represented by a series of interconnected sections to account for its distributed electrical characteristics. The parameters of the sectional model are initially determined analytically from impedance measurements obtained using the connection configurations illustrated in Figure 3.10 and the optimal parameters of the initial GBM model (represented in Figure 3.11) are estimated using similar OA via impedance fitting. Cable parameters consist of a straightforward line impedance Z_l in series and Z_p parallel elements for accurate identification. Their extraction involves short-circuit (SC) and open-circuit (OC) cable impedance measurements in DM schematics using phases.

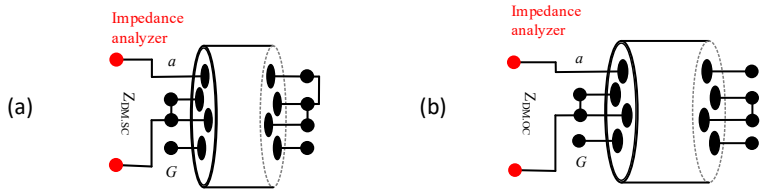


Figure 3.10. DM cable measurement schematics (a) SC mode (b) OC mode.

The HF cable parameters R_{s1}, L_{s1}, are extracted from SC impedance in the DM schematics (Figure 3.10 (a)). The parameters R_{s2} and L_{s2} account for skin and proximity effects, while R_{p1}, C_{p1}, R_{p2}, $C_{p2,}$ represent dielectric losses and parasitic capacitance between phase conductors, identified from DM open-circuit tests (Figure 3.10 (b)).

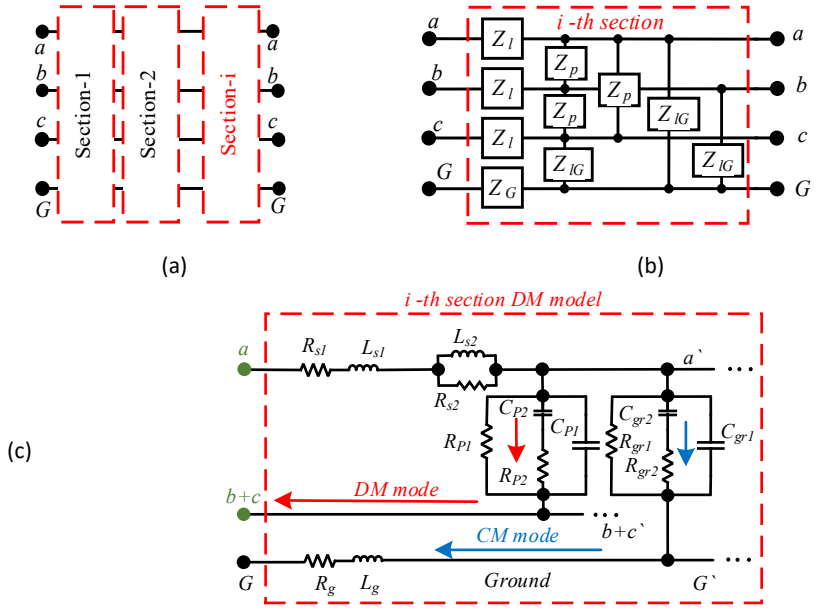


Figure 3.11. Cable HF representation: (a) Multi-section model of a cable, (b) Three-phase representation with HF parameters, and (c) GBM of cable in DM schematics.

Additionally, the parameters for the ground conductor line (R_g , L_g, R_{gr1} , R_{gr2}, C_{gr1}, and C_{gr2}) characterize the ground conductor impedance, which defines the return path of CM currents. The cable used is an unshielded, PVC-insulated, five-core cable with a 6.0 mm² conductor area. Because the same five-conductor cable is used, these parameters remain consistent across sections, ensuring uniform impedance characteristics and accurate representation of the cable's frequency behavior. A unit-length cable model with ten cascaded sections is scaled to the full cable length.

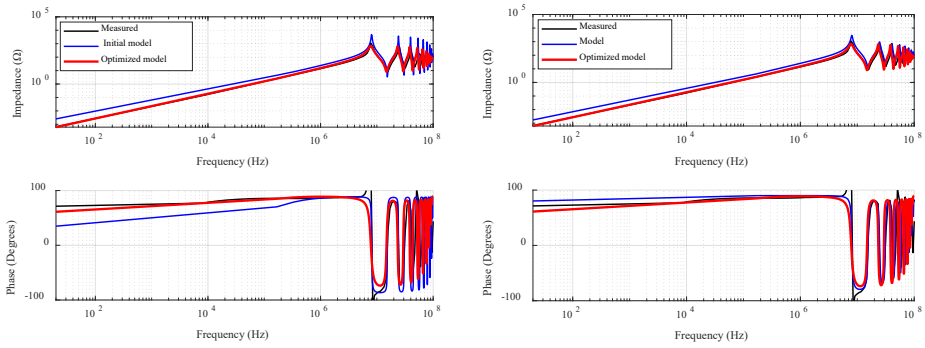
3.3.5 Identification of Cable Model Parameters

GBM simplifies the calculation of impedance parameters using the 20-dB/decade slope in both LF and HF ranges, as detailed in the author's work [47]. This methodology enables the initial identification of frequency-response cable parameters.

Afterward, the optimal parameterization of the cable model follows the same procedure of optimal fitting using MPSO as OA in machine parameter characterization, by applying the error minimization cost function defined in (3.1). As with machine parameter estimation, the optimization starts with analytical initial cable values and a 20% variation range, allowing the OA to refine the parameters for the best fit. The final optimal values again show only a 6% deviation from experimental cable-impedance measurements. This study contributes to developing a precise and efficient impedance modeling approach that minimizes manual tuning time.

3.3.6 Cable's GBM Validation

Figure 3.12(a) and Figure 3.12(b) compare the measured (black), initial (blue), and optimized GBM (red) impedance profile of the cable's DM network in OC and SC configurations, respectively.



(a) (b)

Figure 3.12. Matching impedance profile results of measured, initial model, and optimized model for cable connection topologies: (a) OC and (b) SC.

3.3.7 Error Analysis of Motor and Cable Modeling

To present the percentage error and deviation from practical measurement, an average deviation or mean absolute percentage error (MAPE) is calculated across multiple frequency points (f_i), as (3.24)-(3.25).

$$\Delta(f_i) = \left| \frac{|Z_{optimal}(f_i)| - |Z_{practical}(f_i)|}{|Z_{practical}(f_i)|} \right| \times 100 \tag{3.24}$$

$$MAPE = [\sum_{i=1}^{k} \Delta(f_i)] / k \tag{3.25}$$

To represent robust modeling, a detailed error analysis is provided, with boxplots shown in Figure 3.13 highlighting the impedance magnitude error distribution and GBM improvements. GBM-optimized models significantly improve accuracy: the initial model's mean error was 6.7% for motor CM schematics, and after GBM optimization, it dropped to 5.7%.

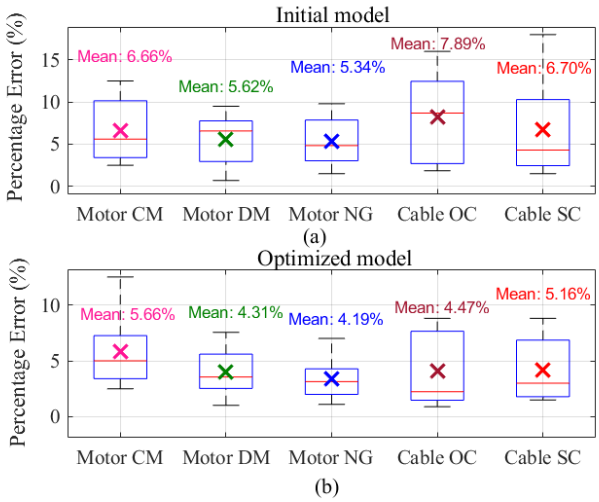


Figure 3.13. Error boxplots for various nominated topologies compared with measurements (a) Universal/initial model (top) (b) Optimized model (bottom).

3.4 Time Domain Analysis

3.4.1 Practical Test-bench Details and Model Simulation

The practical setup involves a 7.5-kW four-pole IM with a star-connected stator winding, powered by a PWM voltage inverter, operating at a 560 V DC-link, 4.5 kHz switching frequency, 2.7% slip, and cables of different lengths. The IM fundamental frequency in the drive system is set to 50 Hz, matching the supply frequency. The voltage and current are measured using high-bandwidth differential voltage probes (100 MHz) and current probes (120 MHz) directly connected to the motor terminals.

Terminal voltage was measured across the line-to-line connection terminals. The CMV was calculated from the measured terminal voltages using the relationship reported in [48]. The practical hardware operates with a 5 ns time step, a 200 MS/s sampling rate, and a 25 ms total measurement time, capturing frequencies up to 100 MHz with a 40 Hz fast Fourier transform (FFT) step size with MATLAB implementation. The proposed model improves on this with a 1 ns time step, a 1 GS/s sampling rate, and a 30 ms simulation time, enabling a 33.3 Hz frequency step and improving the model's accuracy. Simulations were carried out in MATLAB-Simulink environment, allowing flexible motor–cable–inverter modeling and time- and frequency-domain analysis. Figure 3.14 depicts the cable-fed test bench used to capture multiple TOVs and CMV.

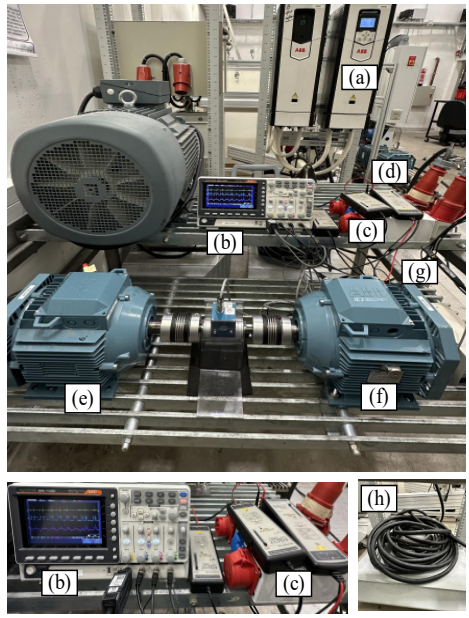


Figure 3.14. Test bench of the IM: (a) ASD inverter, (b) oscilloscope, (c) HF differential probes, (d) junction box, (e) load motor, (f) test motor (IM), (g) HF current probe, and (h) power cable.

3.4.2 Time Domain Analysis of TOV and CMV

Figure 3.15 illustrates validation of the GBM model for TOV, CMV, and motor-fed current I_a in the time domain. The comparison includes measured (blue) and optimized model (red) simulations for motor line-to-line terminal voltage (V_{ab}) as TOV, V_{CM} as CMV, and line current.

The proposed model estimates a peak DM voltage of 800 V, slightly higher than the measured peak value. This small difference confirms GBM's accuracy in reproducing the inverter-fed IM's DM voltage behavior.

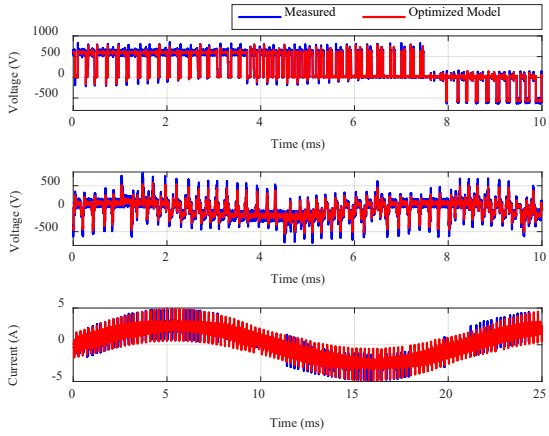


Figure 3.15. Time-domain comparison of measured and optimized-model signals for the IM with a 5 m cable (a) Voltage signal for Vab as TOV (b) voltage signal for VCM, and (c) current signal for I_a.

3.4.3 Frequency Domain Analysis of TOV and CMV

Figure 3.16 demonstrates the GBM's capability to reproduce the motor voltage spectrum from LF PWM switching components to multiple HF resonances. The simulated first TOV resonance at 3.3 MHz closely agrees with the measured 3.4 MHz. Furthermore, the model accurately represents subsequent measured resonance peaks at 15.3, 25.4, and 38.8 MHz, demonstrating reliable characterization of cable-machine interactions, parasitic effects, and HF transient behavior.

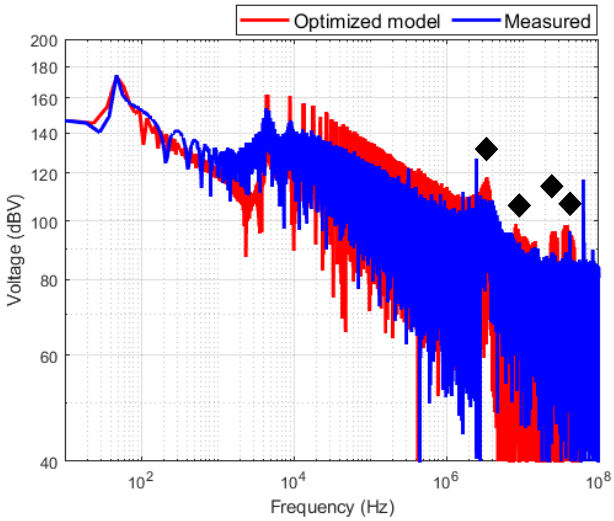


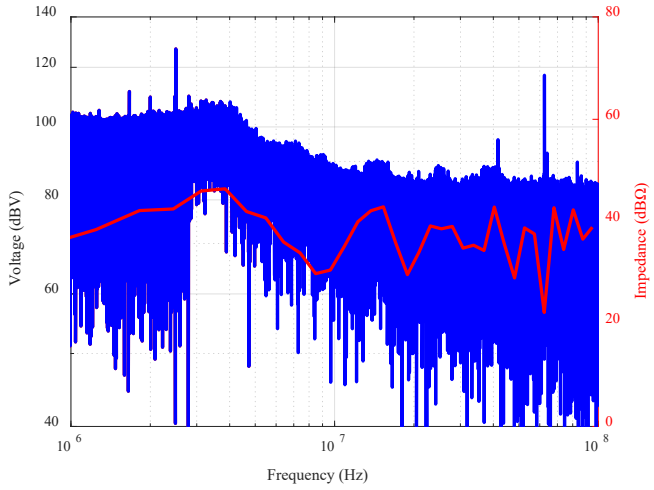
Figure 3.16. Matching of voltage spectra representing V_{ab} with multiple TOV resonance characteristic frequencies (◊ markers).

3.5 Motor Winding TOV Stress Analysis

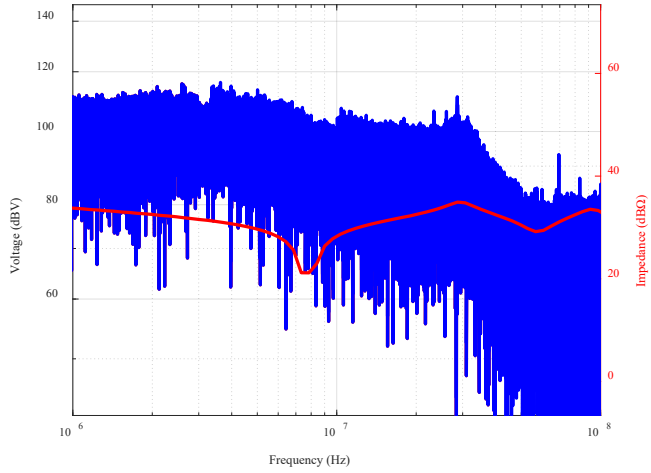
TOVs can threaten winding insulation when their resonance frequencies coincide with DM AR frequencies. Cable layout and machine impedance determine these critical stress frequencies, so identifying them is essential for insulation coordination and reliability.

3.5.1 Motor Winding HF TOV Estimation

Estimating TOV resonance frequencies helps mitigate ARO in cable-fed motor drives. Experimental results for 5 m and 1 m cables show that peaks in the combined DM impedance align with the measured TOV voltage spectra, as presented in Figure 3.17. Two resonance frequencies, ARO-1 (15.8 MHz) and ARO-2 (43.5 MHz), coincide with DM-impedance peaks, indicating the highest HF terminal stress and insulation vulnerability.



(a)



(b)

Figure 3.17. Machine terminal voltage frequency representation across BB' terminal, highlighting multiple TOV resonance frequencies with (a) 5 m cable and (b) 1 m cable.

3.5.2 Motor Winding Terminal ARO Estimation

The collective DM impedance of the cable connected to the motor identifies the critical TOV resonance frequencies associated with AROs. At these frequencies, high TOV stress appears at the motor terminals (*AA*'), increasing the risk of insulation degradation and drive instability. Figure 3.18 shows the peak-DM impedance and corresponding TOV peaks for different cable lengths. Two dominant ARO bands are observed at 15.8 MHz (ARO-1) and 43.5 MHz (ARO-2). The clustering of impedance and TOV peaks around these frequencies highlights regions of elevated insulation stress, demonstrating the effectiveness of DM-impedance analysis for ARO assessment and reliable motor-drive design.

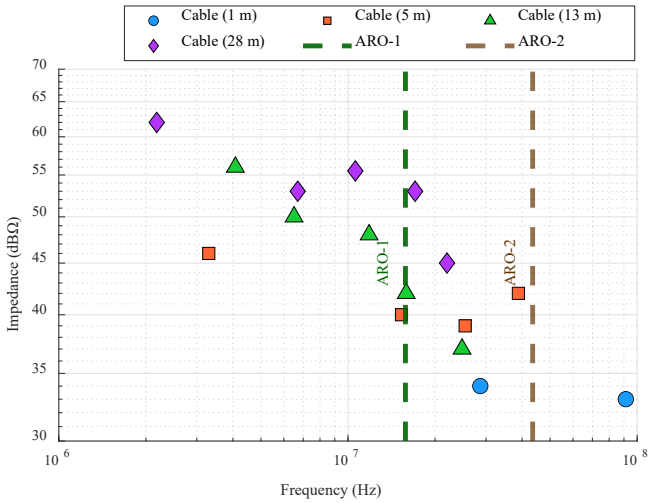


Figure 3.18. Combined cable–motor impedance peaks representing TOV and ARO using 1 m, 5 m, 13 m, and 28 m cables.

Among the cable lengths investigated, the 5 m cable exhibits pronounced impedance peaks at the second and fourth harmonics, which coincide with the ARO-1 and ARO-2 bands; the 13 m cable, meanwhile, shows a clearly visible fourth peak near the ARO-1 band. The 28 m cable also presents a fourth resonance peak near the ARO-1 band, indicating increased stress due to TOVs. To minimize these effects, optimize impedance by adjusting cable length, routing, shielding/grounding connections, or parasitic elements on the machine side. Shifting the dominant impedance peaks away from the critical ARO frequency bands (15.8 MHz and 43.5 MHz) reduces voltage stress and improves reliability; it also establishes a design framework focused on impedance sensitivity and the ROA for cable-fed motor drive systems.

3.6 Parametric Sensitivity Analysis

The proposed cable GBM enables accurate characterization of DM and CM impedance frequency response in the cable-motor system. The model parameters are determined analytically and then optimized to match the measured impedance profiles as closely as possible, improving resonance and ARO prediction over a wide frequency range. Furthermore, a sensitivity analysis, such as the one illustrated in Figure 3.19 shows that the cable's inductance and capacitance have a significant influence on high-frequency resonance behavior of the IM and require attention in addition motor parameters. In contrast, motor inductance and winding capacitance show limited impact on TOV behavior.

3.6.1 ROA Criteria

The condition is (3.26) are applied with the minimum space between all possible TOV and ARO frequency pairs (k) must remain greater than a predefined safety margin Δf_{safe}. This ensures that TOVs do not coincide with low-impedance regions of the machine winding, where voltage amplification and insulation stress increase significantly.

$$\min_k \left| f_{TOV,k} - f_{ARO,k} \right| > \Delta f_{safe} \tag{3.26}$$

This equation defines the safe design condition for avoiding harmful resonance interactions between the cable and motor, as defined in Figure 3.20, within which certain combinations of cable-motor parameters avoid exceeding the coupling between the TOV resonance frequencies and the machine's AR frequencies. When this condition is not satisfied, resonance overlaps occur, which result in elevated electric field stress and increased leakage current through the insulation system.

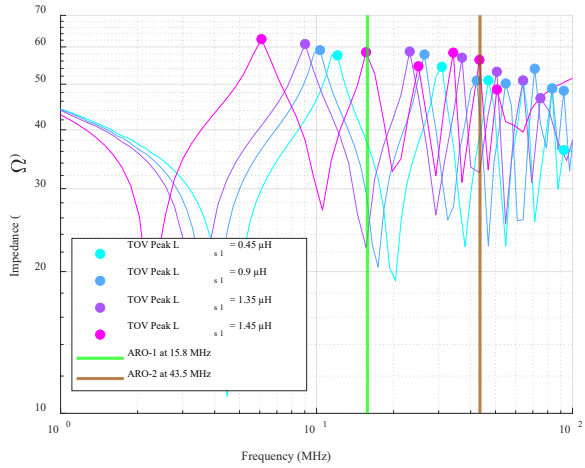


Figure 3.19. Parameter sensitivity analysis showing parametric variation of cable L_{s1} .

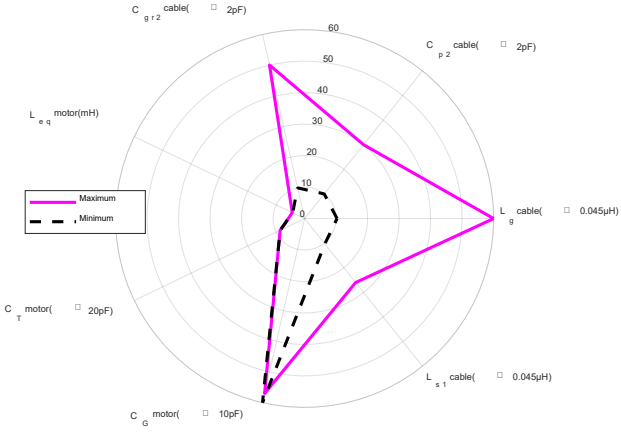


Figure 3.20. ROA defined for the motor-drive system.

From a design perspective, the proposed framework enables impedance sensitivity analysis and reliable operating area (ROA) identification for cable and machine parameters, allowing TOV resonance to be avoided at critical ARO frequencies through cable-parameter optimization without additional filtering hardware or overdesign of the insulation system.

3.7 Discussion

The results demonstrate that the proposed GBM can represent the impedance-frequency-dependent behavior of cable-fed IM drive systems while retaining physically interpretable parameters. The optimized GBM achieved mean estimation errors of 4.7% for TOV and 4.2% for CMV, demonstrating good agreement with the experimental measurements. In the frequency domain, the model reproduced multiple TOV resonance characteristic frequencies within two dominant ARO frequency points.

The analysis further shows that TOV characteristics depend on the interaction between cable parameters and machine winding impedance. In particular, the coincidence of TOV peaks with DM AR frequencies identifies regions of potentially increased winding insulation stress. Sensitivity analysis shows that cable inductance and capacitance significantly influence the resonance points of transient terminal overvoltages. This highlights the importance of cable characteristics in designing and evaluating cable-fed drive systems. The proposed ROA criterion identifies parameter combinations that reduce overlap between TOV frequencies and winding AR frequencies.

3.8 Chapter Summary

This chapter shows that the optimized GBM can precisely represent frequency-dependent impedance and the transient response of cable-fed induction motor drive systems. Experimental validation confirms the model's ability to reproduce TOVs and CMV, including the characteristic resonance frequencies of various TOVs. Comparing these frequencies with the motor winding AR characteristics helps identify operating conditions that may increase insulation stress. Furthermore, the sensitivity analysis highlights that cable inductance and capacitance strongly influence HF resonance behavior. These results provide a quantitative basis for evaluating interactions between the cable and the motor, as well as for identifying operating conditions that lead to higher voltage-level stress on the winding insulation than the inverter's nominated voltage.

4 Signal Processing-Based Approach for Insulation Degradation Estimation

This chapter presents a signal processing-based approach for monitoring the insulation condition of inverter-fed induction machines. The proposed method leverages naturally occurring PWM switching phenomena to assess the state of the winding insulation in inverter-fed electrical machines. The procedure consists of signal acquisition, transient pre-processing, feature extraction, and state estimation. By extracting degradation-sensitive features from responses to high-frequency transients and correlating them with insulation condition, the proposed approach enables early fault detection, condition-based maintenance, and systematic monitoring of insulation degradation throughout the machine's life cycle.

4.1 Proposed Signal Processing-Based Diagnostic Framework

The proposed insulation degradation estimation framework utilizes naturally occurring PWM switching transients and measures the IM-fed current (phase *a*) in high BW for post-processing, as represented in Figure 4.1. The framework acquires, processes, and analyzes HF transient responses to extract degradation-sensitive features associated with insulation aging.

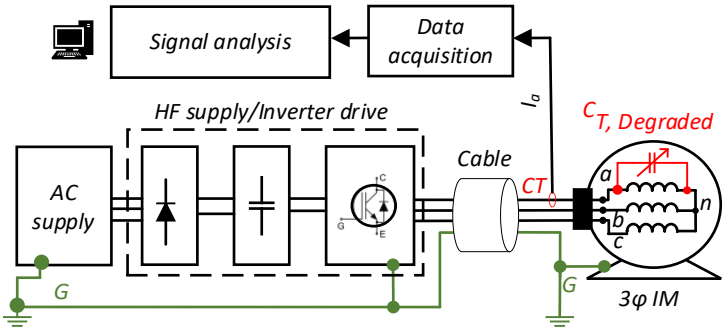


Figure 4.1. Proposed signal acquisition methodology for inverter-fed drive system.

4.1.1 Limitations of Conventional Spectral Analysis

Conventional spectral analysis techniques, including the Fourier transform (FT), fractional Fourier transform (FRFT), and discrete wavelet transform (DWT), are widely used for monitoring electrical machine conditions. However, inverter-generated switching transients are inherently non-stationary and contain rapidly varying frequency components. FT provides limited temporal information, while FRFT performance depends on selecting an appropriate fractional order (*p*) to represent signal characteristics in the fractional domain. DWT performance depends on wavelet selection and decomposition levels. These limitations can reduce sensitivity to incipient insulation degradation. Consequently, degradation-related transient signatures may not be accurately represented, reducing sensitivity to incipient insulation defects. Therefore, more advanced signal-processing approaches are needed to characterize transient phenomena effectively and improve insulation degradation assessment.

4.1.2 Parametric GBM Model of IM

A set of variations in the winding insulation capacitance is simulated by inserting an additional capacitor $C_{T,Degraded}$ at the connection point of the motor's *a*-*a*' phases. These variations serve as key indicators of performance degradation and highlight the need for accurate, sensitive monitoring methods.

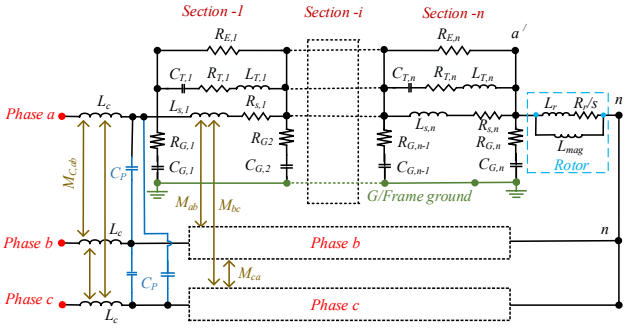


Figure 4.2. Parametric GBM model of IM.

The proposed IM model, depicted in Figure 4.2, employs a physics-informed grey-box modeling approach with detailed low-to-HF response parameters to analyze the motor's impedance behavior. The proposed model of an IM includes key parameters: $R_{E,I}$ (iron-loss resistance), $L_{T,i}$, $R_{T,i}$ and $C_{T,i}$ (phase inter-turn branch elements) for HF behavior. R_S , $L_{S,i}$, and $M_{ab,i}$ are the stator resistance, self- and mutual inductance, while $R_{G,i}$ and $C_{G,i}$ represent the frame grounding resistance and capacitance. C_P and M_C account for phase-to-phase parasitic capacitance and mutual inductances, representing the first turn and connections. Rotor parameters include R_r (resistance), L_r (leakage inductance), and L_{mag} (magnetizing inductance). The motor ground (marked as G) serves as a common reference point; n (set to 10) represents the number of segments into which the machine model is divided for detailed analysis.

Initial estimated values for the IM parameters were determined through numerical calculations based on equations [46], [47]. During optimization, a ±20 % variation range was established to guide the search. Subsequently, a particle swarm optimization (PSO) algorithm was employed to refine these parameters. The objective was to minimize the deviation between the simulation model's behavior and the experimentally obtained impedance and phase data. The cost function evaluates the quality of a given solution based on the objective functions (Obj_1 and Obj_2) defined in (4.1), and the condition of optimization in (4.2). For both objective functions, quality is typically determined by minimizing the mean squared error (MSE) between the actual impedance and phase angle values and the corresponding model results.

$$Obj_1(Z_j) = \frac{1}{n}\sum_{i=1}^{n}[|Z_{ini}(f_i,x_j)| - |Z_{prac}(f_i,x_j)|]^2$$
$$Obj_2(\theta_j) = \frac{1}{n}\sum_{i=1}^{n}[|\theta_{ini}(f_i,x_j)| - |\theta_{prac}(f_i,x_j)|]^2 \quad (4.1)$$

$$\text{Minimize } Obj_1(Z_j) \text{ and } Obj_2(\theta_j) \text{ such that } P_{varied} = (1\pm0.2)\, P_{initial} \quad (4.2)$$

Here, $P_{initial}$ denotes the initial set of motor parameters proposed in the GBM, while P_{varied} represents the set of parameters obtained by varying these initial values. A lower mean squared error (MSE) between the values calculated by the model and the actual values indicates a higher-quality model. PSO algorithm, inspired by the behavioral patterns of bird flocks and employing adaptive strategies, serves as an advanced optimization tool for exploring complex, non-linear, and multimodal solution spaces [49].

4.2 Natural PWM Switching Transients for Insulation Diagnosis

In an adjustable-speed drive as demonstrated in Figure 4.3, the speed or torque of the IM is controlled by an inverter utilizing PWM, leading the machine supply current to contain multiple frequency components, as stated (4.3): a LF fundamental component $i_f(t)$, a medium-frequency PWM ripple current $i_r(t)$, and a HF switching current $i_{SW}(t)$. Switching devices operate with transition times on the order of tens to hundreds of nanoseconds, generating steep voltage rise and fall edges with high voltage at the machine terminals.

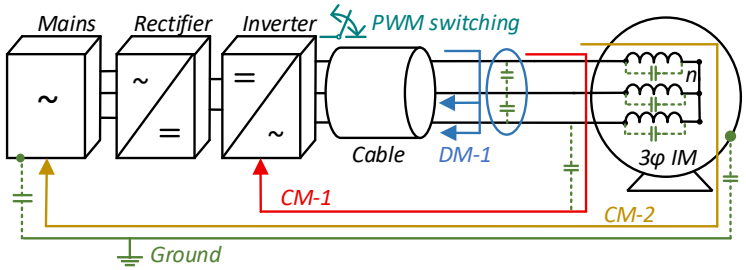


Figure 4.3. HF oscillation modes of PWM switching current in a drive system.

Therefore, the inverter stage acts as a natural HF excitation source, imposing repetitive transient voltages at the switching frequency, typically from 8 kHz and higher. These fast transients excite HF current oscillations extending from tens of kHz to several MHz. The resulting HF switching current is coupled through the parasitic capacitive and inductive paths of the inverter–cable–machine system as demonstrated in Figure 4.3 and can be expressed in three paths as in (4.4). The machine's distributed resistance, inductance, capacitance, and insulation condition strongly influence the propagation, reflection, and attenuation of these transient waves. Therefore, natural PWM switching transients can serve as valuable diagnostic signatures for online condition monitoring and early detection of insulation degradation in inverter-fed electrical machines.

$$i_p(t) = i_f(t) + i_r(t) + i_{sw}(t) \tag{4.3}$$

$$i_{sw}(t) = i_{dm-1}(t) + i_{cm-1}(t) + i_{icm-2}(t) \tag{4.4}$$

These three current paths are further explained as:

1. Differential-Mode 1 (*DM-1*): The HF current (i_{DM-1}) flows from the switching phase and returns through the other phases via inter-phase terminal parasitic capacitances.

2. Common mode 1 (*CM-1*): The current (i_{CM-1}), typically in the MHz range, couples through machine-to-ground parasitic capacitances and returns to the inverter through power-device and heat-sink coupling paths.
3. Common mode 2 (*CM-2*): The current (i_{CM-2}) propagates through the internal winding parasitic capacitances and ground path.

Figure 4.4 presents the inverter output voltage waveform and the associated switching oscillation current during normal operation of the inverter-fed machine.

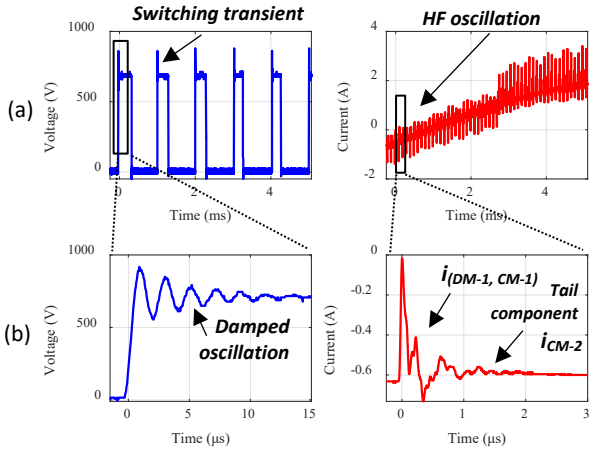


Figure 4.4. Inverter switching transients: (a) switching transient voltage and associated HF current oscillation; (b) zoomed view of damped oscillation response and current components i_{CM-2}.

To evaluate the progressive effects of insulation deterioration, the motor's HF impedance behavior was measured at various stages of inter-turn degradation. As shown in Figure 4.5, increasing fault severity leads to significant shifts in resonance frequency and variations.

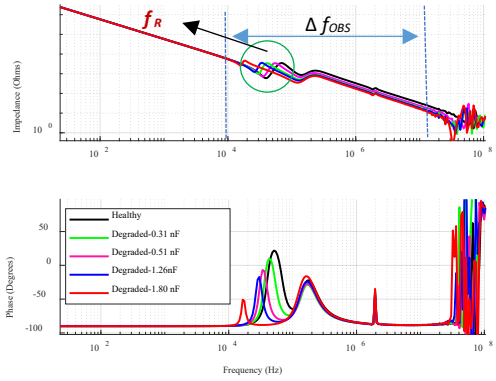


Figure 4.5. Measured DM impedance profile under different turn degradation faults.

The optimal fitting procedure described in Section 4.1.2 was applied again to estimate the inter-turn capacitance under various simulated degradation conditions. Subsequently, these estimated values were compared with the initial values corresponding to the healthy state to evaluate the changes associated with insulation

degradation. Table 4.1 presents the updated mean inter-turn capacitance, C'_T determined by fitting the proposed GBM model in combination with the calculation method based on lumped parameters. The capacitance variation, $\Delta C'_T = C'_T - C_T$, reflects the deviation from the reference value (i.e., C_T in the healthy state). The corresponding percentage change, ($\Delta C'_T / C_T$), indicates the relative variation in inter-turn capacitance for each simulated degradation scenario.

Table 4.1. Extracted IM parameters for varying external capacitances.

$C_{T,Degraded}$ (nF) inserted	Model estimated $\Delta C'_T$ (pF)	Severity $\Delta C'_T / C_T$ (%)
0 (healthy)	0.02	0
0.31	11.2	3.0
0.51	35	9.5
1.3	54	14.6
1.8	94	25

Table 4.2 compares commonly used signal-processing techniques for insulation-condition monitoring in terms of their time-frequency resolution, transient-analysis capability, computational complexity, and sensitivity to early degradation. This comparison helps to identify the most suitable approach for analyzing non-stationary PWM switching oscillations. In particular, the FRFT combined with a resonance-centered filter bank improves feature extraction around sensitive resonance bands, supporting the detection of incipient inter-turn insulation degradation.

Table 4.2. Comparison of multiple signal processing-based insulation condition monitoring techniques.

Aspect	FT	Wavelet	FRFT	FRFT with filter bank
Principle	Transforms the signal to the frequency domain	Generalized FT with fractional order	Generalized FT with fractional rotation	FRFT with filter-bank feature extraction
Domain	Frequency domain	Fractional domain	Fractional domain	Fractional domain + filtered frequency bands
Time localization	Not available	Moderate	Implicit fractional representation	Implicit through fractional representation
Frequency localization	Excellent for stationary signals	Excellent for chirp signals	Excellent for chirp-like signals	Very high around sensitive resonance bands
Resolution	HF resolution only	Adjustable by fractional order	Adjustable via fractional order	Fractional-order and filter-bank optimized
Transient analysis capability	Poor	Very good	Very good	Excellent
Non-stationary signal analysis	Limited	Excellent	Excellent	Excellent
Energy concentration	Low for transients	Very high	Highest at optimal order	Highest in selected resonance-sensitive bands
Computational complexity	Low	High	Higher	High
Physical interpretability	Simple	Less intuitive	Less intuitive	Improved through filtering
Typical output	Frequency spectrum	Fractional spectrum	Fractional-domain spectrum	Filter-bank energy / sensitive features
Machine diagnostics application	Harmonics and resonance	Degradation, resonance tracking	Insulation degradation and resonance tracking	Incipient detection and resonance tracking
Early degradation sensitivity	Low	Very high	Very high	Very high

4.3 Fractional Fourier Transform-Based Diagnostics

FRFT extends the classical FF and operates in the time–frequency domain, making it well suited for analyzing non-stationary and transient signals, such as those generated by inverter-driven machines. Unlike conventional FT and fixed-band filters, the FRFT can adaptively rotate the signal representation in the time-frequency plane to extract degradation-sensitive features [43] as presented in Figure 4.6.

The FRFT can be interpreted as a rotation of the signal representation by an angle αin the time–frequency plane. When α=0, it reduces to the identity transform in the time domain, whereas for α=π/2, it becomes the conventional Fourier transform in the frequency domain. For the fractional Fourier transform, the current signal *i*(*t*) is transformed into the fractional domain as defined in (4.5).

$$FRFT_{\alpha}(x(t)) = X_p(u) = \int_{-\infty}^{\infty} x(t')K_{\alpha}(t,t')dt' \tag{4.5}$$

Where *p* is the fractional order, *u* is the fractional frequency variable and the FRFT Kernel function $K_{\alpha}(t,t')$ is evaluated as (4.6).

$$K_{\alpha}(t,t') = \begin{cases} \sqrt{1-j\cot(\alpha)}e^{j\pi(t^2+t'^2)\cot(\alpha)-2jtt'\cos ec(\alpha)}, & \alpha \neq n\pi \\ \delta(t-t'), & \alpha = 0 \\ \delta(t-t'), & \alpha = \pi \end{cases} \tag{4.6}$$

This tunable transform is important for capturing subtle spectral changes that appear early in insulation degradation. By choosing the fractional order optimally, the method becomes more sensitive to fault-related spectral shifts and improves detection performance [50].

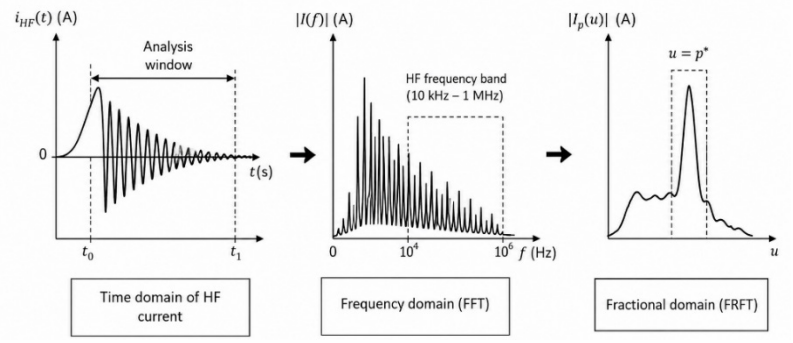


Figure 4.6. Transformation of HF switching oscillation current through signal processing.

4.3.1 Fractional Fourier Transform and Mel Filter Bank

In speech and audio signal processing, the Mel Filter Bank is a fundamental tool, most often used to compute Mel frequency cepstral coefficients (MFCCs). It applies a series of triangular filters to the Mel-scaled frequency spectrum of the signal [51].

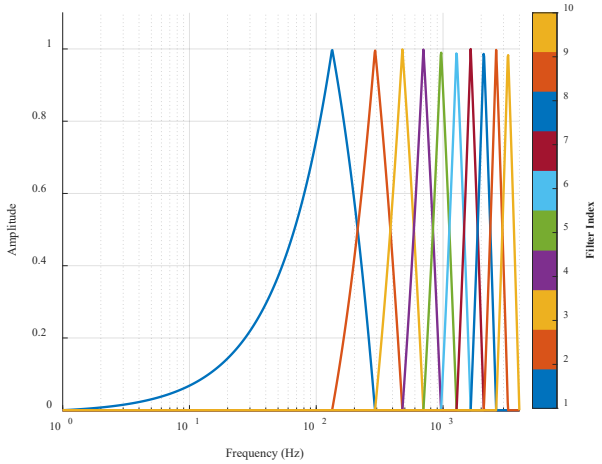


Figure 4.7. Frequency distribution of filters in a standard Mel filter bank.

Mel filter amplitudes increase much faster in the LF range than in the mid and HF ranges. The mapping of Mel frequency proceeds as defined in (4.7).

$$Mel(f) = 2595 \times \log_{10}(1 + \frac{f}{700}) \tag{4.7}$$

Conventional Mel filter banks employ a non-linear frequency scale in which the filters are more densely distributed within the LF range (0–4 kHz), as illustrated in Figure 4.7. However, insulation degradation typically causes spectral changes that appear near the component's HF parallel resonance frequency (f_R).

To address this issue, this work proposes a Mel filter bank centered on this resonance frequency. By redistributing the filters around the adjacent frequency bands (10 kHz-1 MHz), this approach improves the extraction of features sensitive to such degradation, while simultaneously discarding redundant spectral information as in Figure 4.8.

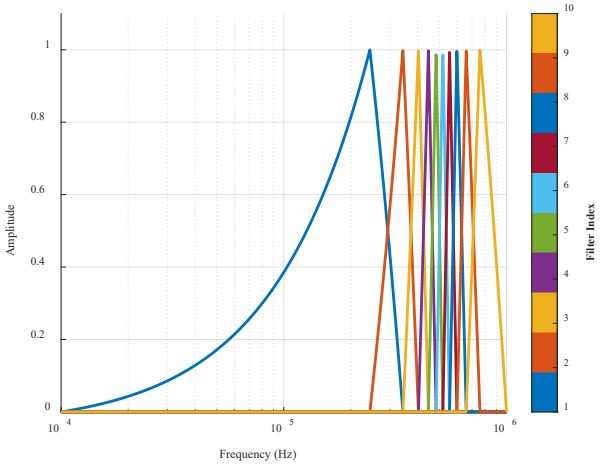


Figure 4.8. Distribution of an adaptive RMFB.

4.3.2 Design of Resonance-Centered Mel Filter Bank

The customized resonance-centered Mel frequency (RMFB) mapping is distributed as (4.8).

$$Mel_{centered}(f) = m.\arctan\left(\log_{10}\left(1+\frac{f}{f_0}\right)\right)+D \tag{4.8}$$

Here, f_0 is set to a relatively high value (in kHz) to align with the high resonance frequency (F_R) of the motor windings; m, (a scaling factor) is set to 2 to adjust the non-linear compression of the representation; and D, (an offset) is set to 0 to ensure continuity at f=f_0. To improve feature extraction, a primary frequency range, Δf_{OBS}, is centered on the reference resonance frequency f_R and spans from 10 kHz to 10 MHz. Features can be extracted effectively, and data volume can be reduced by reconfiguring the feature regions from the LF band to the f_{obs} region and subsequently from the f_{obs} region to the bilateral frequency band. The resulting RMFB feature vector $\overline{E_q}$ is normalized by its maximum value to reduce amplitude-scale variations and enable consistent comparison between healthy and degraded insulation states using the proposed degradation index. For each degradation level q, the feature vector is defined as (4.9).

$$\overline{E_q} = \left[\overline{E}_{q,1},\ \overline{E}_{q,2},\ \overline{E}_{q,3},\ \ldots,\overline{E}_{q,M}\right]^T,\ q\in\{HC-1,\ HC-2,\ HC-3,\ \ldots,HC-20\} \tag{4.9}$$

The degradation index is calculated using MAE in (4.10).

$$MAE_q = \frac{1}{M}\sum_{m=1}^{M}\left|\overline{E}_{q,m}-\overline{E}_{0,m}\right| \tag{4.10}$$

Here, MAE_q is the degradation index for the qth degraded condition. The state estimation factor (SEF) expresses the percentage deviation from the initial healthy state and is calculated using (4.11).

$$SEF = \Delta x_q(\%) = \frac{MAE_q}{\frac{1}{M}\sum_{m=1}^{M}\left|\overline{E}_{0,m}\right|}\times 100 \tag{4.11}$$

Initially, the filter bank uses 10 filters to provide sufficient resolution within the selected frequency band. By concentrating the filters around the relevant resonance region and excluding less relevant frequency components, it improves feature extraction while reducing data size and computational complexity. The FRFT-RMFB algorithm processes HF switching oscillations using FRFT transformations and filter-bank projection, without requiring iterative solvers or large data buffers. These characteristics reduce memory requirements and support potential implementation on embedded CPUs without dedicated accelerators.

4.3.3 Methodology for Insulation State Estimation and Implementation

Figure 4.9 illustrates the procedure for assessing the insulation condition of the windings in an electric motor fed by a variable-frequency signal source (VFS), a VFD and a thermally degraded stator. The steps are as follows:

I. Using a current sensor with a 120 MHz bandwidth, the switching oscillation currents generated by the voltage source are measured. The recorded waveforms are then processed with fractional cycles for detailed analysis.

II. The segmented oscillatory signals are processed using an optimized FRFT combined with a Mel filter bank centered at the resonance frequency (referred to as FRFT-RMFB) to extract information in the time-frequency domain.

III. The mean absolute error (MAE) or the root mean square error (RMSE) is used as a state estimation factor (SEF), a degradation metric to quantify differences in signal characteristics between the healthy state and the degraded state. This metric is defined in (4.12)–(4.13) as below.

$$MAE = \frac{1}{m}\sum_{i=1}^{m}\left|x_i^* - x_i\right| \tag{4.12}$$

$$RMSE = \sqrt{\frac{1}{m}\sum_{i=1}^{m}\left(x_i^* - x_i\right)^2} \tag{4.13}$$

In this case, x_i^* represents the i-th feature value in the healthy reference dataset, x_i represents the comparable feature value under the deteriorated situation, and m indicates the total number of samples. The state estimation factors obtained using the two calculation methods are denoted as SEF_{MAE} and SEF_{RMSE}, corresponding to the MAE- and RMSE-based methods, respectively.

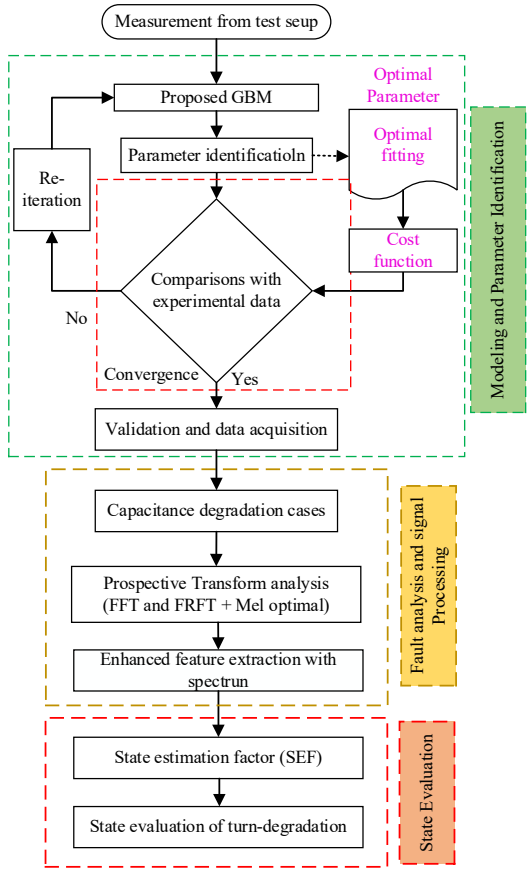


Figure 4.9. Schematic of the proposed optimum FRFT-RMFB framework

4.3.4 Validation of FRFT-RMFB with Variable-Frequency Signal Source

Inter-turn insulation degradation is associated with subtle changes in the machine's phase capacitance. Table 4.3 presents the main specifications of the IM used in the experiments. Figure 4.10 shows the experimental setup to measure the switching-transient response in machine-fed current.

Table 4.3. Main parameters of the test bench motor

Rated parameter	Value	Rated parameter	Value
Power (W)	750 W	Current Δ/Y (A)	3.0/1.7 @ 50 Hz 2.6/1.5 @ 60 Hz
Voltage Δ/Y (V)	230/420 @ 50 Hz 265/460 @ 60 Hz	Speed (r/min)	1440 @ 50 Hz 1750 @ 60 Hz
Cos φ	0.76 @ 50 Hz 0.74 @ 50 Hz	Resistance phase *a* (Ω)	6.4

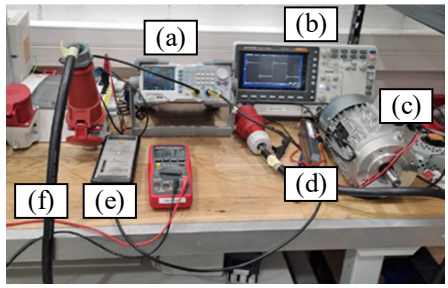


Figure 4.10. VFS test setup: (a) VFS supply (initially at f_{sw}=100 kHz), (b) oscilloscope, (c) motor, (d) current probe (100 MHz), (e) differential probe (100 MHz) (f) 5 m cable.

Winding-insulation degradation produces slight changes in the time-domain current waveform, as shown in Figure 4.11. At a switching frequency (f_{sw}) of 100 kHz, each switching cycle comprises 10 µs. High-resolution signal acquisition is performed at a sampling rate of 100 MS/s, with 1,000 data points per oscillation segment. For analysis and post-processing, each dataset sample consists of 100 consecutive segments over a total acquisition window of 1 ms. The sampled current waveform is then processed using various signal-transform methods for comparative analysis.

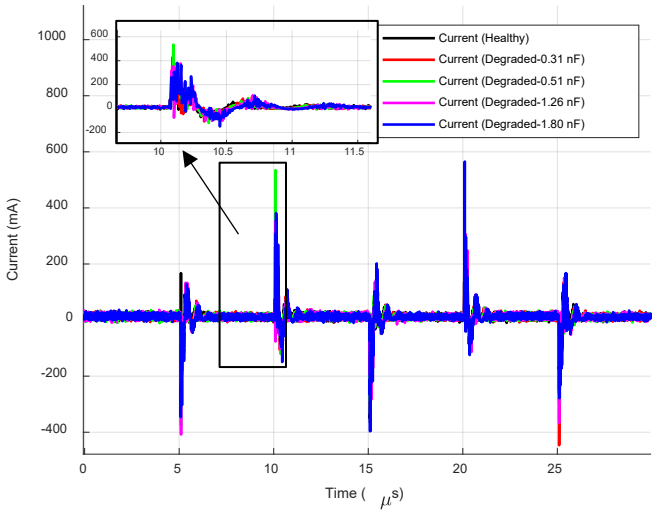


Figure 4.11. Measured switching motor current (Ia) signal in the time domain.

MATLAB functions were used to analyze and post-process the experimental data. The FRFT represents the HF switching-current signals in a fractional domain, with the resulting features depending on the fractional order (*p*). To improve sensitivity to incipient turn-insulation degradation, the optimal value of (*p*) was determined by comparing the healthy-state signal with an initially degraded signal corresponding to an added capacitance of 0.31 nF. The mean absolute error (MAE), calculated using (4.14), was evaluated for different values of (p). The optimal fractional order was then selected by maximizing the MAE, to better distinguish between the healthy and degraded states.

$$Maximize\ \{MAE = \frac{1}{m}\sum_{i=1}^{m}\left|x_i^* - x_i\right|\}\ such\ that\ p_{\mathrm{var}ied} = [0,1] \tag{4.14}$$

Here x_i* and x_i represent healthy-reference and initially degraded datasets, respectively, while (m) denotes the total number of measured values. As shown in Figure 4.12, the mean absolute error (MAE) peaks at the optimal fractional order (*p*=0.71).

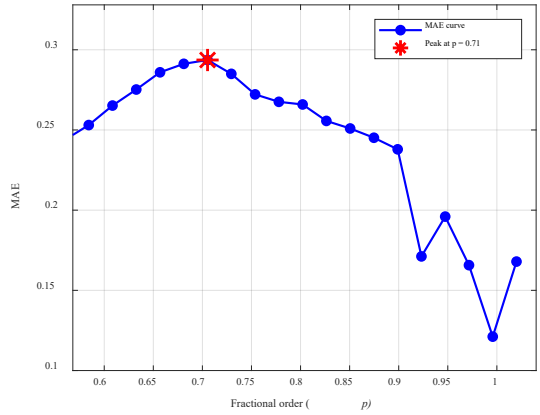


Figure 4.12. Sensitivity analysis for determining the optimal fractional order.

For the proposed FRFT with resonance-centered Mel filter bank (FRFT-RMFB), the center frequency (f_0) was set to 20 kHz, with a designed frequency range of 10 kHz to 10 MHz. The optimized filter distribution is shown in Figure 4.13.

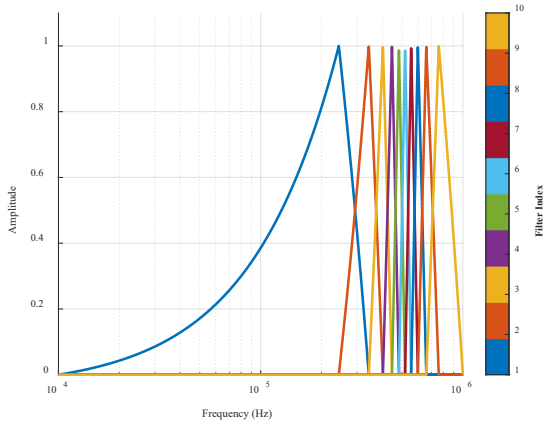
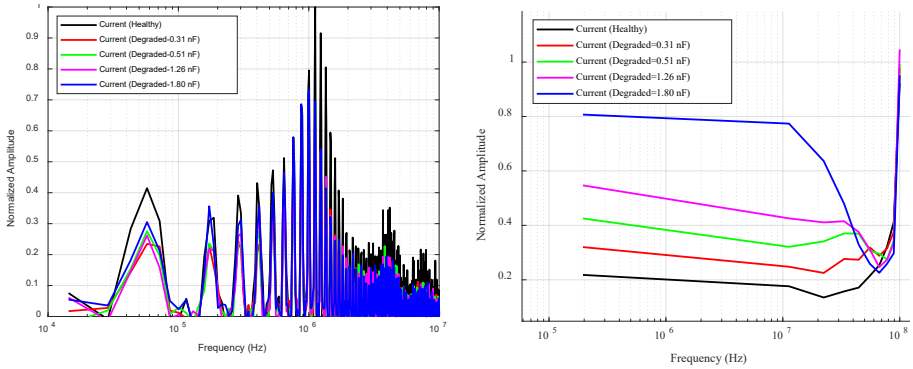


Figure 4.13. Frequency distribution of the proposed FRFT-RMFB filter bank.

4.3.4.1 Performance evaluation

Here x_i* denotes the healthy-reference feature, while x_i represents the corresponding spectral magnitude under each degradation condition. As shown in Figure 4.14, FRFT-RMFB produces more pronounced variations in the switching-oscillation response, improving the distinction between insulation conditions. These results presented in Table 4.4 demonstrate their potential for more sensitive assessment of turn-insulation degradation and clearer tracking of insulation aging. On average, FT presents 6%, and the proposed FRFT-RMFB presents 46%, which is more than seven times better at representing inter-turn degradation faults overall.



(a) *(b)*

Figure 4.14. Spectral representation using methods (a) FT and (b) FRFT-RMFB.

Table 4.4. Comparison of percentage (%) sensitivity (SEF_{MAE}) of different methods.

$C_{T,Degraded}$ (nF)	FT (%)	Bandpass Filter (%)	FRFT (%)	LGFB (%)	Proposed FRFT-RMFB (%)
0.31	3.4	3.9	7.7	19.3	23
0.51	5.1	6.5	16.6	25	35
1.3	6.4	7.6	23	34	50
1.8	9.4	13.1	34	51	76

Figure 4.15 visualizes the sharp incline in SEF_{MAE} for the proposed FRFT-RMFB compared to other methods, emphasizing its superior sensitivity across all degradation levels.

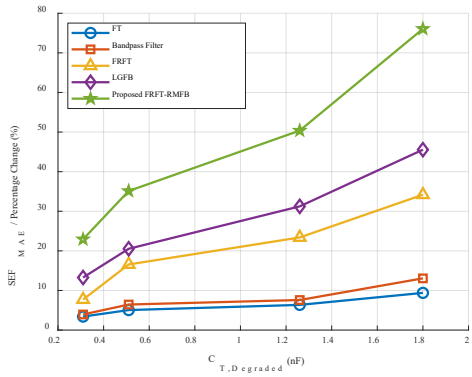


Figure 4.15. Sensitivity comparison results (SEF_{MAE}) across different methods.

4.3.5 Validation of Proposed Methodology with Inverter-Fed Supply

The proposed method was further evaluated under converter-fed operation using an IM. With the test setup as in Figure 4.16, the inverter's switching frequency was set to 10 kHz, and data acquisition was performed at a sampling rate of 100 MS/s.

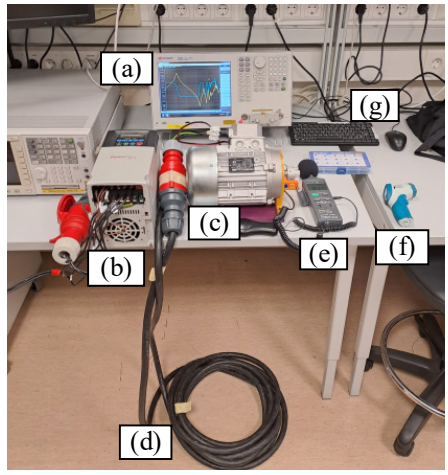


Figure 4.16. Experimental setup for converter-fed operation: (a) impedance analyzer, (b) VFD at a switching frequency of f_{sw}=10 kHz, (c) test motor, (d) 5 m cable, (e) ambient hygrometer, (f) thermometer, and (g) impedance analyzer interface.

Early-stage insulation degradation is difficult to identify because its characteristic signal variations are weak and can overlap with other components of the measured current. The FRFT-RMFB method improves the distinction between healthy and degraded conditions by emphasizing features associated with the machine's CM resonance characteristics.

Figure 4.17 compares the spectral representations obtained using FRFT and FRFT-RMFB, while Table 4.5 summarizes the corresponding *SEF* values for different degradation levels and signal-processing methods.

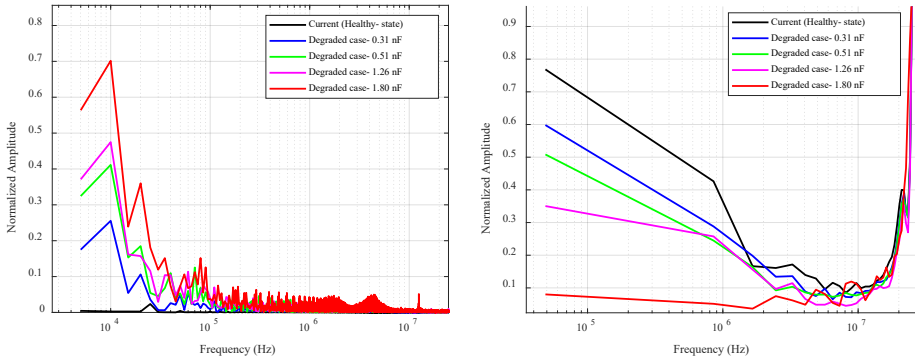


Figure 4.17. Spectral representations obtained using (a) FRFT and (b) proposed FRFT-RMFB method.

Table 4.5. Comparison of percentage SEF_{MAE} values obtained using different signal-processing methods under controlled turn-insulation degradation.

$C_{T,Degraded}$ (nF)	FT (%)	FRFT (%)	SK (%)	HHT (%)	CWT (%)	Proposed FRFT-RMFB (%)
0.31	1.5	4.3	2.2	2.2	0.21	15.8
0.51	2.8	9.3	4.3	5.4	1.8	19.0
1.3	4.9	10.7	9.8	7.8	5.1	29
1.8	6.3	15.5	22	12.4	15.6	44

The advantage of FRFT-RMFB is particularly evident at the lowest investigated degradation level (0.31 nF). At this level, its SEF of 15.8% substantially exceeds the FT outcome of 1.5%. On average, FT margin is 3.8%, while the proposed FRFT-RMFB receives 27%, nearly seven times better in overall representation of degradation indication identification. This comparison shows the proposed method's potential to distinguish early degradation conditions that produce relatively small changes in conventional spectral features.

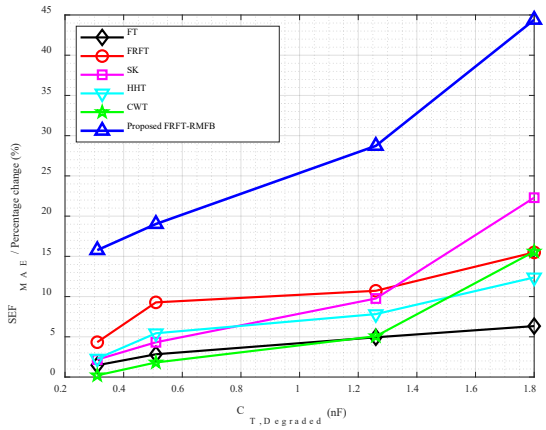


Figure 4.18. Comparison of insulation-degradation sensitivity obtained using different signal-processing methods.

As illustrated in Figure 4.18, FRFT-RMFB provides higher SEF values than the other methods evaluated across the degradation levels listed in Table 4.5. By emphasizing resonance-sensitive features in the fractional domain, the method improves the separation between healthy and degraded insulation responses. These results support using FRFT-RMFB for sensitive assessment of incipient turn-insulation degradation, although further validation is needed to establish its performance across a wider range of machines and operating conditions.

4.4 Implementation of FRFT-RMFB on Thermally Aged Machine Stator

Figure 4.19 illustrates the experimental setup developed to assess stator winding insulation degradation during accelerated thermal-aging cycles, including the inverter supply, signal acquisition, and data-processing stages. HF current measurement probes and an impedance analyzer measured current and impedance profiles.

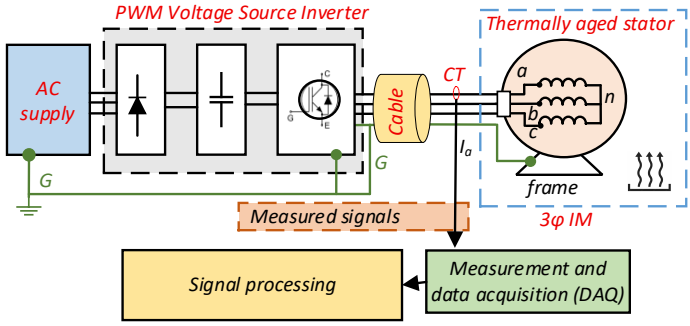


Figure 4.19. Schematic of the experimental setup for diagnosing stator winding insulation degradation during thermal aging.

4.4.1 Accelerated Thermal Aging and Measurement

The stator winding as a sample was subjected to thermal-aging cycles, each lasting 5 h. After each cycle, measurements were performed at ambient temperature to ensure consistent measurement conditions. The aging process continued until a physical short

circuit occurred between the winding phases, with insulation resistance assessed using an insulation resistance tester. HF current probe (5 A/120 MHz) and an impedance analyzer with a measurement range of 20 Hz–120 MHz were used to obtain the electrical machine's CM and DM impedance. Figure 4.20 demonstrates the practical test bench, including the inverter drive system and measurement probes for recording current signals and performing time-frequency analysis.

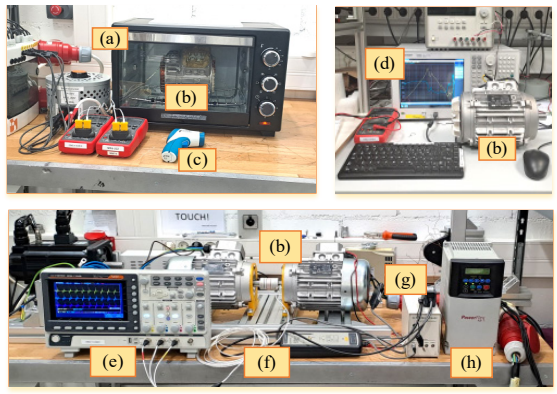


Figure 4.20. Thermal degradation setup: (a) heating chamber, (b) test motor, (c) infrared thermometer, (d) impedance analyzer, (e) oscilloscope, (f) differential probe, (g) current probe, and (h) inverter-fed supply.

The CM and DM impedance measurements were performed to characterize the machine winding's HF parametric response. The measured CM and DM impedance profiles are presented in Figure 4.21.

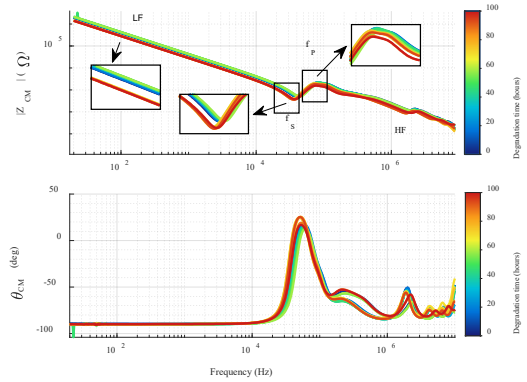


Figure 4.21. Impedance measurement results in CM schematics.

4.4.2 Evolution of Fractional-Domain Features

The FRFT was applied to the measured machine-fed current to extract insulation-sensitive properties. Since the response in the fractional domain varies with the fractional order p, different values of p were evaluated using the mean absolute error (MAE) between the current responses under normal conditions and those in the first degradation. As shown in Figure 4.22, the MAE peaks at p=0.74, indicating the greatest separation between the two insulation states. Therefore, p=0.74 was selected as the

optimal fractional order to achieve the highest degradation sensitivity across different HCs.

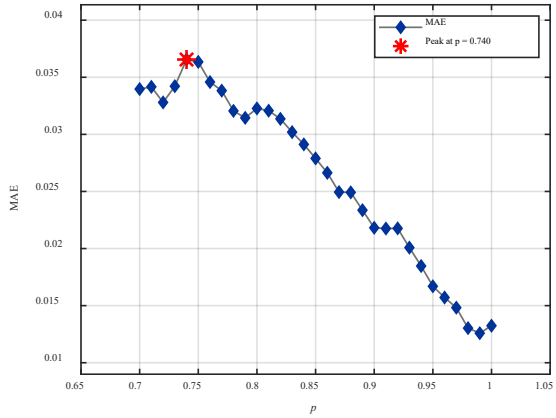


Figure 4.22. Sensitivity analysis for selecting the optimal fractional order.

The parallel resonance frequency f_p was set at approximately 400 kHz. Therefore, the center frequency f_o of the enhanced Mel filter was set at 400 kHz. Figure 4.23 (a-d) present the frequency spectra for the corresponding signal-processing techniques.

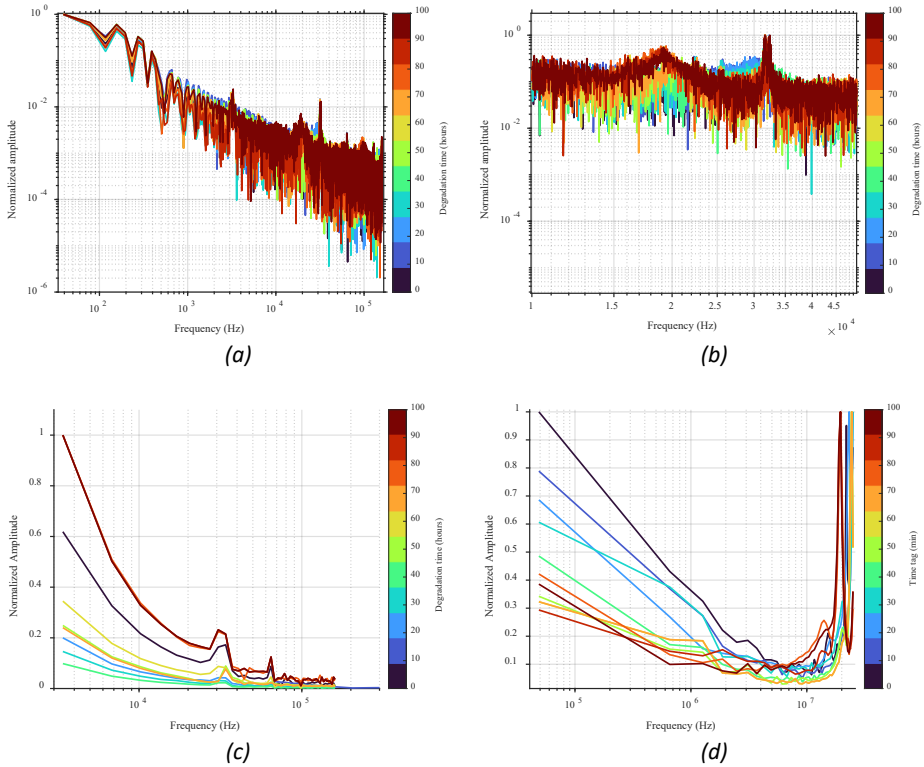


Figure 4.23. Frequency domain representation (a) FT (b) Band-pass filtered (c) FRFT (d) FRFT-RMFB

The core frequency region was selected as 10 kHz – 10 MHz to cover the main insulation-sensitive features associated with turn and ground-wall insulation degradation.

4.4.3 Incipient Degradation Detection Performance

As shown in Figure 4.23, conventional frequency-domain methods struggle to distinguish insulation degradation because the extracted features do not always vary monotonically with sample heat-up cycle time. As shown in Table 4.6, the state estimation factor (SEF_{MAE}) reached approximately 25% for FRFT-RMFB, compared with 5% for FT under the investigated condition. This improvement indicates that fractional-domain processing combined with resonance-centered filtering enhances sensitivity to degradation-related changes in high-frequency switching oscillations.

Table 4.6. Statistical representation of SEF_{MAE} (%) for methods for insulation state changes

Degradation time (Hr)	FT (%)	FT Bandpass (%)	FRFT (%)	Proposed FRFT-RMFB (%)
10	5	22	11	25
20	11	26	30	23
30	2	5	22	38
40	27	1	14	30
50	5	8	41	44
60	6	10	41	48
70	8	21	39	51
80	8	25	44	63
90	9	39	44	79
100	14	45	47	91

As presented in Figure 4.24, the average sensitivity across the ten measurements was 9.5% for FT, 20% for FT bandpass, 33% for FRFT, and 49% for the proposed FRFT-RMFB method. The proposed method achieved approximately 5 times the average sensitivity of conventional FT, demonstrating improved sensitivity to insulation degradation under the investigated conditions.

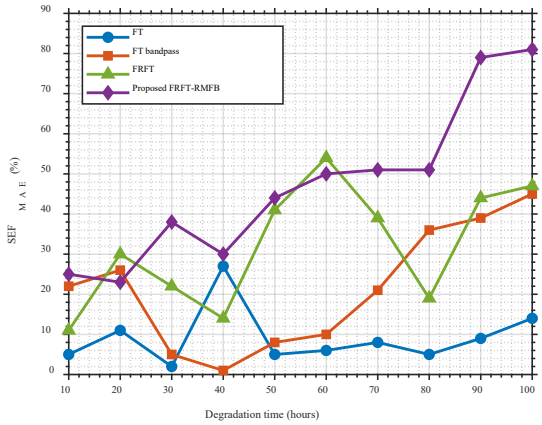


Figure 4.24. *Comparison* of multiple signal processing analyses.

4.5 Discussion

Experimental results show that combining fractional-domain feature extraction with resonance-centered filtering improves insulation-degradation sensitivity compared with conventional spectral analysis. The proposed FRFT-RMFB method emphasizes frequency components associated with the machine's resonance characteristics, making subtle changes in switching transients easier to distinguish between healthy and degraded insulation states.

Experiments on thermally aged stators further confirmed the method's effectiveness. Across ten aging measurements, the average SEF was 49% for FRFT-RMFB and 9.5% for FT, about 5 times as sensitive.

Although the extracted indicators did not increase monotonically throughout all aging stages, FRFT-RMFB provided a stronger overall response to insulation degradation. Its performance nevertheless depends on the machine characteristics, the selected fractional order, and the choice of resonance-sensitive frequency bands.

Consequently, the results show increased sensitivity under the experimental conditions examined; however, they do not support the conclusion that performance is equivalent across all machine types and operating environments.

4.6 Chapter Summary

The results indicate that the proposed method, based on switching oscillations and resonance-centered filter banks in the fractional domain, has achieved the highest average sensitivity among all methods evaluated. This assessment covers three experimental scenarios: capacitor-based degradation emulation with a high-frequency signal generator, an inverter-fed system, and stator windings subjected to thermal aging. These analyses confirm improved diagnostic capability for various degraded winding insulation, while highlighting the potential of fractional-domain, resonance-centered features for detecting incipient insulation damage under the conditions studied.

5 Model-Based Insulation Aging State and Lifetime Evaluation

This chapter investigates the relationship between insulation degradation and the frequency-dependent electrical characteristics of IM. Unlike conventional diagnostic methods that rely on empirical indicators or offline measurements, the proposed approach exploits degradation-sensitive parameters extracted from measurements of degraded samples. Thermal aging experiments progressively degrade the insulation system, while impedance measurements quantify changes in electrical parameters. In this work, FRA over a 120 MHz measurement frequency range was used to track the detailed IDP of the stator-winding insulation of an IM subjected to accelerated thermal aging. A detailed parametric GBM was proposed for the IM using an equivalent RLC network and multiple electrical parameters to capture interactions among the windings.

5.1 Thermal Degradation Phenomena and Parameter Tracking

5.1.1 Induction Machine Stator as a Sample

Four low-voltage IM samples, each rated at 440 V and 750 W with Class-F insulation, were used as test samples and subjected to repeated thermal stress cycles to investigate insulation degradation. The winding insulation coating is a polyester-imide (PEI) enamel, widely used in inverter-fed machines for its high dielectric strength, good thermal stability, PD-free characteristics, and inherent resistance to repetitive stress.

5.1.2 Machine RLC Parameter-Based GBM

A lumped RLC equivalent parameter model of the IM, referred to as the proposed GBM, is presented in Figure 5.1 to represent the various machine parameters. GBM includes eddy-current loss resistive components (R_E), inter-turn branches (R_T, C_T, and L_T), winding resistances (R_s), mutual and self-inductances (L_s, M_{ab}, M_{ca}), initial connection self- and mutual-inductances (L_C and M_C), and terminal phase-phase capacitances (C_{ph}). It also includes winding-to-ground dielectric branches consisting of series capacitance and resistance (R_{G1}, C_{G1}) and (R_{G2}, C_{G2}) referenced to the frame/ground insulation.

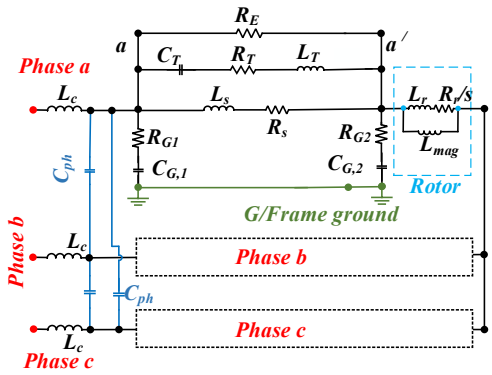


Figure 5.1. Lumped GBM of an IM showing various frequency-response parameters.

Initially, the machine impedance response is measured in CM and DM as presented in Figure 5.2 schematics. These frequency-impedance responses are used to compute the proposed GBM parameters. The parameters of the GBM were first identified analytically as the initial guess, as in the authors' previous work [47], [52] and presented in Section 3.3.3.

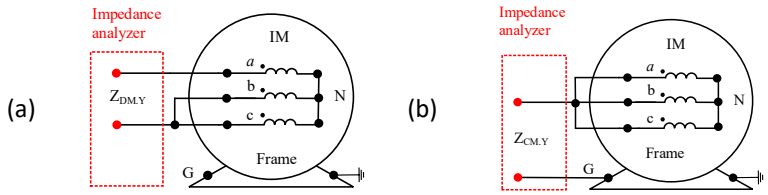


Figure 5.2. IM impedance measurements in (a) DM and (b) CM.

As in the literature, two natural resonance frequencies are observed in the FRA-based CM impedance response: the series resonance (SR) frequency (f_S) and the parallel resonance frequency (f_P), as conceptually illustrated in Figure 5.3. These resonances reflect the interaction of winding inductive and dielectric capacitive elements and can be used to estimate inter-turn and ground-wall degradation [53]. Insulation degradation alters these capacitances, causing shifts in f_S and f_P. The regions before f_S and after f_P are therefore considered sensitive to inter-turn and ground-wall insulation changes. One more important finding is that inter-turn degradation is more evident around (f_P) and in the HF region, whereas ground-wall degradation is more pronounced in the LF region.

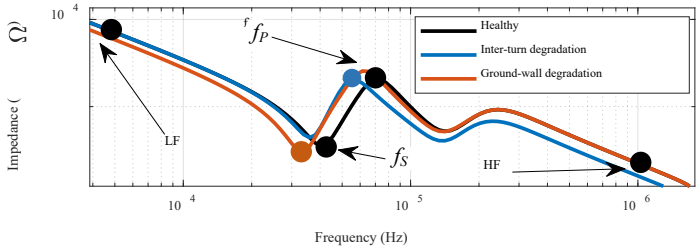


Figure 5.3. CM impedance profile illustrating inter-turn and ground-wall insulation degradation.

The LF region (DC/20 Hz – 10 kHz) provides information on ground-wall insulation capacitance (C_{LF}, C_{G2}), while the MF region (10 kHz – 500 kHz) captures resonance features, the inter-turn insulation capacitance (C_T) and eddy current loss resistance (R_E). The HF region (500 kHz – 10 MHz) is associated with C_{G1} *or* C_{HF} and R_{G1}.

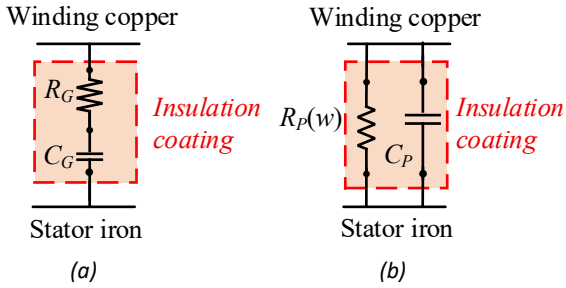


Figure 5.4. CM impedance profile of an electrical machine.

In this work, the parallel *RC* representation (Figure 5.4) was used to derive the equivalent phase-to-ground wall capacitance (C_P), resistance (R_P), and dissipation factor

(*DF*/tanδ) according to (5.1)–(5.3) [54]. The corresponding ground-wall insulation effects are mainly observed in the LF ranges.

$$C_P = \frac{1}{2\pi f_{LF(CM)}} \frac{\sin(-\theta_{LF(CM)})}{\left[Z_{LF(CM)}\right]} \tag{5.1}$$

$$R_P = \frac{1}{\frac{1}{\left|Z_{LF(CM)}\right|}\cos(\theta_{LF(CM)})} \tag{5.2}$$

$$DP = \tan\delta = \frac{1}{2\pi f_{LF(CM)} R_P C_P} \tag{5.3}$$

The LF features, including frequency $f_{\mathrm{LF(CM)}}$, impedance | $Z_{\mathrm{LF(CM)}}$ |, and phase angle $\theta_{\mathrm{LF(CM)}}$, were selected from the CM impedance profile at 1 kHz.

5.1.3 Optimal GBM Parameter Through Optimization

The particle swarm optimization (PSO) objective function minimized the weighted error between measured and modeled impedance magnitude and phase over the selected frequency range. Figure 5.2 illustrates the connection schematic of the IM in DM and CM. The frequency-impedance response was measured from the initial healthy state and after each HC. The parameter bounds were constrained around analytically estimated initial values to preserve physical interpretability. The inductive parameters were fixed during aging-cycle fitting, while dielectric capacitances and loss/leakage resistances were updated.

At each degradation heat cycle (HC), the GBM parameters of IM were re-identified from healthy to degraded conditions, capturing insulation changes reflected in impedance and capacitance variations induced by temperature stress.

5.2 Experimental Degradation Measurements and Evaluation of GBM Parameters

Figure 5.5 illustrates the experimental test bench, including the heating chamber, test samples, impedance measurement, and IR tester. For each machine sample, accelerated aging was performed in HCs. After each thermal exposure, the sample was returned to ambient room temperature (21 – 23°C) and humidity (20 – 40% RH), after which IR and CM/DM impedance spectra were recorded. The IR measurement was performed at 1 kV for 30 seconds, with the machine winding connected to CM mode (Figure 5.2b). An impedance analyzer with a measurement range of 20 Hz–120 MHz was used to obtain the electrical machine's common-mode and differential-mode impedance.

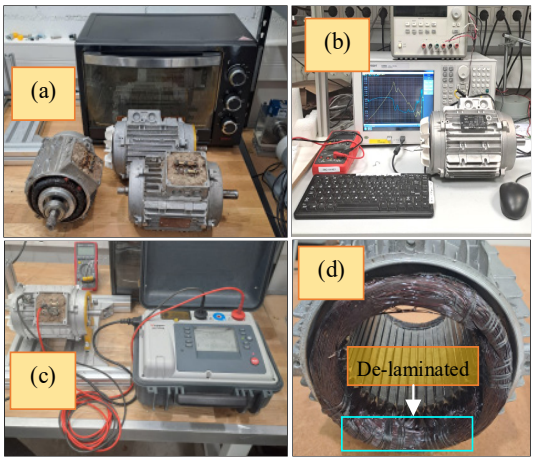


Figure 5.5. Experimental platform: (a) heating chamber and samples, (b) impedance measurement, (c) IR testing, (d) close-up view of the stator's degraded winding.

5.2.1 Heat Cycle and Exposure Time

For this study, four thermal exposure temperatures and the corresponding exposure times for each aging cycle were selected according to the baseline Arrhenius rule described in [55]. To enhance the statistical significance of the predicted time-to-failure, IEEE Std. 117 recommends using at least 10 to 20 aging cycles [26]. Using (5.4), where T_F is the aging temperature considered during the test procedure, T_i is 155^0 C as the class-F index, k_{cycle} is the number of desired aging cycles, and 20,000 h represents the insulation life at the thermal index. Machine 1 was aged using a stepped thermal profile: 200 °C for the first 10 cycles, followed by 250 °C until EoL. Machines 2, 3, and 4 were aged at constant temperatures of 235 °C, 245 °C, and 215 °C, respectively. These temperatures were chosen to provide accelerated aging conditions while remaining at least 10 °C above the thermal index of the machines. For example, 235 °C and 245 °C were selected to keep the aging progression within the recommended range of 10 or more cycles for 11 h and 4 h, respectively

$$t_{\text{exposure}} = \frac{20{,}000 \times 2^{\frac{T_i - T_F}{10}}}{k_{cycle}} \tag{5.4}$$

5.2.2 Insulation breakdown and End-of-life Criterion

The accelerated thermal-aging test for each machine sample was continued independently until physical insulation breakdown was observed. Physical EoL was identified when the winding could no longer sustain the applied IR test condition and a short-circuit condition was observed. The percentage change in IR (Δ*IR* %) by (5.5) was computed after the sample's heating cycle. $R_{INS,br}$ denotes the IR measured just before the final measurement of sample breakdown. The experimentally observed lifetimes of Machines 1–4 were 100, 110, 44, and 360 h, respectively. As shown in Figure 5.6, the IR showed non-monotonic behavior during the early and intermediate heat cycles, followed by a pronounced deterioration near EoL of approximately 87%. This means that the remaining IR was about 13% of the healthy value.

$$\Delta IR\ (\%) = \frac{IR_{healthy} - IR_{\deg raded}}{IR_{healthy}} \times 100 \tag{5.5}$$

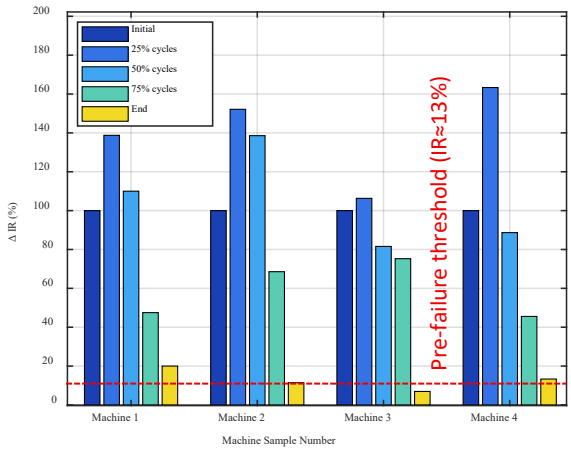
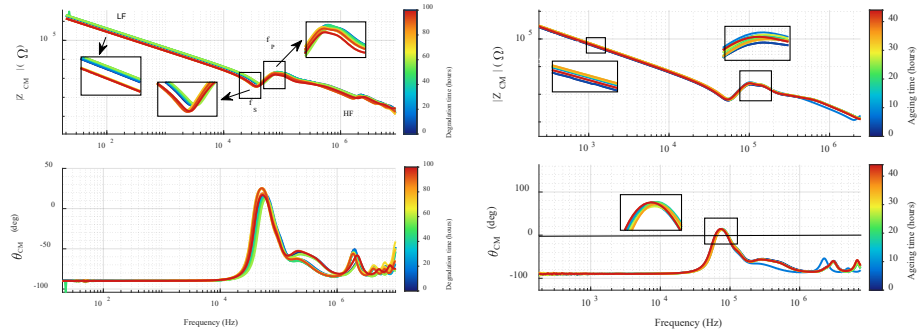


Figure 5.6. IR-change evolution and experimentally determined EoL criterion for the four machine samples.

The measured CM impedance profile for samples 1 and 3 for the heating cycle is presented in Figure 5.7. The resistive and capacitive parameters in the proposed GBM were sensitive to the thermal degradation event, whereas the inductive parameters remained mostly unchanged.



(a) *(b)*

Figure 5.7. FRA-based CM impedance-frequency spectra for (a) sample 1 and (b) sample 3.

5.2.3 GBM Parameter Identification and Model-Fit Assessment

The proposed GBM parameters are identified at each HC to characterize healthy and degraded conditions of the machine stator winding, including variations in dielectric turn (C_T) and ground-wall capacitances (C_{G1}, C_{G2}), R_E behavior, impedance (Z_{CM}), resonance frequency (f_R) and other insulation-related parameters. Figure 5.8 demonstrated matching between the GBM optimal response in CM and the measurement, providing a framework to map existing health.

The coefficient of determination, K_{R^2}, defined in (5.6), was used to quantify the goodness of fit between the measurement (as a reference) and the fitted GBM impedance spectra

$$K_{R^2} = 1 - [\sum_{i=1}^{N} (h_i - \hat{h}_i)^2 / \sum_{i=1}^{N} (h_i - \bar{h})^2] \quad (5.6)$$

where $h_i$is the measured value at the ith sample, $\hat{h}_i$ is the corresponding model estimate, $\bar{h}$ is the sample mean, and N is the number of observations. During the model-fit assessment, the K_{R^2} values for the optimized GBM for healthy and degraded cases were 0.91 and 0.93, respectively. Figure 5.8 presents the matching of measured and optimally fitted GBM impedance response for healthy sample 1.

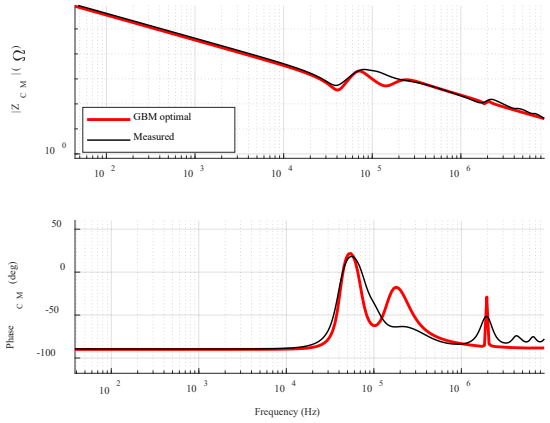


Figure 5.8. Measured and optimally fitted GBM impedance response of machine 1 in healthy state.

5.3 Evolution of Multiple IDPs and Life Estimation

IR alone cannot serve as a reliable health indicator throughout the aging process because it exhibits non-monotonic behavior, with both increases and decreases during degradation. Instead, it primarily indicates pronounced insulation deterioration near the EoL, when the IR decreases substantially relative to its healthy-state value.

For parameter identification, relative percentage variation $(\Delta\%)$ from the healthy state $(x_{healthy})$ to the degraded state (x_{aged}) was calculated with respect to the healthy baseline as in (5.7).

$$\Delta\% \; x = \frac{x_{aged} - x_{healthy}}{x_{healthy}} \times 100 \quad (5.7)$$

Figure 5.9 presents the GBM-derived parameters for machine 3. Insulation resistance increased during the early heat cycles before decreasing in a non-monotonic manner. Its limited variation near the EoL indicates that IR alone may be insufficient as a reliable indicator of insulation degradation.

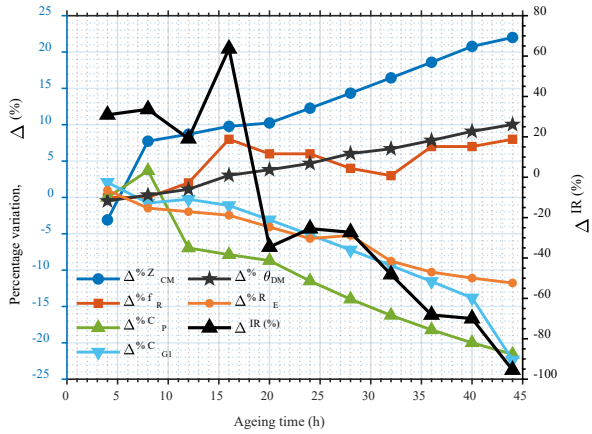


Figure 5.9. Representation of GBM-based IDPs and IR for machine 3.

For machine 3, Z_{CM} increased progressively up to approximately 22% near EoL. The equivalent ground-wall capacitance C_{G1} decreased by about 22%, indicating progressive degradation. The eddy-current loss resistance R_E decreased by about 11%, while the phase-related indicator θ_{DM} as a phase angle at zero crossing showed a gradual increasing trend. Compared with IR as in Figure 5.10, the GBM-derived capacitance and impedance parameters provide more physically interpretable degradation indicators.

As proof of concept, the ground-wall capacitance C_{LF} (or C_P) decreased monotonically near the end of degradation, indicating deterioration before breakdown, consistent with [38], [56], where a decrease of around 25 – 30% was observed just before breakdown. In addition, machine 1 showed a sudden reversal in the capacitance trend, with an increase in capacitance near the end of the aging process. This abrupt change may provide an additional indication of impending insulation breakdown, complementing the progressive capacitance reduction observed during thermal aging.

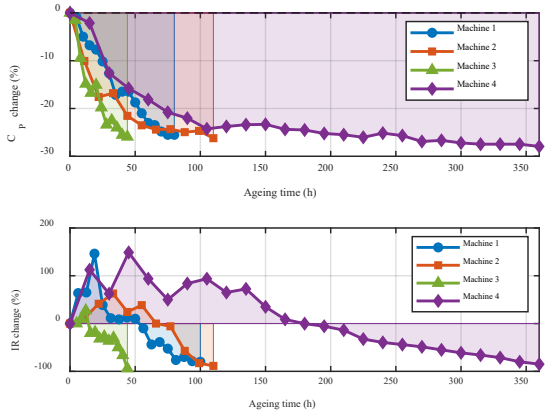


Figure 5.10. Representation of C_P and insulation resistance for all degraded samples.

5.3.1 Lifetime Estimation Model for Samples

The lifetime estimation is based on the Arrhenius thermal endurance model, which relates insulation life to operating temperature [55]. The following scenario is considered an example case in which Arrhenius degradation progression is assumed uniform, even

under large over-temperatures. The reason for selecting such high overtemperature levels is the immense time for insulation aging in actual operation. However, high overtemperature can induce electrical characteristic variations that would otherwise require several years of aging. Here, the key is to thermally overstress the insulation deeply rather than impose chemically correct aging, and to identify parameters that reveal insulation degradation.

Equation (5.8) presents the insulation lifetime evaluation as a function of temperature.

$$t_{LIFE} = A\, e^{\frac{B}{T}} \tag{5.8}$$

where t_{Life} is the total insulation life, T is the absolute temperature, and A and B are material-dependent constants defining the fitted scale factor and temperature-sensitivity term. Converting the equation to logarithmic form makes the relationship linear. Equation (5.8) can be transformed into a logarithmic form by utilizing (5.9)-(5.10).

$$\log_{10} t_{LIFE} = \log_{10} A + \left(log_{10} e \times B\right)\left(\frac{1}{T}\right) \tag{5.9}$$

$$Y = A_1^{'} + B_1^{'} X \tag{5.10}$$

such that:

$\log_{10} t_{LIFE} = Y$, $A^{'} = \log_{10} A$, $B' = log_{10} e \times B$, and $X = 1/T$

The temperature index of class F material is defined as the temperature 155 ^{0}C at which the insulation can maintain a measured physical property for 20,000 h. The aging acceleration factor (AAF), which quantifies the relative aging rate at equivalent temperature $T(t)$ with respect to T_{ref}, is given in (5.11).

$$AAF\,(t) = \frac{t_{LIFE}(T_{ref})}{t_{LIFE}(T(t))} = e^{B\,(\frac{1}{T_{ref}} - \frac{1}{T(t)})} \tag{5.11}$$

The incremental Miner insulation damage is defined as (5.12).

$$d\,D\,(t) = \frac{AAF\,(t)}{t_{LIFE(ref)}}\, d\,t \tag{5.12}$$

where $t_{\mathrm{Life(ref)}}$ denotes the nominal insulation lifetime at the reference temperature T_{ref}. For discretely sampled temperature data T_i with corresponding time intervals Δt_i that define the thermal profile, the cumulative insulation damage (*D*) is evaluated using (5.13).

$$D = \frac{1}{t_{LIFE(ref)}} \sum_{i=1}^{N} AAF_i\, \Delta t_i \tag{5.13}$$

Finally, the RUL expressed in percentage is calculated as in (5.14).

$$RUL\ (\%) = (\,1 - D\,) \times 100 \tag{5.14}$$

For a variable thermal profile, the damage-equivalent temperature T_{eq} was calculated by first computing the equivalent aging acceleration factor using (5.15).

$$AAF_{eq} = \sum_{i=1}^{N} (AAF_i\, \Delta t_i\,) / \sum_{i=1}^{N} (\Delta\, t_i)\,. \tag{5.15}$$

where AAF_i is the acceleration factor at each interval and Δt_i is the corresponding duration. Then, T_{eq} was obtained from the Arrhenius relation such that a constant exposure at T_{eq} produces the same cumulative damage as the variable-temperature profile.

For each machine sample, the Arrhenius coefficients were identified separately using the Class-F reference condition (155 °C/20,000 h) and the experimentally observed EoL condition under accelerated thermal aging. Thus, the resulting coefficients represent sample-specific thermal-endurance characteristics of the investigated insulation systems rather than parameters obtained from an independent validation dataset. The calibrated relationships were subsequently used to calculate aging acceleration factors, cumulative thermal damage, and RUL trajectories for the corresponding aging experiments.

Figure 5.11 presents the experimentally calibrated thermal-endurance trajectories and their consistency with the expected Arrhenius temperature-lifetime relationship.

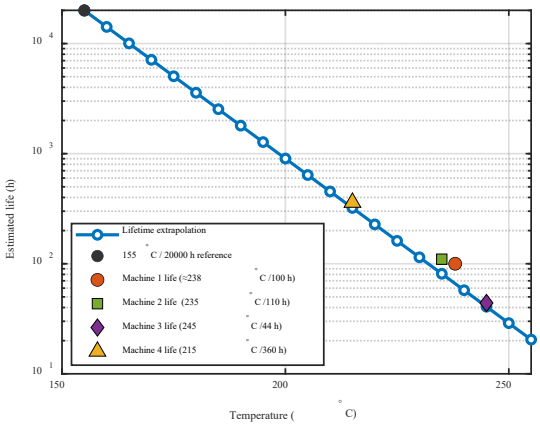


Figure 5.11. Estimation of samples' thermal performance using the Arrhenius diagram.

Initially, sample-1 was aged at 200 °C for the first 10 cycles and then at 250 °C until EoL. The equivalent aging temperatures were 194 °C and 244 °C for the two thermal profiles, respectively. The Arrhenius damage-equivalent temperature was about 238 °C, giving an effective lifetime of about 100 h and an equivalent cumulative damage of about 0.98, corresponding to a near EoL condition. Per 5-hour cycle, damage was 0.5% at 200 °C, 9.3% at 250 °C, and 4.9% at the equivalent temperature of 238 °C. The calibrated Arrhenius trajectory reproduces the experimental EoL condition used for parameter identification and (5.8)-(5.15) provides a continuous thermal-damage representation for RUL calculation. Figure 5.12 presents the time-based evolution of RUL estimations for all four samples. Sample 1 shows that the 200 °C stage contributed about 5% to lifetime consumption, while the 250 °C stage contributed about 95%. Table 5.1 summarizes the estimated Arrhenius parameters for the four samples.

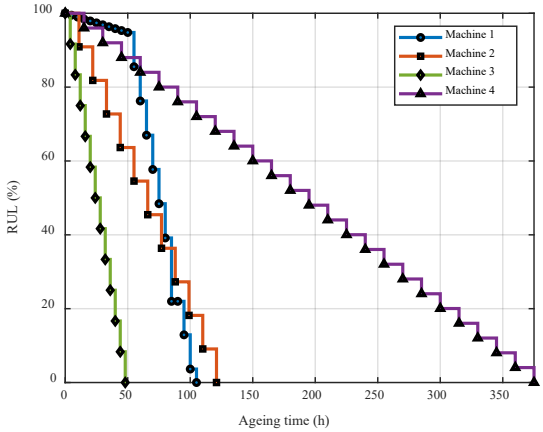


Figure 5.12. Quantitative estimation of RUL for four machine samples under aging time.

Table 5.1. Sample-Specific Estimated Arrhenius Parameters

Machine Sample	A_1'	B_1'	*AAF*	T_{eq} (°C)	*D* per cycle (%)	Thermal cycles
1	-10.7	6270	23 and 407 (≈215)	194 and 245 (≈238)	0.5 and 9.3	21
2	-10.2	6145	181	235	9.1	11
3	−10.5	6324	308	245	8.3	12
4	-9.7	6015	53	215	4	25

5.3.2 Health Index and Lifetime Estimations

Among the investigated IDPs, phase capacitance to ground-wall (C_P) was selected as the health indicator for lifetime estimation because the observed parameters showed degradation-related changes during aging. At EoL, machine samples 1 to 4 showed C_P reductions of nearly 24%, 26%, 26%, and 27%, respectively, corresponding to a relatively narrow normalized EoL range. The aging trajectory was represented using the stretched power-law function utilizing (5.16).

$$C_P(t) = a(t)^b + c \tag{5.16}$$

The capacitive degradation data were fitted to (5.16) using a nonlinear curve-fitting routine in MATLAB to obtain the coefficients a, b, and c. The corresponding upper and lower coefficient confidence limits were used to determine the 95% uncertainty bounds of the fitted degradation trajectory. The EoL threshold was estimated from the variation of C_P values of four machines. The mean EoL level was approximately a 26 % reduction in initial phase capacitance. Owing to the limited sample population ($N = 4$), a student-t distribution was used to determine the confidence threshold boundary point according to (5.17).

$$C_i = \bar{x} \pm t_i \frac{\sigma}{\sqrt{N}} \tag{5.17}$$

where $\bar{x}$, σ, N, and $t_i$denote the mean EoL capacitance, sample standard deviation, number of samples, and Student's t_i coefficient, respectively. For a one-sided 90% confidence threshold level, $t_{0.90,3} = 1.64$, resulting in $C_{\text{threshold}} \approx 24.6\%$. The use of a

one-sided student's t-distribution boundary for a small EoL population follows the statistical rationale of IEEE Std 101 used in the reference methodology [57].

Figure 5.13 presents machine-3 as a representative example of the fitted (C_P) degradation trajectory, including the uncertainty bounds and the 90% confidence threshold used for lifetime estimation. The lifetime estimates for all four machines are summarized in Table 5.2. The fitted lifetimes for machines 1–4 were 88, 97, 45, and 322 h, compared with measured lifetimes of 100, 110, 44, and 360 h, respectively. The corresponding conservative 90% estimations were 81, 79, 38, and 290 h. The fitted estimates differed from the measured EoL times by approximately 2–12%, while the conservative 90% confidence threshold estimates provided earlier maintenance boundaries. Given the small sample size, this is a preliminary, sample-based estimate rather than a statistically robust limit for the wider IM population. Further validation using additional machine samples and independent accelerated-aging experiments is required to establish its generalizability.

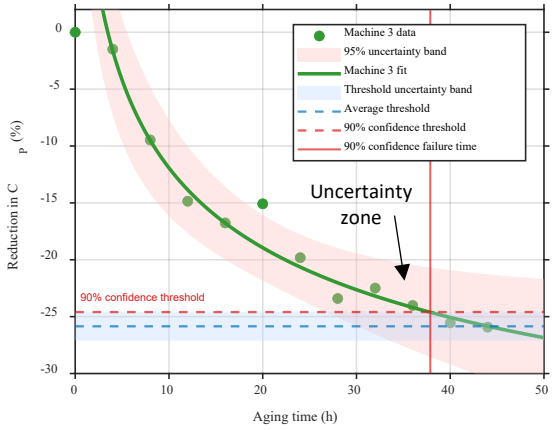


Figure 5.13. Representative machine 3 degradation data, showing curve fitting, uncertainty bounds and 90% confidence threshold.

Table 5.2. Lifetime Estimation Comparison

	Machine 1	**Machine 2**	**Machine 3**	**Machine 4**
Damage equivalent temperature (T_{eq}) (°C)	≈ 238	235	245	215
C_P reduction (%)	24	26	26	27
Arrhenius thermal life estimate (h)	74	81	41	320
Experimental lifetime (h)	100	110	44	360
Fitted lifetime estimation (h)	88	97	45	322
90% confidence threshold estimation (h)	81	79	38	290

5.4 Discussion

This research presents a method for assessing insulation condition in low-voltage induction motors. The approach combines insulation resistance measurements, parameter identification via frequency response analysis, and remaining useful life estimation. Insulation resistance exhibits a non-monotonic trend: it initially increases during the early phase of cyclic thermal stress, then decreases as the motor approaches the end of its useful life. Conversely, certain parameters derived from the proposed impedance model show a stronger correlation with insulation deterioration toward the end of the motor's operational lifespan, providing deeper insight into the insulation aging process itself.

In the four motors analyzed, for example, parameters like capacitance C_P in the low-frequency range consistently decreased by 24% to 27% at the end of useful life; consequently, it was used as the primary health indicator for RUL estimation. The fitted lifetime estimates differed from the experimentally observed EoL times by approximately 2–12%.

However, because the Arrhenius relationships were calibrated using the observed EoL conditions, the reported agreement should not be interpreted as independent validation of predictive accuracy. The approach's generalizability requires further assessment using independent aging experiments and datasets.

Future research could extend the approach by incorporating machine-learning-based health prognostics and synthetic-data generation to improve generalizability across different aging scenarios and operating conditions.

5.5 Chapter Summary

The results show that impedance-derived parameters can provide useful indicators of insulation degradation, particularly near EoL, when IR alone exhibits inconsistent trends. Across the four tested samples, phase capacitance (C_P) decreased by approximately 24–27% at EoL. The fitted lifetime estimates and experimentally measured lifetimes demonstrate the potential of combining impedance-based health indicators with Arrhenius-based thermal degradation calculations to estimate sample-specific lifetimes under the investigated laboratory aging conditions.

6 Thesis Conclusion and Future Work

6.1 Conclusion

This thesis focuses on modeling, diagnosing, and assessing the lifetime of winding insulation in IM and makes three contributions to this field. First, an approach covering a wide-frequency range was developed for cable-fed IM drive systems. The model reproduces frequency-dependent impedance-response behavior using physics-based RLC circuit parameters determined from experimental impedance spectroscopy. Optimizing the initial parameter guess improves agreement with measured responses and enables precise analysis of transient overvoltages (TOVs) and resonance frequencies. These results provide a foundation for evaluating the interactions between the cable and the machine parameters up to 100 MHz, as well as the electrical stresses experienced by the winding insulation.

Second, this work focused on early detection of inter-turn insulation degradation in stator windings using HF switching phenomena. The proposed approach utilizes signal processing based on the fractional Fourier transform and a resonance-centered Mel filter bank to extract features sensitive to degradation. Estimation factors such as SEF_{MAE} and SEF_{RMSE} were used to quantify changes in insulation condition. Experiments on an IM under controlled capacitive degradation conditions showed that combining the FRFT and a Mel filter bank offers greater sensitivity than Fourier-transform-based analysis. This result highlights the potential implementation of fractional-domain signal processing to improve detection of incipient inter-turn insulation degradation.

Third, the assessment of insulation aging and remaining useful life was investigated using frequency-response parametric models. This approach relates aging conditions to reference RUL and parameters such as the aging acceleration factor and equivalent damage. This provides a basis for comparing thermal aging states and estimating insulation remaining useful life.

These three contributions address complementary aspects of evaluating winding insulation. The physics-informed HF GBM characterizes electrical stresses in drive systems fed with power cables. The fractional-domain diagnostic method examines incipient insulation degradation in the windings. Moreover, the aging model estimates the insulation lifetime specific to each sample.

Although these approaches address different aspects of insulation reliability, their interaction within an integrated diagnostic and prognostic system has not yet been experimentally validated. Further work is needed to integrate them in practice and validate performance under representative operating conditions.

6.2 Limitations in the Thesis Work

A limitation of the proposed GBM is that it cannot reproduce LF dynamic transients and load-dependent electromechanical behavior. Although the model accurately characterizes steady-state impedance across a wider frequency range, its steady-state T-equivalent representation cannot reproduce LF transient phenomena as full-order *dq*-axis models. Consequently, it does not fully represent dynamic load variations, torque and speed transients, control-loop interactions, and operating-condition-dependent effects, including magnetic saturation and temperature variations.

The modeling, diagnostic, and insulation lifetime assessment approaches were evaluated through separate experimental investigations rather than as a single

integrated system. Although laboratory accelerated-aging tests provide a repeatable basis for evaluating insulation degradation and tracking changes in health indicators, they cannot fully reproduce the combined thermal, electrical, mechanical, and environmental stresses the machine experiences during operation. Therefore, applying the estimated degradation trends and lifetime estimates to practical operating conditions requires further validation, particularly under representative operating conditions and combined-stress aging scenarios.

Furthermore, the Arrhenius coefficients were derived from experimentally observed EoL data. Consequently, the agreement between estimated and measured lifetimes does not constitute independent validation of predictive accuracy. Further validation using independent accelerated-aging experiments is required to assess the applicability of the lifetime estimates to machines operating under a wider range of conditions, thermal classes and ratings.

6.3 Future Work

To address the limitations identified in this thesis and improve the practical applicability of the proposed framework, future research should focus on the following directions.

1. **Dynamic load and control-system integration:** Extend the proposed GBM with dynamic machine, load, and control-system models to improve the representation of impedance characteristics and transient responses under variable operating conditions.
2. **Real-time diagnostic implementation:** Evaluate the implementation of the proposed HF signal-processing methods on embedded or edge-computing platforms for online insulation-condition monitoring.
3. **Prognostic health management (PHM):** Extend the proposed health indicators toward RUL estimation using larger aging datasets, experimentally established EoL criteria, and independent validation under different aging and operating conditions.

List of Figures

Figure 2.1. Distribution of IM faults according to IEEE-IAS and EPRI reliability surveys. 21
Figure 2.2. Challenges associated with the motor's terminal voltage profile. 23
Figure 2.3. RLC circuit representations: (a) series branch and (b) parallel connection. . 24
Figure 2.4. Impedance characteristics: (a) series RLC resonance, (b) parallel RLC resonance. 24
Figure 2.5. Multi-physical factors driving EIS degradation and PoF-based lifetime estimation. 25
Figure 2.6. Electrical signal measurement for insulation monitoring. 28
Figure 3.1. Typical configuration of a cable-fed motor drive. 31
Figure 3.2. IM impedance measurement topologies: (a) DM, (b) CM. 32
Figure 3.3. Measurement results showing the impedance profile for DM (red) and CM (blue). 32
Figure 3.4. Measurement results showing the terminal voltage spectrum V_{ab} (FT; blue, left axis) with DM impedance (red, right axis), showing four TOVs/ resonance frequencies (◊ marker). 33
Figure 3.5. RLC circuit-based model of an IM: (a) conventional model, (b) proposed GBM. 34
Figure 3.6. The self- and mutual inductances of the connections and internal line conductors schematics in (a) CM, (b) DM. 36
Figure 3.7. Winding self- and mutual inductance representation in (a) CM and (b) DM.37
Figure 3.8. Initial HF IM equivalent circuits above 1 MHz: (a) CM and (b) DM configurations. 37
Figure 3.9. Matching of the impedance profile of measured results, the universal machine model, and the proposed optimal GBM for (a) CM and (b) DM typologies. 38
Figure 3.10. DM cable measurement schematics (a) SC mode (b) OC mode. 39
Figure 3.11. Cable HF representation: (a) Multi-section model of a cable, (b) Three-phase representation with HF parameters, and (c) GBM of cable in DM schematics. 39
Figure 3.12. Matching impedance profile results of measured, initial model, and optimized model for cable connection topologies: (a) OC and (b) SC. 40
Figure 3.13. Error boxplots for various nominated topologies compared with measurements (a) Universal/initial model (top) (b) Optimized model (bottom). 41
Figure 3.14. Test bench of the IM: (a) ASD inverter, (b) oscilloscope, (c) HF differential probes, (d) junction box, (e) load motor, (f) test motor (IM), (g) HF current probe, and (h) power cable. 42
Figure 3.15. Time-domain comparison of measured and optimized-model signals for the IM with a 5 m cable (a) Voltage signal for Vab as TOV (b) voltage signal for VCM, and (c) current signal for I_a. 42
Figure 3.16. Matching of voltage spectra representing V_{ab} with multiple TOV resonance characteristic frequencies (◊ markers). 43
Figure 3.17. Machine terminal voltage frequency representation across BB' terminal, highlighting multiple TOV resonance frequencies with (a) 5 m cable and (b) 1 m cable. 44
Figure 3.18. Combined cable–motor impedance peaks representing TOV and ARO using 1 m, 5 m, 13 m, and 28 m cables. 45
Figure 3.19. Parameter sensitivity analysis showing parametric variation of cable L_{s1} . 46
Figure 3.20. ROA defined for the motor-drive system. 46

Figure 4.1. Proposed signal acquisition methodology for inverter-fed drive system. 48
Figure 4.2. Parametric GBM model of IM. 49
Figure 4.3. HF oscillation modes of PWM switching current in a drive system. 50
Figure 4.4. Inverter switching transients: (a) switching transient voltage and associated HF current oscillation; (b) zoomed view of damped oscillation response and current components i_{CM-2}. 51
Figure 4.5. Measured DM impedance profile under different turn degradation faults. 51
Figure 4.6. Transformation of HF switching oscillation current through signal processing. 54
Figure 4.7. Frequency distribution of filters in a standard Mel filter bank. 55
Figure 4.8. Distribution of an adaptive RMFB. 55
Figure 4.9. Schematic of the proposed optimum FRFT-RMFB framework 57
Figure 4.10. VFS test setup: (a) VFS supply (initially at f_{sw}=100 kHz), (b) oscilloscope, (c) motor, (d) current probe (100 MHz), (e) differential probe (100 MHz) (f) 5 m cable..... 58
Figure 4.11. Measured switching motor current (Ia) signal in the time domain. 59
Figure 4.12. Sensitivity analysis for determining the optimal fractional order. 59
Figure 4.13. Frequency distribution of the proposed FRFT-RMFB filter bank. 60
Figure 4.14. Spectral representation using methods (a) FT and (b) FRFT-RMFB. 60
Figure 4.15. Sensitivity comparison results (SEF_{MAE}) across different methods. 61
Figure 4.16. Experimental setup for converter-fed operation: (a) impedance analyzer, (b) VFD at a switching frequency of f_{sw}=10 kHz, (c) test motor, (d) 5 m cable, (e) ambient hygrometer, (f) thermometer, and (g) impedance analyzer interface. 61
Figure 4.17. Spectral representations obtained using (a) FRFT and (b) proposed FRFT-RMFB method. 62
Figure 4.18. Comparison of insulation-degradation sensitivity obtained using different signal-processing methods. 63
Figure 4.19. Schematic of the experimental setup for diagnosing stator winding insulation degradation during thermal aging. 63
Figure 4.20. Thermal degradation setup: (a) heating chamber, (b) test motor, (c) infrared thermometer, (d) impedance analyzer, (e) oscilloscope, (f) differential probe, (g) current probe, and (h) inverter-fed supply. 64
Figure 4.21. Impedance measurement results in CM schematics. 64
Figure 4.22. Sensitivity analysis for selecting the optimal fractional order. 65
Figure 4.23. Frequency domain representation (a) FT (b) Band-pass filtered (c) FRFT (d) FRFT-RMFB 65
Figure 4.24. *Comparison* of multiple signal processing analyses. 66
Figure 5.1. Lumped GBM of an IM showing various frequency-response parameters... 68
Figure 5.2. IM impedance measurements in (a) DM and (b) CM. 69
Figure 5.3. CM impedance profile illustrating inter-turn and ground-wall insulation degradation. 69
Figure 5.4. CM impedance profile of an electrical machine. 69
Figure 5.5. Experimental platform: (a) heating chamber and samples, (b) impedance measurement, (c) IR testing, (d) close-up view of the stator's degraded winding. 71
Figure 5.6. IR-change evolution and experimentally determined EoL criterion for the four machine samples. 72
Figure 5.7. FRA-based CM impedance-frequency spectra for (a) sample 1 and (b) sample 3. 72

Figure 5.8. Measured and optimally fitted GBM impedance response of machine 1 in healthy state. 73
Figure 5.9. Representation of GBM-based IDPs and IR for machine 3. 74
Figure 5.10. Representation of C_P and insulation resistance for all degraded samples. . 74
Figure 5.11. Estimation of samples' thermal performance using the Arrhenius diagram. 76
Figure 5.12. Quantitative estimation of RUL for four machine samples under aging time. 77
Figure 5.13. Representative machine 3 degradation data, showing curve fitting, uncertainty bounds and 90% confidence threshold. 78

List of Tables

Table 2.1. Classification of IM Faults and Inverter-Related Electrical Stresses. 22
Table 2.2. Summary of Main Techniques for Electrical-Machine Insulation Condition Monitoring. 27
Table 3.1. Motor impedance spectrum measurement 32
Table 4.1. Extracted IM parameters for varying external capacitances..... 52
Table 4.2. Comparison of multiple signal processing-based insulation condition monitoring techniques. 53
Table 4.3. Main parameters of the test bench motor..... 58
Table 4.4. Comparison of percentage (%) sensitivity (SEF_{MAE}) of different methods..... 61
Table 4.5. Comparison of percentage SEF_{MAE} values obtained using different signal-processing methods under controlled turn-insulation degradation. 62
Table 4.6. Statistical representation of SEF_{MAE} (%) for methods for insulation state changes 66
Table 5.1. Sample-Specific Estimated Arrhenius Parameters 77
Table 5.2. Lifetime Estimation Comparison 78

References

[1] International Energy Agency, “Electricity 2026: Analysis and Forecast to 2030,” in *IEA*, Paris, France, 2026.

[2] European Parliament and Council of the European Union, “Regulation (EU) 2021/1119 establishing the framework for achieving climate neutrality (European Climate Law),” *Official Journal of the European Union*, 2021.

[3] European Parliament and Council of the European Union, “Directive (EU) 2023/1791 on energy efficiency,” *Official Journal of the European Union*, 2023.

[4] European Commission, “Commission Regulation (EU) 2019/1781 laying down ecodesign requirements for electric motors and variable speed drives,” *Official Journal of the European Union*, 2019.

[5] J. E. Ruiz-Sarrio, J. A. Antonino-Daviu, A. Navarro-Navarro, and V. Biot-Monterde, “A Review of Broadband Frequency Techniques for Insulation Monitoring and Diagnosis in Rotating Electrical Machines,” *IEEE Trans. Ind. Appl.*, vol. 60, no. 4, pp. 6092–6102, 2024, doi: 10.1109/TIA.2024.3384454.

[6] G. Niu, X. Dong, and Y. Chen, “Motor Fault Diagnostics Based on Current Signatures: A Review,” 2023. doi: 10.1109/TIM.2023.3285999.

[7] G. C. Stone, H. G. Sedding, and C. Chan, “Experience with Online Partial-Discharge Measurement in High-Voltage Inverter-Fed Motors,” in *IEEE Transactions on Industry Applications*, 2018. doi: 10.1109/TIA.2017.2740280.

[8] B. Asad, T. Vaimann, A. Belahcen, A. Kallaste, A. Rassõlkin, and M. Naveed Iqbal, “The cluster computation-based hybrid FEM–analytical model of induction motor for fault diagnostics,” *Applied Sciences (Switzerland)*, vol. 10, no. 21, 2020, doi: 10.3390/app10217572.

[9] W. Zhu, D. De Gaetano, X. Chen, G. W. Jewell, and Y. Hu, “A Review of Modeling and Mitigation Techniques for Bearing Currents in Electrical Machines With Variable-Frequency Drives,” *IEEE Access*, vol. 10, pp. 125279–125297, 2022..

[10] H. Peng *et al.*, “High-frequency Modeling of Permanent Magnet Synchronous Machines using Grey Box Models,” *IEEE Transactions on Transportation Electrification*, 2024, doi: 10.1109/TTE.2024.3363511.

[11] J. E. Ruiz-Sarrio, J. A. Antonino-Daviu, A. Navarro-Navarro, and V. Biot-Monterde, “Broadband Technique Analysis for Insulation Fault Detection and Condition Monitoring in Rotating Electrical Machines,” in *Proceedings of the 2023 IEEE 14th International Symposium on Diagnostics for Electrical Machines, Power Electronics and Drives, SDEMPED 2023*, 2023. doi: 10.1109/SDEMPED54949. 2023.10271498.

[12] D. Venkatar Ramana and S. Baskar, “Fault analysis of voltage source inverter fed induction motor drive,” in *2016 IEEE International Conference on Computational Intelligence and Computing Research, ICCIC 2016*, 2017. doi: 10.1109/ICCIC.2016. 7919657.

[13] T. Vaimann, A. Belahcen, J. Martinez, and A. Kilk, “Detection of broken bars in frequency converter fed induction motor using Park’s vector approach,” in *PQ 2012: 8th International Conference - 2012 Electric Power Quality and Supply Reliability, Conference Proceedings*, 2012. doi: 10.1109/PQ.2012.6256204.

[14] B. Asad, T. Vaimann, A. Belahcen, A. Kallaste, A. Rassõlkin, and M. N. Iqbal, “Modified winding function-based model of squirrel cage induction motor for

fault diagnostics," *IET Electr. Power Appl.*, vol. 14, no. 9, 2020, doi: 10.1049/iet-epa.2019.1002.

[15] T. Vaimann, J. Sobra, A. Belahcen, A. Rassõlkin, M. Rolak, and A. Kallaste, "Induction machine fault detection using smartphone recorded audible noise," *IET Science, Measurement and Technology*, vol. 12, no. 4, 2018, doi: 10.1049/iet-smt.2017.0104.

[16] P. Zhang, Y. Du, T. G. Habetler, and B. Lu, "A survey of condition monitoring and protection methods for medium-voltage induction motors," 2011. doi: 10.1109/TIA.2010.2090839.

[17] B. Asad, T. Vaimann, A. Belahcen, and A. Kallaste, "Broken rotor bar fault diagnostic of inverter fed induction motor using FFT, Hilbert and Park's Vector approach," in *Proceedings - 2018 23rd International Conference on Electrical Machines, ICEM 2018*, 2018. doi: 10.1109/ICELMACH.2018.8506957.

[18] M. U. Sardar *et al.*, "Inverter-Fed Motor Drive System: A Systematic Analysis of Condition Monitoring and Practical Diagnostic Techniques," *Energies (Basel).*, vol. 16, no. 15, p. 5628, Jul. 2023, doi: 10.3390/en16155628.

[19] W. Zhou, M. Diab, and X. Yuan, "Impact of Parasitic and Load Current on the Attenuation of Motor Terminal Overvoltage in SiC-Based Drives," *IEEE Trans. Ind. Appl.*, vol. 58, no. 2, 2022, doi: 10.1109/TIA.2022.3141703.

[20] J. He, C. Somogyi, A. Strandt, and N. A. O. Demerdash, "Diagnosis of stator winding short-circuit faults in an interior permanent magnet synchronous machine," in *2014 IEEE Energy Conversion Congress and Exposition, ECCE 2014*, 2014. doi: 10.1109/ECCE.2014.6953825.

[21] S. Huang, A. Aggarwal, E. G. Strangas, B. Khoshoo, K. Li, and F. Niu, "Mitigation of Interturn Short-Circuits in IPMSM by Using MTPCC Control Adaptive to Fault Severity," *IEEE Trans. Power Electron.*, vol. 37, no. 4, 2022, doi: 10.1109/TPEL.2021.3127538.

[22] S. Huang, A. Aggarwal, E. G. Strangas, K. Li, F. Niu, and X. Huang, "Robust Stator Winding Fault Detection in PMSMs with Respect to Current Controller Bandwidth," *IEEE Trans. Power Electron.*, vol. 36, no. 5, 2021, doi: 10.1109/TPEL.2020.3030036.

[23] Z. Chen *et al.*, "Reliability-Oriented Multiobjective Optimization of Electrical Machines Considering Insulation Thermal Lifetime Prediction," *IEEE Transactions on Transportation Electrification*, vol. 10, no. 1, 2024, doi: 10.1109/TTE.2023.3283516.

[24] P. Tillmann, "Multiphysical Winding Insulation Ageing: Review of Test Benches, Measurements and Standards," in *2025 Energy Conversion Congress and Expo Europe, ECCE Europe 2025 - Proceedings*, 2025. doi: 10.1109/ECCE-Europe62795.2025.11238581.

[25] IEC 60034-18-21:2012, "Rotating electrical machines—Part 18-21: Functional evaluation of insulation systems—Test procedures for wire-wound windings—Thermal evaluation and classification," *International Electrotechnical Commission*, 2012.

[26] IEEE Std 117-2015, "IEEE Standard Test Procedure for Thermal Evaluation of Systems of Insulating Materials for Random-Wound AC Electric Machinery," *IEEE*, May 2016.

[27] IEC 60034-18-41:2014, "Rotating electrical machines - Part 18-41: Partial discharge free electrical insulation systems (Type I) used in rotating electrical

machines fed from voltage converters - Qualification and quality control tests," *International Electrotechnical Commission*, 2014.

[28] G. C. Stone, I. Culbert, E. A. Boulter, and H. Dhirani, *Electrical Insulation for Rotating Machines: Design, Evaluation, Aging, Testing, and Repair: Second Edition*, vol. 9781118057063. 2014. doi: 10.1002/9781118886663.

[29] M. R. Khowja *et al.*, "Lifetime Estimation of Enameled Wires under Accelerated Thermal Aging Using Curve Fitting Methods," *IEEE Access*, vol. 9, 2021, doi: 10.1109/ACCESS.2021.3052058.

[30] C. Park *et al.*, "Automated Testing for Early Identification of PD in the Stator Insulation of Low Voltage VFD Motors," *IEEE Trans. Ind. Appl.*, vol. 59, no. 4, 2023, doi: 10.1109/TIA.2023.3258430.

[31] P. Wang, S. Ma, S. Akram, K. Zhou, Y. Chen, and M. T. Nazir, "Design of Archimedes Spiral Antenna to Optimize for Partial Discharge Detection of Inverter Fed Motor Insulation," *IEEE Access*, vol. 8, 2020, doi: 10.1109/ACCESS.2020.3033300.

[32] F. Niu *et al.*, "A Novel Method for Monitoring Stator Interturn Insulation Degradation of Inverter-Fed Motors Based on Impedance Spectrum Division," *IEEE Transactions on Industrial Electronics*, vol. 72, no. 6, 2025, doi: 10.1109/TIE.2024.3497310.

[33] D. Zheng and P. Zhang, "An Online Groundwall and Phase-to-Phase Stator Insulation Monitoring Method for Inverter-Fed Machine," *IEEE Transactions on Industrial Electronics*, vol. 68, no. 6, 2021, doi: 10.1109/TIE.2020.2988218.

[34] D. Zheng, G. Lu, Y. Wu, Q. Zhang, and P. Zhang, "Online Detection and Classification of Interturn and Groundwall Insulation Aging Based on Broadband Common-Mode Impedance Spectrum," *IEEE Transactions on Industrial Electronics*, vol. 71, no. 3, 2024, doi: 10.1109/TIE.2023.3265024.

[35] M. F. Shaikh, H. Lee, B. Battulga, S. Bin Lee, and G. C. Stone, "Detection of Severe Ground Insulation Deterioration Before Failure in VFD-Fed Motors Using Off-Line Common-Mode Voltage," *IEEE Trans. Ind. Appl.*, vol. 60, no. 1, 2024, doi: 10.1109/TIA.2023.3307344.

[36] D. Xiang, H. Li, H. Yan, Y. Zheng, N. Zhao, and B. Liu, "Online Monitoring of Incipient Turn Insulation Degradation for Inverter-Fed Machine Using Sensitive Tail Component in PWM Switching Oscillations," *IEEE Trans. Power Electron.*, vol. 36, no. 8, 2021, doi: 10.1109/TPEL.2021.3049809.

[37] F. Niu *et al.*, "An Online Groundwall Insulation Monitoring Method Based on Transient Characteristics of Leakage Current for Inverter-Fed Motors," *IEEE Trans. Power Electron.*, vol. 37, no. 8, 2022, doi: 10.1109/TPEL.2022.3157571.

[38] L. E. Azpiazu, Y. Moreno, A. Egea, G. Almandoz, and A. A. Rebollo, "Comparison of Impedance Spectroscopy and Partial Discharge Analysis as Insulation Health Diagnosis Techniques," in *2024 International Conference on Electrical Machines, ICEM 2024*, 2024. doi: 10.1109/ICEM60801.2024.10700230.

[39] H. Peng *et al.*, "Voltage Distribution Modeling Along Stator Windings in Permanent Magnet Synchronous Machines Using Coil-Based Grey Box Models," *IEEE Transactions on Energy Conversion*, vol. 39, no. 3, 2024, doi: 10.1109/TEC.2024.3370800.

[40] V. Madonna, P. Giangrande, G. Migliazza, G. Buticchi, and M. Galea, "A Time-Saving Approach for the Thermal Lifetime Evaluation of Low-Voltage Electrical

Machines," *IEEE Transactions on Industrial Electronics*, vol. 67, no. 11, 2020, doi: 10.1109/TIE.2019.2956378.

[41] G. Turabee *et al.*, "The Role of Neural Networks in Predicting the Thermal Life of Electrical Machines," *IEEE Access*, vol. 8, 2020, doi: 10.1109/ACCESS.2020.2975985.

[42] R. J. Kerkman, D. Leggate, and G. L. Skibinski, "Interaction of drive modulation and cable parameters on ac motor transients," *IEEE Trans. Ind. Appl.*, vol. 33, no. 3, 1997, doi: 10.1109/28.585863.

[43] L. Wang, Y. Zhang, M. S. Ali, G. Chen, J. M. Guerrero, and J. C. Vasquez, "High-frequency modeling and filter design for PWM drives with long cables," *Energies (Basel).*, vol. 14, no. 4, Feb. 2021, doi: 10.3390/en14041155.

[44] M. Mohammadi-Rostam and M. Shahabi, "Modeling Induction Motor for Prediction of High frequency problems," *Iranian Journal of Science and Technology - Transactions of Electrical Engineering*, vol. 40, no. 1, 2016, doi: 10.1007/s40998-016-0007-z.

[45] L. Wang, C. N. M. Ho, F. Canales, and J. Jatskevich, "High-frequency modeling of the long-cable-fed induction motor drive system using TLM approach for predicting overvoltage transients," *IEEE Trans. Power Electron.*, vol. 25, no. 10, 2010, doi: 10.1109/TPEL.2010.2047027.

[46] J. Sun and L. Xing, "Parameterization of three-phase electric machine models for EMI simulation," *IEEE Trans. Power Electron.*, vol. 29, no. 1, 2014, doi: 10.1109/TPEL.2013.2264750.

[47] M. U. Sardar, T. Vaimann, L. Kütt, B. Asad, A. Kallaste, and K. Kudelina, "Characterization of High-Frequency Impedance-Based Models for Transient Terminal Overvoltage Estimation in Cable-Fed Motor Drive Systems," in *2024 International Conference on Electrical Machines (ICEM)*, IEEE, Sep. 2024, pp. 1–7. doi: 10.1109/ICEM60801.2024.10700495.

[48] S. Baig, S. Ebrahimi, J. Jatskevich, L. Wang, and A. Fani, "Wide-Band Constant-Parameter Voltage-Behind-Reactance Model of Squirrel-Cage Induction Machines," *IEEE Transactions on Energy Conversion*, 2024, doi: 10.1109/TEC.2024.3420897.

[49] H. Liu, X. W. Zhang, and L. P. Tu, "A modified particle swarm optimization using adaptive strategy," *Expert Syst. Appl.*, vol. 152, 2020, doi: 10.1016/j.eswa.2020.113353.

[50] X. Bi, S. Guo, Y. Yang, and Q. Shu, "Adaptive Target Extraction Method in Sea Clutter Based on Fractional Fourier Filtering," *IEEE Transactions on Geoscience and Remote Sensing*, vol. 60, 2022, doi: 10.1109/TGRS.2022.3192893.

[51] R. Muralishankar, D. Ghosh, and S. Gurugopinath, "A Novel Modified Mel-DCT Filter Bank Structure with Application to Voice Activity Detection," *IEEE Signal Process. Lett.*, vol. 27, 2020, doi: 10.1109/LSP.2020.3006447.

[52] M. U. Sardar, T. Vaimann, L. Kütt, B. Asad, A. Kallaste and A. Rassõlkin, "Modeling Cable-Fed Induction Motor Drives With Optimized Impedance Characterization Across a Low to High-Frequency Spectrum," in *IEEE Transactions on Energy Conversion*, vol. 41, no. 2, pp. 1055-1069, June 2026, doi: 10.1109/TEC.2025.3630465.

[53] R. Fan, X. Lei, T. Jia, M. Qin, H. Li, and D. Xiang, "High-sensitive state perception method for inverter-fed machine turn insulation based on FrFT-Mel," *Global*

Energy Interconnection, vol. 7, no. 2, pp. 155–165, Apr. 2024, doi: 10.1016/j.gloei.2024.04.004.

[54] I. Tsyokhla, A. Griffo, and J. Wang, "Online condition monitoring for diagnosis and prognosis of insulation degradation of inverter-fed machines," *IEEE Transactions on Industrial Electronics*, vol. 66, no. 10, 2019, doi: 10.1109/TIE.2018.2885740.

[55] X. Zhou, Y. Ji, P. Giangrande, W. Zhao, and M. Galea, "Temperature Cycling Life Prediction of Low-Voltage Transportation Electric Machines Winding: From Lifetime Model Proposal to Applications," *IEEE Transactions on Transportation Electrification*, 2025, doi: 10.1109/TTE.2025.3648430.

[56] D. Zheng, G. Lu, and P. Zhang, "An Improved Online Stator Insulation Monitoring Method Based on Common-Mode Impedance Spectrum Considering the Effect of Aging Position," *IEEE Trans. Ind. Appl.*, vol. 58, no. 3, 2022, doi: 10.1109/TIA.2022.3160131.

[57] IEEE Std 101-1987 (R2010), "IEEE Guide for the Statistical Analysis of Thermal Life Test Data," *IEEE*, 2011, doi: 10.1109/IEEESTD.2011.5970069.

Acknowledgements

I would like to express my sincere gratitude to my supervisor, Dr. Toomas Vaimann, and co-supervisor, Dr. Lauri Kütt, for their continuous support and guidance throughout my doctoral studies. I am also grateful to Dr. Bilal Asad, my mentor, Prof. Ants Kallaste, Head of the Research Group, co-authors and my colleagues for their valuable advice, knowledge, experience, and encouragement, which have contributed significantly to my academic and research journey.

I would also like to thank Dr. Raul Land for the opportunity to conduct experimental testing in the Thomas Johann Seebeck Department of Electronics. I am equally grateful to Dr. Ivar Kiitam and Dr. Paul Taklaja for providing testing facilities in the High Voltage Engineering Laboratory. Their support was invaluable in carrying out the experimental work presented in this thesis.

Finally, I would like to express my deepest gratitude to my wife, Ammara Khalid, for her unwavering love, endless patience, understanding, and unconditional support throughout my doctoral journey.

Abstract

High-Frequency Modeling and Diagnostics of Winding Insulation Degradation in Induction Machines

Power electronic converters expose the induction machine's winding insulation to rapid switching transients, high voltage gradients, transient terminal overvoltages, and common-mode voltages. These effects accelerate insulation aging. Conventional models have limited capacity to represent interactions among the inverter, cable, and machine, while existing diagnostic methods lack the sensitivity needed to detect early-stage degradation. This thesis develops a parametric approach for high-frequency machine modeling, insulation diagnostics, and lifetime assessment.

First, a physics-based grey-box model (GBM) is developed to characterize the high-frequency electrical behavior of induction machines and power cables using experimentally measured impedance responses obtained through frequency response analysis (FRA). An optimization algorithm refines the model's initial analytical parameter calculations through an optimal fitting procedure, providing a more accurate representation of electrical behavior. Experimental validation shows that the model's average error decreased from 6.4% to 4.8% for combined cable and IM frequency-response representation, and from 5.9% to 4.5% for terminal overvoltages and common-mode voltage representations in the frequency domain. Furthermore, it identifies frequency ranges where the windings experience increased voltage stress.

Second, a diagnostic method uses switching transients that naturally occur during pulse-width modulation to detect the onset of insulation degradation in the windings. It combines an optimized fractional Fourier transform (FRFT) with a resonance-centered Mel filter bank (RMFB), enabling the extraction of features sensitive to such degradation from high-frequency current oscillations. Experiments involving controlled capacitance variations demonstrated approximately seven times higher average sensitivity than conventional FT-based analysis. For thermally aged stator windings, the proposed method achieved an average SEF approximately five times higher than that of the Fourier transform.

Third, FRA-based impedance measurements, performed during accelerated thermal aging of multiple machine winding samples, allow tracking of multiple parameters sensitive to insulation degradation. These include inter-turn and ground-wall capacitances, resistive losses, impedances, resonant-frequency shifts, and phase-angle characteristics. Phase-to-ground wall capacitance is a useful indicator of the machine's insulation condition and decreases by approximately 24–27% at end of life. This thermal-aging analysis is combined with cumulative damage models to estimate lifetime. The fitted lifetime estimates differed from experimentally observed end-of-life times by about 2–12%.

In summary, this thesis links high-frequency electrical characterization with precise degradation diagnostics and model-based insulation lifetime assessment. Therefore, it provides an insightful, physics-informed approach to condition monitoring and improved reliability assessment of induction machines.

Lühikokkuvõte

Asünkroonmasinate mähiste isolatsiooni degradeerumise kõrgsageduslik modelleerimine ja diagnostika

Jõuelektroonilised muundurid avaldavad asünkroonmasinate mähiste isolatsioonile kiireid lülitustransiente, suuri pingetõusu kiirusi, transientseid klemmipinge ülepingeid ja ühismoodpingeid. Need nähtused kiirendavad isolatsiooni vananemist. Tavapäraste mudelite võime kirjeldada sagedusmuunduri, toitekaabli ja elektrimasina vastastikmõjusid on piiratud, samas kui olemasolevate diagnostikameetodite tundlikkus ei pruugi olla piisav isolatsiooni degradeerumise varajases staadiumis tuvastamiseks. Käesolevas doktoritöös arendatakse parameetripõhist lähenemisviisi kõrgsageduslikuks modelleerimiseks, isolatsiooni diagnostikaks ja kasutusea hindamiseks.

Esiteks kirjeldab füüsikalistel põhimõtetel põhinev hallkastmudel asünkroonmasinaid ja toitekaableid, kasutades impedantsspektroskoopia abil saadud mõõtetulemusi. Optimeerimisalgoritm täpsustab esialgseid analüütiliselt arvutatud parameetreid sobitusprotseduuri abil, võimaldades elektrilise käitumise täpsemat kirjeldamist sageduse funktsioonina. Eksperimentaalne valideerimine näitab, et mudel kirjeldab mitut jada- ja rööp-resonantsi ning transientseid klemmipinge ülepingelisi nähtusi. Lisaks võimaldab see tuvastada sagedusvahemikke, milles mähiste elektriline koormus on suurenenud.

Teiseks kasutatakse diagnostikameetodis impulsslaiusmodulatsiooni (PWM) käigus loomulikult tekkivaid lülitustransiente mähiste isolatsiooni degradeerumise algstaadiumi tuvastamiseks. Meetod ühendab optimeeritud fraktsionaalse Fourier' teisenduse (FRFT) resonantsikeskse Mel-filtripangaga (RMFB), võimaldades eraldada kõrgsageduslikest vooluostsillatsioonidest isolatsiooni degradeerumise suhtes tundlikke tunnuseid. Kontrollitud mahtuvusmuutustega ja termiliselt vanandatud staatorimähistega tehtud katsed näitavad suuremat tundlikkust võrreldes tavapäraste signaalitöötlusmeetoditega. Sagedusmuunduriga toidetud süsteemi katsetes termiliselt vanandatud staatoriga saavutas meetod isolatsiooni seisundi hindamisteguri, mis oli keskmiselt viis korda suurem kui kiire Fourier' teisenduse (FT) korral.

Kolmandaks võimaldavad kiirendatud termilise vanandamise käigus tehtud sageduskarakteristikute analüüsil (FRA) põhinevad impedantsmõõtmised jälgida degradeerumisprotsesside suhtes tundlikke parameetreid. Nende hulka kuuluvad keerdudevaheline ja maa suhtes mõõdetav mahtuvus, kadudega seotud takistused, impedants, resonantssageduste nihked ning faasinurga muutused. Faasi ja maa vaheline mahtuvus on masina isolatsiooni seisundi kasulik näitaja, mis väheneb eluea lõpus ligikaudu 24–27%. Seda analüüsi kombineeritakse termilise vananemise ja kumulatiivse kahjustuse mudelitega, et hinnata isolatsiooni kasutusiga. Sobitatud kasutusea hinnangud erinesid eksperimentaalselt määratud eluea lõpu aegadest ligikaudu 2–12%.

Kokkuvõttes seob käesolev doktoritöö kõrgsagedusliku elektrilise karakteriseerimise, tundliku degradeerumisdiagnostika ja mudelipõhise isolatsiooni kasutusea hindamise. Seega loob see aluse füüsikalistel põhimõtetel põhinevale seisundiseirele ning asünkroonmasinate töökindluse täpsemale hindamisele.

Appendix 1

Publication I

M. U. Sardar et al., “Inverter-fed motor drive system: A systematic analysis of condition monitoring and practical diagnostic techniques,” Energies, vol. 16, no. 15, Jul. 2023, Art. no. 5628, doi: 10.3390/en16155628.

energies

MDPI

Review

Inverter-Fed Motor Drive System: A Systematic Analysis of Condition Monitoring and Practical Diagnostic Techniques

Muhammad Usman Sardar [1,*], Toomas Vaimann [1,*], Lauri Kütt [1], Ants Kallaste [1], Bilal Asad [1,2], Siddique Akbar [1] and Karolina Kudelina [1]

[1] Department of Electrical Power Engineering and Mechatronics, Tallinn University of Technology, 12616 Tallinn, Estonia; lauri.kutt@taltech.ee (L.K.)
[2] Department of Electrical Power Engineering, The Islamia University of Bahawalpur, Bahawalpur 63100, Pakistan
* Correspondence: muhammad.sardar@taltech.ee (M.U.S.); toomas.vaimann@taltech.ee (T.V.)

Abstract: Due to their efficiency and control capabilities, induction motors fed with inverters have become prevalent in various industrial applications. However, ensuring the reliable operation of the motor and diagnosing faults on time are crucial for preventing unexpected failures and minimizing downtime. This paper systematically analyzes condition monitoring and practical diagnostic techniques for inverter-fed motor drive systems. This study encompasses a thorough evaluation of different methods used for condition monitoring and diagnostics of induction motors, with the most crucial faults in their stator, rotor, bearings, eccentricity, shaft currents, and partial discharges. It also includes an assessment of their applicability. The presented analysis includes a focus on the challenges associated with inverter-fed systems, such as high-frequency harmonics, common-mode voltages causing the bearing currents, and high voltage gradients (dv/dt) due to fast switching frequency, which can impact the motor operation, as well as its faults analysis. Furthermore, this research explores the usefulness and efficiency of various available diagnostic methods, such as motor current signature analysis and other useful analyses using advanced signal processing techniques. This study aims to present findings that provide valuable insights for developing comprehensive condition monitoring strategies, and practical diagnostic techniques that enable proactive maintenance, enhanced system performance, and improved operational reliability of inverter-fed motor drive systems.

Keywords: condition monitoring; induction motors; pulse width modulation inverters; principal component analysis; spectral analysis; switching circuits

check for updates

Citation: Sardar, M.U.; Vaimann, T.; Kütt, L.; Kallaste, A.; Asad, B.; Akbar, S.; Kudelina, K. Inverter-Fed Motor Drive System: A Systematic Analysis of Condition Monitoring and Practical Diagnostic Techniques. *Energies* **2023**, *16*, 5628. https://doi.org/10.3390/en16155628

Academic Editor: Frede Blaabjerg

Received: 3 July 2023
Revised: 17 July 2023
Accepted: 24 July 2023
Published: 26 July 2023

Copyright: © 2023 by the authors. Licensee MDPI, Basel, Switzerland. This article is an open access article distributed under the terms and conditions of the Creative Commons Attribution (CC BY) license (https://creativecommons.org/licenses/by/4.0/).

1. Introduction

Today, industries utilize many electrical machines, particularly induction motors (IM), with wattages ranging from several watts to megawatts to convert electrical power to the required mechanical power. IM has a lower power-by-weight (W/kg) ratio than a synchronous machine of the same rating, has lower costs, is more durable, and requires less maintenance. Hence, they are known as the workhorse of the industry. They are more useful in about 80% of the industry's operations, such as the petrochemical industry, vehicular technology, mining process, propulsion systems, aerospace, nuclear-reactor plants etc. Their healthy and continued operation is required, because motor failure can shut down the whole plant process. This situation will generate significant financial loss and should be avoided to the maximum extent. Hence, early detection of faults with appropriate condition monitoring and diagnostic techniques within the motor is always required in terms of all means of time and money [1–3].

Many publications [4–7] investigated the condition monitoring (CM) and fault diagnostics (FD) of IM faults related to electrical, mechanical, and environmental scenarios

when operated with the grid supply. However, inverter-fed machines also undergo faults due to the impacts of the Pulse Width Modulation (PWM) technique, which has a high-frequency transition, and high steepness in the waveform or high voltage gradient (dv/dt) due to switching frequency (f_{sw}) of power electronic wide band-gap drives (WBG). These WBG devices have demonstrated superior material properties that are accepted worldwide, allowing their high-switching and high-voltage operation, as well as capabilities to operate at high-temperature profiles [8–11].

1.1. PWM Inverter-Fed Motor Drive System

These inverters drive the IM while improving the operation's safety and reliability, but increasing harmonic-frequency traces. The PWM modulation technique and switching frequency determine these harmonic amplitudes and wide-band frequencies. PWM-controlled inverters employed with WBG devices such as SiC (Silicon Carbide), GaN (Gallium Nitride), GaAs (Gallium Arsenide), AlN (Aluminum Nitride), etc. have critical switchinits g frequencies ranging from a few kHz to tens of kHz. Other than generating the increased harmonic contents at the output terminal of the inverter, they also generate a high-frequency common-mode voltage (CMV), a major problem in switching power converter fed IM. This happens with the shaft voltage and generates the bearing current through the AC machine's stray capacitive and inductive coupled paths [12]. High modulation frequency attenuates low-order harmonics and increases the inverter's loss. These low-order harmonics are quite unhealthy for motors, because they cause torsional oscillations, pulsating torques in the shaft, and rotor bar-broken damage. Researchers are trying to reduce switching losses and increase the power converter efficiency with different inverter control strategies, and some novel designs such as [13–16] used discontinuous PWM (DPWM), sine triangle PWM-based DPWM, and space vector-based synchronized DRWM types of design techniques. A typical one-line diagram of an alternating current (AC) source with a voltage-source inverter (VSI), a rectifier system, filters with smoothing capacitors, and an IM operated with inverters is shown in Figure 1. It is worth mentioning that the failure rate of inverter-fed IM drives is 12 times faster than line or grid-fed drives, and this is demonstrated in the literature by a questionnaire survey of 3934 grid-fed drives and 286 variable-speed inverter drives [17].

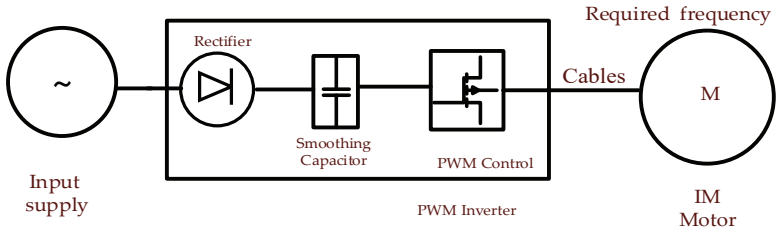


Figure 1. The schematics of a conventional inverter-fed electric motor drive system [17].

Inverter-based supply harmonics have a wide frequency spectrum compared to grid-fed variants, with a simple odd multiple of fundamental components. Since modern inverter-driven motors have high controllability, precision, dependability, and efficiency, they have become an integral component of modern drive systems. With the features described here, the common utilization issues of inverters are increased costs, increased switching losses, iron losses, high torque pulsations, electromagnetic compatibility issues, and acoustics noise. Due to switching frequency and high dv/dt, these high-frequency components are not designed with consideration of the motor's effective response and operation, leading to a high potential research gap in the motor field [7,18]. These random harmonic distributions in the current create an additional frequency spectrum in the wide band. Hence, these drawbacks encourage potential research to develop solutions [19–21].

1.2. Potential Challenges with Inverter-Fed Supply

Since PWM-based inverter-fed induction motors have certain advantages over grid-fed power supply, such as variable speed control, energy efficiency, and flexibility, they also face challenges with regard to condition monitoring and fault diagnostics. Table 1 presents a comparison, based on the available literature, between Pulse Width Modulation (PWM)-based inverter-fed induction motors and those with grid-fed supplies, with regard to the challenges, complexity, and problems they face in their condition monitoring and fault diagnostics.

Table 1. Comparison of challenges posed by supplies to motor drive system.

Sr. No.	Challenges	PWM Inverter-Fed Motors	Grid-Fed Motors	Reference
1.	Noise and distortion	• Harmonics and high-frequency noise. • Lowers the accuracy of methods.	• Lower harmonics and distortion. • Provides stable and reliable signal for fault diagnosis.	[22]
2.	Sensor compatibility	• Complex power electronics require more sensors or interfaces. • Complexity and cost addition.	• Standardized sensors and measurement points. • Simplified CM and FD implementation.	[23,24]
3.	Variable operating conditions	• Feasibility with various load and speed conditions. • Dynamic system behavior and different failure signature complicate the fault diagnosis.	• More stable operation and predictable conditions. • FD is more straightforward.	[25]
4.	Nonlinear-system dynamics	• Nonlinear behavior due to the switching nature. • Greater challenges in FD and assumption with linearity or relying on linear models.	• Linear characteristics. • Simplified in linear-based FD and modeling approaches.	[26,27]
5.	Power quality and transient response	• Adds voltage sags, harmonics, and transients. • Affects power quality and perhaps masks fault signatures.	• Provide stable and high-quality power with minimal transients. • Cleaner environment for FD.	[28,29]
6.	The complexity of fault signatures and analysis	• Power electronics, motor dynamics, and fault conditions create complex and non-traditional scenarios in fault signatures. • Requires advanced signal processing or customized fault detection algorithms.	• Straightforward and conventional in CM and FD. • Simple fault analysis, detection, and interpretation.	[30]

This review article briefly analyzes induction motor faults, condition monitoring, and practical diagnosis and highlights the scientific results of different approaches and their applicability in this field of diagnostics, specifically with motor drive systems. The authors present a thorough detail of induction motor fault classification in Section 2. Then authors include various condition monitoring schemes and diagnostics with various applicability details in Section 3.

A comprehensive analysis of potential induction motor faults, including monitoring and mitigation methods, is covered in Section 4. The authors add the details of most occur-

ring faults like stator, inter-turn short circuits, broken rotor faults known as BRB, mechanical bearing damage, air-gap eccentricity, common-mode voltage development faults, and bearing currents leading towards partial discharges in the induction motor. Additionally, the authors outline the most advanced machine learning and artificial intelligence-based CM and DF techniques of recent times in Section 5. Section 6 of this paper addresses the potential research gaps as a future direction for the research, based on an extensive literature analysis by the authors.

2. Classification of Various Faults in Induction Motor

Based on the available literature, Figure 2 shows various IM fault types, which effectively influence the continuous and reliable operation when operated by an inverter-based power supply [27]. The IM faults are classified into three main categories: mechanical, electrical, or environmental. Electrical faults in particular are initiated at the stator side of IM. Mechanical faults have the most impact on the remaining useful life of the motor, as they are degenerative and tend to increase these faults over time.

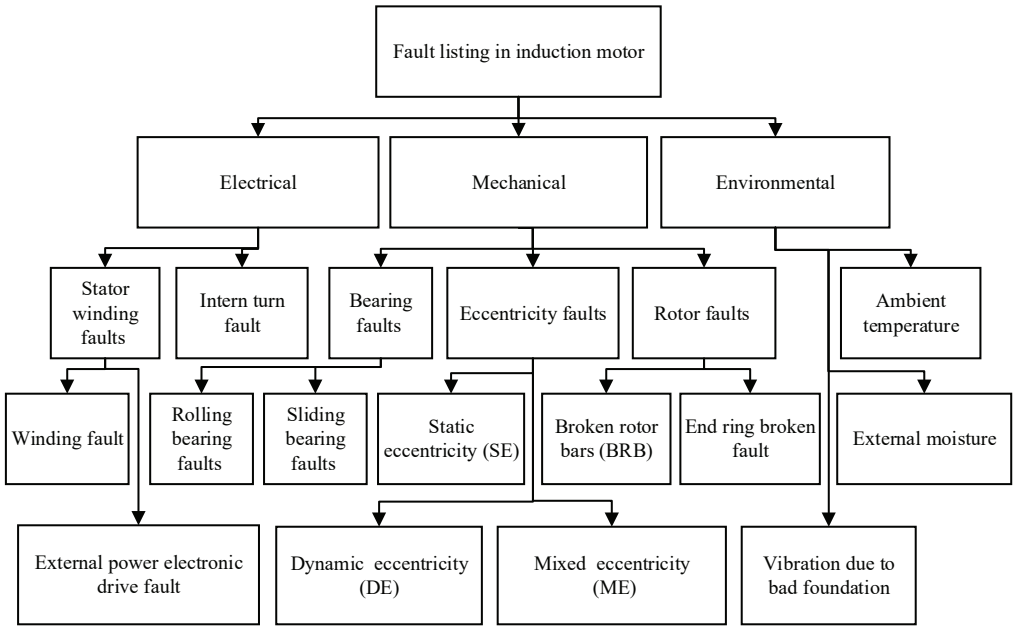


Figure 2. Induction motor various faults classifications [27].

2.1. Fault Type Classification

These faults are likely to be avoided in advance with early detection, and good condition monitoring schemes are required for the motor, before going into catastrophic failure. These faults are more critical and difficult to detect earlier but are equally important to trace. This article highlights the electric motor fault, the diagnosis technique mainly associated with using a power electronic converter [31,32].

Three institutions, named the Institution of Electrical and Electronics Engineers (IEEE), Electric Power Research Institute (EPRI), and Asea Brown Boveri (ABB), have evaluated the IM fault types and their performances. Their surveys, which are depicted in Figure 3, reflect the importance of condition monitoring and diagnostics in different parts of motors, and show the percentage contribution of the faults related to motor's stator, rotor, bearing, and other related considerations [33,34].

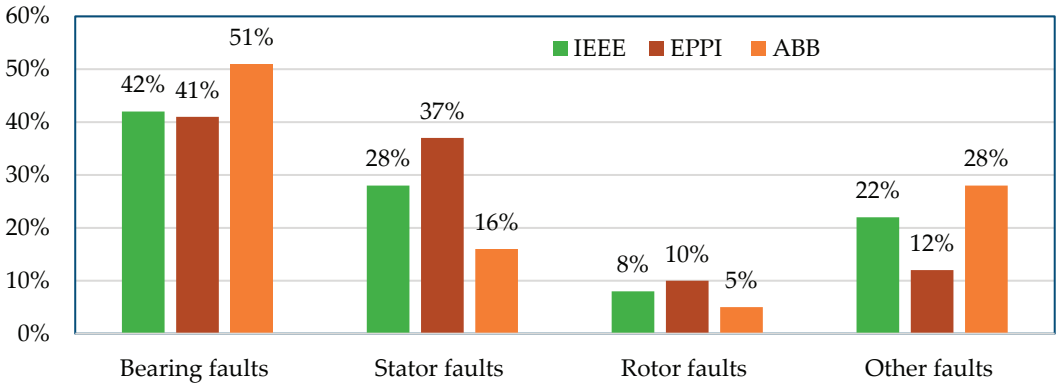


Figure 3. IM percentage fault contribution by the institutions: IEEE study results, EPRI study results and ABB [35].

2.2. Typical Faults with Inverter-Fed Induction Motor

Table 2 illustrates the various faults in an induction motor when supplied with a Pulse Width Modulation (PWM) inverter. It presents a comparative analysis table encompassing various faults and corresponding diagnostic techniques. These CM and FD methods are crucial in facilitating the precise interpretation of fault signatures, offering valuable insights into motor faults' underlying causes and severity. The researchers consistently aimed to improve the dependability and efficiency of inverter-fed induction motors by implementing effective strategies for detecting and diagnosing faults.

Table 2. Fault and companion diagnostics in an inverter-fed induction motor.

Sr. No.	Faults	Diagnostic Techniques	Reference
1.	Stator winding phase(s) faults, inter-tern faults, vibration, and conductor displacements	• Motor current signature analysis (MCSA); ○ Signal spectrum analysis; ○ Wavelet transform; ○ Fast Fourier transform (FFT); ○ Park's vector approach; ○ Artificial intelligence techniques (AI); • Relays and switches.	[36,37]
2.	Rotor faults, mechanical faults	• FEA analysis; • Vibration analysis; • Motor current signature analysis; ○ Fast Fourier transform (FFT); ○ Wavelet transform; ○ Time frequecny analysis, etc.	[11,38,39]
3.	Bearing faults, misalignment of bearings, lubrication loss in bearings, mechanical and thermal imbalance in the rotor	• MCSA; ○ Instantaneous power FFT; • Flux measurement method.	[40–43]
4.	Shaft voltage stress and transient overvoltage	• Parasitic capacitance calculation; • RLC transient modeling; • Shaft current and stray flux analysis; • 2D and 3D analysis.	[29,44]

Table 2. *Cont.*

Sr. No.	Faults	Diagnostic Techniques	Reference
5.	Bearing voltages and leakage currents, corrosion, and failure	• Vibration analysis; • Chemical analysis.	[45,46]
6.	Common-mode voltage (CMV) issues and high dv/dt	• New electrostatic shielded design; • RLC transient modelling.	[47,48]
7.	PWM switching harmonic losses, distortion, and heating	• Infrared thermography; • Infrared recognition; • Thermal monitoring; • Signal spectrum analysis.	[22,49]
8.	Insulation system damages	• Monitoring of winding's temperature, gases composition; • Stray flux analysis; • Partial discharge; • Filtered voltage impulse and partial discharge (PD) spectra; • AI.	[50–52]
9.	Electromagnetic interference (EMI) issues	• High resonance circuit equivalent modeling and analysis.	[53]
10.	Switching harmonic and frequency loss analysis	• Discontinuous Pulse Width Modulation (DPWM) and space vector bases DPWM; • Electromagnetic field monitoring.	[54–56]

3. Condition Monitoring and Diagnostic Techniques

This paper reviews the research on condition monitoring and fault diagnosis and draws attention to the methods proven to be the most reliable and helpful. Fault diagnosis techniques can be categorized based on whether they require invasive or non-invasive methods to assess the condition of the motor drive system. Non-invasive fault diagnosis techniques do not require physical intervention or direct contact with the motor drive system being monitored. These methods rely on external measurements or signals to analyze the system's behavior and detect potential faults. Invasive fault diagnosis techniques involve physical intervention or direct contact with the system to diagnose faults. These methods typically require accessing the internal components or subsystems of the machine [57].

3.1. Common Condition Monitoring Techniques

There are common condition monitoring (CM) techniques based on electrical signature analysis (ESA) through sensor data, which are useful not only for the condition monitoring of induction motors, but also for electrical generators, transformers, and other equipment. The most common type of signature analysis is motor current signature analysis (MCSA), in which the current signal signature is analyzed to trace the faults within the induction motor [38,58]. ESA also includes the motor circuit analysis involving parameters like resistance, phase angle, current response, frequency response, equivalent impedance, inductance, and ground faults. Some of the common condition monitoring techniques used in identifying IM faults are listed below [41,50,59–65]:

- Motor current signature analysis (MCSA) [66];
- Voltage signature analysis (VSA) [67];
- Extended Park vector approach (EPVA) [68];
- Instantaneous power signature analysis (IPSA) [69];

- State monitoring analysis like temperature, noise, speed fluctuation, magnetic flux;
- Condition Monitoring Sensors:
    a. Vibration sensors: accelerometers, proximity probes;
    b. Temperature sensors: thermocouples, resistance temperature detectors;
    c. Current sensors: Hall effect sensors, current transformers;
    d. Acoustic sensors: microphones, ultrasonic sensors;
    e. Emissions-based monitoring;
- Partial discharge and surge testing;
- Motor circuit analysis.

Fault diagnosis methods are mainly divided into categories, i.e., signal processing and model-based techniques. Signal-based techniques for condition monitoring and fault diagnosis of electrical machines involve analyzing various signals acquired from the machines to detect abnormalities, deviations, or fault signatures [31,70,71]. These techniques focus on extracting relevant information from the signals to assess the machine's condition. Some common signal-based techniques are shown in Figure 4.

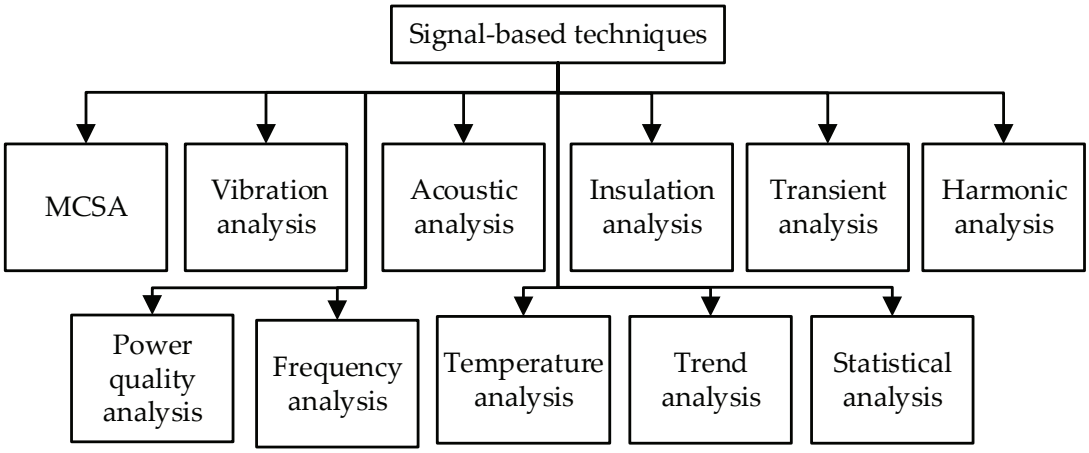


Figure 4. Types of signal-based techniques [71,72].

Model-based techniques for CM and FD of electrical machines are based on mathematical modeling to evaluate the behavior of the motor and detect the relevant faults or deviance from the common operating requirements [73,74]. The most common model-based techniques in FD are analytical models, finite element analysis (FEA), signal processing techniques, Kalman filtering (KF) and state estimation, artificial intelligence (AI), stochastic resonance, and machine learning (ML), as shown in Figure 5. These model-based techniques provide valuable tools for the CM and FD of electrical machines, allowing pre-condition of faults, predictive maintenance, legible reliability, and high performance. The divisions above can also be used in artificial intelligence (AI) based techniques for diagnostics. An artificial intelligence approach to predictive maintenance necessitates both human intelligence and machine learning or training of algorithms for machine fault diagnostics [75–79].

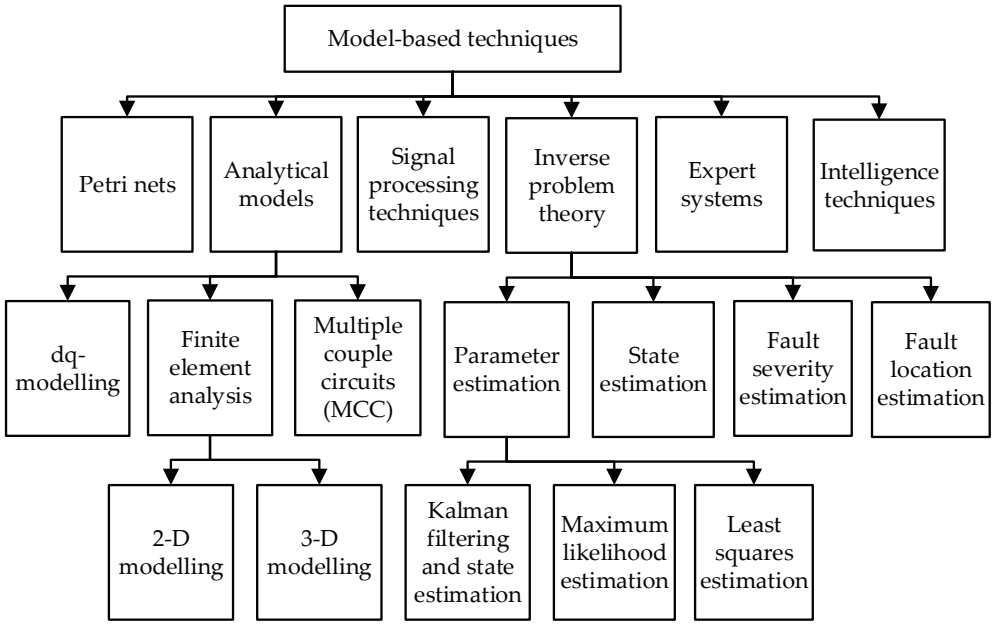


Figure 5. Types of model-based techniques [80].

IM-related faults caused by high-frequency inverter transients and behavior that generate the faults. Academia, and industry are investing heavily in their research and development (R&D) related to condition monitoring and diagnostics [81,82]. Figure 6 shows a tie of an electric machine with an intelligent diagnostics system, which integrates the motor's real-time parameters, for example, electrical, mechanical, flux, optical, acoustic, chemical, partial discharges, and others, to form a diagnostic [83–85].

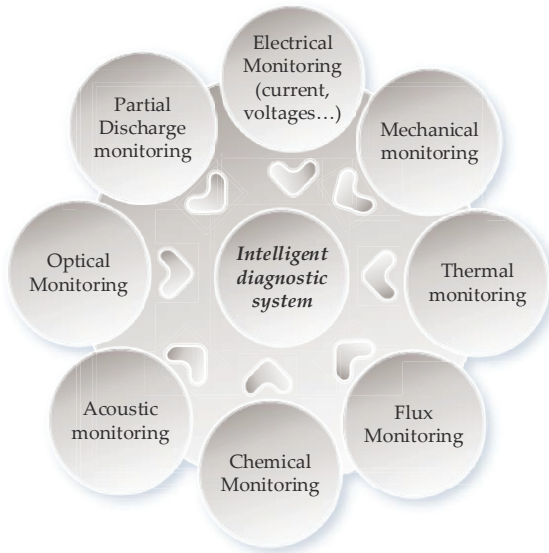


Figure 6. Recent developments in intelligent diagnostics [83–85].

3.2. Latest Trends in Condition Monitoring for IM Faults

Advanced condition monitoring and fault diagnostic methods for induction motor faults have emerged due to advancements in technology and research. The authors present a list of the latest more advanced condition monitoring methods for induction motor (IM) faults, along with their types and further subtypes in Table 3.

Table 3. Condition monitoring and diagnostics with latest trends.

Sr. No.	Latest FD Technique	Feature Application
1.	Advanced signal processing techniques	• Time-domain analysis [86]; ○ Amplitude and RMS analysis [87,88]; ○ Kurtosis analysis; ○ Harmonic order tracking analysis [89]; ○ Time synchronous averaging (TSA) [90–92]; ○ Statistical analysis [93]; ■ Stochastic resonance; ○ Signal decomposition [89]; • Frequency-domain Analysis; ○ Fast Fourier transform (FFT); ○ Wavelet transform [90]; ○ Higher-order spectral analysis [37]; • Time-frequency analysis [70,94]; ○ Spectrogram; ○ Scalogram; ○ Hilbert–Huang transform and its extension; ■ Empirical mode decomposition; ■ Intrinsic mode function; ■ Extracting instantaneous amplitude and frequency; ○ Short-Time Fourier Transform (STFT); ○ Wavelet packet transform [95]; ○ Wigner–Ville distribution [91]; • High-resolution analysis techniques [38,45,92,93]; ○ MUSIC [96].
2.	Intelligent technique	• Artificial intelligence (AI) [97]; • Machine learning (ML) [98]; • Data-driven approach [99–101]; ○ High-dimensional feature reduction [102–104]; • Data mining: date fusion and pattern recognition [105].
3.	Expert Systems	• Rule-based systems [106–108]; ○ Fuzzy logic [109]; ○ Knowledge-based rules [110]; • Case-based reasoning [111]; ○ Experience-based reasoning; • Fault diagnosis from historical cases.
4.	Model-based prognostics and health management (PHM)	• Advanced diagnosis recognition [112]; • Smart classifier-based prognostics [105].
5.	Model-based prognostics and health management (PHM)	• Advanced diagnosis recognition [104,112]; • Smart classifier-based prognostics [105].
6.	Digital twin technology	• Ramanujan digital twin (RDT) [113]; • Model approach [113].
7.	Image processing and computer vision	• Advanced image processing and hyperspectral imaging [110,114]; • Histogram of oriented gradients approach [115]; • Thermal imaging: infrared thermography, temperature mapping [116].

Table 3. *Cont.*

Sr. No.	Latest FD Technique	Feature Application
8.	Hardware-in-the-Loop (HIL) condition monitoring methods	• Virtual HIL; ○ Software-in-the-Loop (SIL); ○ Processor-in-the-Loop (PIL) [117]; • Hardware-in-the-Loop (HIL) with real motors [118]; • Hybrid HIL: a combination of virtual and real components [119,120].
9.	Advanced Fault Detection Methods	• Ensemble methods [121]; ○ Random forest; ○ AdaBoost; ○ Bagging. • Bayesian networks: probabilistic graphical models, fault propagation [122]; • Genetic algorithms: optimization [123], feature selection, parameter tuning [124–126].
10.	Inverse problem theory	• Parameter estimation: Kalman's prediction [127,128]; • State estimation [129]; • Fault location estimation [130]; • Fault severity estimation.

Recent trends include time–frequency analysis (*tf*) methods, such as Short-Time Fourier Transform (STFT), wavelet transform, and Wigner–Ville transform, which provide valuable insights into motor signal transient and frequency-varying components. Applying these techniques makes it possible to detect and diagnose faults that may manifest as changes in frequency content or time-varying patterns. Different methods can identify certain faults in machines, such as the power spectrum graph, phase spectrum graph, cepstrum-graph, autoregressive (AR) spectrum-graph, spectrogram, wavelet scalogram, wavelet phase graph, etc. However, these methods often present several problems in terms of complexity and cost. The conventional signal-based methods are not always reliable, as they depend on the operating conditions of motors [121].

To improve the detection of incipient fault issues, the field of fault feature extraction has also taken advantage of stochastic resonance. Using straightforward techniques, researchers and diagnostic designers can better understand the motor drive system faults. In this approach, the system is represented by a network of interconnected neurons, where each neuron stands for a particular quality or feature of the signals the machinery generates [131]. The optimal signal-to-noise ratio and the misclassification rate are two examples of multi-objective optimization techniques used to determine the ideal coupling strengths between the neurons.

3.3. CM Implementation Strategy

A well-designed implementation strategic plan is important, because it ensures a systematic and organized approach to condition monitoring. It improves the monitoring process's efficacy and efficiency, enables proactive maintenance, reduces downtime, and optimizes resource utilization. Furthermore, a well-defined strategic plan encourages uniformity, standardization, and scalability, allowing organizations to reap the benefits of condition monitoring across various assets and facilities. Figure 7 shows the implementation of a strategic layout of condition monitoring, which refers to the systematic approach and framework for implementing condition monitoring techniques.

Potential future research is always required to precisely analyze the electrical machine's service life expectancy deterioration with improved CM, FD, and prediction methodologies. This predictive maintenance would reduce the cost of the process in its downtime and prevent unexpected motor failures.

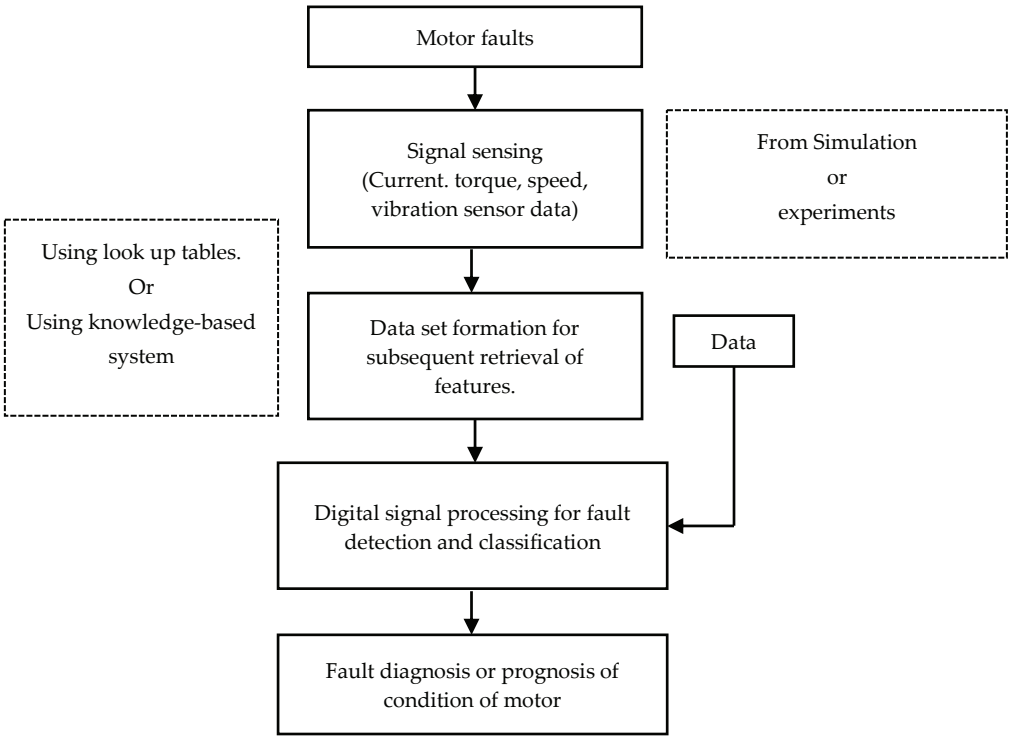


Figure 7. CM implementation strategic layout [75].

4. Fault Monitoring and Diagnosis of Induction Motor

Monitoring and diagnosing fault conditions is crucial to maintaining induction motors' dependable and efficient performance. Utilizing modern sensors and data acquisition systems permits the early identification of fault conditions, such as bearing wear, rotor faults, stator winding faults, and imbalance. Simultaneously, fault diagnostics analyzes the collected data to determine the defect's specific type and severity. Various techniques, such as signal processing, pattern recognition, and machine learning algorithms, identify fault varieties. These techniques extract relevant characteristics from the collected data and classify the fault type [98,132]. The information obtained through fault diagnostics enables maintenance personnel to promptly implement corrective measures, reduce inactivity periods, and prevent further damage to the induction motor. The subsequent subchapters will comprehensively analyze each fault [71,97,133–135], and present condition monitoring and fault diagnosis according to the fault.

4.1. IM Stator's Faults

Stator faults in the induction motor account for approximately 16–37% of the total occurred faults [35]. Induction motor stator faults include winding faults and external drive faults. The stator winding fault (SWF) can be caused by turn-to-turn, coil-to-coil, phase-to-phase, or phase-to-ground faults, as shown in Figure 8. Most stator faults involve broken winding insulation. MCSA can detect broken thread insulation, which can cause phase insulation to break and kill the motor. Insulation is most affected by thermal stress [136]. The combination of different electric stresses generated through the transient voltages is particularly undesirable [137].

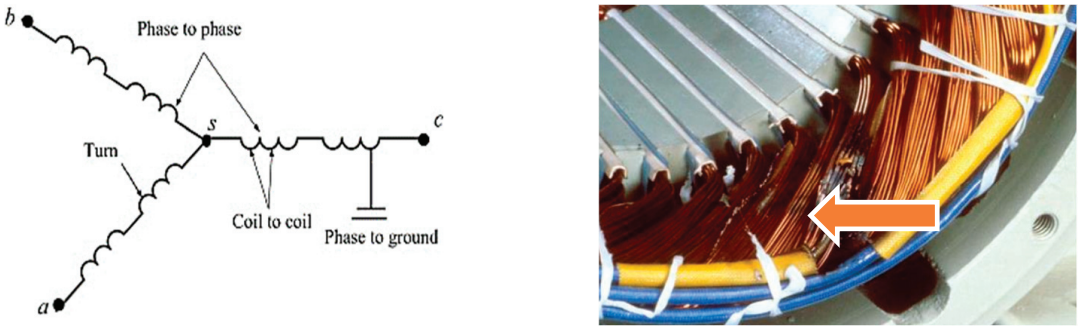


Figure 8. IM stator faults. (**a**) Stator winding multiple fault provision, (**b**) stator winding damage due to coil-coil fault within it [138].

The stator is stressed by thermal, electrical, mechanical, and environmental factors, causing faults [139–141]. Table 4 presents the types of fault diagnostics techniques for induction motor (IM) stator faults.

Table 4. Types of fault diagnostics techniques for induction motor (IM) stator faults.

Sr. No.	FD Technique	Group	Pros	Con	Reference
1.	Motor current signature analysis (MCSA)	Motor current signals (current spectrum)	• Non-invasive. • Specific harmonics specify the fault. • Provides real-time monitoring of motor health. • Diagnose turn-to-turn short circuits, open circuits, and insulation degradation related. • Cost-effective and relatively simple to implement.	• Limited effectiveness for incipient faults. • Expert knowledge is required when analyzing the spectrum. • Difficult in fault segregation in the case of inverter-fed motors. • Influenced by external noise and interferences.	[34]
2.	Motor current Park's vector analysis (MCPVA)	Stator current signal (vector components analysis)	• Provides insights into motor health and faults. • Provides a broad view of motor behavior. • Divides signal into orthogonal components. • Effective in both steady-state and transient conditions. • Early detection of motor faults.	• Requires accurate measurement. • Complex in evaluating vector relationships and deviations from predicted values. • Influenced by noise and measurement uncertainties. • Requires expertise in vector analysis and interpretation. • Limited effectiveness for incipient or small faults.	[68,142]
3.	Neural network techniques	Current or voltage signals	• Capable of handling non-linear and dynamic systems. • Adaptive and self-learning nature. • Can identify fault patterns and diagnose based on their responses. • Robust performance. • Handle multi-variate and high-dimensional data. • fault detection and diagnosis in early stages.	• Require large amounts of training data. • Lack of interpretability and explainability. • Computationally intensive and time-consuming training • Complex in learning to implement in linking between input patterns and fault states. • Limited effectiveness for unknown fault types.	[143–145]

Table 4. *Cont.*

Sr. No.	FD Technique	Group	Pros	Con	Reference
4.	Wavelet transform analysis	Stator current signal	• Effective for time-frequency analysis. • Can handle non-stationary and transient signals. • Ability to detect transitory phenomena, frequency fluctuations, and disruptions. • Offers multi-resolution analysis. • Can diagnose stator faults such as short circuits, broken rotor bars (BRB), and bearing faults.	• Appropriate wavelet basis can be challenging in selection. • Computational complexity • Interpretation of wavelet coefficients requires expertise. • Requires a careful balance between time and frequency resolution. • Compromise in effectiveness for very high or very low frequencies. • Proper selection of wavelet parameters is crucial.	[101–105]

4.1.1. Classification of the Stator Fault

Incipient stator faults fall into the following broad categories.

1. Laminations that create a hotspot in the core and cause slackening in the core.
2. Faults in the frame due to unbalanced vibration, circulating current within it due to shaft voltages, coolant loss, or a potential earth fault.
3. Faults in the end portion, insulation fretting, insulation contamination by moisture, oil, or dirt, damage to connectors, cracking of insulation, discharge erosion of insulation, and the displacement of conductors.
4. Faults in portions from the slot due to the misplacement of conductors.

4.1.2. Inter-Turn Short-Circuit Faults

Industrial drives have a 16–28% stator inter-turn short circuit (ITSC) fault [136]. Inverter-fed induction machines have more harmonics than line-connected motors. The harmonic current heats the stator winding, deteriorating the insulation quickly [37,146]. If undetected, a three-phase IM stator winding short circuit starts with an inter-turn fault and progresses to a phase-phase or phase-ground fault. MCSA detects inter-turn faults in inverter-fed IM. If a PWM inverter feeds the machine, MCSA fails due to high-frequency inverter switching, and the current spectrum is noisy, making fault detection difficult. If undetected, a three-phase IM stator winding short circuit starts with an inter-turn fault, and progresses to a phase–phase or phase–ground fault. MCSA detects inter-turn faults in inverter-fed IM. If a PWM inverter feeds, the machine MCSA fails due to high-frequency inverter switching, and the current spectrum is noisy, making fault detection difficult [147,148]. The details of the current harmonics that the stator intern short circuit has caused and the two-level inverter's currents harmonic are explained below.

4.1.3. Current Harmonics Due to Stator ITSC Fault

In the case of stator inter-turn short circuits (ITSCs), the number of coil turns is reduced, and the remaining coils are used to carry fault current. A short circuit current reduces the faulty phase's MMF, and the air gap's spatial flux distributions are disturbed [149]. The motor's current components at some frequencies are limited to shorted turns. This is described by Equation (1) [150].

$$f_{st} = f_g[\frac{n}{p}(1-s) \pm k] \quad (1)$$

where f_{st} is the component related to shorted turn, f_g is the fundamental electrical frequency, n is $1, 2, 3, \ldots$, p is pole pairs (number), s is slip (per unit), k = 1, 2, 3.

4.1.4. II-Level Inverter's Current Harmonics

The II-level triangular carrier PWM inverter-fed IM has the per phase voltage in Equation (2) [25].

$$\begin{aligned} V(t) &= \tfrac{MV_{dc}}{2}\cos(\omega_f t) \\ &+ \tfrac{2V_{dc}}{\pi}\sum_{m=1}^{\infty} j_0 mM\tfrac{\pi}{2}\sin(m\tfrac{\pi}{2})\cos(m\omega_c t) \\ &+ \tfrac{2V_{dc}}{\pi}\sum_{m=1}^{\infty}\sum_{n=\pm 1}^{\infty}\tfrac{j_n mM}{m}\tfrac{\pi}{2}\sin[(m+n)\tfrac{\pi}{2}]\cos(m\omega + m\omega_f t) \end{aligned} \quad (2)$$

where V_{dc} = DC link voltage, M is Modulation index, ωf is the fundamental frequency, ωc is the carrier frequency, m is the integer, J_0, & J_n are the Bessel functions, and $V(t)$ = fundamental voltage.

Equation (2) shows the modulation index's analytical function (which is defined as M), while the second and third term reflect the carrier frequency band harmonics. By varying the coefficients ωf, ωc stated in Equation (2), the output of the inverter is varied, and the required voltage for the fed induction is achieved. Since the voltages are non-sinusoidal, they are being fed to the motor; they cause the harmonics in the phase current, and most reflecting harmonics are along the side of switching frequency ($\omega c \pm 3\omega f$, $2\omega c$) [151]. ITSC fault generates the current i_f, and the R_f fault resistance is reflected as shorted turns in the phase winding undergone to the fault, as shown in Figure 9.

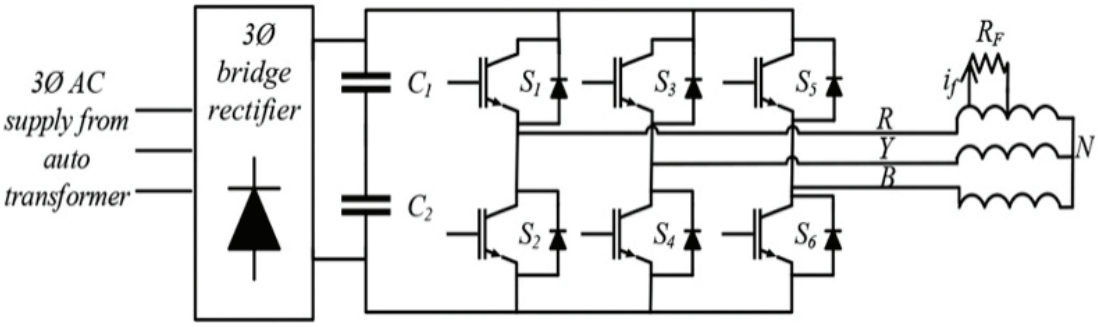


Figure 9. Induction motor ITSC fault [36].

Researchers recently proposed the most efficient and applicable fault diagnostic techniques using the observer coil based FFT analysis and measuring the internal flux methodology [152]. Furthermore, coil based FFT analysis and sensors based on the Hall effect are separately installed inside the motor's geometry, which requires extra labor [63].

Also, it is not influential for implementation because of being sensitivity-dependent due to load variation, current harmonics, and an unbalanced supply voltage.

Table 5 summarizes different motor ratings, implemented schemes, and different parameters in the event of inter-turn short faults.

Table 5. Summary of inter-turn short circuit faults in different motors.

Sr. No.	Motor Specification	FD Technique	Fault Resistance (Ω)	Fault Current I_f (A)	Fault Severity I_f/I_r (%)	References
1.	3.7-kW,41-V, 4-pole, 50-Hz,	Wavelet transform analysis on the Stator current	2	0.7	12.73	[69]
2.	400-V, 11-kW, 50-Hz, 4-pole	Fast Fourier transform and stray-flux	0	3.75	16.66	[70]

Table 5. *Cont.*

Sr. No.	Motor Specification	FD Technique	Fault Resistance (Ω)	Fault Current I_f (A)	Fault Severity I_f/I_r (%)	References
3.	15-kW, 400-V, 50-Hz, 4-pole	Stator current multi-reference frames	0.012	6	20.33	[71]
4.	400-V, 5.5-kW, 50-Hz, 4-pole	Symmetrical components of the stator-current (input current)	-	2	18.18	[72]
5.	110-V, 1-kW, 50-Hz, 4 pole	IM stator current phase averaging	6	1.3	26.00	[73]
6.	415-V, 3-kW, 50-Hz, 4-pole	Discrete wavelet transform (DWT)	0.5	10	200	[74]
7.	380-V, 3.7-kW, 60-Hz, 4-pole	Discrete Fourier transform (DFT)	0	12	100	[75]
8.	460-V, 3.7-kW, 60-Hz, 6-pole	Waveform envelope construction	1	3.5	71.86	[76]

4.2. Rotor Faults

The induction motor rotor can undergo the following faults, which are stated below as:

1. Broken rotor bars (BRB);
2. Rotor bar displacement;
3. Rotor bar eccentricity;
4. Rotor end ring damage;
5. Rotor core faults and overheating;
6. Rotor skewing issues;
7. Rotor short circuits.

Rotors can be divided into wound types and squirrel cage types. In the case of the squirrel cage rotor, the windings are a cage of conducting bars that meet at the end ring [153]. The wound rotor consists of the winding made on the rotor with different winding topologies. The main faults occur with the motor due to irregular fluctuations and high pulses. Figure 10 shows the rotor bar broken faults within it.

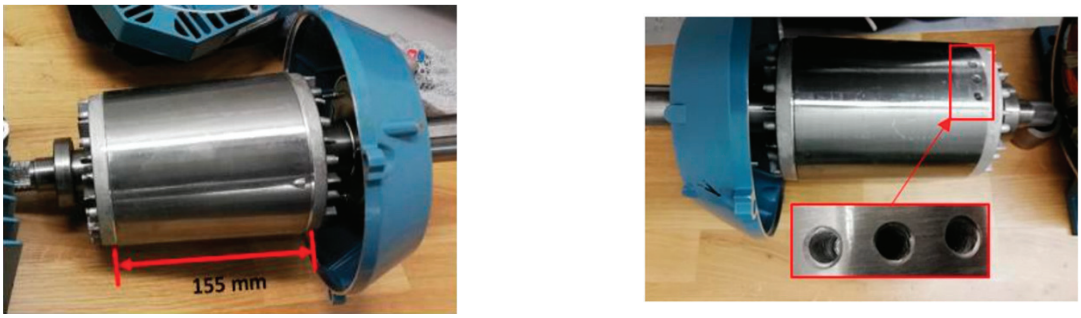


Figure 10. IM rotor images showing broken rotor bars (BRB): (**a**) healthy-rotor, (**b**) three-bars broken [9].

Most MCSA-based methods take advantage of electrical machine faults leaving fault-frequency components in the current spectrum. Poor materials, overloading, or heavy starts can cause these faults. BRB faults can increase resistance or break the electrical circuit. Rotor bar failures mostly affect motor starting and parasitic moments. The missing bar (due to an open circuit within it) current path increases the current in other bars, causing

more faults (where one bar is broken). The current components in the stator windings can be identified at the frequencies mentioned in Equation (3), in case of a BRB [154,155].

$$f_{brb} = f_g[\frac{n}{p}(1-s) \pm k] \quad (3)$$

where f_{brb} is a broken rotor bar (BRB) frequency, f_g is the electrical input inverter primary frequency, k is 1, 2, 3, . . ., p is the number of pole pairs, s is slip (per unit).

The typical problem with commercial induction motors is BRB faults. The authors of [156] presented the diagnostic techniques based on the existence of the motor current signature analysis. In [157], a low-complexity fault detection algorithm was implemented based on the analytic current signal's sub-Nyquist sampling. The algorithm was tested for BRB-related faults. The proposed techniques in [94] are based on advanced signal processing tools, such as spectrogram, scalogram, and Hilbert–Huang transform. Results demonstrated the effectiveness of these approaches in simulation and experimental validation. The author of [158] adopted SOGI-ANF, a new time domain signal processing algorithm for stator current envelope extraction in induction motors, suitable for embedded devices, and its adaptive nature allows accurate tracking of envelope variations. Based on the literature, Table 6 compares different diagnostic methods.

Table 6. Induction motor BRB fault diagnosis methods in the MCSA group.

Sr. No.	FD Technique	Group	Pros	Cons	Reference
1.	Active and reactive currents	FFT (MCSA)	• Non-invasive. • Can segregate load vibration effects. • Moderate level of mathematical calculation.	• Medium level of memory required.	[159]
2.	Ant clustering	Park's vector, FFT	• Non-invasive. • No speed estimation is required.	• Difficult to segregate different faults. • Large mathematical calculations and memory required.	[99]
3.	Autoregressive method	DTFT and Notch	• Non-invasive. • No speed estimation is required.	• Operated on steady-state current.	[160]
4.	Information entropy and fuzzy inference	Fuzzy logic	• Non-invasive. • A medium level of mathematical calculation is required.	• Requires steady-state current. • Large memory required.	[107]
5.	Homogeneity estimation	FPGA	• Non-invasive. • Used with transient current. • No speed estimation is required. • A low level of mathematical calculation is required.	• Segregation of faults is difficult.	[161]

Table 6. *Cont.*

Sr. No.	FD Technique	Group	Pros	Cons	Reference
6.	Principle slot harmonics	FFT	• Non-invasive. • Used with an unbalanced power supply.	• Segregation of different faults is difficult. • Large mathematical calculations and memory required.	[162]
7.	Harmonic order tracking	Gabor transform	• Non-invasive. • Capable of segregating faults and non-stationary conditions.	• A medium level of memory is required to use.	[89]
8.	Hilbert Transform (Envelope detection)	Hilbert transform	• Non-invasive. • Steady-state analysis. • A low level of mathematical calculation and memory is required.	• Segregation of different faults is difficult. • Problems with varying load conditions.	[163]
9.	Reduced envelope	Hilbert transform	• Non-invasive. • Suitable for diagnostic on low slip • Suitable to implement on DSP and FPGA kits.	• Segregation of different faults is difficult.	[164]
10.	Notch-filter	Fast Fourier transform	• Non-invasive. • Suitable for diagnostic on low-slip. • Difficult under varying load conditions.	• Segregation of different faults is difficult.	[165]
11.	Parameters estimation	Analytical	• Non-invasive. • It can be more accurate under steady-state conditions. • It can be used to segregate faults.	• The high mathematical calculation is required. • High memory is required.	[166,167]
12.	Pendulous oscillation	Analytical	• Non-invasive. • Suitable for implementing under low slip conditions and steady-state conditions. • It can be used to segregate faults.	• The complex mathematical calculation is required.	[168,169]
13.	Power spectral density	Short-time FT and wavelet	• Non-invasive. • Suitable to implement under low slip conditions. • Cab be applied under varying load conditions. • It can be used to segregate faults.	• An accurate sampling rate is required. • Selection of mother wavelet required.	[170]

Table 6. *Cont.*

Sr. No.	FD Technique	Group	Pros	Cons	Reference
14.	Spectrum synch technique	Local band synch, central kurtosis analysis	• Non-invasive. • It is suitable to implement under low slip conditions and can be used to segregate faults.	• Difficult to implement under varying load conditions.	[168]
15.	Zero-sequence voltages	Analytical	• Non-invasive. • Suitable for constant load conditions.	• Segregation of different faults is complicated.	[171]
16.	Wavelet transform (WT)	t-f analysis	• Non-invasive. • It can be used to segregate faults • It can be used for varying load conditions.	• The sampling rate and selection of the mother wavelet are important.	[172]
17.	Adaptive neuro-fuzzy inference system	Time domain analysis	• Non-invasive. • Used with stator current. • Detectability with a wide speed range. • Can detect BRB and air gap eccentricity. • Reduced complexity and high accuracy.	• High computational burden. • Extensive training of the network.	[173,174]

4.3. Bearing Faults

Bearing mechanical faults contribute to an impact of 40–50% of overall rotating electric machine failures [35]. IMs use ball or roller bearings with the rolling element, outer race, inner race, and train (or cage) defects, as shown in Figure 11, due to mechanical stress and bearing currents, poor installation, assembling, temperature rise, and maintenance cause most bearing failures. Pollution or contamination added from outdoors also cause bearing failures due to adverse impact on the bearing lubricant. Dust and liquid contamination entering the seal cause bearing failures [175]. Most diagnostic methods for machine electrical and mechanical failures use MCSA [43,176,177].



(a) **(b)** **(c)**

Figure 11. Depict of bearing structural faults: (**a**) ball bearing, (**b**) outer raceway fault, (**c**) inner raceway [178].

Bearing faults can have the following causes:

1. The rotor vibrates heavily and increases the fatigue stress due to high output load torque;
2. Loss of lubrication brought on by a shaft voltage;
3. A high bearing current result in the heat that the shaft can conduct.

Different sensor data, such as vibration measurements, motor current, input voltage, stray flux, and temperatures at different motor locations, are used in conventional bearing condition monitoring and diagnostics.

Motor vibration analysis gives the frequencies produced by the failures can be expressed in Equations (4)–(7):

$$f_{outer} = \frac{N_b f_r}{2}(1 - \frac{d\cos\phi}{D}) \tag{4}$$

$$f_{inner} = \frac{N_b f_r}{2}(1 + \frac{d\cos\phi}{D}) \tag{5}$$

$$f_{cage} = \frac{f_r}{2}(1 - \frac{d\cos\phi}{D}) \tag{6}$$

$$f_{ball} = \frac{d f_r}{2D}\{1 - (\frac{d\cos\phi}{D})^2\} \tag{7}$$

where f_{cage} is the cage failure frequency, f_{outer} is the outer race frequency, f_{inner} is the inner race f_r quency, f_{ball} is the ball defect frequency, d is the ball diameter, D is the pitch diameter, and f_r is the frequency of the rotor (mechanical).

$$f_{cur-harmonics} = |f_i - nf_c| \tag{8}$$

where $f_{cur\text{-}harmonics}$ is the harmonic current frequency, f_i is the fundamental inverter frequency, f_c is the characteristic vibration frequency, and n is an integer. Figure 12 summarizes different approaches from the spectrum waveform and signals, illustrating faulty or abnormal attributes [42,178,179].

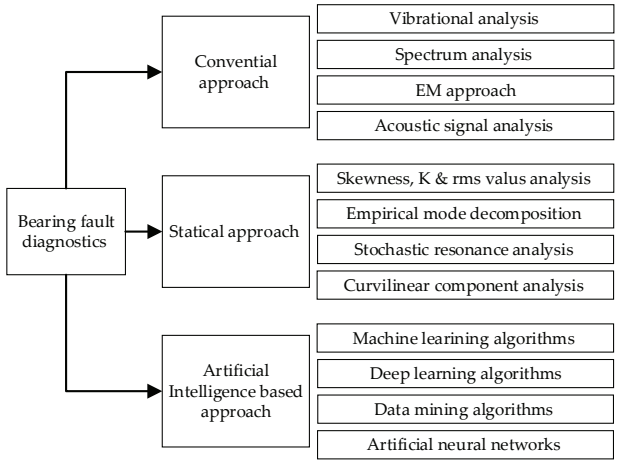


Figure 12. Bearing fault diagnostic approach [178].

The inaccurate and air-gap irregularity in stator–rotor structure and bearing stiffness can cause excessive motor vibration by affecting shaft dynamics. IM break or destroy early due to rotor bar failures caused by bearing failures. Using the homogeneity algorithm (HA), the authors of [180] presented the fault traces in outer race-bearing in IM that use the vibration signals to estimate the change on the normal structural line and initiate the fault detection.

The author of [181] proposed the mechanical fault of bearing using the motor current signature analysis based on the normalized triple co-variance in the IM. The author of [182] proposes a prospective Envelope Harmonic Spectrum (EHS) and adaptive second

order cyclo-stationarity blind deconvolution algorithm. This research implementation can estimate the IM bearings. Based on the literature, Table 7 compares different traditional diagnostic methods.

Table 7. Induction motor bearing fault diagnosis methods.

Sr. No.	FD Technique	Pros	Cons	Type of Fault	Reference
1.	Harmonics in motor current signature analysis (MCSA)	• Features are extracted well. • Immune to noisy environments.	• Stationary signals are excluded.	• Ball bearing.	[62,131]
2.	Instantaneous frequency-power spectrum	• Identify the useful information.	• Measurement errors of faulty signals.	• Ball bearings • roller bearings.	[183–185]
3.	FFT and current-voltage information	• Measures value quickly. • Isolates bearing faults.	• Inclusion with data manipulation.	• Ball bearings.	[186,187]
4.	Phase modulation and high-resolution stator current spectral analysis	• Accurate. • Measures faults where segregation is difficult.	• Nonlinear. • Expensive.	• Inner race. • Outer race faults.	[188]

4.4. Air-Gap Eccentricity Faults

Non-uniformity in the airgap in the motor's rotor-stator physical structure creates these eccentricity faults. Three types of these faults as stated below [189,190].

1. Static eccentricity (SE);
2. Dynamic eccentricity (DE);
3. Mixed eccentricity (ME).

SE has a fixed minimal radial air gap, and the rotor center of the axis remains fixed regardless of the center stator diameter. In contrast, in DE, the center of the rotor moves with the stator, while ME includes both SE and DE. The rotor in ME rotates around the third fixed center of rotation other than the center of the stator or the rotor [191]. Figure 13 shows the state of change of the center of rotation in operation and Table 8 shows the induction motor diagnosis methods related to eccentricity fault.

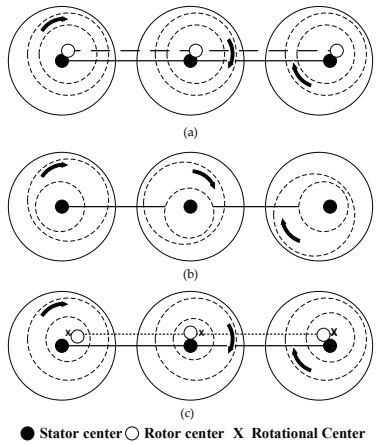


Figure 13. Eccentricity faults: (**a**) static eccentricity, (**b**) dynamic eccentricity, (**c**) mixed eccentricity [192,193].

Table 8. Induction motor eccentricity fault diagnosis methods.

Sr. No.	FD Technique	Pros	Cons	Reference
1.	Air gap eccentricity monitoring using magnetic flux	• High accuracy.	• Various sensors are required. • Complex representation.	[194,195]
2.	Stator current analysis in time and frequency domain	• Non invasive. • FFT measures value quickly. • Isolates bearing faults.	• Difficult in fault segrigation. • Expertise required in implementation. • Inclusion with data manipulation.	[196]
3.	Instantaneous frequency-power spectrum	• Identify the useful information.	• Measurement errors of faulty signals.	[197]
4.	Wavelet transform analysis (WT)	• Only current or voltage signal are required. • t-f analysis. • High resolution analysis. • Can segrigate faults amoung PHS and fault sidebands.	• Can be used to segregate faults. • Can be used for varying load conditions.	[198]
5.	Eddy current testing	• Easy in detection due to variations in magnetic fields.	• Multiple sensors required. • Complex FD technique.	[199]
6.	Neural network technique	• High accuracy in model. • Accounts for turn-to-turn capacitances and 3D end winding.	• Difficulty in training ANNs with historical data.	[200,201]

Equations (9)–(11) below show the eccentricity fault frequency, and f_c shows the central frequency.

$$f_{ec} = f_g\{(R \pm n_d)(\frac{1-s}{p}) \pm n_{ws}\} \quad (9)$$

$$s = \frac{N_s - N_r}{N_s} \quad (10)$$

where, f_{ec} is the eccentricity frequency (also called the irregularity frequency), f_g is the fundamental frequency, R is the number of rotor bars, n_{ws} is 1, 3, 5, 7, . . ., N_s is rotor slip, N_r is synchronous speed, s is slip (per unit), and slip is calculated from the equation, n_d is +1 or −1. Central frequency f_c on the air gap-static eccentricity spectrum is determined by Equation (11).

$$f_c = Rf_g \quad (11)$$

4.5. Common-Mode Voltage (CMV) and Bearing Current Faults

Each pulse's voltage waveform at the inverter terminals has steep lines at the start and end. Recent studies have shown that PWM inverter's common-mode voltage (CMV) is the

primary reason for this, which creates the bearing current (BC) as a serious side effect [48]; the most effective reasons for this are as follows.

1. The voltage at the equipment terminals is doubled because of reflections, putting extra strain on the windings' insulation.
2. In windings, capacitive currents and non-uniform voltage distribution can cause electrical machines to experience a circulating current nominated as a bearing current.
3. Charges stored in the ground capacitors.

The common-mode voltage and bearing current faults are discussed below.

4.5.1. Common-Mode Voltage (CMV)

PWM inverters usually cause motor bearing failures. Bearing currents, also known as shaft voltages, flow from the shaft through the bearings and must be monitored and diagnosed when PWM inverter sources feed an electric machine. This issue is usually caused by bearing material erosion and mechanical failures like rotor eccentricity, homopolar flux effects, and electrostatic discharge in electric devices [48]. Since the phase output voltages alternate between $+V_{dc}$ and $-V_{dc}$. The neutral-to-ground voltage in a star-connected machine is the zero-sequence voltage, expressed in Equation (12). Figure 14 shows that the voltage change rate and CMV frequency is three times more than the switching frequency. The overall CMV activity is done by the parasitic capacitance, starting from the stator winding point to the rotor [24,27].

$$V_{com} = \frac{V_A + V_B + V_C}{3} \tag{12}$$

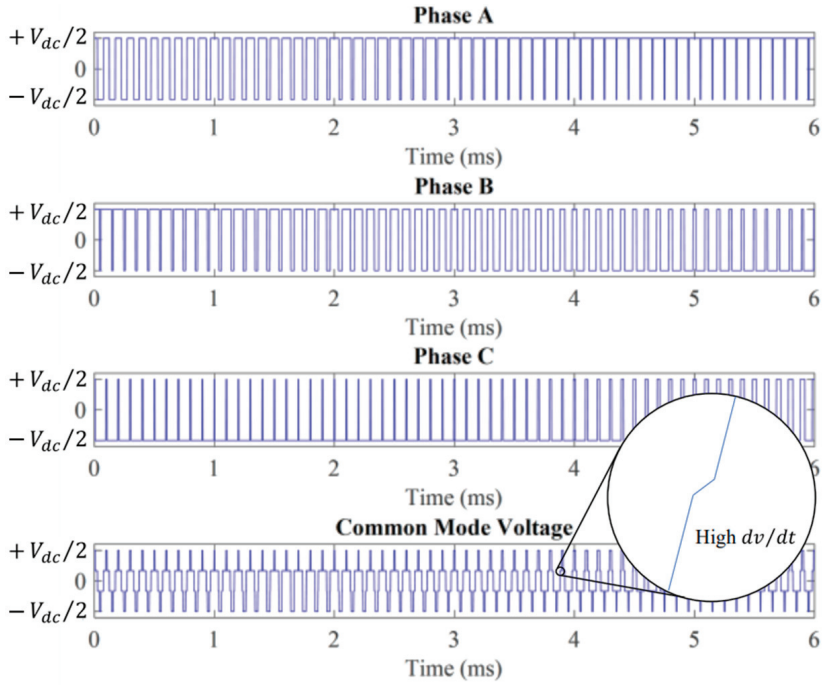


Figure 14. Impact of PWM inverter with CMV [12].

Since each pulse's voltage waveform at the inverter terminals has very steep lines at the start and end, this is the root cause of the negative effects on the motors' service lives and the overall system's vulnerability. Recent studies have shown that PWM inverters' CMV is the primary reason for these side effects [81]:

1. The voltage at the equipment terminals is doubled because of reflections, putting extra strain on the windings' insulation.
2. In windings, capacitive currents and non-uniform voltage distribution can cause electrical machines to experience a circulating current nominated as a bearing current.
3. Charges are stored in the ground capacitors.

Charging current is generated due to the developed common mode capacitive coupling. It flows from the rotor to the end bearing due to the highest switching application of PWM drives for the induction motor with the high *dv*/*dt*. Bearing currents are classified by their courses inside the machine and origin:

1. Capacitive BC,
2. Non-circulating BC,
3. Circulating BC (electric discharge machining),
4. Current in rotor-ground.

As depicted in Figure 15, the bearing current I_{brg} comes from a simple inverter with one phase (phase a) and an impedance Z_{inv} between the DC-link and the ground. Stator winding and the rotor create capacitance C_{wr}, which starts charging the rotor shaft current when the inverter current flows into the motor's main windings.

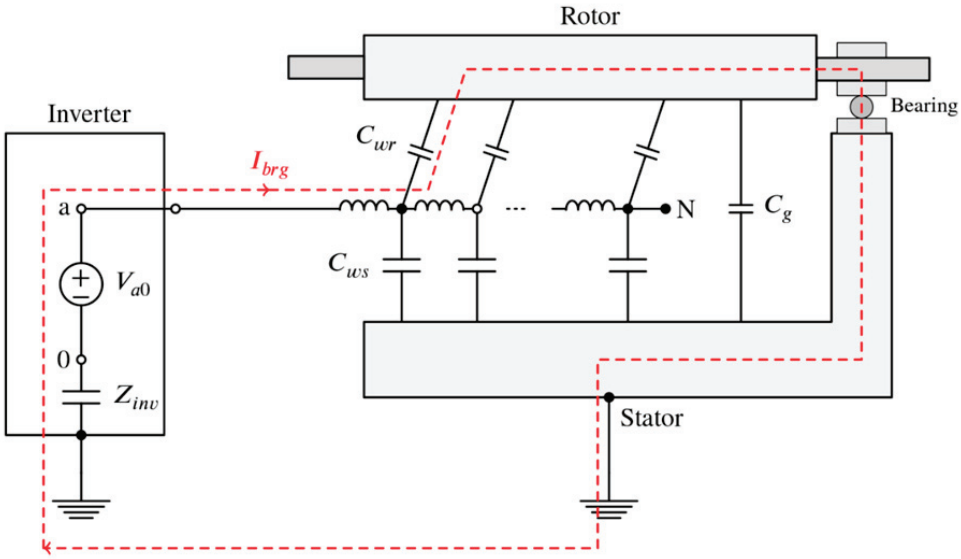


Figure 15. Bearing currents with the ground return [26].

C_g is the capacitance across the bearing C_{ws} and C_{wr} are parasitic capacitance in motor, respectively. Z_{inv} is the inverter-ground capacitive coupling. This is non-circulating because the bearing current returns to the inverter instead of the machine. Stray capacitances in the stator winding cause bearing leakage currents generated by the parasitic capacitive coupling between the rotor and stator alone. the second circulating current arises due to the electromagnetic induction caused by the stray magnetic flux path field within the winding coils, due to uneven current distributions.

High dv/dt generates capacitive currents to the stator iron, causing this uneven current distribution. Terminal-end currents are higher than far-end currents, creating a current unbalance on each coil side, as shown in Figure 16.

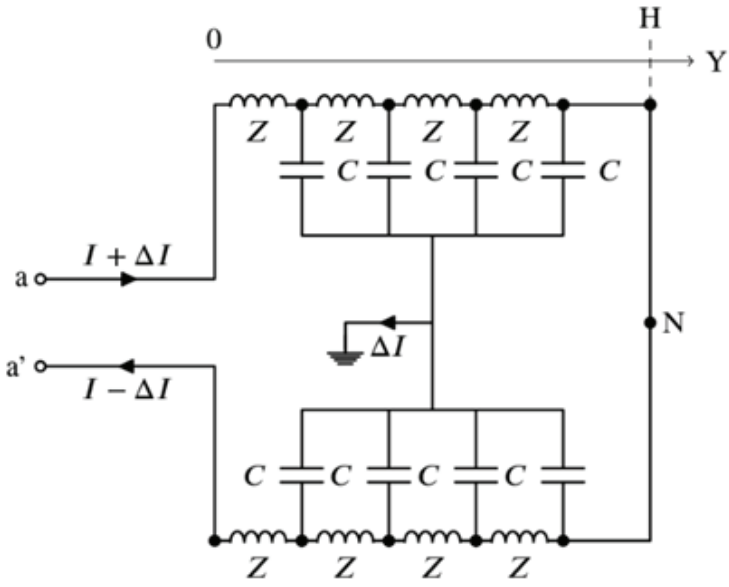


Figure 16. Stray capacitances between winding and stator iron [202].

A fast and accurate method of fault diagnosis using a common-mode voltage and an open switch has been proposed and implemented. An active common-mode voltage injection (ACMVI) is used to improve the algorithm's robustness applicability, reduce the false frequency alarms, and enhance fault diagnosis accuracy [203]. For the modeling of current faults and circuit parameters, it is required to have an in-depth analysis of the reflection of typical electrical machines' complex geometry and their material composition. Different Analytical (DA), Finite Element Analysis (FEA) two-dimensional (2D), and FEA three-dimensional (3D) modeling techniques evaluate the bearing or shaft currents process [12]. A comparative summary of the different parameter identification for the parasitic capacitance for the bearing current estimation and further analysis for the condition monitoring and diagnostics is presented in Table 9.

Table 9. Machine parasitic capacitance calculation methods in fault mitigation.

Sr. No.	FD Technique	Pros	Cons	Reference
1.	Impedance fitting algorithm	• Accurate and validating. • No assumptions; naturally consider all factors.	• Inspection points. • Difficulty in decoupling specific capacitances from adjacent capacitances. • Turn–turn capacitances.	[204]
2.	Geometrically simplified analytical methods	• Have low computational burden. • Featured with the estimation of stray capacitance.	• Inedequete approximations. • Difficult in end-winding modelling to quantify the effect.	[205]

Table 9. *Cont.*

Sr. No.	FD Technique	Pros	Cons	Reference
3.	2D FEM	• Better in estimation of turn to turn capacitance. • End-winding is simplified by the axis-symmetric modelling.	• Non-consideration of turn-to-turn capacitance. • Non-consideration of end-winding.	[206,207]
4.	3D FEM	• High accuracy in model. • Accounts for turn-to-turn capacitances and 3D end winding.	• Calculation difficulty in the material and geometry.	[208–210]

4.5.2. Diagnostic of Bearing Currents Faults

Inverter-fed IM drives have more potential impact on generating more shaft voltages and subsequently cause bearing current, so their diagnostic is a pre-condition for a prognostic of the overall power system [211]. For an effective motor fault diagnostic, authors suggested several mitigation methods based on the motor's physical, analytical modeling, which considers the overall surrounding of the motor containing the whole bearing current path installation [212].

The primary methods for reducing bearing current are depicted in Figure 17 based on the inverter, motor, and connection side. New inverter topologies and modulation strategies have been devised to reduce the CMV amplitude and voltage and impact of high dv/dt, which also feature the bearing-current diagnostic approaches from the input source side [213–215].

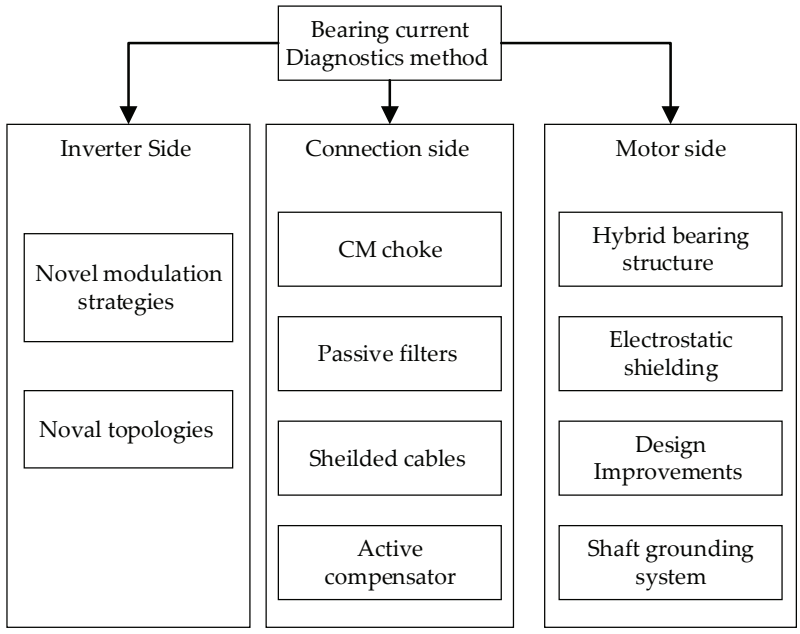


Figure 17. Main bearing current mitigation strategies [12].

Table 10 summarizes the mitigation method's pros and cons. It shows that not all mitigation methods reduce all bearing current types. Understanding the bearing current mechanism is necessary before choosing mitigation methods. Most mitigation methods are costly and require high accuracy bearing current modeling to determine their necessity.

Table 10. Methods of bearing current fault mitigation.

Sr. No.	FD Technique	Pros	Cons	Reference
1.	Filtered-hybrid selective elimination of harmonic with Pulse Width Modulation	• Harmonic elimination. • HF noise mitigation with PWM.	• Feasible for fans or pumps.	[216]
2.	Space vector PWM control design	• PWM rectifiers/inverters' CMV can be greatly reduced.	• Fully controlled rectifier needed.	[217]
3.	1-φ half-bridge, multi-level-inverter system	• A potential reduction of 98.67% of bearing currents.	• Extra hardware.	[218]
4.	An LC-filtered fourth leg	• Eliminates CMV.	• Extra hardware.	[219]
5.	Dual-bridge inverter	• Significant mitigation of leakage-current. • Eliminating the shaft voltage. • Reduction of bearing currents.	• Additional six IGBTs devices. • Additional three-phase machine. • Costly.	[220]
6.	Dual/Paired IV-level inverter with a strategic switching strategy	• CMV is suppressed down.	• System complexity.	[221]
7.	Active common noise canceler	• Reduce shaft voltage, ground current, and EMI.	• Hardware and control complexity.	[222,223]
8.	Shielded cables	• EMI and voltage reflection reduction.	• Increased circulating bearing currents.	[224]
9.	Ceramic-ball hybrid bearings	• Simple design.	• Bearings cost more.	[225]
10.	Multiple conductive microfibers	• Low friction. • Good electrical contact.	• Costly.	[226]
11.	Oblique in slots	• A 98% shaft-to-frame voltage reduction.	• Compromise the electromagnetic performances. • Reduced electromagnetic capabilities.	[227]

4.6. Partial Discharge (PD)

The dielectric of the electric motor insulation system deteriorates with high terminal voltage stresses, transient voltages, and an elevated exchange rate of voltage fed at the output terminal of inverter utilization with the PWM faster wide-bandgap devices (WBG) [228]. There is acceleration aging by stimulating partial discharges. Motor terminal

surges most often cause drive failure. To avoid motor partial discharge faults, multiple HF motor models have been developed, analyzed, and presented [26,229,230].

The output terminal of the inverter has high voltage gradient attributes (high dv/dt), and high transient frequency generates the partial discharge (PD). Therefore, its output terminal voltage stresses the IM stator winding, and electrical stress at the insulation with a high impact compared with grid-fed machines leads to a permanent insulation failure [231–233]. Therefore, high-frequency modeling and lumped parameters estimation has been implemented for the condition monitoring and fault diagnostic in IM. This shows the research and development work that has been carried out in critical parameters and overvoltage mitigation to avoid partial discharges. As a result, the PD impacts and accelerated gaining parameters are necessary for effective predictive maintenance through numerical modeling.

Partial discharges lead to the ongoing degradation of the protective enamel, resulting in delamination, erosion, and breakage. These factors caused the conducting surface area in the whole component to register short circuits and signaling through the current relay with autonomous detection, as explained by the authors in [234,235]. There are four types of PDs, as depicted in Figure 18.

A summary of insulation aging analyses according to the available literature is depicted in Figure 19.

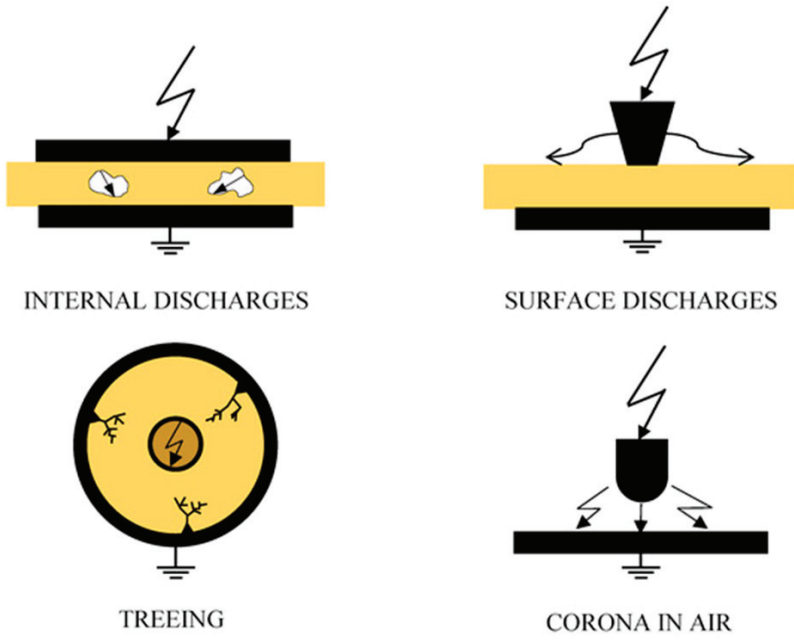


Figure 18. Partial discharge types [236].

The impedance analysis of the motor is used for a response measurement with a wide frequency range, starting from low frequency to several megahertz frequency levels. For this purpose, parameterized motor models are estimated within a motor, connection cables, and inverter, along with the corresponding series and branch impedance and an effective lumped parameter value. The LTspic software tool was used to estimate the building of numerous models, with a motor, cable, and inverter setup, as well as one-phase estimation and in-depth analysis.

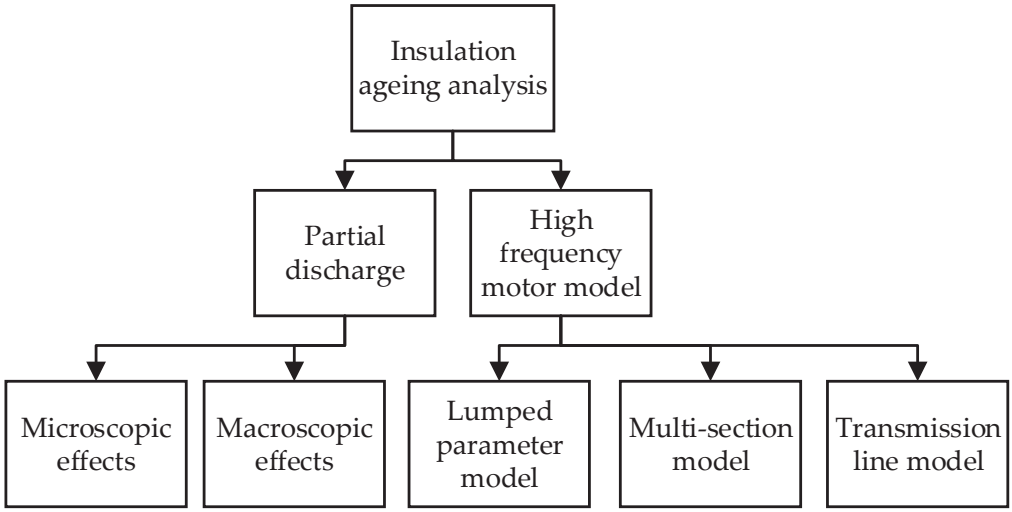


Figure 19. Review of aging insulation [234].

5. Intelligent Diagnostic Techniques

Intelligent diagnostic techniques for induction motor condition monitoring and diagnostics include fuzzy logic (FL), as well as model-free optimization methods like genetic algorithms, a hidden Markov model, a Bayesian classifier, a support vector machine (SVM), deep learning, and artificial neural networks (ANN) [98,237,238]. Figure 20 shows multiple diagnosis types based on artificial intelligence algorithms used in modern computations.

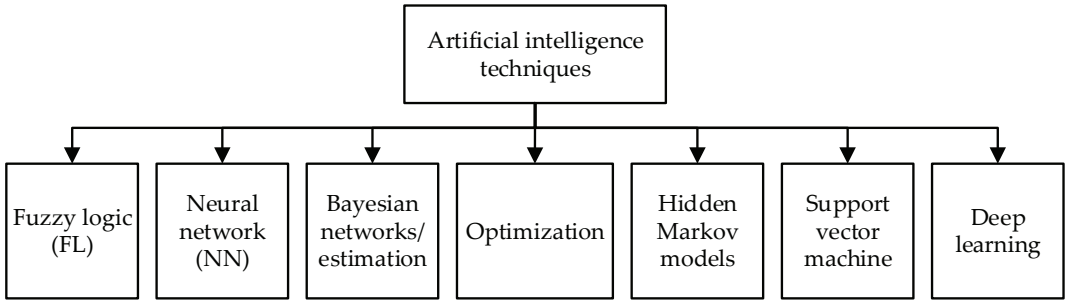


Figure 20. Artificial intelligence-based fault diagnosis of IMs.

Thus, the system should monitor algorithms with input–output mapping, dynamics, and control expressions. An artificial neural network (ANN) is used in a system for prospective detection of bearing faults in IM using MCSA [94]. ANN uses Levenberg–Marquardt-trained three-layered backpropagation.

There is another type of neural network called a Trained Neural Network (T-ANN), which is now confirmed for implementation and validity with the use of the trained data. Residuals are obtained from the output of the ANN. The resultant output data can be monitored for the delivered accuracy and validity in which the residues threshold illustrates the potential fault estimation.

Author study [99] used machine learning and k-means clusters as assessment criteria for condition monitoring and fault diagnostics, among other behaviors. The author of [239] proposed a neural network structure for detecting the induction motor bearing fault. Real-time torque and voltage unbalance monitoring was used to examine faults further. In [102], the author demonstrated the hybrid feature reduction process using the motor vibration

signature analysis in a novel way. The following features listed below can help to recognize and show the fault or failure in IM:

- Decomposition methods of the signal,
- Statistical time-based feature prediction,
- Genetic algorithm (GA) optimization based on the feature,
- Component analysis based on integrating principal,
- Selection procedure based on the feature,
- Selection based on the Fisher score,
- Extraction of the feature.

Additionally, fuzzy logic (FL) can be used for the condition monitoring of the IM. The following algorithms concerning the real-time implementation of the artificial intelligence (AI) field for condition monitoring and fault diagnostics are listed below:

- Adaptive neuro-fuzzy inference systems (ANFIS),
- Fuzzy wavelet logic,
- Wavelet packet transform (WPT),
- Support vector machine (SVM).

K-function, also known as Kernel function, and wavelet transform were added to SVM techniques for fault diagnostics goals. Wavelet fusion features and decision analysis can also detect IM faults [240,241].

6. Summary and Future Directions

Modern drives operated by WBG-based power electronic converters are more effective when used in electric traction or propulsion systems because they work better, are more portable, and have fewer moving parts than traditional Si-based drives. The main challenges affecting the reliable operation of electric motors are the sharp pulse steps with large over-voltage transients and high-switching frequency in the operation of inverters observed at motor input terminals. The impact of the inverter on the electric machines must be considered according to the faults, and, hence, its CM and FD increase their service life. In the case of inverter-operated machines, the complexity level of segregating the fault frequency trances and investigation becomes higher.

Limitations such as discontinuities in available data, a lower sampling rate of the sensor signals, and fractional signal data at the start and end lead to enduring spectral leakage when applying some FFT algorithms. Spectrum resolution also has limitations for some of its complexity in the available fault condition monitoring and diagnostics. The application of advanced signal processing techniques makes the process more extensively complex, and places a high computational burden on addressing the abovementioned issues. Therefore, there is good research potential in simple algorithm development to improve the spectrum resolution without the complexity of advanced signal processing techniques. Furthermore, based on the research gap, some recent directions and research ideas for future studies in CM and FD for IM operated by PWM high-frequency inverters are stated below and explained in detail.

1. FD in IM fed with high-frequency PWM inverter: Research into the impact of high-frequency PWM switching on the motor insulation, partial discharge impacts, bearing mechanical faults, common-mode voltage adverse effects, and other components, and to foster techniques to detect and diagnose faults specifically related to the PWM operation.
2. Sensor-less fault detection techniques: Analyze some of the advanced sensorless FD techniques that can be used to supervise the condition and identify the faults in IM, without relying on additional usages of the sensor's entity, without much complexity, and overall cost of FD strategic implementation,
3. FD with machine learning (ML): This area highlights the investigation related to applying machine learning algorithms, such as deep learning or reinforcement learning, with improved models of high accuracy in IM operated by high PWM inverters.

4. FD in multi-level inverters: This is also a potential research area to study the impact of multi-level PWM inverters on motor operation, output performance, transient response caused to load changes, operation in high-speed environments, and flux weaken range, while operating in wide-beyond speed, tailored to the characteristics of multi-level modulation techniques.
5. Condition monitoring in harsh environments: Development of robust fault diagnostic technique suitable for IM operated in harsh environments, such as in the zone of extremely high temperature, high humidity, contaminated environments, and the high duty cycle of operation, which create indigenous faults within IM. The robustness defines the compactness of the algorithm or FD techniques, which shows insensitivity in its output, with some changes in input-sensitive parameters. The probability of robustness can be analyzed through different statical analyses and analytical techniques, especially in the time domain signal analysis that include RMS value, standard deviation, skewness, kurtosis, high statical moments. It can be enhanced with optimization algorithms, such as particle swarm optimization, genetic algorithms, and other naturally inspired algorithms.
6. IoT for remote access: The most feasible and influential process can be implemented by exploring the IoT integration techniques with FD. Real-time remote monitoring of IM operated by a high transient inverter allows continuous time monitoring and early detection from anywhere.
7. Model-based predictive maintenance: For this type of FD, state-of-the-art, physics-based IM models; real-time sensor instrumentation; and measurement capability can be utilized to establish a FD scheme for predictive maintenance strategy. For the high-performance output of FD technique, the maintenance schedule can be optimized to minimize the IM motor's downtime.
8. FD in mechanical faults: Examine methods for fault identification and diagnosis in bearing, e.g., outer, inner race, and roller fault. Examples of rotor faults include broken rotor (BRB) faults and eccentricity. It is necessary to consider the one-of-a-kind difficulties and negative impact that high-PWM inverters present.
9. Online-parameter estimation: Developing the online-parameter estimation methods to accurately access the motor parameters, which can detect the fault and generate a potentially viable solution for FD. These parameters are resistance, inductances, load torque, and speed response, which vary with IM operation and employ monitoring criteria and algorithms for the FD.
10. Hybrid FD techniques: A good combination of numerous techniques, such as advanced signal processing techniques, artificial intelligence, machine learning, and model-based techniques, can be used to create a hybrid FD approach that can improve overall performance and reliability by taking advantage of the strengths inherent in each diagnostic procedure.

The above-described directions can provide an area for new research in the field of CM and FD.

7. Conclusions

In conclusion, this research paper comprehensively analyzes condition monitoring and practical diagnostic techniques for induction motors fed by inverters. With a systematic approach, this paper reviewed the impact and challenges associated with an inverter-fed system on the induction motor, different fault scenarios, and concern approach of condition monitoring and diagnostics. This study emphasized the practicality and applicability of diagnostics schemes with its pros and cons, starting from conventional methods such as MCSA, monitoring analysis, and acoustics emission. The authors also highlighted the most advanced techniques, such as data-driven prognostics, artificial intelligence (AI) and machine learning (ML), model-based fault detection and diagnosis, fault signature analysis using advanced signal processing techniques, and condition-based maintenance optimization. The fault condition monitoring and diagnostics schemes discussed in this

study utilize state-of-the-art technologies to enhance the precision, productivity, and efficacy of fault detection and diagnosis across diverse systems and industries.

The presented case studies of the literature demonstrate the effectiveness of these techniques in detecting and diagnosing different induction motor faults in its stator, rotor, bearing, shaft voltages development, and partial discharge. The insights gained from this research contribute to advancing condition monitoring strategies and practical diagnostic techniques, thereby benefiting industries that rely on inverter-fed motor drive systems and researchers in the field of diagnostics.

Author Contributions: Conceptualization, T.V. and B.A.; methodology, L.K., B.A. and M.U.S.; formal analysis, L.K. and A.K.; investigation, B.A.; resources, S.A. and K.K.; data curation, B.A.; writing—original draft preparation, M.U.S.; writing—review and editing, M.U.S., T.V. and K.K.; visualization, S.A.; supervision, T.V.; project administration, L.K. and A.K.; funding acquisition, T.V. All authors have read and agreed to the published version of the manuscript.

Funding: This work was supported by Estonian research council.

Data Availability Statement: Not applicable.

Acknowledgments: Research is supported by the joint Baltic-Nordic Energy Research programme project "Guidelines for Next Generation Buildings as Future Scalable Virtual Management of Micro-Grids [Next-uGrid]", No. 117766.

Conflicts of Interest: The authors declare no conflict of interest.

References

1. Venkatar Ramana, D.; Baskar, S. Fault Analysis of Voltage Source Inverter Fed Induction Motor Drive. In Proceedings of the 2016 IEEE International Conference on Computational Intelligence and Computing Research, ICCIC 2016, Chennai, India, 15–17 December 2016.
2. Soufi, Y.; Bahi, T.; Harkat, M.F.; Rouaibia, R. Diagnosis and Fault Detection in Induction Motor Drive Fed by PWM Voltage Source Inverter. *J. Electr. Syst.* **2010**, *6*, 2.
3. Vaimann, T.; Belahcen, A.; Martinez, J.; Kilk, A. Detection of Broken Bars in Frequency Converter Fed Induction Motor Using Park's Vector Approach. In Proceedings of the PQ 2012: 8th International Conference—2012 Electric Power Quality and Supply Reliability, Tartu, Estonia, 11–13 July 2012.
4. Asad, B.; Vaimann, T.; Kallaste, A.; Rassolkin, A.; Belahcen, A. Winding Function Based Analytical Model of Squirrel Cage Induction Motor for Fault Diagnostics. In Proceedings of the 2019 26th International Workshop on Electric Drives: Improvement in Efficiency of Electric Drives, IWED 2019, Moscow, Russia, 30 January–February 2019.
5. Vaimann, T.; Kallaste, A.; Kilk, A. Sensorless Detection of Induction Motor Rotor Faults Using the Clarke Vector Approach. *Sci. J. Riga Tech. Univ. Power Electr. Eng.* **2011**, *28*, 2011. [CrossRef]
6. Asad, B.; Vaimann, T.; Belahcen, A.; Kallaste, A.; Rassõlkin, A.; Iqbal, M.N. Modified Winding Function-Based Model of Squirrel Cage Induction Motor for Fault Diagnostics. *IET Electr. Power Appl.* **2020**, *14*, 1722–1734. [CrossRef]
7. Vaimann, T.; Sobra, J.; Belahcen, A.; Rassõlkin, A.; Rolak, M.; Kallaste, A. Induction Machine Fault Detection Using Smartphone Recorded Audible Noise. *IET Sci. Meas. Technol.* **2018**, *12*, 554–560. [CrossRef]
8. Rassõlkin, A.; Vaimann, T.; Belahcen, A.; Kallaste, A.; Petrov, A.; Plokhov, I.; Kotelnikov, A. Adjusted Electrical Equivalent Circuit Model of Induction Motor with Broken Rotor Bars. In Proceedings of the 10th International Conference—2016 Electric Power Quality and Supply Reliability, PQ 2016, Tallinn, Estonia, 29–31 August 2016.
9. Asad, B.; Vaimann, T.; Belahcen, A.; Kallaste, A.; Rassõlkin, A.; Ghafarokhi, P.S.; Kudelina, K. Transient Modeling and Recovery of Non-Stationary Fault Signature for Condition Monitoring of Induction Motors. *Appl. Sci.* **2021**, *11*, 2806. [CrossRef]
10. Asad, B.; Vaimann, T.; Belahcen, A.; Kallaste, A.; Rassolkin, A.; Van Khang, H.; Ghahfarokhi, P.S.; Naseer, M.U.; Iqbal, M.N. The Modeling and Investigation of Slot Skews and Supply Imbalance on the Development of Principal Slotting Harmonics in Squirrel Cage Induction Machines. *IEEE Access* **2021**, *9*, 165932–165946. [CrossRef]
11. Asad, B.; Vaimann, T.; Belahcen, A.; Kallaste, A.; Rassolkin, A. Rotor Fault Diagnostic of Inverter Fed Induction Motor Using Frequency Analysis. In Proceedings of the 2019 IEEE 12th International Symposium on Diagnostics for Electrical Machines, Power Electronics and Drives, SDEMPED 2019, Toulouse, France, 27–30 August 2019.
12. Zhu, W.; De Gaetano, D.; Chen, X.; Jewell, G.W.; Hu, Y. A Review of Modeling and Mitigation Techniques for Bearing Currents in Electrical Machines with Variable-Frequency Drives. *IEEE Access* **2022**, *10*, 125279–125297. [CrossRef]
13. Oikonomou, N.; Holtz, J. Closed-Loop Control of Medium-Voltage Drives Operated with Synchronous Optimal Pulsewidth Modulation. *IEEE Trans. Ind. Appl.* **2008**, *44*, 115–123. [CrossRef]

14. Napoles, J.; Leon, J.I.; Portillo, R.; Franquelo, L.G.; Aguirre, M.A. Selective Harmonic Mitigation Technique for High-Power Converters. *IEEE Trans. Ind. Electron.* **2010**, *57*, 2315–2323. [CrossRef]
15. Zhang, Y.; Zhao, Z.; Zhu, J. A Hybrid PWM Applied to High-Power Three-Level Inverter-Fed Induction-Motor Drives. *IEEE Trans. Ind. Electron.* **2011**, *58*, 3409–3420. [CrossRef]
16. Vargas, R.; Ammann, U.; Rodríguez, J.; Pontt, J. Reduction of Switching Losses and Increase in Efficiency of Power Converters Using Predictive Control. In Proceedings of the PESC Record—IEEE Annual Power Electronics Specialists Conference, Rhodes, Greece, 15–19 June 2008.
17. Kerszenbaum, I. Shaft Currents in Electric Machines Fed by Solid-State Drives. In Proceedings of the IEEE Conference Record of Industrial and Commercial Power Systems Technical Conference, Pittsburgh, PA, USA, 4–7 May 1992.
18. Rosales, A.; Sarikhani, A.; Mohammed, O.A. Evaluation of Radiated Electromagnetic Field Interference Due to Frequency Swithcing in PWM Motor Drives by 3D Finite Elements. *IEEE Trans. Magn.* **2011**, *47*, 1474–1477. [CrossRef]
19. Lee, K.; Shen, G.; Yao, W.; Lu, Z. Performance Characterization of Random Pulse Width Modulation Algorithms in Industrial and Commercial Adjustable-Speed Drives. *IEEE Trans. Ind. Appl.* **2017**, *53*, 1078–1087. [CrossRef]
20. Kim, T.H.; Lee, J. Comparison of the Iron Loss of a Flux-Reversal Machine under Four Different PWM Modes. *IEEE Trans. Magn.* **2007**, *43*, 1725–1728. [CrossRef]
21. Jung, H.S.; Hwang, C.E.; Kim, H.S.; Sul, S.K.; Hee-Won, A.; Yoo, H. Minimum Torque Ripple Pulse Width Modulation with Reduced Switching Frequency for Medium-Voltage Motor Drive. *IEEE Trans. Ind. Appl.* **2018**, *54*, 3315–3325. [CrossRef]
22. Rajkamal, R.; Karthi, A. Analysis of PWM Techniques for Inverters Driving AC Motors. *Pertanika J. Sci. Technol.* **2017**, *25*, 1211–1222.
23. Lavanya, S.N.; Reddy, T.B.; Kumar, M.V. Performance of Random PWM Techniques for Induction Motor Drive. *Int. J. Eng. Adv. Technol.* **2019**, *8*, 133–139.
24. Chen, S.; Lipo, T.A.; Fitzgerald, D. Modeling of Motor Bearing Currents in PWM Inverter Drives. *IEEE Trans. Ind. Appl.* **1996**, *32*, 1365–1370. [CrossRef]
25. Hamman, J.; Van Der Merwe, F.S. Voltage Harmonics Generated by Voltage-Fed Inverters Using PWM Natural Sampling. *IEEE Trans. Power Electron.* **1988**, *3*, 297–302. [CrossRef]
26. Persson, E. Transient Effects in Application of PWM Inverters to Induction Motors. *IEEE Trans. Ind. Appl.* **1992**, *28*, 1095–1101. [CrossRef]
27. Chen, S.; Lipo, T.A.; Fitzgerald, D. Source of Induction Motor Bearing Currents Caused by PWM Inverters. *IEEE Trans. Energy Convers.* **1996**, *11*, 25–32. [CrossRef]
28. Soufi, Y.; Bahi, T.; Harkat, M.F.; Mohammedi, M. Fault Diagnosis Methods for Three Phase PWM Inverter Fed Induction Motor. *Int. J. Eng. Appl.* **2018**, *6*, 122. [CrossRef]
29. Sundeep, S.; Wang, J.; Griffo, A.; Alvarez-Gonzalez, F. Peak Voltage Stress on Stator Winding in PWM Inverter Fed Drives. In Proceedings of the 2020 International Conference on Electrical Machines, ICEM 2020, Gothenburg, Sweden, 23–26 August 2020.
30. Esmaeli, A.; Tavassoli, F. A Novel Passive Filter to Reduce PWM Inverters Adverse Effects in Electrical Machine System. *World Appl. Sci. J.* **2011**, *13*, 2536–2544.
31. Benbouzid, M.E.H.; Vieira, M.; Theys, C. Induction Motors' Faults Detection and Localization Using Stator Current Advanced Signal Processing Techniques. *IEEE Trans. Power Electron.* **1999**, *14*, 14–22. [CrossRef]
32. Benbouzid, M.E.H. A Review of Induction Motors Signature Analysis as a Medium for Faults Detection. *IEEE Trans. Ind. Electron.* **2000**, *47*, 984–993. [CrossRef]
33. Albrecht, P.F.; Appiarius, J.C.; McCoy, R.M.; Owen, E.L.; Sharma, D.K. Assessment of the Reliability of Motors in Utility Applications—Updated. *IEEE Trans. Energy Convers.* **1986**, *EC-1*, 39–46. [CrossRef]
34. Choudhary, A.; Goyal, D.; Shimi, S.L.; Akula, A. Condition Monitoring and Fault Diagnosis of Induction Motors: A Review. *Arch. Comput. Methods Eng.* **2019**, *26*, 1221–1238. [CrossRef]
35. Vaimann, T.; Belahcen, A.; Kallaste, A. Necessity for Implementation of Inverse Problem Theory in Electric Machine Fault Diagnosis. In Proceedings of the SDEMPED 2015: IEEE 10th International Symposium on Diagnostics for Electrical Machines, Power Electronics and Drives, Guarda, Portugal, 1–4 September 2015.
36. Akhil Vinayak, B.; Anjali Anand, K.; Jagadanand, G. Wavelet-Based Real-Time Stator Fault Detection of Inverter-Fed Induction Motor. *IET Electr. Power Appl.* **2020**, *14*, 82–90. [CrossRef]
37. Skowron, M.; Orlowska-Kowalska, T.; Wolkiewicz, M.; Kowalski, C.T. Convolutional Neural Network-Based Stator Current Data-Driven Incipient Stator Fault Diagnosis of Inverter-Fed Induction Motor. *Energies* **2020**, *13*, 1475. [CrossRef]
38. Asad, B.; Vaimann, T.; Kallaste, A.; Belahcen, A. Harmonic Spectrum Analysis of Induction Motor with Broken Rotor Bar Fault. In Proceedings of the 2018 IEEE 59th Annual International Scientific Conference on Power and Electrical Engineering of Riga Technical University, RTUCON 2018, Riga, Latvia, 12–13 November 2018.
39. Martin-Diaz, I.; Morinigo-Sotelo, D.; Duque-Perez, O.; Arredondo-Delgado, P.A.; Camarena-Martinez, D.; Romero-Troncoso, R.J. Analysis of Various Inverters Feeding Induction Motors with Incipient Rotor Fault Using High-Resolution Spectral Analysis. *Electr. Power Syst. Res.* **2017**, *152*, 18–26. [CrossRef]

40. Kudelina, K.; Vaimann, T.; Rassõlkin, A.; Kallaste, A.; Demidova, G.; Karpovich, D. Diagnostic Possibilities of Induction Motor Bearing Currents. In Proceedings of the 2021 18th International Scientific Technical Conference Alternating Current Electric Drives, ACED 2021, Ekaterinburg, Russia, 24–27 May 2021.
41. Kudelina, K.; Vaimann, T.; Rassolkin, A.; Kallaste, A.; Asad, B.; Demidova, G. Induction Motor Bearing Currents-Causes and Damages. In Proceedings of the 2021 28th International Workshop on Electric Drives: Improving Reliability of Electric Drives, IWED 2021, Moscow, Russia, 27–29 January 2021.
42. Kudelina, K.; Asad, B.; Vaimann, T.; Rassolkin, A.; Kallaste, A. Effect of Bearing Faults on Vibration Spectrum of BLDC Motor. In Proceedings of the 2020 IEEE Open Conference of Electrical, Electronic and Information Sciences, eStream 2020, Vilnius, Lithuania, 30 April 2020.
43. Kudelina, K.; Autsou, S.; Asad, B.; Vaimann, T.; Rassolkin, A.; Kallaste, A. Implementation and Analysis of Rolling Bearing Faults Caused by Shaft Currents. In Proceedings of the International Workshop on Electric Drives, IWED, Moscow, Russia, 26–29 January 2022; Volume 2022.
44. De Paula, H.; de Andrade, D.A.; Chaves, M.L.R.; Domingos, J.L.; de Freitas, M.A.A. Methodology for Cable Modeling and Simulation for High-Frequency Phenomena Studies in PWM Motor Drives. *IEEE Trans. Power Electron.* **2008**, *23*, 744–752. [CrossRef]
45. Garcia-Perez, A.; Romero-Troncoso, R.J.; Cabal-Yepez, E.; Osornio-Rios, R.A.; Lucio-Martinez, J.A. Application of High-Resolution Spectral Analysis for Identifying Faults in Induction Motors by Means of Sound. *JVC/J. Vib. Control* **2012**, *18*, 1585–1594. [CrossRef]
46. Xu, Y.; Liang, Y.; Yuan, X.; Wu, X.; Li, Y. Experimental Assessment of High Frequency Bearing Currents in an Induction Motor Driven by a SiC Inverter. *IEEE Access* **2021**, *9*, 40540–40549. [CrossRef]
47. Chen, H.; Zhao, H. Review on Pulse-Width Modulation Strategies for Common-Mode Voltage Reduction in Three-Phase Voltage-Source Inverters. *IET Power Electron.* **2016**, *9*, 2611–2620. [CrossRef]
48. Erdman, J.M.; Kerkman, R.J.; Schlegel, D.W.; Skibinski, G.L. Effect of PWM Inverters on Ac Motor Bearing Currents and Shaft Voltages. *IEEE Trans. Ind. Appl.* **1996**, *32*, 250–259. [CrossRef]
49. Huang, Y.; Xu, Y.; Zhang, W.; Zou, J. Modified Single-Edge SVPWM Technique to Reduce the Switching Losses and Increase PWM Harmonics Frequency for Three-Phase VSIs. *IEEE Trans Power Electron* **2020**, *35*, 10643–10653. [CrossRef]
50. Kumar, S.; Mukherjee, D.; Guchhait, P.K.; Banerjee, R.; Srivastava, A.K.; Vishwakarma, D.N.; Saket, R.K. A Comprehensive Review of Condition Based Prognostic Maintenance (CBPM) for Induction Motor. *IEEE Access* **2019**, *7*, 90690–90704. [CrossRef]
51. Cabanas, M.F.; Norniella, J.G.; Melero, M.G.; Rojas, C.H.; Cano, J.M.; Pedrayes, F.; Orcajo, G.A. Detection of Stator Winding Insulation Failures: On-Line and off-Line Tests. In Proceedings of the 2013 IEEE Workshop on Electrical Machines Design, Control and Diagnosis, WEMDCD 2013, Paris, France, 11–12 March 2013.
52. Unsal, A.; Kara, O. Modeling of Broken Rotor Bars in a Squirrel-Cage Induction Motor. In Proceedings of the International Conference on Power Engineering, Energy and Electrical Drives, Istanbul, Turkey, 13–17 May 2013.
53. Han, P.; Zhang, Y.; Kesgin, M.G.; Heins, G.; Patterson, D.; Thiele, M.; Ionel, D.M. On the Modeling of Bearing Voltage and Current in PWM Converter-Fed Electric Machines Using Electromagnetic Finite Element Analysis. In Proceedings of the 2021 IEEE Energy Conversion Congress and Exposition, ECCE 2021, Virtual, 10–14 October 2021.
54. Yamazaki, K.; Iida, K.; Terai, Y. Fast Estimation of Harmonic Losses Caused by Inverter Carrier in Interior Permanent-Magnet Synchronous Motors by Using Combination of Time- And Frequency-Domain Finite-Element Analyses. *IEEE Trans. Magn.* **2020**, *56*, 1–4. [CrossRef]
55. Prieto, J.; Jones, M.; Barrero, F.; Levi, E.; Toral, S. Comparative Analysis of Discontinuous and Continuous PWM Techniques in VSI-Fed Five-Phase Induction Motor. *IEEE Trans. Ind. Electron.* **2011**, *58*, 5324–5335. [CrossRef]
56. Holmes, D.G.; Lipo, T.A. *Pulse Width Modulation for Power Converters*; John Wiley & Sons: Hoboken, NJ, USA, 2010.
57. Nandi, S.; Toliyat, H.A.; Li, X. Condition Monitoring and Fault Diagnosis of Electrical Motors—A Review. *IEEE Trans. Energy Convers.* **2005**, *20*, 719–729. [CrossRef]
58. Asad, B.; Vaimann, T.; Belahcen, A.; Kallaste, A. Broken Rotor Bar Fault Diagnostic of Inverter Fed Induction Motor Using FFT, Hilbert and Park's Vector Approach. In Proceedings of the 2018 23rd International Conference on Electrical Machines, ICEM 2018, Alexandroupoli, Greece, 3–6 September 2018.
59. Dorrell, D.G.; Makhoba, K. Detection of Inter-Turn Stator Faults in Induction Motors Using Short-Term Averaging of Forward and Backward Rotating Stator Current Phasors for Fast Prognostics. *IEEE Trans. Magn.* **2017**, *53*, 1–7. [CrossRef]
60. Devi, N.R.; Siva Sarma, D.V.S.S.; Ramana Rao, P.V. Detection of Stator Incipient Faults and Identification of Faulty Phase in Three-Phase Induction Motor—Simulation and Experimental Verification. *IET Electr. Power Appl.* **2015**, *9*, 540–548. [CrossRef]
61. Tallam, R.M.; Lee, S.B.; Stone, G.C.; Kliman, G.B.; Yoo, J.; Habetler, T.G.; Harley, R.G. A Survey of Methods for Detection of Stator-Related Faults in Induction Machines. *IEEE Trans. Ind. Appl.* **2007**, *43*, 920–933. [CrossRef]
62. Jung, J.; Park, Y.; Lee, S.B.; Cho, C.; Kim, K.; Wiedenbrug, E.; Teska, M. Monitoring of Journal Bearing Faults Based on Motor Current Signature Analysis for Induction Motors. In Proceedings of the 2015 IEEE Energy Conversion Congress and Exposition, ECCE 2015, Montreal, QC, Canada, 20–24 September 2015.
63. Mirzaeva, G.; Saad, K.I. Advanced Diagnosis of Stator Turn-to-Turn Faults and Static Eccentricity in Induction Motors Based on Internal Flux Measurement. *IEEE Trans. Ind. Appl.* **2018**, *54*, 3961–3970. [CrossRef]

64. Asad, B.; Eensalu, L.; Vaimann, T.; Kallaste, A.; Rassolkin, A.; Belahcen, A. The FEM Based Modeling and Corresponding Test Rig Preparation for Broken Rotor Bars Analysis. In Proceedings of the 2019 IEEE 60th Annual International Scientific Conference on Power and Electrical Engineering of Riga Technical University, RTUCON 2019, Riga, Latvia, 7–9 October 2019.
65. Shirazian, S.; Alibabaei, M. Using Neural Networks Coupled with Particle Swarm Optimization Technique for Mathematical Modeling of Air Gap Membrane Distillation (AGMD) Systems for Desalination Process. *Neural Comput. Appl.* **2017**, *28*, 2099–2104. [CrossRef]
66. Halder, S.; Bhat, S.; Zychma, D.; Sowa, P. Broken Rotor Bar Fault Diagnosis Techniques Based on Motor Current Signature Analysis for Induction Motor—A Review. *Energies* **2022**, *15*, 8569. [CrossRef]
67. Duque-Perez, O.; Garcia-Escudero, L.A.; Morinigo-Sotelo, D.; Gardel, P.E.; Perez-Alonso, M. Analysis of Fault Signatures for the Diagnosis of Induction Motors Fed by Voltage Source Inverters Using ANOVA and Additive Models. *Electr. Power Syst. Res.* **2015**, *121*, 1–13. [CrossRef]
68. Vilhekar, T.G.; Ballal, M.S.; Suryawanshi, H.M. Application of Multiple Parks Vector Approach for Detection of Multiple Faults in Induction Motors. *J. Power Electron.* **2017**, *17*, 972–982. [CrossRef]
69. Maouche, Y.; Oumaamar, M.E.K.; Boucherma, M.; Khezzar, A. Instantaneous Power Spectrum Analysis for Broken Bar Fault Detection in Inverter-Fed Six-Phase Squirrel Cage Induction Motor. *Int. J. Electr. Power Energy Syst.* **2014**, *62*, 110–117. [CrossRef]
70. Braham, A.; Lachiri, Z. Diagnosis of Broken Bar Fault in Induction Machines Using Advanced Digital Signal Processing. *Int. Rev. Electr. Eng.* **2010**, *5*. [CrossRef]
71. Gangsar, P.; Tiwari, R. Signal Based Condition Monitoring Techniques for Fault Detection and Diagnosis of Induction Motors: A State-of-the-Art Review. *Mech. Syst. Signal Process.* **2020**, *144*, 106908. [CrossRef]
72. Yakhni, M.F.; Cauet, S.; Sakout, A.; Assoum, H.; Etien, E.; Rambault, L.; El-Gohary, M. Variable Speed Induction Motors' Fault Detection Based on Transient Motor Current Signatures Analysis: A Review. *Mech. Syst. Signal Process.* **2023**, *184*. [CrossRef]
73. Lin, C.K.; Liu, T.H.; Yu, J.T.; Fu, L.C.; Hsiao, C.F. Model-Free Predictive Current Control for Interior Permanent-Magnet Synchronous Motor Drives Based on Current Difference Detection Technique. *IEEE Trans. Ind. Electron.* **2014**, *61*, 667–681. [CrossRef]
74. Nguyen, V.; Seshadrinath, J.; Wang, D.; Nadarajan, S.; Vaiyapuri, V. Model-Based Diagnosis and RUL Estimation of Induction Machines under Interturn Fault. *IEEE Trans. Ind. Appl.* **2017**, *53*, 2690–2701. [CrossRef]
75. Toliyat, H.A.; Nandi, S.; Choi, S.; Meshgin-kelk, H. *Electric Machines: Modeling, Condition Monitoring, and Fault Diagnosis*; CRC Press: Boca Raton, FL, USA, 2017.
76. Benbouzid, M.E.H.; Kliman, G.B. What Stator Current Processing-Based Technique to Use for Induction Motor Rotor Faults Diagnosis? *IEEE Trans. Energy Convers.* **2003**, *18*, 238–244. [CrossRef]
77. Yaghobi, H.; Arkan, M.; Perović, D.K.; Unsworth, P.; Citation, O.; Chattopadhyay, S.; Mitra, M.; Sengupta, S.; Bengal, W.; Roshanfekr, R.; et al. Interpretation, and Industrial Case Histories. *IEEE Trans. Ind. Electron.* **2017**, *13*, 145–156.
78. Kowalski, C.T.; Wierzbicki, R.; Wolkiewicz, M. Stator and Rotor Faults Monitoring of the Inverter-Fed Induction Motor Drive Using State Estimators. *Autom. J. Control Meas. Electron. Comput. Commun.* **2013**, *54*, 348–355. [CrossRef]
79. Kudelina, K.; Asad, B.; Vaimann, T.; Rassolkin, A.; Kallaste, A. Production Quality Related Propagating Faults of Induction Machines. In Proceedings of the 2020 11th International Conference on Electrical Power Drive Systems, ICEPDS 2020, Saint Petersburg, Russia, 4–7 October 2020.
80. Isermann, R. Model-Based Fault Detection and Diagnosis—Status and Applications. *IFAC Proc. Vol.* **2004**, *37*, 49–60. [CrossRef]
81. Willwerth, A.; Roman, M. Electrical Bearing Damage—A Lurking Problem in Inverter-Driven Traction Motors. In Proceedings of the 2013 IEEE Transportation Electrification Conference and Expo: Components, Systems, and Power Electronics—From Technology to Business and Public Policy, ITEC 2013, Metro Detroit, MI, USA, 16–19 June 2013.
82. Vaimann, T. Advances in Machine Fault Diagnosis. *Appl. Sci.* **2021**, *11*, 7348. [CrossRef]
83. Chen, X.; Wang, S.; Qiao, B.; Chen, Q. Basic Research on Machinery Fault Diagnostics: Past, Present, and Future Trends. *Front. Mech. Eng.* **2018**, *13*, 264–291. [CrossRef]
84. Karlis, A. (Ed.) *Advances in the Field of Electrical Machines and Drives*; MDPI: Basel, Switzerland, 2022.
85. Jiao, J.; Zhao, M.; Lin, J.; Liang, K. A Comprehensive Review on Convolutional Neural Network in Machine Fault Diagnosis. *Neurocomputing* **2020**, *417*, 36–63. [CrossRef]
86. Zhen, D. A Study of Non-stationary Signal Processing for Machinery Condition Monitoring. Ph.D. Thesis, University of Huddersfield, Huddersfield, UK, 2012.
87. Leite, V.C.M.N.; Borges Da Silva, J.G.; Veloso, G.F.C.; Borges Da Silva, L.E.; Lambert-Torres, G.; Bonaldi, E.L.; De Lacerda De Oliveira, L.E. Detection of Localized Bearing Faults in Induction Machines by Spectral Kurtosis and Envelope Analysis of Stator Current. *IEEE Trans. Ind. Electron.* **2015**, *62*, 1855–1865. [CrossRef]
88. Othman, M.S.; Nuawi, M.Z.; Mohamed, R. Vibration and Acoustic Emission Signal Monitoring for Detection of Induction Motor Bearing Fault. *Int. J. Eng. Res. Technol.* **2015**, *4*, 924–929.
89. Sapena-Bano, A.; Burriel-Valencia, J.; Pineda-Sanchez, M.; Puche-Panadero, R.; Riera-Guasp, M. The Harmonic Order Tracking Analysis Method for the Fault Diagnosis in Induction Motors under Time-Varying Conditions. *IEEE Trans. Energy Convers.* **2017**, *32*, 244–256. [CrossRef]

90. Sabir, H.; Ouassaid, M.; Ngote, N.; Benbouzid, M. A Novel Experimental Method to Detect Early Rotor Faults in Induction Machines. *Int. J. Energy Convers.* **2021**, *9*, 191. [CrossRef]
91. Ngote, N.; Guedira, S.; Ouassaid, M.; Cherkaoui, M.; Maaroufi, M. On the Monitoring of Rotor Fault in Induction Machine by the Use of the TSA Method Applied to Stator Current. *Int. Rev. Electr. Eng.* **2012**, *7*, 4822–4828.
92. Ngote, N.; Ouassaid, M.; Guedira, S.; Cherkaoui, M. On the Detection of Induction-Motor Rotor Fault by the Combined "Time Synchronous Averaging-Discrete Wavelet Transform" Approach. *J. Electr. Eng. Technol.* **2015**, *10*, 2315–2325. [CrossRef]
93. Dey, S.; Roy, S.S.; Samanta, K.; Modak, S.; Chatterjee, S. Autocorrelation Based Feature Extraction for Bearing Fault Detection in Induction Motors. In Proceedings of the 2019 International Conference on Electrical, Electronics and Computer Engineering, UPCON 2019, Aligarh, India, 8–10 November 2019.
94. Dehina, W.; Boumehraz, M.; Kratz, F. Detectability of Rotor Failure for Induction Motors through Stator Current Based on Advanced Signal Processing Approaches. *Int. J. Dyn. Control* **2021**, *9*, 1381–1395. [CrossRef]
95. Granda, D.; Aguilar, W.G.; Arcos-Aviles, D.; Sotomayor, D. Broken Bar Diagnosis for Squirrel Cage Induction Motors Using Frequency Analysis Based on MCSA and Continuous Wavelet Transform. *Math. Comput. Appl.* **2017**, *22*, 30. [CrossRef]
96. Lu, J.; Wang, P.; Duan, S.; Shi, L.; Han, L. Detection of Broken Rotor Bars Fault in Induction Motors by Using an Improved MUSIC and Least-Squares Amplitude Estimation. *Math. Probl. Eng.* **2018**, *2018*, 1–12. [CrossRef]
97. Alshorman, O.; Irfan, M.; Saad, N.; Zhen, D.; Haider, N.; Glowacz, A.; Alshorman, A. A Review of Artificial Intelligence Methods for Condition Monitoring and Fault Diagnosis of Rolling Element Bearings for Induction Motor. *Shock. Vib.* **2020**, *2020*, 1–20. [CrossRef]
98. Kudelina, K.; Vaimann, T.; Asad, B.; Rassõlkin, A.; Kallaste, A.; Demidova, G. Trends and Challenges in Intelligent Condition Monitoring of Electrical Machines Using Machine Learning. *Appl. Sci.* **2021**, *11*, 2761. [CrossRef]
99. Soualhi, A.; Clerc, G.; Razik, H. Detection and Diagnosis of Faults in Induction Motor Using an Improved Artificial Ant Clustering Technique. *IEEE Trans. Ind. Electron.* **2013**, *60*, 4053–4062. [CrossRef]
100. Nandi, S.; Ilamparithi, T.; Lee, S.B.; Hyun, D. Pole Pair and Rotor Slot Number Independent Frequency Domain Based Detection of Eccentricity Faults in Induction Machines Using a Semi On-Line Technique. In Proceedings of the 2009 IEEE International Symposium on Diagnostics for Electric Machines, Power Electronics and Drives, SDEMPED 2009, Cargese, France, 31 August–3 September 2009.
101. Di, C.; Bao, X.; Wang, H.; Lv, Q.; He, Y. Modeling and Analysis of Unbalanced Magnetic Pull in Cage Induction Motors with Curved Dynamic Eccentricity. *IEEE Trans. Magn.* **2015**, *51*, 1–7. [CrossRef]
102. Saucedo-Dorantes, J.J.; Delgado-Prieto, M.; Osornio-Rios, R.A.; De Jesus Romero-Troncoso, R. Multifault Diagnosis Method Applied to an Electric Machine Based on High-Dimensional Feature Reduction. *IEEE Trans. Ind. Appl.* **2017**, *53*, 3086–3097. [CrossRef]
103. Toma, R.N.; Prosvirin, A.E.; Kim, J.M. Bearing Fault Diagnosis of Induction Motors Using a Genetic Algorithm and Machine Learning Classifiers. *Sensors* **2020**, *20*, 1884. [CrossRef]
104. Toma, R.N.; Piltan, F.; Kim, J.M. A Deep Autoencoder-Based Convolution Neural Network Framework for Bearing Fault Classification in Induction Motors. *Sensors* **2021**, *21*, 8453. [CrossRef]
105. Yeh, C.C.; Povinelli, R.J.; Mirafzal, B.; Demerdash, N.A.O. Diagnosis of Stator Winding Inter-Turn Shorts in Induction Motors Fed by PWM-Inverter Drive Systems Using a Time-Series Data Mining Technique. In Proceedings of the 2004 International Conference on Power System Technology, POWERCON 2004, Singapore, 21–24 November 2004; Volume 1.
106. Ye, Z.; Sadeghian, A.; Wu, B. Mechanical Fault Diagnostics for Induction Motor with Variable Speed Drives Using Adaptive Neuro-Fuzzy Inference System. *Electr. Power Syst. Res.* **2006**, *76*, 742–752. [CrossRef]
107. Romero-Troncoso, R.J.; Saucedo-Gallaga, R.; Cabal-Yepez, E.; Garcia-Perez, A.; Osornio-Rios, R.A.; Alvarez-Salas, R.; Miranda-Vidales, H.; Huber, N. FPGA-Based Online Detection of Multiple Combined Faults in Induction Motors through Information Entropy and Fuzzy Inference. *IEEE Trans. Ind. Electron.* **2011**, *58*, 5263–5270. [CrossRef]
108. Akar, M.; Cankaya, I. Broken Rotor Bar Fault Detection in Inverter-Fed Squirrel Cage Induction Motors Using Stator Current Analysis and Fuzzy Logic. *Turk. J. Electr. Eng. Comput. Sci.* **2012**, *20*, 1077–1089. [CrossRef]
109. Bozorgi, A.M.; Farasat, M.; Jafarishiadeh, S. Improved Model Predictive Current Control of Permanent Magnet Synchronous Machines with Fuzzy Based Duty Cycle Control. In Proceedings of the ECCE 2016—IEEE Energy Conversion Congress and Exposition, Milwaukee, WI, USA, 18–22 September 2016. [CrossRef]
110. Zaripova, A.D.; Zaripov, D.K.; Usachev, A.E. Visualization of High-Voltage Insulators Defects on Infrared Images Using Computer Vision Methods. *Sci. Vis.* **2019**, *11*, 88–98. [CrossRef]
111. Tao, H.; Peng, T.; Yang, C.; Gao, J.; Yang, C.; Gui, W. Voltage and Current Sensor Fault Diagnosis Method for Traction Converter with Two Stator Current Sensors. *Sensors* **2022**, *22*, 2355. [CrossRef]
112. Kraleti, R.S.; Zawodniok, M.; Jagannathan, S. Model Based Diagnostics and Prognostics of Three-Phase Induction Motor for Vapor Compressor Applications. In Proceedings of the PHM 2012—2012 IEEE Int. Conf. on Prognostics and Health Management: Enhancing Safety, Efficiency, Availability, and Effectiveness of Systems through PHM Technology and Application, Conference Program, Denver, CO, USA, 18–21 June 2012.
113. Hu, W.; Wang, T.; Chu, F. A Novel Ramanujan Digital Twin for Motor Periodic Fault Monitoring and Detection. *IEEE Trans. Ind. Inform.* **2023**. [CrossRef]

114. Silva, L.C.; Dias, C.G.; Alves, W.A.L. A Histogram of Oriented Gradients for Broken Bars Diagnosis in Squirrel Cage Induction Motors. In Proceedings of the Lecture Notes in Computer Science (Including Subseries Lecture Notes in Artificial Intelligence and Lecture Notes in Bioinformatics), Rhodes, Greece, 4–7 October 2018; Volume 11139. LNCS.
115. Dias, C.G.; Da Silva, L.C.; Luz Alves, W.A. A Histogram of Oriented Gradients Approach for Detecting Broken Bars in Squirrel-Cage Induction Motors. *IEEE Trans. Instrum. Meas.* **2020**, *69*, 6968–6981. [CrossRef]
116. Redon, P.; Picazo-Rodenas, M.J.; Antonino-Daviu, J. Processing Tool for Failure Diagnosis Based on Isothermal Representation for Infrared-Based Fault Detection in Induction Motors under Transient State. In Proceedings of the IECON 2017—43rd Annual Conference of the IEEE Industrial Electronics Society, Beijing, China, 29 October–1 November 2017; Volume 2017-January.
117. Freire, N.M.A.; Estima, J.O.; Cardoso, A.J.M. A Voltage-Based Approach without Extra Hardware for Open-Circuit Fault Diagnosis in Closed-Loop PWM AC Regenerative Drives. *IEEE Trans. Ind. Electron.* **2014**, *61*, 4960–4970. [CrossRef]
118. Zhang, X.; Han, K.; Cao, H.; Wang, Z.; Huo, K. Fault Injection Model of Induction Motor for Stator Interturn Fault Diagnosis Research Based on Hils. *World Electr. Veh. J.* **2021**, *12*, 170. [CrossRef]
119. Sapena-Bano, A.; Riera-Guasp, M.; Martinez-Roman, J.; Pineda-Sanchez, M.; Puche-Panadero, R.; Perez-Cruz, J. FEM-Analytical Hybrid Model for Real Time Simulation of IMs under Static Eccentricity Fault. In Proceedings of the 2019 IEEE 12th International Symposium on Diagnostics for Electrical Machines, Power Electronics and Drives, SDEMPED 2019, Toulouse, France, 27–30 August 2019.
120. Prochazka, F.; Krüger, S.; Stomberg, G.; Bauer, M. Development of a Hardware-in-the-Loop Demonstrator for the Validation of Fault-Tolerant Control Methods for a Hybrid UAV. *CEAS Aeronaut. J.* **2021**, *12*, 549–558. [CrossRef]
121. Cevallos, H.; Intriago, G.; Plaza, D. Ensemble Kalman Filter and Particle Filter-Based State Estimation on Electrical Power Systems. *J. Phys. Conf. Ser.* **2021**, *2090*. [CrossRef]
122. Kumar, D.; Jana, D.; Gupta, S.; Yadav, P.K. Bayesian Network Approach for Dragline Reliability Analysis: A Case Study. *Min. Metall. Explor.* **2023**, *40*, 347–365. [CrossRef]
123. Qiao, Z.; Shu, X. Coupled Neurons with Multi-Objective Optimization Benefit Incipient Fault Identification of Machinery. *Chaos Solitons Fractals* **2021**, *145*, 110813. [CrossRef]
124. Kostov, I.; Spasov, V.; Rangelova, V. Application of Genetic Algorithms for Determining the Parameters of Induction Motors. *Teh. Vjesn.* **2009**, *16*, 49–53.
125. Pillay, P.; Nolan, R.; Haque, T. Application of Genetic Algorithms to Motor Parameter Determination for Transient Torque Calculations. *IEEE Trans. Ind. Appl.* **1997**, *33*, 1273–1282. [CrossRef]
126. Allah Bukhsh, Z.; Stipanovic, I.; Doree, A.G. Multi-Year Maintenance Planning Framework Using Multi-Attribute Utility Theory and Genetic Algorithms. *Eur. Transp. Res. Rev.* **2020**, *12*, 1–13. [CrossRef]
127. Ondel, O.; Boutleux, E.; Clerc, G.; Blanco, E. FDI Based on Pattern Recognition Using Kalman Prediction: Application to an Induction Machine. *Eng. Appl. Artif. Intell.* **2008**, *21*, 961–973. [CrossRef]
128. Nair, D.G.; Rasilo, P.; Arkkio, A. Sensitivity Analysis of Inverse Thermal Modeling to Determine Power Losses in Electrical Machines. *IEEE Trans. Magn.* **2018**, *54*, 1–5. [CrossRef]
129. Duan, F.; Živanović, R. Induction Motor Stator Fault Detection by a Condition Monitoring Scheme Based on Parameter Estimation Algorithms. *Electr. Power Compon. Syst.* **2016**, *44*, 1–11. [CrossRef]
130. Martinez-Roman, J.; Puche-Panadero, R.; Sapena-Bano, A.; Terron-Santiago, C.; Burriel-Valencia, J.; Pineda-Sanchez, M. Analytical Model of Induction Machines with Multiple Cage Faults Using the Winding Tensor Approach. *Sensors* **2021**, *21*, 5076. [CrossRef] [PubMed]
131. Lu, S.; He, Q.; Yuan, T.; Kong, F. Online Fault Diagnosis of Motor Bearing via Stochastic-Resonance-Based Adaptive Filter in an Embedded System. *IEEE Trans. Syst. Man Cybern. Syst.* **2017**, *47*, 1111–1122. [CrossRef]
132. Akhil Vinayak, B.; Varma, S.; Jagadanand, G. Precise Wavelet Selection for Condition Monitoring of Inverter-Fed Induction Machine. In Proceedings of the 2017 IEEE International Conference on Signal Processing, Informatics, Communication and Energy Systems, SPICES 2017, Kollam, India, 8–10 August 2017.
133. Zhang, P.; Du, Y.; Habetler, T.G.; Lu, B. A Survey of Condition Monitoring and Protection Methods for Medium-Voltage Induction Motors. *IEEE Trans. Ind. Appl.* **2011**, *47*, 34–46. [CrossRef]
134. Lu, S.; Chai, H.; Sahoo, A.; Phung, B.T. Condition Monitoring Based on Partial Discharge Diagnostics Using Machine Learning Methods: A Comprehensive State-of-the-Art Review. *IEEE Trans. Dielectr. Electr. Insul.* **2020**, *27*, 1861–1888. [CrossRef]
135. Kumar, R.R.; Andriollo, M.; Cirrincione, G.; Cirrincione, M.; Tortella, A. A Comprehensive Review of Conventional and Intelligence-Based Approaches for the Fault Diagnosis and Condition Monitoring of Induction Motors. *Energies* **2022**, *15*, 8938. [CrossRef]
136. Sarma, N.; Mohammed, A.; Melecio, J.I.; Tshiloz, K.; Djurović, S. An Experimental Study of Winding Fault Induced Slot Harmonic Effects in the Cage Rotor Induction Machine Stator Current. In Proceedings of the IET Conference Publications, Glasgow, UK, 19–21 April 2016; Volume 2016.
137. Siddique, A.; Yadava, G.S.; Singh, B. A Review of Stator Fault Monitoring Techniques of Induction Motors. *IEEE Trans. Energy Convers.* **2005**, *20*, 106–114. [CrossRef]

138. Bonnett, A.H. Analysis of Winding Failures in Three-Phase Squirrel Cage Induction Motors. *IEEE Trans. Ind. Appl.* **1978**, *IA-14*, 223–226. [CrossRef]
139. Bonnett, A.H.; Soukup, G.C. Cause and Analysis of Stator and Rotor Failures in Three-Phase Squirrel-Cage Induction Motors. *IEEE Trans. Ind. Appl.* **1992**, *28*, 921–937. [CrossRef]
140. Sarma, N.; Tuohy, P.; Djurović, S. Condition Monitoring of Rotating Electrical Machines. In *Encyclopedia of Electrical and Electronic Power Engineering*; IET: Hongkong, China, 2023.
141. Shukla, A.; Shukla, S.P.; Chacko, S.T.; Mohiddin, M.K.; Fante, K.A. Monitoring of Single-Phase Induction Motor through IoT Using ESP32 Module. *J. Sens.* **2022**, *2022*, 8933442. [CrossRef]
142. Aydin, I.; Karaköse, M.; Akin, E. Artificial Immune Based Support Vector Machine Algorithm for Fault Diagnosis of Induction Motors. In Proceedings of the International Aegean Conference on Electrical Machines and Power Electronics and Electromotion ACEMP'07 and Electromotion'07 Joint Conference, Bodrum, Turkey, 10–12 September 2007.
143. Senthil Kumar, R.; Gerald Christopher Raj, I.; Suresh, K.P.; Leninpugalhanthi, P.; Suresh, M.; Panchal, H.; Meenakumari, R.; Sadasivuni, K.K. A Method for Broken Bar Fault Diagnosis in Three Phase Induction Motor Drive System Using Artificial Neural Networks. *Int. J. Ambient. Energy* **2022**, *43*, 5138–5144. [CrossRef]
144. Jigyasu, R.; Mathew, L.; Sharma, A. Multiple Faults Diagnosis of Induction Motor Using Artificial Neural Network. In Proceedings of the Communications in Computer and Information Science, Lima, Peru, 16–18 November 2019; Volume 955.
145. Gupta, K.; Kaur, A. A Review on Fault Diagnosis of Induction Motor Using Artificial Neural Networks. *Int. J. Sci. Res.* **2012**, *3*, 680–684.
146. Tang, J.; Chen, J.; Dong, K.; Yang, Y.; Lv, H.; Liu, Z. Modeling and Evaluation of Stator and Rotor Faults for Induction Motors. *Energies* **2019**, *13*, 133. [CrossRef]
147. Loiselle, R.; Xu, Z.; Voloh, I. Essential Motor Health Monitoring: Making Informed Decisions about Motor Maintenance before a Failure Occurs. *IEEE Ind. Appl. Mag.* **2018**, *24*, 8–13. [CrossRef]
148. Liang, H.; Chen, Y.; Liang, S.; Wang, C. Fault Detection of Stator Inter-Turn Short-Circuit in Pmsm on Stator Current and Vibration Signal. *Appl. Sci.* **2018**, *8*, 1677. [CrossRef]
149. Jung, J.H.; Lee, J.J.; Kwon, B.H. Online Diagnosis of Induction Motors Using MCSA. *IEEE Trans. Ind. Electron.* **2006**, *53*, 1842–1852. [CrossRef]
150. Prasob, K.; Kumar, N.P.; Isha, T.B. Inter-Turn Short Circuit Fault Analysis of PWM Inverter Fed Three-Phase Induction Motor Using Finite Element Method. In Proceedings of the IEEE International Conference on Circuit, Power and Computing Technologies, ICCPCT 2017, Kollam, India, 20–21 April 2017.
151. Liang, W.; Fei, W.; Luk, P.C.K. Analytical Investigation of Sideband Torque Ripple in Induction Machine Drive with SPWM and SVPWM Techniques. In Proceedings of the 2014 17th International Conference on Electrical Machines and Systems, ICEMS 2014, Hangzhou, China, 22–25 October 2014.
152. Surya, G.N.; Khan, Z.J.; Ballal, M.S.; Suryawanshi, H.M. A Simplified Frequency-Domain Detection of Stator Turn Fault in Squirrel-Cage Induction Motors Using an Observer Coil Technique. *IEEE Trans. Ind. Electron.* **2017**, *64*, 1495–1506. [CrossRef]
153. Kudelina, K.; Raja, H.A.; Autsou, S.; Asad, B.; Vaimann, T.; Rassolkin, A.; Kallaste, A.; Shabbir, N. The Impact of Load on Global Parameters of Electrical Machines in Case of Healthy and Broken Rotor Bars. In Proceedings of the Biennial Baltic Electronics Conference, BEC, Tallinn, Estonia, 4–6 October 2022; Volume 2022.
154. Asad, B.; Vaimann, T.; Belahcen, A.; Kallaste, A.; Rassõlkin, A.; Iqbal, M.N. Broken Rotor Bar Fault Detection of the Grid and Inverter-Fed Induction Motor by Effective Attenuation of the Fundamental Component. *IET Electr. Power Appl.* **2019**, *13*, 2005–2014. [CrossRef]
155. Asad, B.; Vaimann, T.; Belahcen, A.; Kallaste, A.; Rassõlkin, A.; Naveed Iqbal, M. The Cluster Computation-Based Hybrid Fem–Analytical Model of Induction Motor for Fault Diagnostics. *Appl. Sci.* **2020**, *10*, 7572. [CrossRef]
156. Asad, B.; Vaimann, T.; Rassõlkin, A.; Kallaste, A.; Belahcen, A. A Survey of Broken Rotor Bar Fault Diagnostic Methods of Induction Motor. *Electr. Control Commun. Eng.* **2018**, *14*, 117–124. [CrossRef]
157. Naha, A.; Samanta, A.K.; Routray, A.; Deb, A.K. Low Complexity Motor Current Signature Analysis Using Sub-Nyquist Strategy with Reduced Data Length. *IEEE Trans. Instrum. Meas.* **2017**, *66*, 3249–3259. [CrossRef]
158. Malekpour, M.; Phung, B.T.; Ambikairajah, E. Stator Current Envelope Extraction for Analysis of Broken Rotor Bar in Induction Motors. In Proceedings of the 2017 IEEE 11th International Symposium on Diagnostics for Electrical Machines, Power Electronics and Drives, SDEMPED 2017, Tinos, Greece, 29 August–1 September 2017; Volume 2017.
159. Bossio, G.R.; De Angelo, C.H.; Bossio, J.M.; Pezzani, C.M.; García, G.O. Separating Broken Rotor Bars and Load Oscillations on IM Fault Diagnosis through the Instantaneous Active and Reactive Currents. *IEEE Trans. Ind. Electron.* **2009**, *56*, 4571–4580. [CrossRef]
160. Ayhan, B.; Trussell, H.J.; Chow, M.Y.; Song, M.H. On the Use of a Lower Sampling Rate for Broken Rotor Bar Detection with DTFT and AR-Based Spectrum Methods. *IEEE Trans. Ind. Electron.* **2008**, *55*, 1421–1434. [CrossRef]
161. Lizarraga-Morales, R.A.; Rodriguez-Donate, C.; Cabal-Yepez, E.; Lopez-Ramirez, M.; Ledesma-Carrillo, L.M.; Ferrucho-Alvarez, E.R. Novel FPGA-Based Methodology for Early Broken Rotor Bar Detection and Classification through Homogeneity Estimation. *IEEE Trans. Instrum. Meas.* **2017**, *66*, 1760–1769. [CrossRef]
162. Khezzar, A.; Kaikaa, M.Y.; Oumaamar, M.E.K.; Boucherma, M.; Razik, H. On the Use of Slot Harmonics as a Potential Indicator of Rotor Bar Breakage in the Induction Machine. *IEEE Trans. Ind. Electron.* **2009**, *56*, 4592–4605. [CrossRef]

163. Puche-Panadero, R.; Pineda-Sanchez, M.; Riera-Guasp, M.; Roger-Folch, J.; Hurtado-Perez, E.; Perez-Cruz, J. Improved Resolution of the MCSA Method via Hilbert Transform, Enabling the Diagnosis of Rotor Asymmetries at Very Low Slip. *IEEE Trans. Energy Convers.* **2009**, *24*, 52–59. [CrossRef]
164. Sapena-Baño, A.; Pineda-Sanchez, M.; Puche-Panadero, R.; Martinez-Roman, J.; Kanović, Ž. Low-Cost Diagnosis of Rotor Asymmetries in Induction Machines Working at a Very Low Slip Using the Reduced Envelope of the Stator Current. *IEEE Trans. Energy Convers.* **2015**, *30*, 1409–1419. [CrossRef]
165. Supangat, R.; Ertugrul, N.; Soong, W.L.; Gray, D.A.; Hansen, C.; Grieger, J. Detection of Broken Rotor Bars in Induction Motor Using Starting-Current Analysis and Effects of Loading. *IEE Proc. Electr. Power Appl.* **2006**, *153*, 848–855. [CrossRef]
166. Braham, A.; Keskes, H.; Lachiri, Z. Multiclass Support Vector Machines for Diagnosis of Broken Rotor Bar Faults Using Advanced Spectral Descriptors. *Int. Rev. Electr. Eng.* **2010**, *5*, 2095–2105.
167. Bachir, S.; Tnani, S.; Trigeassou, J.C.; Champenois, G. Diagnosis by Parameter Estimation of Stator and Rotor Faults Occurring in Induction Machines. *IEEE Trans. Ind. Electron.* **2006**, *53*, 963–973. [CrossRef]
168. Mirafzal, B.; Demerdash, N.A.O. Effects of Load Magnitude on Diagnosing Broken Bar Faults in Induction Motors Using the Pendulous Oscillation of the Rotor Magnetic Field Orientation. *IEEE Trans. Ind. Appl.* **2005**, *41*, 771–783. [CrossRef]
169. Mirafzal, B.; Demerdash, N.A.O. Induction Machine Broken-Bar Fault Diagnosis Using the Rotor Magnetic Field Space-Vector Orientation. *IEEE Trans. Ind. Appl.* **2004**, *40*, 534–542. [CrossRef]
170. Cusidó, J.; Romeral, L.; Ortega, J.A.; Rosero, J.A.; Espinosa, A.G. Fault Detection in Induction Machines Using Power Spectral Density in Wavelet Decomposition. *IEEE Trans. Ind. Electron.* **2008**, *55*, 633–643. [CrossRef]
171. Hou, Z.; Huang, J.; Liu, H.; Ye, M.; Liu, Z.; Yang, J. Diagnosis of Broken Rotor Bar Fault in Open- and Closed-Loop Controlled Wye-Connected Induction Motors Using Zero-Sequence Voltage. *IET Electr. Power Appl.* **2017**, *11*, 1214–1223. [CrossRef]
172. Sapena-Bañó, A.; Pineda-Sanchez, M.; Puche-Panadero, R.; Martinez-Roman, J.; Matić, D. Fault Diagnosis of Rotating Electrical Machines in Transient Regime Using a Single Stator Current's FFT. *IEEE Trans. Instrum. Meas.* **2015**, *64*, 3137–3146. [CrossRef]
173. Nguyen, N.T.; Lee, H.H. An Application of Support Vector Machines for Induction Motor Fault Diagnosis with Using Genetic Algorithm. In Proceedings of the Lecture Notes in Computer Science (Including Subseries Lecture Notes in Artificial Intelligence and Lecture Notes in Bioinformatics), Rhodes, Greece, 4–7 October 2018; Volume 5227. LNAI.
174. Ghate, V.N.; Dudul, S.V. Cascade Neural-Network-Based Fault Classifier for Three-Phase Induction Motor. *IEEE Trans. Ind. Electron.* **2011**, *58*, 1555–1563. [CrossRef]
175. Gundewar, S.K.; Kane, P.V. Condition Monitoring and Fault Diagnosis of Induction Motor. *J. Vib. Eng. Technol.* **2021**, *9*, 643–674. [CrossRef]
176. Gritli, Y.; Bellini, A.; Rossi, C.; Casadei, D.; Filippetti, F.; Capolino, G.A. Condition Monitoring of Mechanical Faults in Induction Machines from Electrical Signatures: Review of Different Techniques. In Proceedings of the 2017 IEEE 11th International Symposium on Diagnostics for Electrical Machines, Power Electronics and Drives, SDEMPED 2017, Tinos, Greece, 29 August–1 September 2017; Volume 2017.
177. Tiboni, M.; Remino, C.; Bussola, R.; Amici, C. A Review on Vibration-Based Condition Monitoring of Rotating Machinery. *Appl. Sci.* **2022**, *12*, 972. [CrossRef]
178. Khan, M.A.; Asad, B.; Kudelina, K.; Vaimann, T.; Kallaste, A. The Bearing Faults Detection Methods for Electrical Machines—The State of the Art. *Energies* **2023**, *16*, 296. [CrossRef]
179. Kudelina, K.; Asad, B.; Vaimann, T.; Rassõlkin, A.; Kallaste, A.; Van Khang, H. Methods of Condition Monitoring and Fault Detection for Electrical Machines. *Energies* **2021**, *14*, 7459. [CrossRef]
180. Perez-Ramirez, C.A.; Rodriguez, M.V.; Dominguez-Gonzalez, A.; Amezquita-Sanchez, J.P.; Camarena-Martinez, D.; Troncoso, R.J.R. Homogeneity-Based Approach for Bearing Fault Detection in Induction Motors by Means of Vibrations. In Proceedings of the 2017 IEEE International Autumn Meeting on Power, Electronics and Computing, ROPEC 2017, Ixtapa, Mexico, 8–10 November 2017; Volume 2018.
181. Ciszewski, T. Induction Motor Bearings Diagnostic Indicators Based on MCSA and Normalized Triple Covariance. In Proceedings of the 2017 IEEE 11th International Symposium on Diagnostics for Electrical Machines, Power Electronics and Drives, SDEMPED 2017, Tinos, Greece, 29 August–1 September 2017; Volume 2017.
182. Zhang, B.; Miao, Y.; Lin, J.; Yi, Y. Adaptive Maximum Second-Order Cyclostationarity Blind Deconvolution and Its Application for Locomotive Bearing Fault Diagnosis. *Mech. Syst. Signal Process.* **2021**, *158*, 107736. [CrossRef]
183. Gong, X.; Qiao, W. Current-Based Online Bearing Fault Diagnosis for Direct-Drive Wind Turbines via Spectrum Analysis and Impulse Detection. In Proceedings of the PEMWA 2012—2012 IEEE Power Electronics and Machines in Wind Applications, Denver, CO, USA, 16–18 July 2012.
184. Zanini, R.A.A.; Freitas, T.; Silva, L.N.; Gutierres, A.; Santos, G. *Evaluation of the Method of Failure Analysis in Angular Contact Bearings through the Envelope Technique*; SAE Technical Papers; SAE: London, UK, 2012.
185. Dalvand, F.; Kalantar, A.; Safizadeh, M.S. A Novel Bearing Condition Monitoring Method in Induction Motors Based on Instantaneous Frequency of Motor Voltage. *IEEE Trans. Ind. Electron.* **2016**, *63*, 364–376. [CrossRef]
186. Kudelina, K.; Baraškova, T.; Shirokova, V.; Vaimann, T.; Rassõlkin, A. Fault Detecting Accuracy of Mechanical Damages in Rolling Bearings. *Machines* **2022**, *10*, 86. [CrossRef]

187. Tischmacher, H. Bearing Wear Condition Identification on Converter-Fed Motors. In Proceedings of the SPEEDAM 2018—Proceedings: International Symposium on Power Electronics, Electrical Drives, Automation and Motion, Amalfi, Italy, 20–22 June 2018.
188. Xie, S.; Wang, X.; Qu, C.; Wang, X.; Guo, J. Impacts of Different Wind Speed Simulation Methods on Conditional Reliability Indices. *Int. Trans. Electr. Energy Syst.* **2013**, *20*, 1–6. [CrossRef]
189. Polat, A.; Ertuğrul, Y.D.; Ergene, L.T. Static, Dynamic and Mixed Eccentricity of Induction Motor. In Proceedings of the SDEMPED 2015: IEEE 10th International Symposium on Diagnostics for Electrical Machines, Power Electronics and Drives, Guarda, Portugal, 1–4 September 2015.
190. Sheikh, M.A.; Bakhsh, S.T.; Irfan, M.; Nor, N.B.M.; Nowakowski, G. A Review to Diagnose Faults Related to Three-Phase Industrial Induction Motors. *J. Fail. Anal. Prev.* **2022**, *22*, 1546–1557. [CrossRef]
191. Milkovic, D. Brief Review of Motor Current Signature Analysis. *HDKBR INFO Mag.* **2015**, *5*, 14–26.
192. Liu, Z.; Zhang, P.; He, S.; Huang, J. A Review of Modeling and Diagnostic Techniques for Eccentricity Fault in Electric Machines. *Energies* **2021**, *14*, 4296. [CrossRef]
193. Li, H.; Zou, Z.; Sun, X.; Gu, F.; Ball, A.D. A Numerical Study of Rotor Eccentricity and Dynamic Load in Induction Machines for Motor Current Analysis Based Diagnostics. *Maint. Reliab. Cond. Monit.* **2021**, *1*, 71–86. [CrossRef]
194. Dorrell, D.G.; Thomson, W.T.; Roach, S. Analysis of Airgap Flux, Current and Vibration Signals as a Function of the Combination of Static and Dynamic Airgap Eccentricity in 3-Phase Induction Motors. *IEEE Trans. Ind. Appl.* **1995**, *33*, 24–34. [CrossRef]
195. Jover Rodríguez, P.V.; Belahcen, A.; Arkkio, A.; Laiho, A.; Antonino-Daviu, J.A. Air-Gap Force Distribution and Vibration Pattern of Induction Motors under Dynamic Eccentricity. *Electr. Eng.* **2008**, *90*, 209–218. [CrossRef]
196. Metatla, A.; Benzahioul, S.; Bahi, T.; Lefebvre, D. Eccentricity Fault Monitoring by Analysis Stator Phase Currents. *Int. Rev. Model. Simul.* **2010**, *3*, 533–537.
197. Zhou, Y.; Bao, X.; Di, C.; Wang, L. Analysis of Dynamic Unbalanced Magnetic Pull in Induction Motor with Dynamic Eccentricity during Starting Period. *IEEE Trans. Magn.* **2016**, *52*, 1–4. [CrossRef]
198. Toliyat, H.A.; Levi, E.; Raina, M. A Review of RFO Induction Motor Parameter Estimation Techniques. *IEEE Power Eng. Rev.* **2002**, *22*, 52. [CrossRef]
199. Georgoulas, G.; Climente-Alarcon, V.; Antonino-Daviu, J.A.; Stylios, C.D.; Arkkio, A.; Nikolakopoulos, G. A Multi-Label Classification Approach for the Detection of Broken Bars and Mixed Eccentricity Faults Using the Start-up Transient. In Proceedings of the IEEE International Conference on Industrial Informatics (INDIN), Poitiers, France, 19–21 July 2016.
200. Lv, Q.; Bao, X.; He, Y.; Fang, Y.; Cheng, X. Inductances Evaluation of a Squirrel-Cage Induction Motor with Curved Dynamic Eccentricity. *J. Electr. Eng. Technol.* **2014**, *9*, 1623–1631. [CrossRef]
201. Yang, Z.; Sun, C.; Sun, X.; Sun, Y. An Improved Dynamic Model for Bearingless Induction Motor Considering Rotor Eccentricity and Load Change. *IEEE Trans. Ind. Electron.* **2022**, *69*, 3439–3448. [CrossRef]
202. Chen, S.; Lipo, T.A. Circulating Type Motor Bearing Current in Inverter Drives. *IEEE Ind. Appl. Mag.* **1998**, *4*, 32–38. [CrossRef]
203. Cheng, Y.; Sun, Y.; Li, X.; Dan, H.; Lin, J.; Su, M. Active Common-Mode Voltage-Based Open-Switch Fault Diagnosis of Inverters in IM-Drive Systems. *IEEE Trans. Ind. Electron.* **2021**, *68*, 103–115. [CrossRef]
204. Naik, R.; Nondahl, T.A.; Melfi, M.J.; Schiferl, R.; Wang, J.S. Distributed Parameter Circuit Model for Shaft Voltage Prediction in Induction Motors Fed by PWM Based Ac Drives. *IEEE Ind. Appl. Soc.* **2001**, *2*, 1118–1122. [CrossRef]
205. Muetze, A.; Binder, A. Calculation of Circulating Bearing Currents in Machines of Inverter-Based Drive Systems. *IEEE Trans. Ind. Electron.* **2007**, *54*, 932–938. [CrossRef]
206. Kindl, V.; Skala, B.; Pechanek, R.; Byrtus, M.; Hruska, K. Calculation of Induction Machine Parasitic Capacitances Using Finite Element Method. In Proceedings of the ELEKTRO 2016—11th International Conference, Kuala Lumpur, Malaysia, 2–3 June 2016.
207. Liu, Y.; Cao, J.; Song, Y.; Xu, G.; Li, L. Research on Bearing Current Detection Method of High-Speed Motor Driven by PWM Inverter. In Proceedings of the 2019 22nd International Conference on Electrical Machines and Systems, ICEMS 2019, Harbin, China, 11–14 August 2019.
208. Bubert, A.; Zhang, J.; De Doncker, R.W. Modeling and Measurement of Capacitive and Inductive Bearing Current in Electrical Machines. In Proceedings of the 14th Brazilian Power Electronics Conference, COBEP 2017, Juiz de Fora, Brazil, 19–22 November 2017; Volume 2018.
209. Jaeger, C.; Grinbaum, I.; Smajic, J. Numerical Simulation and Measurement of Common-Mode and Circulating Bearing Currents. In Proceedings of the 2016 22nd International Conference on Electrical Machines, ICEM 2016, Lausanne, Switzerland, 4–7 September 2016.
210. Êvo, M.T.A.; De Paula, H. Electrostatic Shielding for Bearings Discharge Currents Attenuation: Analysis of Its Effectiveness, Losses and Impact on the Motor Performance—A Study for Design Guidelines. *IET Electr. Power Appl.* **2020**, *14*, 1050–1059. [CrossRef]
211. Arora, T.G.; Renge, M.M.; Aware, M.V. Effects of Switching Frequency and Motor Speed on Common Mode Voltage, Common Mode Current and Shaft Voltage in PWM Inverter-Fed Induction Motors. In Proceedings of the 2017 12th IEEE Conference on Industrial Electronics and Applications, ICIEA 2017, Siem Reap, Cambodia, 18–20 June 2017; Volume 2018.
212. Schiferl, R.F.; Melfi, M.J. Bearing Current Remediation Options: Sources, Investigative Measurements, and Installation Modifications to Reduce Damage as a Result of Bearing Currents. *IEEE Ind. Appl. Mag.* **2004**, *10*, 40–50. [CrossRef]

213. Elsayed, N.B.; Ibrahim, M.E.; Izzularab, M.A. Mitigation of Overvoltages at Induction Motor Terminals Fed from an Inverter through Long Cable. In Proceedings of the 2018 20th International Middle East Power Systems Conference, MEPCON 2018, Cairo, Egypt, 18–20 December 2018.
214. Plazenet, T.; Boileau, T.; Caironi, C.; Nahid-Mobarakeh, B. An Overview of Shaft Voltages and Bearing Currents in Rotating Machines. In Proceedings of the IEEE Industry Application Society, 52nd Annual Meeting: IAS 2016, Portland, OR, USA, 2–6 October 2016.
215. Ferreira, F.J.T.E.; Cistelecan, M.V.; De Almeida, A.T. Evaluation of Slot-Embedded Partial Electrostatic Shield for High-Frequency Bearing Current Mitigation in Inverter-Fed Induction Motors. *IEEE Trans. Energy Convers.* **2012**, *27*, 382–390. [CrossRef]
216. Zhao, Z.; Zhong, Y.; Gao, H.; Yuan, L.; Lu, T. Hybrid Selective Harmonic Elimination PWM for Common-Mode Voltage Reduction in Three-Level Neutral-Point-Clamped Inverters for Variable Speed Induction Drives. *IEEE Trans. Power Electron.* **2011**, *27*, 1152–1158. [CrossRef]
217. De Broe, A.M.; Julian, A.L.; Lipo, T.A. Neutral-to-Ground Voltage Minimization in a Pwm-Rectifier/Inverter Configuration. *Electr. Mach. Power Syst.* **1998**, *26*, 741–748. [CrossRef]
218. Xiang, Y.Q. Novel Active Common-Mode-Voltage Compensator (ACCom) for Bearing Current Reduction of PWM VSI-Fed Induction Motors. In Proceedings of the IEEE Applied Power Electronics Conference and Exposition—APEC, Anaheim, CA, USA, 15–19 February 1998; Volume 2.
219. Robles, E.; Fernandez, M.; Andreu, J.; Ibarra, E.; Zaragoza, J.; Ugalde, U. Common-Mode Voltage Mitigation in Multiphase Electric Motor Drive Systems. *Renew. Sustain. Energy Rev.* **2022**, *157*, 111971. [CrossRef]
220. Von Jouanne, A.; Zhang, H. A Dual-Bridge Inverter Approach to Eliminating Common-Mode Voltages and Bearing and Leakage Currents. *IEEE Trans. Power Electron.* **1999**, *14*, 43–48. [CrossRef]
221. Rajeevan, P.P.; Gopakumar, K. A Hybrid Five-Level Inverter with Common-Mode Voltage Elimination Having Single Voltage Source for Im Drive Applications. *IEEE Trans. Ind. Appl.* **2012**, *48*, 2037–2047. [CrossRef]
222. Ogasawara, S.; Zhang, S.; Akagi, H. Configurations and Characteristics of Active Canceling and Compensating Circuits for Reducing Common-Mode Voltage Generated by Voltage-Source Pwm Inverters. *Electr. Eng. Jpn.* **2001**, *137*, 57–65. [CrossRef]
223. Ogasawara, S.; Ayano, H.; Akagi, H. An Active Circuit for Cancellation of Common-Mode Voltage Generated by a PWM Inverter. *IEEE Trans. Power Electron.* **1998**, *13*, 835–841. [CrossRef]
224. Bartolucci, E.J.; Finke, B.H. Cable Design for PWM Variable-Speed AC Drives. *IEEE Trans. Ind. Appl.* **2001**, *37*, 415–422. [CrossRef]
225. Muetze, A.; Binder, A. Experimental Evaluation of Mitigation Techniques for Bearing Currents in Inverter-Supplied Drive-Systems—Investigations on Induction Motors up to 500 KW. In Proceedings of the IEMDC 2003—IEEE International Electric Machines and Drives Conference, Madison, WI, USA, 1–4 June 2003; Volume 3.
226. Muetze, A.; Oh, H.W. Current-Carrying Characteristics of Conductive Microfiber Electrical Contact for High Frequencies and Current Amplitudes: Theory and Applications. *IEEE Trans. Power Electron.* **2010**, *25*, 2082–2092. [CrossRef]
227. Yea, M.; Han, K.J. Modified Slot Opening for Reducing Shaft-to-Frame Voltage of AC Motors. *Energies* **2020**, *13*, 760. [CrossRef]
228. Gerada, D.; Mebarki, A.; Brown, N.L.; Gerada, C.; Cavagnino, A.; Boglietti, A. High-Speed Electrical Machines: Technologies, Trends, and Developments. *IEEE Trans. Ind. Electron.* **2013**, *61*, 2946–2959. [CrossRef]
229. Liu, X.; Wu, G.; Tong, L.; Lin, T.; Zhang, G. Influence of Impulse Frequency on Partial Discharge under PWM. In Proceedings of the IEEE International Symposium on Electrical Insulation, Toronto, ON, Canada, 11–14 June 2007; Volume 2007.
230. Cui, Q.; Weng, Y. Mining Partially Labeled Data from Edge Devices to Detect and Locate High Impedance Faults. In Proceedings of the iSPEC 2019—2019 IEEE Sustainable Power and Energy Conference: Grid Modernization for Energy Revolution, Beijing, China, 21–23 November 2019.
231. Cavallini, A.; Montanari, G.C.; Fabiani, D.; Tozzi, M. The Influence of PWM Voltage Waveforms on Induction Motor Insulation Systems: Perspectives for the End User. In Proceedings of the SDEMPED 2011—8th IEEE Symposium on Diagnostics for Electrical Machines, Power Electronics and Drives, Bologna, Italy, 5–8 September 2011.
232. Haq, S.U.; Jayaram, S.H.; Cherney, E.A. Insulation Problems in Medium-Voltage Stator Coils under Fast Repetitive Voltage Pulses. *IEEE Trans. Ind. Appl.* **2008**, *44*, 1004–1012. [CrossRef]
233. Kang, T.J.; Hong, J.; Lee, S.B.; Yoon, Y.W.; Hwang, D.H.; Kang, D. The Influence of the Rotor on Surge Pd Testing of Low Voltage AC Motor Stator Windings. *IEEE Trans. Dielectr. Electr. Insul.* **2013**, *20*, 762–769. [CrossRef]
234. Tanaka, T. Internal Partial Discharge and Material Degradation. *IEEE Trans. Electr. Insul.* **1986**, *EI-21*, 899–905. [CrossRef]
235. Montanari, G.C. Bringing an Insulation to Failure: The Role of Space Charge. *IEEE Trans. Dielectr. Electr. Insul.* **2011**, *18*, 339–364. [CrossRef]
236. D'Amato, D.; Loncarski, J.; Monopoli, V.G.; Cupertino, F.; Di Noia, L.P.; Del Pizzo, A. Impact of PWM Voltage Waveforms in High-Speed Drives: A Survey on High-Frequency Motor Models and Partial Discharge Phenomenon. *Energies* **2022**, *15*, 1406. [CrossRef]
237. Wang, W. An Intelligent System for Machinery Condition Monitoring. *IEEE Trans. Fuzzy Syst.* **2008**, *16*, 110–122. [CrossRef]
238. Russell, B.D.; Benner, C.L. Intelligent Systems for Improved Reliability and Failure Diagnosis in Distribution Systems. *IEEE Trans. Smart Grid* **2010**, *1*, 48–56. [CrossRef]
239. Garcia-Bracamonte, J.E.; Ramirez-Cortes, J.M.; De Jesus Rangel-Magdaleno, J.; Gomez-Gil, P.; Peregrina-Barreto, H.; Alarcon-Aquino, V. An Approach on MCSA-Based Fault Detection Using Independent Component Analysis and Neural Networks. *IEEE Trans. Instrum. Meas.* **2019**, *68*, 1353–1361. [CrossRef]

240. Widodo, A.; Yang, B.S. Wavelet Support Vector Machine for Induction Machine Fault Diagnosis Based on Transient Current Signal. *Expert Syst. Appl.* **2008**, *35*, 307–316. [CrossRef]
241. Niu, G.; Widodo, A.; Son, J.D.; Yang, B.S.; Hwang, D.H.; Kang, D.S. Decision-Level Fusion Based on Wavelet Decomposition for Induction Motor Fault Diagnosis Using Transient Current Signal. *Expert Syst. Appl.* **2008**, *35*, 918–928. [CrossRef]

Disclaimer/Publisher's Note: The statements, opinions and data contained in all publications are solely those of the individual author(s) and contributor(s) and not of MDPI and/or the editor(s). MDPI and/or the editor(s) disclaim responsibility for any injury to people or property resulting from any ideas, methods, instructions or products referred to in the content.

Appendix 2

Publication II

M. U. Sardar, T. Vaimann, L. Kütt, B. Asad, A. Kallaste and K. Kudelina, "Characterization of High-Frequency Impedance-Based Models for Transient Terminal Overvoltage Estimation in Cable-Fed Motor Drive Systems," 2024 International Conference on Electrical Machines (ICEM), Torino, Italy, 2024, pp. 1-7, doi: 10.1109/ICEM60801.2024.10700495.

Characterization of High-Frequency Impedance-Based Models for Transient Terminal Overvoltage Estimation in Cable-Fed Motor Drive Systems

Muhammad Usman Sardar
Department of Electrical Power Engineering and Mechatronics
Tallinn University of Technology
Tallinn, 19086 Tallinn
muhammad.sardar@taltech.ee

Toomas Vaimann
Department of Electrical Power Engineering and Mechatronics
Tallinn University of Technology
Tallinn 19086, Tallinn
toomas.vaimann@taltech.ee

Lauri Kütt
Department of Electrical Power Engineering and Mechatronics
Tallinn University of Technology
Tallinn 19086, Tallinn
lauri.kutt@taltech.ee

Bilal Asad
Department of Electrical Power Engineering and Mechatronics
Tallinn University of Technology
Tallinn 19086, Tallinn
bilal.asad@taltech.ee

Ants Kallaste
Department of Electrical Power Engineering and Mechatronics
Tallinn University of Technology
Tallinn 19086, Tallinn
ants.kallaste@taltech.ee

Karolina Kudelina
Department of Electrical Power Engineering and Mechatronics
Tallinn University of Technology
Tallinn 19086, Tallinn
karolina.kudelina@taltech.ee

2024 International Conference on Electrical Machines (ICEM) | 979-8-3503-7060-7/24/$31.00 ©2024 IEEE | DOI: 10.1109/ICEM60801.2024.10700495

***Abstract*— High-frequency parametric modeling of cable-fed induction machines is essential in investigating issues such as estimating terminal transient overvoltage and electromagnetic interference problems. Characterizing high-frequency impedance parametric models requires accurate and practical measurements of cable and motor in differential mode and common-mode coupling connections in a wideband frequency range of up to 120 MHz. In this paper, a measurement setup is presented and applied to have reproducible tests to measure impedance parameters of the induction motor and cable. Differential mode and common mode coupling tests in wider frequency range are performed and comprehensive circuit-based models (CBM) are proposed to characterize the cable-fed drive system. These comprehensive and extendable models have been matched with an experimental drive setup using a 7.5 kW induction motor fed with power cable. This parametric modeling framework effectively matches the motor's transient terminal overvoltage phenomena, exhibiting strong agreement with practical measurement results and comparable significant improvement over the conventional model.**

***Keywords*— circuit modeling, frequency-domain analysis, impedance measurement, induction motors, motor drives**

I. Introduction

The digitalization of the industrial sector and the Industrial Revolution in power electronic based inverter-machine drive systems have significantly progressed technological fields, including electrical machine diagnostics, operation, and machine condition monitoring [1], [2], [3].The semiconductor's switching transients in inverters generates pulse voltages with steep fronts, leading to transient wave propagation phenomena in motor drive systems connected to supply cables [4], [5]. Transient overvoltage (TOV) ringing on the motor terminals which is also called reflected wave phenomena (RWP) results from an imbalance between the cable characteristic impedance and the surge impedance of the motor [6]. Overvoltage reflected wave spikes of two oven three times of input DC-bus voltage causes early breakdown and accelerating the deterioration of bearings and winding insulation health [7], [8]. It is crucial for accurately estimating overvoltage ringing in the induction machine (IM) by modeling it for high frequency (HF) ranges with the influence of power cable impedance. RLC equivalent circuit models, derived from analytical calculations and verified experimentally by impedance measurements, can be used to construct HF models for machines and power-feeding cables [9]. Likewise, In [10], numerous HF machine models were proposed to depict frequency-dependent impedance responses using a lumped parameter equivalent winding circuit model by considering its HF characteristics.

The induction motor RLC circuit-based model (CBM) characterizes the motor's behaviour at various frequencies (from low to high frequency) to estimate the TOV with the impact of cable, which is the main contribution of this paper. To improve the accuracy and extendibility in wider frequency range, models are developed by incorporating the low frequency (LF) parameters and HF impedance lumped parameters for the motor and cable identified from the curve fitting equations.

The main contributions of this research are summarized as follows:

1. CBM utilizes a comprehensive and computationally efficient parametric identification of induction motor and cable to examine their impedance behavior in wideband frequency and extendable for typical length of the cable.
2. Impedance parameters are initially identified from the practical measurement setup using impedance analyzer 20 Hz-120 MHz, 7.5 kW 6-lead induction motor in Y-connection and Drakaflex H07RN-F 450/750 V 5G6 cable. These parameters are realized to fit into the proposed CBM models accordingly.
3. CBMs are validated experimentally using a 30-kW inverter drive system and compared with conventional models as in section V, which shows their validity and significant improvements in the estimation of TOV or RWP.

Section II outlines CBM models and section III describes the motor and power cable practical measurement setup and their impedance parameter identification. Section IV demonstrates

Authorized licensed use limited to: Tallinn University of Technology. Downloaded on February 04,2026 at 11:45:46 UTC from IEEE Xplore. Restrictions apply.

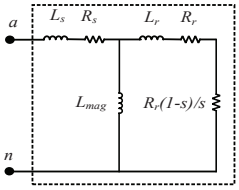
the development procedures and validations, section V presents the acquired results in time domain estimation, and section VI concludes the paper.

II. Proposed HF Circuit Based Models (CBM)

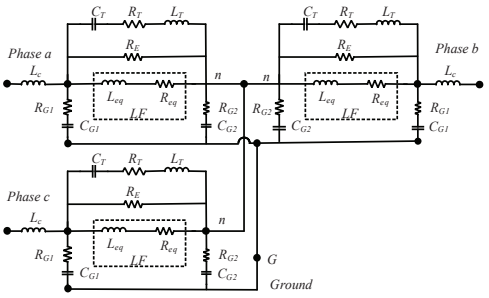
A. Induction Motor Proposed CBM

The low-frequency circuit model of the induction motor was initially used with its equivalent inductance and resistance circuit values as shown in Fig. 1 (a). However, this model is not capable of high-frequency response modelling and analysis. The proposed IM HF CBM schematic is shown in Fig. 1 (b) deals with the LF response of machine as well as factors such as turn-to-turn resistance and inductance, eddy currents, and parasitic capacitances. Two primary branches are considered: stator winding to motor frame and turn-to-turn winding.

The proposed CBM design considers the lumped equivalent circuit values of LF parameters and HF impedance response for the actual motor characterization and further analysis. L_s, R_s, L_r and R_r are stator and rotor inductance and resistances respectively, whereas L_{mag} shows magnetizing inductance. These parameters are calculated from the preliminary no load and blocked rotor motor's tests. C_T, R_T, and L_T represent the skin effect for HF response phenomenon. R_E represents eddy current resistance. L_{eq} and R_{eq} represent equivalent winding leakage inductances and resistance which are calculated from LF IM circuit model as shown in Fig. 1 (a). R_{G1} and C_{G1} are terminal side parasitic ground resistance and capacitance, R_{G2} and C_{G2} are parasitic resistance and capacitance from the neutral side respectively. L_c displays motor internal winding's inductance at phase start.



(a)



(b)

Fig. 1. Per-phase motor winding model (a) *LF* IM winding impedance circuit model [11] (b) RLC circuit-based model (CBM) of induction motor including LF equivalent parameters and HF machine parameters.

C_T, R_T, and L_T are responsible for 2nd resonance and are inevitable due to the capacitances of inter-turn stator windings and the skinning effect.

B. Power Cable Proposed CBM

Based on the transmission line modelling (Pi-TLM) approach for power feeding cable [6], an improved and comprehended circuit-based models (CBM) of cable is proposed as depicted in Fig. 2. CBM shows per section standard DM schematics in which its parameters are calculated based on the short circuit (SC) and open circuit (OC) modes with phase *a* and other *b* and *c* are short-circuited (named as *b*+*c*).

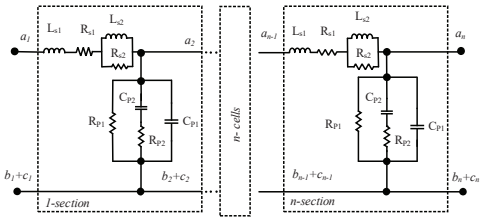


Fig. 2. A n-section cable CBM model based on transmission line modelling for a unit length of cable.

Ten series sections are proposed to make one meter/unit length and further by assuming number of units per total length of the cable are demonstrated for a particular length of cable and their transfer function is formulated to analyzed.

Here, the parameters L_s and R_s are associated with SC impedance behavior. L_p and R_p show the parallel inductance and resistance considered in OC. L_{s1}, R_{s1} and L_{s2}, R_{s2} include skin and proximity effects in series, C_{p1} and R_{p1} shows the dielectric losses in parallel branches as associated criteria for HF phenomena for resonance in higher orders.

III. Impedance Measurement Practical Setup

To ensure reliable and reproducible measurement, a custom aluminum (*Al*) frame box with a BNC connector array is provided to interface instrument inputs. Connections points include motor phase terminals and frame ground connections as depicted in Fig. 3 below. Initially, the motor windings terminals are connected in star and 10 mm thickness copper strips are used for the inside connections.

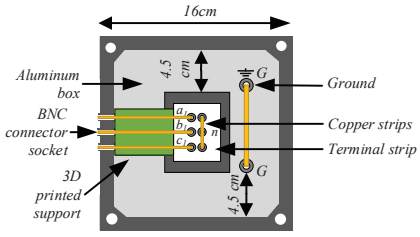


Fig. 3. Standard measurement box for motor connection interface.

Authorized licensed use limited to: Tallinn University of Technology. Downloaded on February 04,2026 at 11:45:46 UTC from IEEE Xplore. Restrictions apply.

A. Machine Impedance Measurement Tests

Induction motor with six terminals, 7.5 kW, 400Y/230Δ is used in test. Two fundamental modes, common mode (CM) and differential mode (CM), are performed on IM in star (Y) connection to identify the HF CBM parameters in the motor. The cable and induction motor are tested with impedance analyzer which is shown in Fig. 4 below.

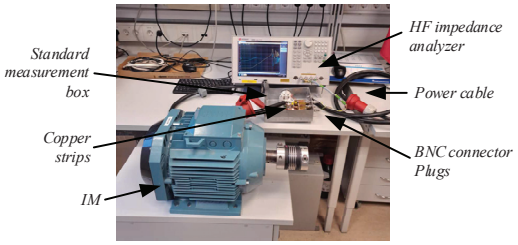
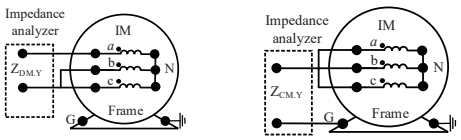


Fig. 4. Measurement setup for motor and cable high frequency impedance parameters using high frequency impedance

Fig. 5 (a) demonstrates the DM impedance measurement test implementation conducted between phase 'a' and the remaining two short-circuited phases (named as '*b*' + '*c*'). During the CM test, all three phases are connected in a short-circuit configuration (named as '*a*'+'*b*'+'*c*'), and the motor is in star connection scheme. The CM impedance measurement test is determined by measuring the impedance between the machine's combined input terminals and ground frame terminal, as illustrated in Fig. 5 (b).



(a) (b)

Fig. 5. Experimental connection schematics (a) differential mode (DM) (b) common mode (CM).

Equations (1)-(9) are utilized to compute the model parameters; these equations are based on the asymptotic tracing equation [12], [13]. The stator winding resistance (R_{eq}) limits the phase current of the motor and computed by the LF circuit model as shown in Fig. 1. C_{HF} is the total capacitance in HF region of CM model and calculated from the equation (1) below.

$$C_{HF} = \frac{1}{2\pi f_{HF} Z_{HF.CM}} \tag{1}$$

C_{G1} is terminal side parasitic ground resistance and capacitance C_{SUM} is the total LF common mode capacitance calculated from the equation (2) as given below.

$$C_{SUM} = \frac{1}{2\pi f_{LF} Z_{LF.CM}} \tag{2}$$

$$C_{G1} = \frac{1}{3} C_{HF}, C_{G2} = \frac{1}{3}(C_{SUM} - C_{HF}) \tag{3}$$

$$R_{G1} = \frac{2}{3}|Z_3|, R_{G2} \approx \frac{1}{3}|Z_1| \tag{4}$$

The high-frequency iron loss resistance R_E is estimated from the f_4 frequency-impedance points as follows.

$$R_E = \frac{2}{3}|Z_4| \tag{5}$$

$$C_T \approx \frac{1}{10}(C_{G1} + C_{G2}), L_T \approx \frac{1}{C_T}\left(\frac{1}{2\pi f_2^2}\right)^2 \tag{6}$$

$$R_T = |Z_2|\cos(\theta_2) \tag{7}$$

$$L_{CM} = \frac{1}{12\pi^2 C_{G2} f_1^2}, L_{DM} = \frac{|Z_{DM.LF}|}{2\pi f_{LF}} \sin(\theta_{DM.LF}) \tag{8}$$

The combined stator leakage inductance L_{eq} is obtained from LF IM winding impedance circuit model Fig. 1 (a).

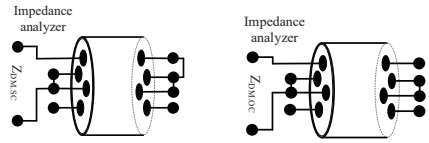
$$L_C = \frac{3}{16\pi^2 C_{G1} f_3^2} \tag{9}$$

The high-frequency model parameters for the considered 7.5 kW IM are tabulated in Table I.

B. Cable Impedance Measurement Tests

For the practical measurement, H07RN-F 450/750 V cable (*5G6*) with five conductors each with a cross-sectional area of 6mm^2 is used for impedance measurement as shown in Fig. 4.

Phase '*a*' and the two short-circuited phases ('*b*'+'*c*') are employed in differential mode in SC and OC schematics which are shown in Fig. 6 below.



(a) (b)

Fig. 6. Differential mode power feeding cable schematics (a) short circuit (SC) mode (b) open circuit (OC) mode.

Similarly, equations (10)-(15) below are used to calculate the cable HF model parameters from the direct measured SC and OC characteristics using the practical setup [13], [14].

$$L_{s1} = L_{SC-HF} = \frac{Z_{sc}}{2\pi f_{HF}}, L_{s2} = L_{SC-LF} - L_{s1} \tag{10}$$

$$R_{s1} = |Z_{SC-LF}|\cos(\theta_{SC-LF}) \tag{11}$$

$$R_{s2} = |Z_{SC-HF}|\cos(\theta_{SC-HF}) - R_{s1} \tag{12}$$

Open circuit capacitance at high frequency and low frequency are calculated from the corresponding frequency and impedance experimental values as specified in equation (13)-(15). These parallel branches are responsible for characterizing the dielectric losses and leakage current in insulation of cable.

Authorized licensed use limited to: Tallinn University of Technology. Downloaded on February 04,2026 at 11:45:46 UTC from IEEE Xplore. Restrictions apply.

$$C_{p1} = C_{OC-HF}, C_{p2} = C_{OC-LF} - C_{p1} \quad (13)$$

$$R_{p1} = \frac{|Z_{OC-LF}|}{\cos(\theta_{OC-LF})}, R_{p1\square p2} = \frac{|Z_{OC-HF}|}{\cos(\theta_{OC-HF})} \quad (14)$$

$$R_{p2} = \left[\frac{1}{R_{p1\square p2}} - \frac{1}{R_{p1}}\right]^{-1} \quad (15)$$

The high frequency model parameters for the available power cable are extracted according to above equations and are presented in Table II.

IV. Development Procedure and Validation

The overall CBM characterization and parameter identification procedure is comprehended in Fig. 7 below and simulation is carried out using the PSIM® computer software tool. The numerical calculations assume values from the fitting method are used to identify the parameters.

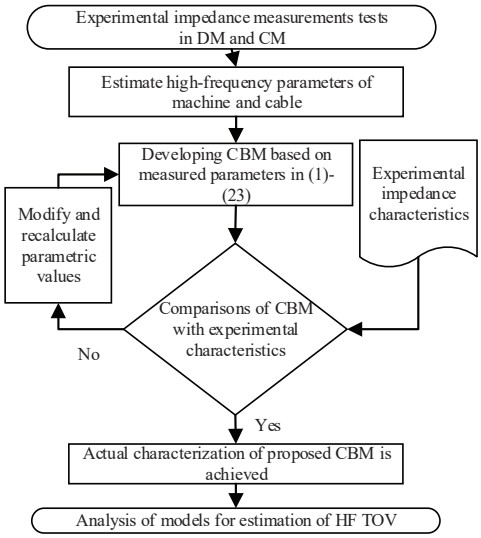


Fig. 7. Flowchart for high frequency characterization of proposed circuit-based models for cable-fed inverter drive system.

A. Motor CBM Parameters Identification

Fig. 8 and 9 compares the impedance response of the motor obtained from experiments and estimated by the CBM model. The comparison covers a wide frequency range, starting from 12 Hz and extending up to 120 MHz. $Z_{DM.LF}$ $\angle\theta_{LF}$ represent DM impedance (Ω) at the lower frequency and phase angle (*degree*) and, similarly $Z_{CM.LF}$ $\angle\theta_{LF}$ represent CM impedance at the starting frequency (Ω) and corresponding phase angle (*degree*).

Frequency points f_1, f_2, f_3, and f_4 are resonant frequency points showing the 1st resonant zero frequency in CM, 1st resonant zero frequency point in DM, 2nd resonant zero frequency point in DM and 1st resonant pole frequency point in DM respectively. The wideband frequency points and their associated impedance magnitudes are used to characterize the proposed CBM. L_{DM} is extracted from measured DM impedance characteristics. The parameters of the proposed CBM for the machine are obtained using equations (1)-(15) and are listed in Table I.

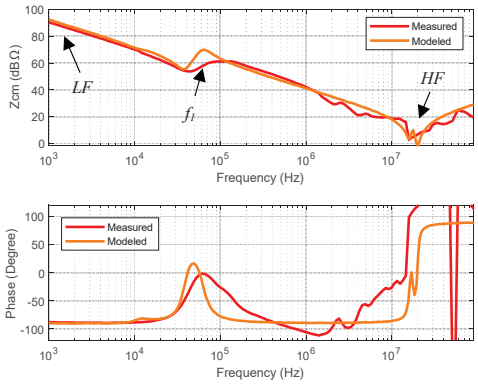


Fig. 8. Comparison between experimental and simulation result of proposed CBM model of motor in common mode-CM.

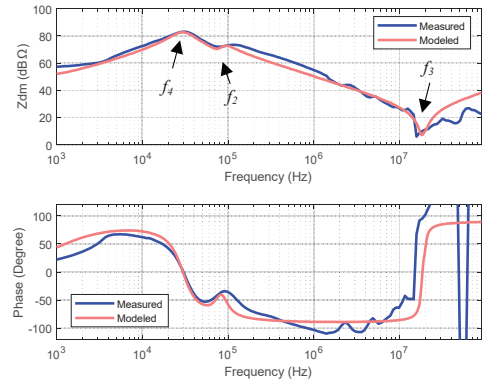


Fig. 9. Comparison between experimental and simulation result of proposed CBM model of motor in differential mode-DM.

TABLE I. 7.5 KW IM HF MACHINE PARAMETERS

Parameters	Values	Parameters	Values
R_{eq} (Ω)	0.56	L_T (mH)	24.16
C_{G1} (pF)	601	R_T (kΩ)	2.69
C_{G2} (pF)	1112	L_{DM} (mH)	28.80
R_{G1} (Ω)	1.34	L_{CM} (mH)	4.30
R_{G2} (Ω)	325	L_{eq} (mH)	2.40
R_E (kΩ)	6.62	L_c (nH)	126.73
C_T (pF)	171		

B. Cable CBM Parameters Identification

In DM, cable parameter calculation is carried out using OC and SC modes in pratical setup and rebuilt with the impedance frequency response by the CBM and matching of measured and modeled are shown in Fig. 10 and 11.

Authorized licensed use limited to: Tallinn University of Technology. Downloaded on February 04,2026 at 11:45:46 UTC from IEEE Xplore. Restrictions apply.

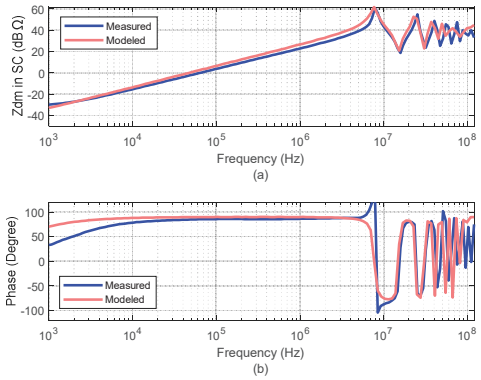


Fig. 10. Measured and proposed impedance magnitude and phase of cable in SC.

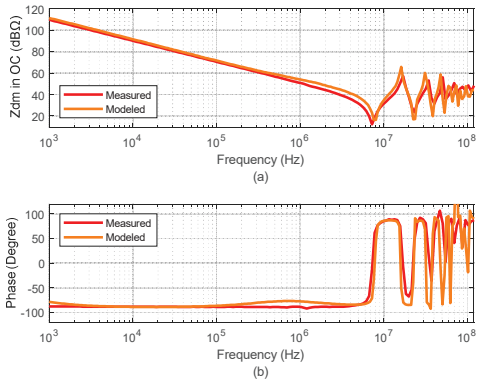


Fig. 11. Measured and modeled data of impedance response of cable in OC.

TABLE II. CABLE HF CBM PARAMETERS PER UNIT LENGTH

Parameters	Values	Parameters	Values
R_{s1} (mΩ)	5.40	C_{p1} (pF)	93.40
R_{s2} (mΩ)	39.40	C_{p2} (pF)	20.32
L_{s1} (μH)	0.48	R_{p1} (MΩ)	13.55
L_{s2} (μH)	7.84	R_{p2} (kΩ)	11.17

For comparing CBM with the available models, as depicted in Fig. 12.

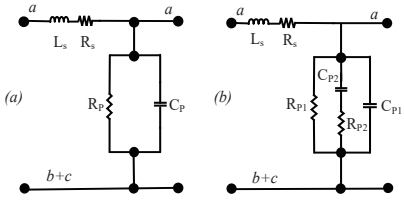


Fig. 12. Transmission line model-based DM power cable schematics (a) standard model-1 (b) Standard model-2. [15]

Cable parameter values based on the available model-1 and model-2 are calculated and demonstrated in Table IV and V below.

TABLE III. CABLE STANDARD MODEL-1 HF PARAMETERS PER UNIT LENGTH

Parameters	Values	Parameters	Values
R_s (mΩ)	5.20	C_{p2} (pF)	2.04
L_s (μH)	0.46	R_{p1} (MΩ)	4.26
C_{p1} (nF)	8.66	R_{p2} (kΩ)	11.15

TABLE IV. CABLE STANDARD MODEL-2 HF PARAMETERS PER UNIT LENGTH

Parameters	Values	Parameters	Values
R_s (mΩ)	5.20	C_p (pF)	93.29
L_s (μH)	0.41	R_p (MΩ)	16.49

V. TIME DOMAIN EVALUATIONWITH PROPOSED CBMS

Both the DM and CM circuits of the motor and cable are employed to assess the applicability of CBM. Target here, is to estimate TOV level at the motor terminals. The schematic diagram of induction machine fed with cable-fed inverter and practical setup is shown in Fig. 13 (a) and (b). Along with the hardware test setup simulation tool is used to model the transient behavior of the motor-inverter system.

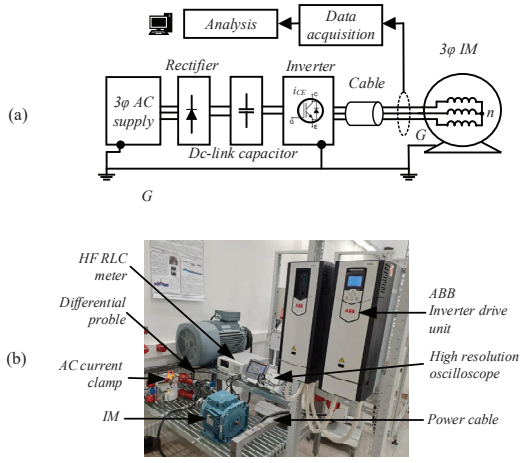


Fig. 13. Test setup (a) Layout/schematics of drive system for the test procedure (b) practical cable-fed inverter drive setup.

For data acquisition oscilloscope with sampling rate of 100 MSps is utilized. The inverter employs modern IGBT switching components with a switching frequency f_{sw} of up to 4.5 kHz. The 13-m cable length between the inverter and motor is a key factor in TOV/RWP. The cable's inductance and capacitance interact with the high-speed switching events of the inverter, leading to reflected waves and resonance effects that can amplify the voltage at the motor terminals.

Fig. 14 presents the experimentally obtained motor's current that exhibits significant transients in its waveform and TOV on the induction motor terminal fed through 13 m cable case fed with inverter.

Authorized licensed use limited to: Tallinn University of Technology. Downloaded on February 04,2026 at 11:45:46 UTC from IEEE Xplore. Restrictions apply.

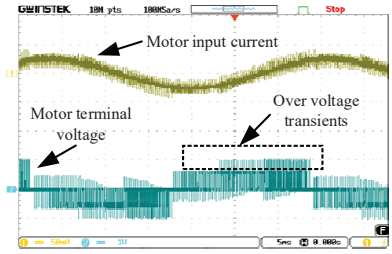


Fig. 14. Experimental induction machine terminal voltage in a 13-m cable.

The HF CBM are interconnected in the simulation software to depict the TOV at machine's terminal (V_{ab}) and compared with practical setup. This demonstrates a strong agreement when comparing with practical setup, as seen in Fig. 15. It is observed that the transient peak overvoltage reached 930 V in comparison to 560 V voltage source converter's (VSC) DC bus voltage, i.e., this provides 1.7 per unit rise in the voltage level compared to DC voltage value. Investigating the long-term effects of repeated exposure to TOV on the motor's insulation system and overall health is essential.

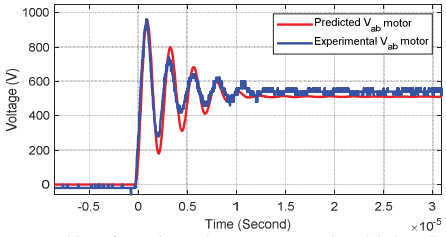


Fig. 15. Matching of experimental measurement and modeled predicted terminal overvoltage (TOV) at induction motor with 13-meter cable in a more extended time-period.

Fig. 16 shows the estimated details of the TOV phenomenon at the machine terminal, which degrades its insulation and decreases the remaining useful life of the machine. The time delay t_p (μs) in the voltage signal is defined by the reference of the inverter voltage signal, and T_{osc} (μs) represents the oscillation time of the reflected terminal voltage wave. Both t_p, and T_{osc} can also be estimated using the equation below with the cumulative values of cable capacitance C_{cable} and inductance L_{cable} with cable length x [12].

$$t_p = x\sqrt{L_{cable}C_{cable}} \tag{16}$$

$$f_{osc} = \frac{1}{4x\sqrt{L_{cable}C_{cable}}} \tag{17}$$

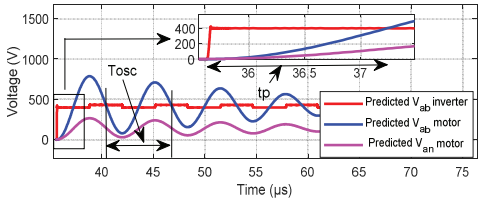


Fig. 16. Estimated voltage at inverter and motor with a 13 m cable.

As seen in Fig. 17, the delay time is linear with the cable length and standard model 1 significantly lower slope then actual estimated measurement because it relies on the LF parameters. Also, standard model 2 is a less accurate estimation of the overvoltage feature values of the cable drive system.

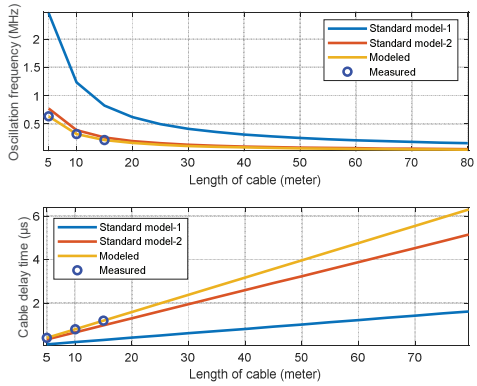


Fig. 17. Estimated oscillation frequency (top) and delay time (bottom) in cable representations with standard models 1 and 2, proposed model and practical measurement.

VI. Conclusion

This paper introduces a high-frequency parametric circuit-based model (CBM) for accurately estimating TOV at the motor terminal in the long-cable-fed motor drive system at high frequency ranges. Condition monitoring is crucial in ensuring electrical drive systems' proper functioning and longevity. It helps identify and address issues related to winding insulation stress and failure, bearing discharge current, and electromagnetic noise emission. Detailed and comprehended circuit-based motor and cable models have been proposed, which provide an accurate representation of the impedance characteristics in both the differential mode (DM) and common mode (CM) at high frequencies ranging from tens of hertz to hundreds of megahertz.

Similarly, the cable model considers skin and proximity effects and dielectric losses to characterize the motor drive system accurately. The proposed methodology is validated through experimental verification and compared to standard modeling techniques as well. Moreover, the proposed approach can be extended to estimate common mode shaft voltages, bearing leakage currents, and EMI noise emissions.

References

[1] A. Belahcen, J. Martinez, and T. Vaimann, "Comprehensive computations of the response of faulty cage induction machines," in *Proceedings - 2014 International Conference on Electrical Machines, ICEM 2014*, 2014. doi: 10.1109/ICELMACH.2014.6960382.

[2] B. Asad, T. Vaimann, A. Belahcen, A. Kallaste, A. Rassõlkin, and M. Naveed Iqbal, "The cluster computation-based hybrid fem–analytical model of induction motor for fault diagnostics," *Applied Sciences (Switzerland)*, vol. 10, no. 21, 2020, doi: 10.3390/app10217572.

Authorized licensed use limited to: Tallinn University of Technology. Downloaded on February 04,2026 at 11:45:46 UTC from IEEE Xplore. Restrictions apply.

[3] B. Asad, T. Vaimann, A. Rassõlkin, A. Kallaste, and A. Belahcen, "Review of Electrical Machine Diagnostic Methods Applicability in the Perspective of Industry 4.0," *Electrical, Control and Communication Engineering*, vol. 14, no. 2, 2018, doi: 10.2478/ecce-2018-0013.

[4] R. J. Kerkman, D. Leggate, and G. L. Skibinski, "Interaction of drive modulation and cable parameters on ac motor transients," *IEEE Trans Ind Appl*, vol. 33, no. 3, 1997, doi: 10.1109/28.585863.

[5] M. U. Sardar *et al.*, "Inverter-Fed Motor Drive System: A Systematic Analysis of Condition Monitoring and Practical Diagnostic Techniques," *Energies (Basel)*, vol. 16, no. 15, p. 5628, Jul. 2023, doi: 10.3390/en16155628.

[6] L. Wang, Y. Zhang, M. S. Ali, G. Chen, J. M. Guerrero, and J. C. Vasquez, "High-frequency modeling and filter design for PWM drives with long cables," *Energies (Basel)*, vol. 14, no. 4, Feb. 2021, doi: 10.3390/en14041155.

[7] M. Yea, J. Kim, and K. J. Han, "Frequency-Dependent Bearing Voltage Model for Squirrel-Cage Induction Motors," *IEEE Transactions on Industrial Electronics*, vol. 69, no. 5, pp. 5071–5080, May 2022, doi: 10.1109/TIE.2021.3082065.

[8] S. Akbar, T. Vaimann, B. Asad, A. Kallaste, M. U. Sardar, and K. Kudelina, "State-of-the-Art Techniques for Fault Diagnosis in Electrical Machines: Advancements and Future Directions," *Energies (Basel)*, vol. 16, no. 17, p. 6345, Sep. 2023, doi: 10.3390/en16176345.

[9] M. U. Sardar *et al.*, "Analysis of Common Mode and Rapidly Varying Voltage Profile on Stator Current Harmonics of an Inverter-fed Induction Motor," in *2023 IEEE 64th International Scientific Conference on Power and Electrical Engineering of Riga Technical University (RTUCON)*, IEEE, Oct. 2023, pp. 1–6. doi: 10.1109/RTUCON60080.2023.10413067.

[10] Y. Azadeh *et al.*, "Cable and Motor Winding Impedance Interactions in Motor Drive Systems and Its Impact on HF Overvoltages," *IEEE Trans Power Electron*, Jan. 2023, doi: 10.1109/TPEL.2023.3322639.

[11] M. Degano, P. Zanchetta, L. Empringham, E. Lavopa, and J. Clare, "HF induction motor modeling using automated experimental impedance measurement matching," *IEEE Transactions on Industrial Electronics*, vol. 59, no. 10, 2012, doi: 10.1109/TIE.2012.2189535.

[12] M. Mohammadi-Rostam and M. Shahabi, "Modeling Induction Motor for Prediction of High frequency problems," *Iranian Journal of Science and Technology - Transactions of Electrical Engineering*, vol. 40, no. 1, 2016, doi: 10.1007/s40998-016-0007-z.

[13] L. Wang, C. N. M. Ho, F. Canales, and J. Jatskevich, "High-frequency modeling of the long-cable-fed induction motor drive system using TLM approach for predicting overvoltage transients," *IEEE Trans Power Electron*, vol. 25, no. 10, 2010, doi: 10.1109/TPEL.2010.2047027.

[14] M. S. Toulabi, L. Wang, L. Bieber, S. Filizadeh, and J. Jatskevich, "A universal high-frequency induction machine model and characterization method for arbitrary stator winding connections," *IEEE Transactions on Energy Conversion*, vol. 34, no. 3, pp. 1164–1177, 2019, doi: 10.1109/TEC.2019.2891349.

[15] Y. Wu, K. Choksi, M. Ul Hassan, and F. Luo, "An Extendable and Accurate High- Frequency Modelling of Three-phase Cable for Prediction of Reflected Wave Phenomenon," in *Conference Proceedings - IEEE Applied Power Electronics Conference and Exposition - APEC*, 2022. doi: 10.1109/APEC43599.2022.9773493.

VII. Biographies

Muhammad Usman Sardar was born in 1989 in Rahim Yar Khan, Pakistan. He obtained his B.Sc. and M.Sc. in Electrical Power Engineering from The Islamia University of Bahawalpur, Punjab, Pakistan and is pursuing a Ph.D. at Tallinn University of Technology in Estonia. His research interests include condition monitoring and fault diagnostics of electrical machines.

Toomas Vaimann (S'11-M'14-SM'20) was born in Pärnu, Estonia, in 1984 and received his BSc, MSc and PhD degrees in electrical engineering from Tallinn University of Technology, Estonia, in 2007, 2009 and 2014 respectively. He is currently a research professor at Tallinn University of Technology, Department of Electrical Engineering. Internationally, he has been a postdoctoral researcher at the Department of Electrical Engineering and Automation, Aalto University, Espoo, Finland. His main research interest is the diagnostics of electrical machines.

Lauri Kütt (Senior Member, IEEE) received the B.Sc. degree in computer and automation technology and the M.Sc. degree in electrical power engineering from the Tallinn University of Technology, Tallinn, Estonia, in 2002 and 2004, respectively, and the Ph.D. degree from the Department of Energy and Geotechnology, Tallinn University of Technology, in 2012. He is currently a Professor with the Department of Electrical Power Engineering and Mechatronics, Tallinn University of Technology. His current research interests include fast transients on electric power lines, power line diagnostics, power quality, and electromagnetic compatibility.

Bilal Asad was born in 1986 in Pakistan. He received his BSc in Electronics Engineering from The Islamia University of Bahawalpur and MSc in Electrical Engineering from University of Engineering and Technology (UET) Lahore, Pakistan and PhD from Tallinn University of Technology, Estonia and Department of Electrical Engineering and Automation, Aalto University, Espoo Finland. His area of interest includes design, modeling and fault diagnostics of electrical machines.

Ants Kallaste was born in Pärnu, Estonia in 1980 and received his BSc, MSc and PhD degrees in electrical engineering from Tallinn University of Technology, Estonia, in 2004, 2006 and 2013 respectively. He is currently a Professor of Electrical Machines at Tallinn University of Technology, Department of Electrical Power Engineering and Mechatronics. In addition, he holds the position of Head of Electrical Machines Research Group. He is the senior researcher of IEEE and member of Estonian Society of Moritz Hermann Jacobi.

Karolina Kudelina was born in Narva, Estonia in 1997. She received BSc and MSc degrees in electrical engineering in 2015 and 2018 respectively. She is currently a PhD student and Junior Researcher in the Department of Electrical Power Engineering and Mechatronics in Tallinn University of Technology. Her main research interest is condition monitoring methods for electrical machines and drive systems. Since 2021, Karolina is a member of Council of the Department of Electrical Power Engineering and Mechatronics in Tallinn University of Technology.

Authorized licensed use limited to: Tallinn University of Technology. Downloaded on February 04,2026 at 11:45:46 UTC from IEEE Xplore. Restrictions apply.

Appendix 3

Publication III

M. U. Sardar, T. Vaimann, L. Kütt, B. Asad, A. Kallaste and A. Rassõlkin, "Modeling Cable-Fed Induction Motor Drives with Optimized Impedance Characterization Across a Low to High-Frequency Spectrum," in *IEEE Transactions on Energy Conversion*, vol. 41, no. 2, pp. 1055-1069, June 2026, doi: 10.1109/TEC.2025.3630465.

Modeling Cable-Fed Induction Motor Drives With Optimized Impedance Characterization Across a Low to High-Frequency Spectrum

Muhammad Usman Sardar, *Student Member, IEEE*, Toomas Vaimann, *Senior Member, IEEE*, Lauri Kütt, *Senior Member, IEEE*, Bilal Asad, *Senior Member, IEEE*, Ants Kallaste, *Senior Member, IEEE*, and Anton Rassõlkin, *Senior Member, IEEE*

***Abstract*—Pulse-width modulation in cable-fed motor drive systems can generate high-frequency effects, which include terminal overvoltage (TOV) stress and common mode voltage (CMV) imbalance. This work presents a grey-box model (GBM) of the cable–induction motor system that describes impedance behavior over a frequency range from low to high, up to 100 MHz. The proposed GBM includes self and mutual inductances and parasitic capacitances, with parameters identified from common-mode and differential-mode impedance spectroscopy. Analytical initial values are refined via an optimization process, avoiding finite-element simulations (FEA/FEM) while reducing the modeling effort. Compared with a conventional lumped model, the GBM lowers complexity and improves agreement with practical measurements, achieving an average frequency-domain validation error below 5% and TOV and CMV estimation errors of 4.72% and 4.19%, respectively. Time-domain tests further confirm accuracy and robustness. The GBM also locates TOV resonance frequencies associated with differential-mode anti-resonance conditions in the winding, enabling targeted analysis of TOV voltage stress, insulation degradation risk, and electromagnetic behavior in cable-fed motor drives. The model provides a flexible framework for transient simulation, parametric sensitivity analysis, and evaluation of potential fault conditions.**

***Index Terms*—Circuit optimization, high-frequency modeling, impedance measurement, induction motors, motor drives, machine windings.**

NOMENCLATURE

ASD	Adjustable speed drives
IM	Induction motor
TOV	Line-to-line terminal overvoltage (V_{ab})
CMV	Common mode voltage (V_{CM})
TLM	Transmission line modeling
GBM	Grey-box models
CM/DM	Common/ Differential mode
LF/MF/HF	Low/ Medium/ High-frequency
RO	Resonance occurrence
PR/AR	Parallel resonance/Anti-resonance (series resonance)
ARO	Anti-resonance occurrence
OA	Optimization algorithm

Received 5 November 2024; revised 13 April 2025, 5 August 2025, and 28 October 2025; accepted 1 November 2025. Date of publication 7 November 2025; date of current version 26 May 2026. Paper no. TEC-01265-2024. *(Corresponding author: Muhammad Usman Sardar.)*

The authors are with the Department of Electrical Engineering and Mechatronics, Tallinn University of Technology, 19086 Tallinn, Estonia (e-mail: muhammad.sardar@taltech.ee).

Color versions of one or more figures in this article are available at https://doi.org/10.1109/TEC.2025.3630465.

Digital Object Identifier 10.1109/TEC.2025.3630465

I. INTRODUCTION

THE digitalization of the industrial sector and advancements in power electronic-based inverter-fed machine drive systems have significantly impacted technological fields, including electrical machine condition monitoring, operation, and diagnostics [1], [2]. The growing use of adjustable speed drives (ASD) in industrial settings has drawn much focus to the production of multiple harmonics at high-frequency (HF) up to several MHz caused by pulse width modulation (PWM) voltages [3].

The existing literature emphasizes that the maximum line-to-line terminal overvoltage (TOV) at HF, also called reflected overvoltage wave phenomena, can reach instantly two or more times the DC-link voltage due to cable-motor impedance mismatch [4], [5]. TOV stress across insulation directly relates to the value of overvoltage over the machine's impedance magnitude (magnitude of voltage per impedance) and the occurrence of multiple TOV resonance frequencies. Also, the voltage imbalance or non-zero common voltage at phase-to-frame/ground with high spikes, called common-mode terminal voltage (V_{CM} /CMV), is developed [6]. These existing issues are commonly referred to as HF problems in cable-fed motor drive systems. These challenges lead to several unfavorable effects, such as the deterioration of bearings [6], [7] discharging bearing currents [8], [9], causing micro-arcing [10], dielectric insulation failure with partial discharge, leading to inter-turn faults in stator windings, accelerated ageing and electromagnetic noise (EMI) emission [11]. These multiple TOV resonances and the associated development of unbalanced CMV [12] present significant challenges, which have been repeatedly emphasized in condition monitoring studies, along with the need for mandatory remedial measures. Given these challenges, as illustrated in Fig. 1, frequency response modeling of machines and cables becomes crucial for understanding and analyzing converter-cable-machine interactions [6], [13].

0885-8969 © 2025 IEEE. All rights reserved, including rights for text and data mining, and training of artificial intelligence and similar technologies. Personal use is permitted, but republication/redistribution requires IEEE permission. See https://www.ieee.org/publications/rights/index.html for more information.

Authorized licensed use limited to: Tallinn University of Technology. Downloaded on July 07,2026 at 09:03:38 UTC from IEEE Xplore. Restrictions apply.

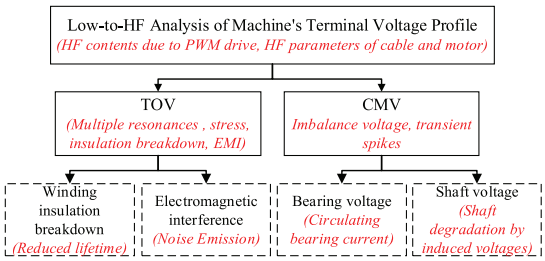


Fig. 1. Challenges associated with the motor's terminal voltage profile.

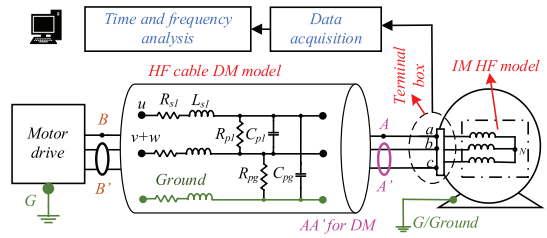


Fig. 2. Typical motor drive setup with feeding cable under study.

Accurate low–to–HF modeling involves a broad spectral bandwidth covering from low to HF regimes. Typically, the low-frequency (LF) range extends from DC or around 10 Hz to 10 kHz, where resistive and inductive properties mainly influence impedance behavior. The medium frequency (MF) range, from 10 kHz to 500 kHz, is where skin effect, proximity effect, and minor resonances begin to affect impedance. At HF, ranging from 500 kHz to 100 MHz, parasitic capacitance, resonant behavior, and electromagnetic interference are the primary concerns.

Accurate estimation of TOV resonance frequencies in the HF range requires crucial frequency-domain modelling of cable-fed motor drives. This study represents a detailed parametric model of cable-fed machines based on impedance response, capturing the key interaction characteristics between cables and motors. While the validity of induction motor models and cables at several megahertz is well documented in the literature, a machine model with identifiable parameters and demonstrated validity across the broader low–to–HF range remains lacking; the present formulation is intended to close that gap.

Multiple TOV resonance frequencies, corresponding to voltage stress peaks, significantly affect the reliability of machine insulation life, especially when they coincide with the anti-resonance (AR) points of the machine's differential mode (DM) impedance. This phenomenon adds additional stress to the machine winding, as the impedance is at its lowest at that point. This phenomenon is called anti-resonance occurrence (ARO), and specific frequency bands are termed as AR frequencies [10]. Therefore, the systematic identification and capturing of distinct AROs in the presence of multiple TOV resonances are critical for reliability. This can enable early recognition of undesired matching resonances such as ARO, mitigate insulation stress, and inform electromagnetic design and insulation-coordination decisions [13].

Impedance parameter-identification for low–to–HF models generally follow two main approaches: white-box models (WBM) and grey-box models (GBM)] [16]. WBM are derived directly from first principles and require extensive parameterization and substantial modelling effort. They are often derived by using distributed parameter-based or transmission line modelling and finite element analysis (FEA/FEM) [17].

In research work [18], a motor winding FEA model was developed to improve voltage prediction accuracy. However, it relies on complex analytical formulas for the end winding region, which limits its ability to capture all the complexities. In contrast, the GBM extends the analysis to external entities, such as cables and inverters. It estimates lumped parameter electrical circuits using impedance measurements [19] but these models are still limited in covering the full range of the frequency spectrum [20], [21].

Modeling based on the LF to some MF ranges, typically up to 50 kHz, is classified into four types: magnetic equivalent circuit (MEC), magnetically coupled circuit (MCC), two-axis (dq) theory, and FEM models [22], [23]. For low-to-medium frequency ranges, simplified GBM-like phase domain (PD), classical qd0, and voltage-behind-reactance (VBR) models are commonly used [24], [25].

In the cable-fed motor model parameterization, individual experimental measurements are required for both differential mode (DM) and common mode (CM) configurations. A typical motor drive setup, illustrated in Fig. 2, serves as a reference for this process. In the DM configuration, phases b and c are connected at both ends as bc, leaving phase a and bc (AA′) for measurements. In the CM configuration, all three phases (abc) are connected together, with measurements taken between the combined abc terminal and ground, operating as a two-port network. Thorough details on the motor and cable's DM and CM connection topologies are provided in subsequent sections.

Although most state-of-the-art models can capture the TOV resonance frequency up to 10 MHz or higher, this paper addresses the most crucial phenomenon: multiple ARO occurrences at the motor terminal. In this study, a comprehensive analysis is conducted up to 100 MHz to precisely capture both TOV resonance frequencies and multiple ARO frequency components resulting from the complex interactions among the inverter, cable, and motor impedances. This study employs fast Fourier transform (FFT) analysis to examine TOV waveforms under varying cable lengths and motor normal operating conditions. Additionally, this paper characterizes the frequency response of motor winding DM impedance in the complete drive system. The experimentally validated waveforms clarify how the drive behaves across frequency and highlight bands of elevated TOV stress; these observations are discussed in detail in the following sections.

Modeling cable-fed drives to characterize multiple AROs in a machine's DM impedance and to locate TOV resonance frequencies is difficult because system-level behavior depends on frequency-dependent inductances (with mutual couplings), resistances, and capacitances. To handle this complexity, we

Authorized licensed use limited to: Tallinn University of Technology. Downloaded on July 07,2026 at 09:03:38 UTC from IEEE Xplore. Restrictions apply.

TABLE I
SUMMARY OF FEATURES OF THE PROPOSED MACHINE MODEL WITH RESPECT TO THE EXISTING STATE-OF-THE-ART MODELS

		Model (ARO)	Model (HF Universal model)	Model (Grey-Box)	Model (WBDC-PVBR)	Model (Low-to-high Universal model)	Proposed GBM
References		[13]	[28]	[29]	[6], [10], [24]	[8], [26], [27]	–
Model Complexity level		Low	Low	High	Low	Low	Medium
Interfacing and extension in the circuit		Constant and direct	Constant and direct	Constant and direct	Constant and direct	Constant and direct	Constant and direct
Parameterization methods		Analytical	Analytical	Optimal fitting	Analytical	Analytical	Analytical & optimal fitting
Equation for parameter identification		Derived	Derived	Not derived	Derived	Derived	Derived
Valid frequency range (Hz)		10^5–10^8	10^3–10^6	10^2–10^6	DC–10^7	10^2–10^7	DC–10^8
LF behavior and analysis	Transient	No	No	Yes	Yes	No	No
	Steady state	No	No	Yes	Yes	Yes	Yes
	Motor slip variation	No	No	Yes	Yes	Yes	Yes
HF behavior and analysis	Transient	No	Yes	Yes	Yes	Yes	Yes
	Steady state	Yes	Yes	Yes	Yes	Yes	Yes
	DM impedance	HF	MF, & HF	MF, & HF	LF,MF, & HF	LF, MF, & HF	LF, MF, & HF
	CM impedance	HF	MF, & HF	MF, & HF	LF,MF, & HF	LF, MF, & HF	LF MF, & HF
	TOV	Yes	No	Yes	Yes	Yes	Yes
	Multiple AROs	Yes	No	No	No	No	Yes
	CMV	No	Yes	No	Yes	Yes	Yes
Cable HF modeling	Transient	Yes	No	Yes	Yes	No	Yes
	Steady state	Yes	No	Yes	Yes	No	Yes
	Parameterization method	Analytical	No	No	No	No	Analytical & optimal fitting
	RWP	Yes	No	Yes	Yes	No	Yes

extend low–to–HF modeling, improve resonance estimation, and refine the representation of drive system elements. Building on the authors' previous circuit/impedance formulation in [5], this research study extends the circuit-based model (previously referred to as CBM in the authors [5]) by incorporating additional frequency response parameters, now referred to as GBM in this study. Although the proposed GBM retains the CBM's physics-guided structure, it introduces a comprehensive parameterization that yields a more accurate, frequency-dependent description of the cable–motor network. In addition, we implement an optimal parameter identification procedure that uses an optimization algorithm (OA) to fit the model to measured impedance data. This automates the fine-tuning of cable and machine model parameters, providing a more efficient and precise alternative to purely manual tuning.

To develop a low–to–HF frequency characteristic machine model for efficient simulation of cable-fed adjustable speed drive (ASD) systems, a MATLAB-Simulink environment is utilized. The simulation employs a comprehensive low–to–HF parametric framework [26], complemented with additional parameters from the IEEE Standard 112-2017 for induction machine (IM) steady-state modeling [27]. By combining LF impedance characterization with the proposed model, the GBM maintains accuracy and steady-state consistency, and it is readily implemented in MATLAB/Simulink.

GBM captures impedance behavior from DC/10 Hz within a steady-state T-equivalent framework. It does not reproduce LF dynamic transients with the same accuracy as full-order dq-axis-based models. It is intended for steady-state impedance-based analysis across a broad frequency range, with emphasis on medium to HF effects (including multiple TOV resonances and ARO events). For applications requiring detailed LF dynamics, a *dq*-axis formulation such as [24], validated from DC/10 Hz to 10^7 Hz, is more appropriate.

The GBM uses a constant-parameter, directly interfaced structure, so external circuits can be attached uniformly without requiring additional transformations. Parameters remain fixed across configurations, which streamlines comparative studies and sensitivity analyses. It enables direct implementation on platforms such as MATLAB and Simulink, independent of any specific simulation tool.

Table I summarizes the key features and advantages of the proposed GBM compared to state-of-the-art models. The main contributions are as follows.

- A parametric GBM for the machine-cable system is proposed, capturing detailed low–to–HF behavior with explicit self/mutual inductances and parasitic capacitances. The initial parameters are identified from impedance measurements using the analytical relations.
- These parameters serve as initial guesses for an optimal impedance-fitting stage, yielding precise parameter estimation with lower analytical complexity and reduced computational effort.
- The GBM is validated in the frequency domain up to 100 MHz, enabling analysis of inverter–cable–machine impedance interaction.
- Using an adjustable-speed drive (ASD) testbed, time-domain experiments show accurate estimation of TOV and CMV (mean errors of 4.72% and 4.19%, respectively), supporting the model's robustness.
- This study quantifies cable–winding interactions over varying cable lengths, estimates multiple TOV from combined cable–motor DM impedance peaks that identify AROs supporting the insulation coordination and EMI-aware design.

Authorized licensed use limited to: Tallinn University of Technology. Downloaded on July 07,2026 at 09:03:38 UTC from IEEE Xplore. Restrictions apply.

TABLE II
MOTOR IMPEDANCE SPECTRUM MEASUREMENT

Symbol	Configuration	Meaning/ elaboration
$a-bc$	$Z_{DM,Y}$	Impedance between phase a and phase bc
$abc-G$	$Z_{CM,Y}$	Impedance between phase abc and G
$N-G$	$Z_{NG,Y}$	Impedance between N/*neutral* point and G

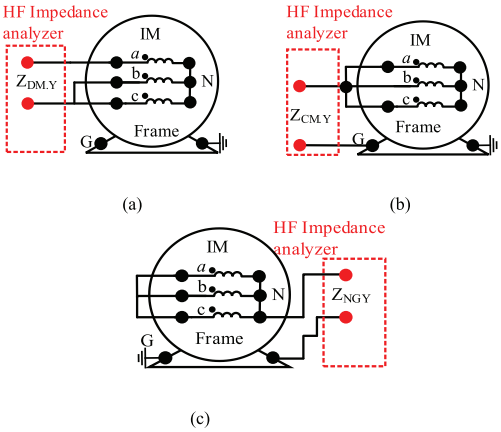


Fig. 3. IM impedance measurement topologies (a) DM (b) CM (c) NG (Z_{NG}).

This work explicitly targets cable–motor impedance interactions and TOV/ARO behavior across the low–to–HF spectrum. Therefore, aspects such as LF transient performance, bearing currents, or shaft voltage estimation are beyond the current scope and are not included in the comparative analysis. Nonetheless, the proposed model offers a flexible framework that can be readily extended to address these phenomena in future studies.

The rest of this article is organized as follows: Section II describes the impedance measurement setup and results. Section III focuses on the characterization of impedance parameters. Sections IV and V present the model validations in the frequency and time domains, respectively. Section VI discusses the motor winding stress analysis, and Section VII concludes the paper.

II. IMPEDANCE MEASUREMENT SETUP AND RESULTS

A. The Machine Impedance Measurement Setup

The impedance spectrum is measured using an impedance analyzer (20 Hz–120 MHz). It records the impedance amplitude and phase profiles as frequency functions for various terminal connections of IM under study, as detailed in Table II.

Determining low–to–HF GBM model parameters involves measuring CM and DM impedances for analytical calculations, followed by iterative optimization to achieve the best-fit impedance response. Fig. 3 shows the experimental measurement schematics for the machine in DM, CM, and NG. The machine is tested in standstill conditions, where different motor winding modes enable tracing of the internal frequency response characteristics. A similar process is applied to the cable to measure the DM impedance in both open and short-circuit conditions. Fig. 4 demonstrates the setup for measuring low–to–HF impedance spectra of machine and cable separately using an impedance analyzer (20 Hz–100 MHz).

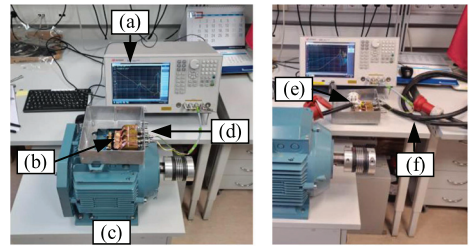


Fig. 4. Impedance measurement (a) impedance analyzer, (b) IM interfacing box, (c) IM, (d) BNC connectors, (e) cable interface, and (f) cable in DM.

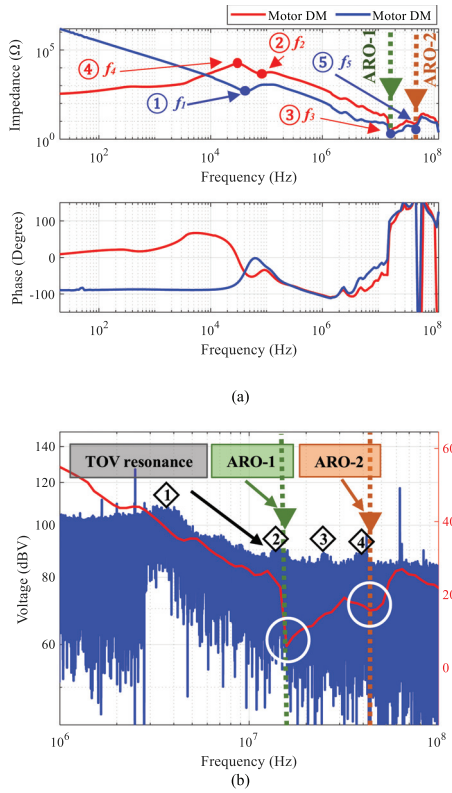


Fig. 5. Measurement results (a) impedance profile DM (red) and CM (blue) (b) terminal voltage spectrum V_{ab} (FFT; blue, left axis) with DM impedance (red, right axis), presenting four TOVs/ resonance frequencies (◊ marker).

The setup features a standard aluminum box via copper connection strips and a Bayonet Neill–Concelman (BNC) connector, enabling a reproducible impedance profile.

B. Impedance Measurement Results

Fig. 5(a) shows the DM and CM impedance profile (magnitude and phase) of the induction machine without the power

Authorized licensed use limited to: Tallinn University of Technology. Downloaded on July 07,2026 at 09:03:38 UTC from IEEE Xplore. Restrictions apply.

cable. The labeled frequencies f_1 ①–$f_1$⑤ denote the dominant series- and parallel-resonance points.

C. Introduction of ARO Occurrence

AR occurrence arises when the series resonance (or anti-resonance) frequency of the machine's DM impedance coincides with the TOV resonance frequencies of V_{ab} voltage. This phenomenon of series resonances (AR) typically results in a sharp dip in the winding's impedance, reaching a minimum value of 2.01 Ω in this IM case.

Fig. 5(b) compares the terminal line-to-line voltage spectrum V_{ab} (FFT; blue, left axis), along with the DM impedance magnitude of IM. It is observed that the machine DM impedance magnitude excluding the cable's impedance exhibits two sensitive AR frequencies of $f_{ARO\text{-}1} = 15.8$ MHz and $f_{ARO\text{-}2} = 43.5$ MHz. The blue trace highlights five distinct TOV resonance frequencies (◊ marker) across the motor terminal, measured across terminal AA' (see Fig. 2).

By superimposing the TOV resonance frequencies of the drive system with the motor's DM impedance in the frequency domain, it is observed that the second and fourth TOV resonance frequencies align with the DM impedance AR frequency. In contrast, the first and third resonances are significantly offset from the impedance AR frequency. This finding indicates that TOV stress is very critical due to the occurrence of ARO phenomena, despite their lower TOV magnitudes. Therefore, mitigating TOV resonances that coincide with the AR of the motor's winding DM looks to be essential. Notably, previous studies [8], [9], and [11] have primarily focused on analyzing and mitigating only the first/primary TOV resonance frequency in motor drive systems. This underscores the significance of the present study in addressing multiple TOV resonance frequencies, which play a crucial role in the event of multiple AR causing ARO.

III. Impedance Parameter Characterization of GBM

A. Proposed GBM Modeling Approach

The GBM re-estimates the key machine and cable impedance parameters by refining the initial analytical guesses through parameter search algorithms with OA, using the measured impedance profile.

B. Cost Function for Optimal Impedance Parameter

The cost function, as defined in (1), evaluates how good a particular solution is based on two objective functions. Fitness for an individual x_j is typically based on minimizing the mean squared error (MSE) between practical and modeled impedances and phase angles.

$$Obj_1(x_j) = \frac{1}{n}\sum_{i=1}^{n}\left[|Z_{ini}(f_i,x_j)| - |Z_{prac}(f_i,x_j)|\right]^2$$

$$Obj_2(x_j) = \frac{1}{n}\sum_{i=1}^{n}\left[|\theta_{ini}(f_i,x_j)| - |\theta_{prac}(f_i,x_j)|\right]^2 \quad (1)$$

A lower mean squared error (MSE) indicates higher model fitness. Modified particle swarm optimization (MPSO) using the adaptive strategy as OA, inspired by bird flocking behavior, is used as an advanced optimization algorithm to navigate complex, nonlinear, and multimodal solution spaces [30]. MPSO mitigates premature convergence and balances global exploration with local exploitation by combining chaos-based, non-linear inertia weights with adaptive position updates and terminal substitution, thereby improving the robustness of the obtained optima in complex search spaces.

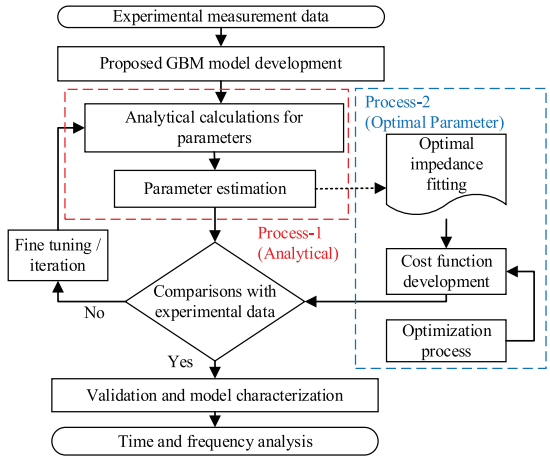


Fig. 6. Flowchart for impedance parameter characterization.

The low–to–HF characterization flowchart, as demonstrated in Fig. 6, begins with experimental impedance measurements and proceeds in two parametric stages: (i) analytical parameter identification and (ii) optimal parameter estimation via impedance matching using an optimization algorithm (OA). The resulting time- and frequency-domain simulations show strong agreement with the measurements, effectively capturing the frequency behavior of the cable–motor drive system.

C. Proposed Machine GBM

The proposed GBM for IM is presented in Fig. 7(b), compared to the existing/universal circuit-based model Fig. 7(a) [26]. The proposed low–to–HF GBM model incorporates detailed frequency response parameters. Each parameter, including inductance and parasitic capacitance, is precisely defined based on the machine's frequency behavior. The steady-state LF parameters of IM, including stator (R_a, L_a) and rotor winding impedance parameters, are derived from preliminary tests.

Additional parameters, such as the series turn-to-turn branch components (C_T, R_T, L_T) for capturing the skin effect and inter-turn capacitance, eddy current loss resistance (R_E), and frame parasitic capacity, resistances, and capacitances $(R_{G1}, R_{G2}, C_{G1}, C_{G2})$, are identified from the impedance measurement data. The phase-to-phase parasitic capacitance C_P, phase winding-to-rotor shaft parasitic capacitance (C_{WR}), rotor-to-ground capacitances (C_{RG}), and bearing capacitance (C_B) are used to account for bearing voltage and the associated shaft current. In this study, we introduced the incorporation of

Authorized licensed use limited to: Tallinn University of Technology. Downloaded on July 07,2026 at 09:03:38 UTC from IEEE Xplore. Restrictions apply.

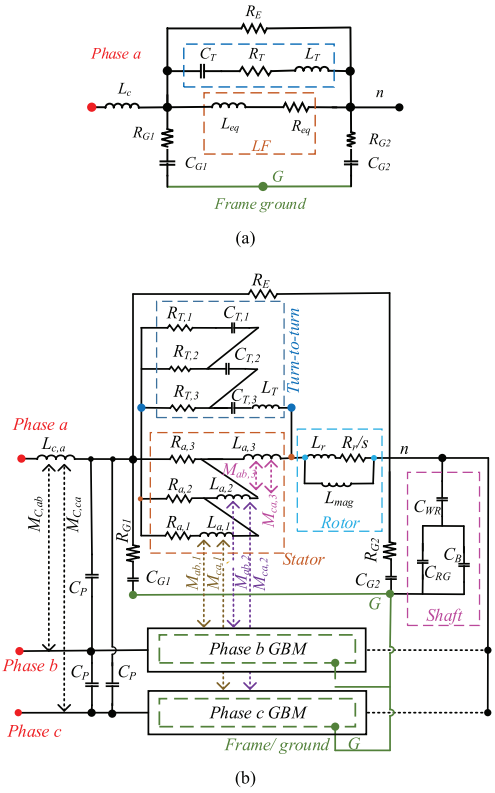


Fig. 7. IM model (a) Universal HF model [26] (b) Proposed GBM model.

self (L_a), multiple mutual inductances/coupling between stator phases M_{ab}, and mutual coupling of the connectors and internal feed conductors (M_c) to enhance the accuracy and estimation capability of the GBM parameters. The details of parameter identification and the corresponding analytical calculations are presented in the subsequent section of the paper.

This model addresses two resonance regions: one below 500 kHz as a low–to–MF and another from 500 kHz to 100 MHz. The stator winding–to–frame capacitance C_{WS} is partitioned into C_{G1} and C_{G2}, each in series with R_{G1} and R_{G2}, respectively to improve the agreement between measured and modeled CM and DM impedances.

1) Analytical Parametric Identification of Machine: The analytical derivations are provided in the authors' previous work [5]. In continuation of the proposed GBM, the turn–to–turn series branch resistance R_T and inductance L_T are represented by a ladder network following (2):

$$Z_T(\omega) = \frac{1}{j\omega C_{T,2}} + \left[\frac{1}{R_{T,2}} + \frac{1}{(\frac{1}{j\omega C_{T,1}} + R_{T,1})}\right]. \quad (2)$$

The connector/internal-feed inductance for phase–a, L_c, as defined in (3), together with capacitance C_{G1}, produces the anti-resonance at point f_3 in DM impedance:

$$L_C = L_{C,a} - M_{C,ab}. \quad (3)$$

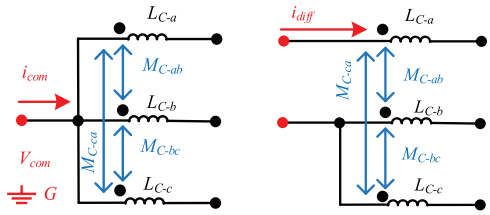


Fig. 8. The self- and mutual inductances of the connections and internal line conductors schematics in (a) CM, (b) DM.

Here, $L_{C,a}$ and $\{M_{C,ab},\ M_{C,ca}\}$ denoted the self- and mutual coupling inductances of the connectors and internal feed/line conductors associated with phase–a (Fig. 8).

In the CM connection, the machine's CMV drives a ground current through a parallel path formed by ground-insulation capacitance (C_{G1}). The equivalent CM inductance L_5, which combines the connection-lead inductance L_{lead} and the connector/internal-lead contribution $L_c = L_{ca} + 2M_{c,ab}$ (Fig. 8a), is obtained in (4):

$$L_5 = L_{lead} + \frac{1}{3}(L_{c,a} + 2M_{c,ab}) = \frac{1}{3}\left(\frac{1}{(2\pi f_5)^2 C_{G1}}\right). \quad (4)$$

Accounting explicitly for L_{lead} at f_5 further refines the system's impedance behavior

In DM connection, DM current returns through the equivalent capacitance $2C_{G1}/3$ and the equivalent inductance L_3 is given by (5) (Fig. 8(a)):

$$L_3 = L_{lead} + \frac{3}{2}(L_{c,a} - M_{c,ab}) = L_{lead} + \frac{3}{2}(L_C)$$

$$L_3 = \frac{3}{2}\left(\frac{1}{(2\pi f_3)^2 C_{G1}}\right). \quad (5)$$

Accounting for the measuring-cable lead inductance L_{lead}, at the AR frequency f_3, further refines the system's impedance behavior.

Using (5), the HF first-turn stator inductance L_C is obtained. Solving (3)–(5) yields the self and mutual inductances terms that define the inductive coupling coefficients $\kappa_{C\text{-}ab}$, $\kappa_{C\text{-}bc}$, $\kappa_{C\text{-}ca}$ for the other connection terminals as given in (6):

$$M_{C,ab} = \kappa_{C,ab}\sqrt{L_{C,a}L_{C,b}}, \quad M_{C,bc} = \kappa_{C,bc}\sqrt{L_{C,b}L_{C,c}}$$

$$M_{C,ca} = \kappa_{C,ca}\sqrt{L_{C,c}L_{C,a}}. \quad (6)$$

These coefficients enable an accurate, high bandwidth approximation of magnetic coupling in a MATLAB/Simscape implementation. The equivalent inductances of the winding (L_{DM} and L_{CM}) are determined for each DM and CM measurement, as the scheshown in Fig. 9.

This process identifies the per-phase self and mutual inductances using (7)–(8):

$$L_{DM} = \frac{3}{2}(L_a - M_{ab}) = \frac{|Z_{DM.LF}|}{2\pi f_{LF}}\sin(\theta_{DM.LF}), \quad (7)$$

$$L_{CM} = \frac{1}{3}(L_a + 2M_{ab}) \approx \frac{1}{3(2\pi f_1)^2 C_{G2}}. \quad (8)$$

Authorized licensed use limited to: Tallinn University of Technology. Downloaded on July 07,2026 at 09:03:38 UTC from IEEE Xplore. Restrictions apply.

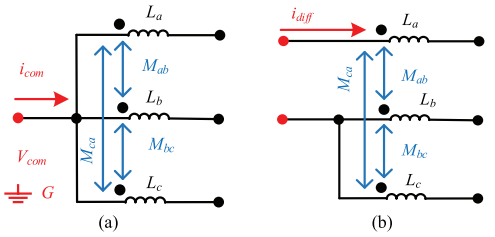


Fig. 9. The self- and mutual inductances of winding schematic representation in (a) CM, (b) DM.

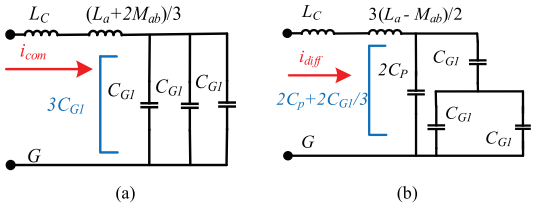


Fig. 10. Equivalent circuits of IM for HF above 1 MHz for the initial estimation, schematics in (a) CM, (b) DM.

The self and mutual inductances are defined in (7) and (8) are then used to compute phase-to-phase coupling coefficients κ_{ab}, κ_{bc}, κ_{ca}. These coupling coefficients quantify the magnetic interaction between windings and depend on winding configuration and core properties. They are defined in (9), which improves the model's representation of machine behavior:

$$M_{ab} = \kappa_{ab}\sqrt{L_a L_b},\ M_{bc} = \kappa_{bc}\sqrt{L_b L_c},\ M_{ca} = \kappa_{ca}\sqrt{L_c L_a}. \tag{9}$$

The number of mutual inductances incorporated into the model can be adjusted according to the desired level of complexity. Notably, each mutual inductance introduces three additional parameters, as three additional inductive coupling coefficients are needed to represent a three-phase mutual inductor. In this study, the coupling of phase a with corresponding three ladder sub-branches $\{M_{ab,1},\ M_{ca,1}\}$, $\{M_{ab,2},\ M_{ca,2}\}$, and $\{M_{ab,3},\ M_{ca,3}\}$ is illustrated in Fig. 7(b). These define the corresponding coupling coefficients $\{\kappa_{ab,1},\ \kappa_{ca,1}\}$and $\{\kappa_{ab,2}\ \kappa_{ca,2}\}$, $\{\kappa_{ab,3},\ \kappa_{ca,3}\}$ together with other phase sub-branches. The initial values are obtained using (9), and the mutual inductances are defined in (10):

$$M_{ab,1} = \kappa_{ab,1}\sqrt{L_{a,1}L_{b,1}},\quad M_{bc,1} = \kappa_{bc,1}\sqrt{L_{b,1}L_{c,1}}$$
$$M_{ca,1} = \kappa_{ca,1}\sqrt{L_{c,1}L_{a,1}}. \tag{10}$$

These identified elements are utilized in a Simulink-based IM model to parametrize interphase mutual coupling, thereby improving the proposed GBM's accuracy in representing these effects.

Due to the symmetry of the proposed machine GBM across the three phases, only parameters related to phase a are represented and utilized. Fig. 10 illustrates the equivalent parametric circuit of IM for HF in both CM and DM configurations.

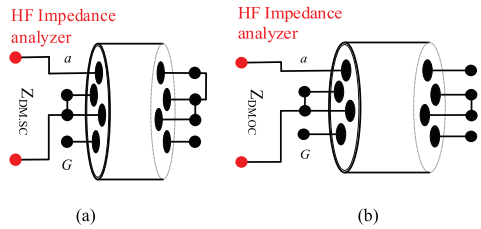


Fig. 11. DM cable measurement schematics (a) SC mode (b) OC mode.

Also, the parameters C_{CM} and C_{DM} are obtained as in (11) [17],

$$C_{CM} = 3C_{G1},\ \ C_{DM} = 2C_P + \frac{2C_{G1}}{3} = \left(\frac{1}{(2\pi f_4)^2 L_{DM}}\right). \tag{11}$$

Similarly, a ladder network for HF modeling represents the stator branch, and the parameters $(R_a,\ L_a)$ are extended accordingly as given in (12),

$$Z_a(\omega) = j\omega L_{a,2} + \left[\frac{1}{R_{a,2}} + \frac{1}{(j\omega L_{a,1} + R_{a,1})}\right]. \tag{12}$$

2) Optimal Characterization of Machine GBM Parameters: The MPSO algorithm is employed to fit the model parameters of the proposed GBM, ensuring accurate estimation through an effective parameter fitting process. The optimization begins with analytically calculated initial values/guesses, allowing a 20% variation range, within which the algorithm efficiently identifies the optimal values.

The difference between the modeled and measured impedance spectra is quantified using a cost function, which serves as the optimization criterion for parameter fitting. The final optimal parameters fall within a 6% deviation, demonstrating robustness with minimal variance from calculations obtained from measurements.

D. Cable's GBM

To accurately demonstrate the reflected wave/TOV phenomena caused by cable wave propagation effects in the IM drive system, a Y-connected configuration of the same motor fed through a cable is considered in this study. An HF model of power cable connecting the inverter and the motor is introduced to support the validation of the HF modeling of the IM.

For HF impedance parametric characterization of cables, the model [29] is considered an initial GBM to enable further robust parametric modeling. TLM-based distributed parameters are identified analytically from measurements, as the connection mode schematics are represented in Fig. 11 and the optimal parameter of the initial GBM model (represented in Fig. 12) are estimated using similar OA via impedance fitting. Cable parameters consist of straightforward line impedance Z_l in series and Z_p parallel elements for accurate identification. Their extraction involves short circuit (SC) and open circuit (OC) cable impedance measurements in DM schematics using phase lines.

Authorized licensed use limited to: Tallinn University of Technology. Downloaded on July 07,2026 at 09:03:38 UTC from IEEE Xplore. Restrictions apply.

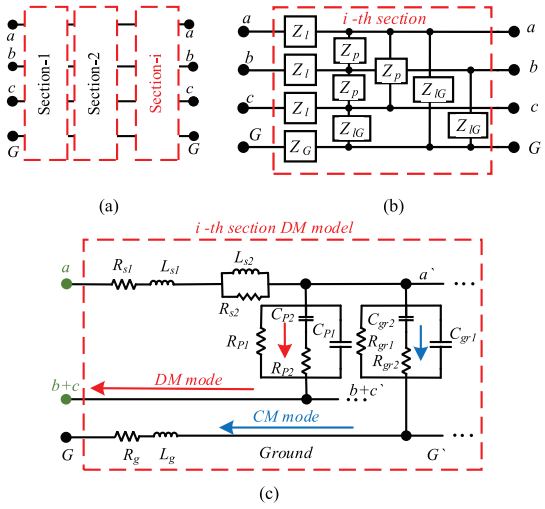


Fig. 12. Cable HF representation (a) Multi-section model of a cable (b) Three-phase representation with HF parameters (c) GBM of cable in DM schematics.

The cable used is an unshielded, PVC-insulated, five-core cable with a 5.0 mm^2 conductor area.

The HF cable parameters R_{s1}, L_{s1}, are extracted from SC impedance in DM schematics (Fig. 11(a)). The parameters R_{s2} and L_{s2} account for skin and proximity effects, while R_{p1}, C_{p1}, R_{p2}, C_{p2}, represent dielectric losses and parasitic capacitance between phase conductors, identified from DM open-circuit tests (Fig. 11(b)). Additionally, the parameters for the ground conductor line (R_g, L_g, R_{gr1}, R_{gr2}, C_{gr1}, and C_{gr2}) characterize the ground conductor impedance, which defines the return path of common-mode currents. As the same five-conductor cable is used, these parameters remain consistent across different sections, ensuring uniform impedance characteristics and precise representation of frequency behavior in the system.

A unit-length cable model with ten cascaded sections is scaled for full cable length. The DM connection schematics, primarily used for impedance measurements, are already defined.

1) Parametric Identification of Cable Model Parameters: GBM simplifies the calculation of impedance parameters using the 20-dB/decade slope in both LF and HF ranges, as detailed in the author's recent work [5]. This approach enables the initial estimation of HF cable parameters.

2) Optimal Characterization of Cable Parameters: The optimal parameterization of the cable model follows the same procedure as the MPSO algorithm/OA used for the motor model, applying the error minimization cost function defined in (1). Like machine parameter estimation, the optimization process starts with analytical initial values of the cable and a 20% variation range, allowing the OA to refine the parameters for the best optimal fitting. The final optimal values show again only a 6% deviation from experimental cable-impedance measurements. This study contributes to developing a precise and efficient impedance modeling approach that minimizes time consumption with manual tuning.

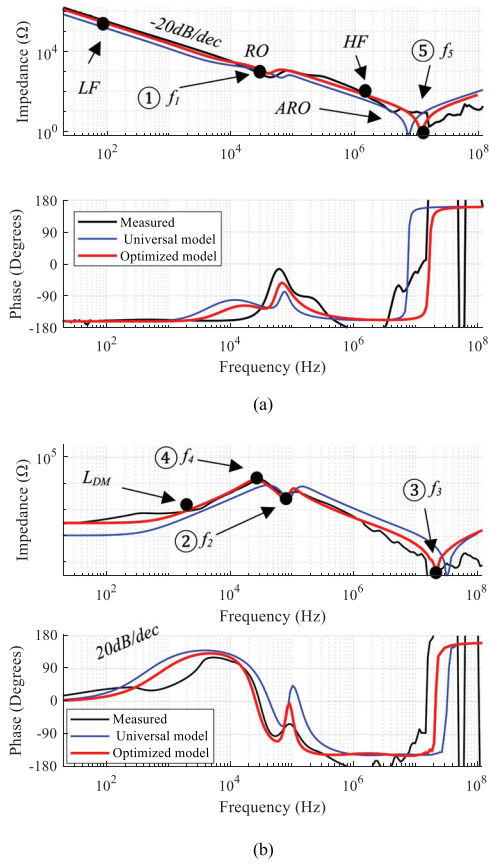


Fig. 13. Matching impedance profile result of measured results, universal machine model, and proposed optimal GBM for (a) CM and (b) DM typologies.

IV. Impedance Model Validation

A. IM's GBM Validation

In Fig. 13(a) and (b), compare the impedance profile showing impedance (Ω) and phase (Degrees) of the proposed GBM, the universal IM model, and the experimentally measured data. GBM closely matches the measured impedance response across the entire frequency spectrum, demonstrating its effectiveness in accurately modeling both LF and HF characteristics. At low frequencies (DC–to–10 kHz), the GBM follows a classic −20 dB/decade slope, dominated by stator–rotor inductances and resistances, aligned with steady-state behavior. This agreement indicates the model captures the machine's low-frequency characteristics reliably.

B. Cable's GBM Validation

Fig. 14(a) and (b) compare the measured (black), initial (blue), and optimized GBM (red) impedance profile of the cable's DM network in OC and SC configurations, respectively.

Authorized licensed use limited to: Tallinn University of Technology. Downloaded on July 07,2026 at 09:03:38 UTC from IEEE Xplore. Restrictions apply.

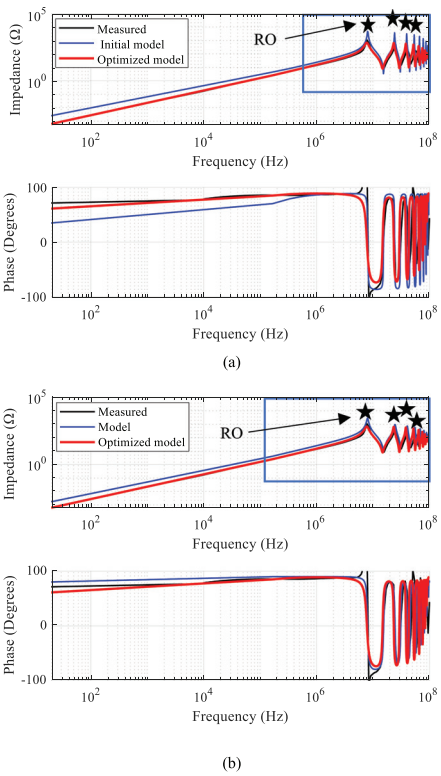


Fig. 14. Matching impedance profile result of measured, initial model, and optimized model for cable connection topologies: (a) OC and (b) SC.

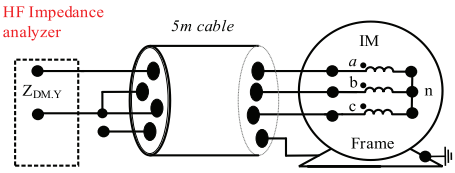


Fig. 15. Measurement for the machine DM impedance fed with a 5-meter supply cable.

C. Combined Cable-Fed Machine Model

Adding the cables clearly changes the impedance curve, especially at high frequencies where resonance starts to appear. The phase angle plot further shows the shift caused by cable impedance, emphasizing the importance of accounting for it in the design and analysis of motor drive systems.

To validate the GBM for the combined cable–machine system in DM, the schematics of Fig. 15 was used to measure the impedance of an induction motor fed through a 5 m supply cable.

Impedance profile results, shown in Fig. 16, demonstrate that the optimized GBM (red), characterized for the 5 m cable-fed machine, closely matches the measured impedance (black) in both magnitude and phase across the band and, at HF, reproduces the resonance and anti-resonance features (star markers). In

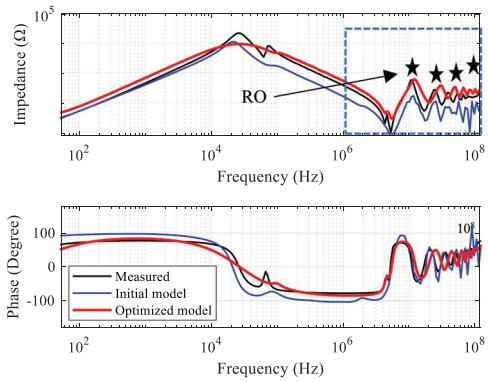


Fig. 16. Impedance profile comparison for a 5 m cable-fed motor in DM: measurement (black), initial model (blue; universal IM plus initial cable), and optimized model (red; optimized IM plus optimized cable).

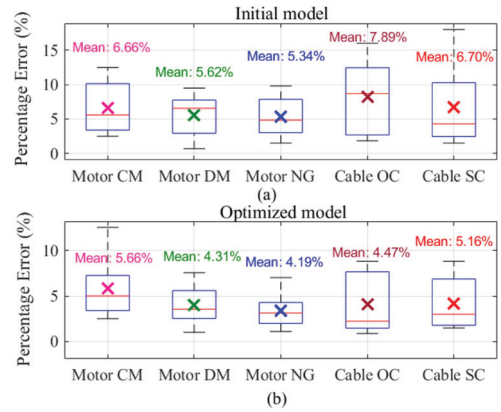


Fig. 17. Error boxplots for various nominated topologies compared with measurements (a) Universal/initial model (top) (b) Optimized model (bottom).

contrast, the initial universal-parameter model impedance (blue) shows clear deviations from the measured impedance profile.

D. Error Analysis of Motor and Cable Modeling

1) Average Deviation of Models With Measurements: Equation (13) yields the percentage error showing deviation from practical measurement and similarly, average deviation or mean average percent error (MAPE) is calculated based on the multiple frequency points (f_i) as expressed below.

$$\Delta(f_i) = \left| \frac{|Z_{optimal}(f_i)| - |Z_{practical}(f_i)|}{|Z_{practical}(f_i)|} \right| \times 100 \quad (13)$$

$$MAPE = \frac{\sum_{i=1}^{k} \Delta(f_i)}{k} \quad (14)$$

To achieve robust modeling, a detailed error analysis is provided, with boxplots shown in Fig. 17 highlighting the

Authorized licensed use limited to: Tallinn University of Technology. Downloaded on July 07,2026 at 09:03:38 UTC from IEEE Xplore. Restrictions apply.

impedance's magnitude error distribution and the model's improvements. GBM-based optimized models (Fig. 17(b)) significantly improve accuracy. Initial mean errors were 6.66% for motor CM and 7.89% for cable SC (Fig. 17(a)). After GBM optimization, these errors dropped to 5.66% and 4.47%, respectively.

The initial and optimal parameters of the proposed GBM that are treated with an optimization problem are listed in Appendix A separately. These parameters provide a detailed and comprehensive description of low–to–HF behavior modeling of cable and motor.

V. Validation of Proposed GBM in Time Domain

A. Practical Test-bench Details and Model Simulation

The practical setup involves a 7.5-kW four-pole IM with a star-connected stator winding, powered by a PWM voltage inverter, operating at 560 V DC-link, 4.5 kHz switching frequency, slip 2.67%, and cable of different lengths. The fundamental frequency of the IM in the drive system is set 50 Hz, as the supply frequency of the drive. Voltage and current were measured using HF (100 MHz bandwidth) differential and current probes directly connected to the motor terminals. The terminal overvoltage (TOV/V_{ab}) was measured across the line-to-line connection terminals. The common-mode voltage (CMV) was obtained using (16) from various terminal voltages, following [24].

The practical hardware operates with a 5 ns time step, 200 mega samples per second (MS/s) sampling rate, and 25 ms signal total time, capturing frequencies up to 100 MHz with a 40 Hz frequency step-size for FFT representation.

The proposed model improves upon this with a 1 ns time step, a 1.0 GS/s sampling rate, and a 30 ms simulation time, enabling the capture of frequencies up to 500 MHz with a 33.3 Hz frequency step, thus improving the model's accuracy. Simulations were carried out in MATLAB/Simulink, allowing flexible motor–cable–inverter modeling and frequency/time-domain analysis. Fig. 18 depicts the cable-fed test bench used to capture multiple TOV resonance peaks and common-mode voltages.

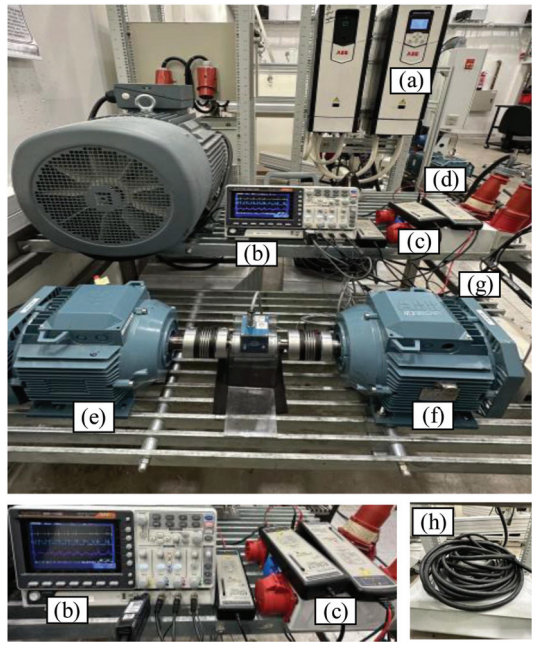


Fig. 18. Practical test bench of the IM drives comprising (a) ASD inverter, (b) oscilloscope, (c) HF differential probes, (d) junction box, (e) load motor, (f) test motor (IM), (g) HF current probe, and (h) power cable.

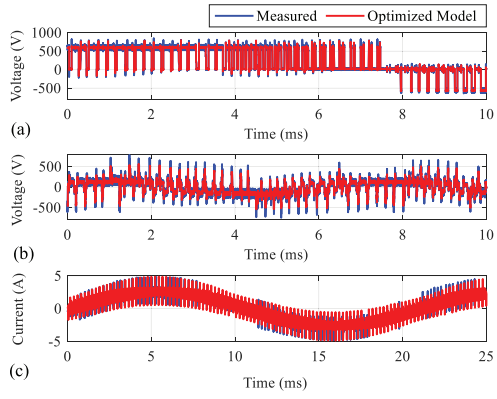


Fig. 19. Time-domain comparison of measured and optimized-model signals for the IM with a 5 m cable (a)Voltage signal for V_{ab} as TOV(b) voltage signal for V_{CM}, and (c) current signal for I_a.

B. Time Domain Analysis of TOV and CMV

The validation of the GBM model representing terminal overvoltage/TOV, CMV, and motor-fed current I_a in the time domain is illustrated in Fig. 19. The comparison includes measured (blue) and optimized model (red) simulations for motor line-line voltage V_{ab} as a TOV and $_{VCM}$ as CMV and line current. A magnified view, as in Fig. 20, of these signals further highlights the model's accuracy in capturing transient and steady-state behaviors.

To investigate the reflected transient TOV phenomenon caused by wave propagation effects in cable-fed IM drives, a series-Y configuration of the motor fed through a 5-meter cable is considered. As presented in Fig. 20, the overvoltage peak (786 V) is approximately 1.4 times the DC bus voltage (560 V). This is a direct result of wave reflections and propagation between the motor and the variable frequency drive (VFD) or adjustable speed drive (ASD). These reflections occur due to the impedance mismatch between the motor and the cable, resulting in multiple TOV resonances (or peaks) at the motor terminals.

The proposed model estimates a peak DM voltage of 799 V, slightly higher than the measured peak value. This small difference confirms the GBM's accuracy in reproducing the inverter-fed IM's DM voltage behavior. This approach effectively captures the underlying wave propagation phenomena, including traveling waves and voltage amplification.

Authorized licensed use limited to: Tallinn University of Technology. Downloaded on July 07,2026 at 09:03:38 UTC from IEEE Xplore. Restrictions apply.

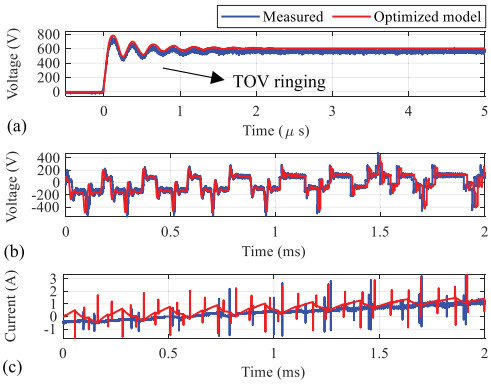


Fig. 20. Zoomed view of the same time domain signals (a) voltage signal for V_{ab} as TOV, (b) voltage signal V_{CM}, and (c) current signal for I_a.

C. Frequency Domain Analysis of TOV and CMV

Fig. 21 illustrates the frequency spectrum of the motor line-to-line voltage V_{ab} (TOV) and CMV using FFT representation. At LF (DC–10 kHz), the dominant PWM switching frequency of 4.5 kHz and its harmonics (e.g., 9 kHz, or others) are observed and introduced by the inverter's switching operation. These harmonics interact with the machine's impedance, generating additional frequency components.

At higher frequencies (typically above 500 kHz), the impact of parasitic elements, CMV, and cable reflections becomes more significant. The TOV resonance frequency after the switching transient is recorded as 3.3 MHz in simulation, closely matching the measured value of 3.4 MHz, which confirms the model's precision in reflecting HF behavior. The subsequently measured TOV resonance frequencies are 15.31 MHz, 25.41 MHz, and 38.83 MHz, which are also well reproduced by the proposed model.

A closer agreement between the measured (blue) and optimized model (red) spectra shows that the GBM represents low–to–HF components more precisely. This makes the model well-suited for power electronics and motor drive system applications.

D. Interpretation of Modeling Errors

Fig. 22 presents an expanded frequency-domain error analysis for TOV and CMV, comparing the initial and optimized GBM. After optimization, both the mean error and its spread decrease clearly, indicating improved estimation across the low-to-HF band.

The mean error for TOV representation by GBM decreases from 6.02% to 4.72%, resulting in a 21.59% reduction. Also, the CMV mean error falls from 5.71% to 4.19%, a 26.62% improvement. Together, these improvements show that the optimization improves the GBM's estimation fidelity across the low-to-HF band. A side-by-side comparison of the error-reduction representation between the initial model and GBMl, quantified using the error-reduction index (ERI), is presented in Appendix A.

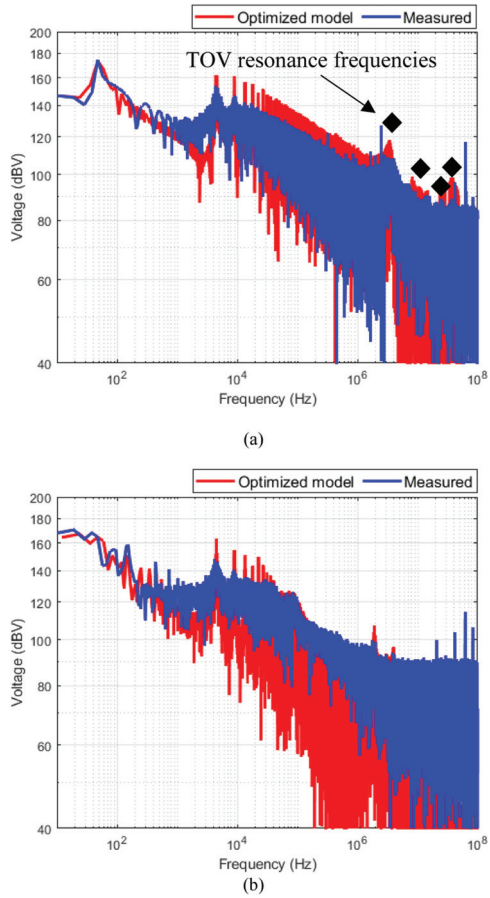


Fig. 21. Matching frequency spectrum (FFT) of measured and optimized model (a) Voltage spectrum representing V_{ab} with TOV resonance frequencies ($\Diamond$ markers) (b) Voltage spectrum representing V_{CM} as CMV.

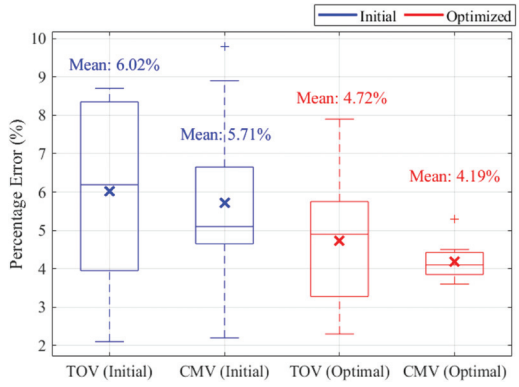


Fig. 22. Percentage error boxplots of frequency-response for TOV and CMV signals using the initial model (left, blue) and optimized model (right, red) calculated with measurements.

Authorized licensed use limited to: Tallinn University of Technology. Downloaded on July 07,2026 at 09:03:38 UTC from IEEE Xplore. Restrictions apply.

VI. Motor Winding TOV Stress Analysis

TOVs can threaten motor-winding insulation, particularly if their resonance frequencies coincide with DM AR frequencies of the machine impedance. The combination of cable layout and machine impedance determines the critical frequencies at which voltage stress peaks; identifying these points is central to insulation coordination. The analysis below, in this study, presents the observed AR/ARO frequency bands and discusses their implications for insulation reliability.

A. Motor Winding HF TOV Estimation

Estimating TOV resonance frequencies is beneficial for mitigating ARO during the design of cable-fed motor drives. This article presents an impedance-based method that combines the DM impedances of the cable and machine to locate the resonance/antiresonance. The procedure applies across various cable lengths, motor configurations, and electrical layouts, providing a practical tool for design and optimization of motor-drive systems in the low–to–high range.

The voltage between any two potential points (nodes) is directly influenced by the impedance characteristics between them [26]. Therefore, to estimate the TOV resonance frequencies across the motor using impedance analysis, it is essential to evaluate the combined impedance of the cable and motor at the motor terminal BB′, as illustrated in Fig. 1. In this study, the developed testbench of cable-fed motor drive systems under TOV and ARO investigations provides comprehensive insights into HF behavior.

Fig. 23 compares the terminal line-to-line voltage spectrum across BB′ with the differential-mode impedance of the cable–machine system for two cable lengths (5 m and 1 m). In both additional-axis figures, the red curves represent the DM impedance magnitude of the combined cable and motor, while the blue curves show the corresponding measured TOV voltage spectra. Two distinct AR frequencies, labeled ARO-1 and ARO-2, are marked with vertical dashed lines and annotated with arrows.

At approximately 15.8 MHz and 43.5 MHz, the motor's DM-impedance peaks coincide with TOV resonance, marking frequency bands where the terminal stress is highest. This overlap identifies the ARO condition that governs HF TOV behavior and pinpoints the frequencies at which insulation is most vulnerable.

A key outcome of this research study is that TOV resonance is directly tied to the combined DM impedance of the cable–motor network: the resonance points are visible as peaks in the measured impedance of the cable-fed motor setup. Therefore, the proposed GBM estimates these TOV resonance frequencies across different cable lengths and layouts, providing a practical basis for the insulation coordination and EMI aware design.

B. Motor Winding Terminal ARO Estimation

The combined DM impedance of the cable–motor network identifies the critical TOV resonance frequencies associated with the AROs. At these frequencies, the motor can present minimal input impedance with excessive TOV voltage stress at the terminals (AA′), increasing the risk of insulation degradation and motor drive instability. Locating these points is therefore essential for reliability and for planning effective ARO-mitigation measures.

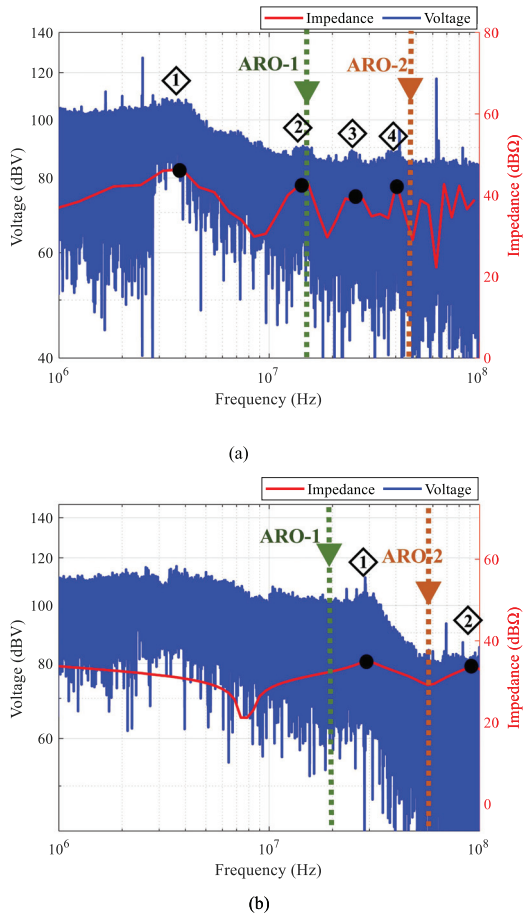


Fig. 23. Terminal voltage spectrum measured across BB′, highlighting TOV resonances for (a) a 5 m cable and (b) a 1 m cable.

Fig. 24 maps the peak-impedance locations for several cable lengths and marks the corresponding TOV peaks with distinct color markers. The two vertical dashed lines denote the most critical ARO bands (15.8 MHz–ARO-1 and 43.5 MHz–ARO-2). The clustering of impedance per TOV peaks around these frequency bands indicates elevated risk of TOV-induced voltage stress and possible insulation breakdown, underscoring the value of DM-impedance analysis for assessing ARO proximity and ensuring robust motor-drive operation.

Among the tested cable lengths, the 5 m cable shows strong 2nd and 4th impedance peaks that coincide with ARO-1 and ARO-2; and 13 m cable shows a pronounced 4th peak near the ARO-1. These alignments make them the most critical contributors to ARO formation, increasing the risk of voltage stress and

Authorized licensed use limited to: Tallinn University of Technology. Downloaded on July 07,2026 at 09:03:38 UTC from IEEE Xplore. Restrictions apply.

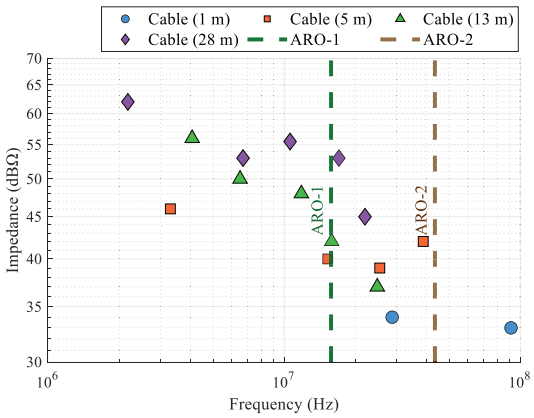


Fig. 24. Cable–motor impedance interaction presenting TOV peaks vs multiple ARO margin using 1 m, 5 m, 13 m, and 28 m cables.

insulation degradation at the motor terminals. Moreover, the 28 m cable shows a resonance peak (4th) occurring near the ARO-1 frequency, indicating a risk at that specific point.

Mitigating the ARO-driven stress is best approached through targeted impedance shaping rather than broad filtering. This study presents that certain cable configurations exhibit impedance peaks near ARO frequency bands. The goal is to shift dominant peaks away from the adverse ARO bands by modest adjustments to cable machine parameters. The idea is to tune cable length or routing, modify shield/ground terminations, or adjust machine-side parasitic elements that set the DM/CM paths. This impedance-sensitivity strategy avoids the overdesign associated with generic filters and achieves practical relief by aligning the cable–motor impedance profile to miss the critical ARO frequencies, thereby improving reliability without excess components or complexity.

This study aims to formulate an impedance-sensitivity and reliable operating area (ROA) design framework for cable-fed motor drive systems to reduce the TOV events and mitigate the ARO-band interactions. Analyzing the coupling between impedance and resonance provides a practical basis for optimizing cable and motor system configurations to steer voltage stress away from ARO bands or suppress harmful resonances. In this role, the method can function as a design tool for ARO mitigation via impedance-based tuning and targeted drive-system changes.

VII. Conclusion and Outlooks

This study presents a comprehensive GBM for an induction machine that characterizes behavior from low–to–HF up to 100 MHz by incorporating steady-state parameters, self- and mutual-coupling inductances, and parasitic capacitances. Parameters are initialized analytically and then refined through optimization, enabling precise yet less labor-intensive simulations whose frequency responses reproduce critical waveforms such as multiple TOV and CMV.

GBM reduces the analytical and computational burden while maintaining high fidelity in the frequency-dependent interactions among inverters, cables, and machine windings. Experimental results show consistent agreement between measured and modeled responses across the low–to–HF bands. Unlike conventional lumped models, the GBM reproduces multiple TOV and DM-impedance resonances and links them to estimated terminal overvoltage and common-mode voltage stress, providing a clearer basis for EMI-aware design and insulation assessment. A current limitation is that the model targets wider band steady-state behavior and does not capture LF dynamic performance (e.g., electromechanical transients, control-loop interactions, or saturation/temperature effects); these aspects are left for future integration into a unified LF–HF modeling workflow.

Additionally, the GBM framework provides valuable insights into system-level impedance representation, fault analysis, and insulation-stress evaluation, making it a valuable resource for electromagnetic transient simulations and the design of diagnostic systems spanning low–to–HF.

Appendix A

Tables III and IV present the initial analytical and final optimized parameters for the IM and cable GBMs, respectively. The optimized parameters were obtained through a parameter-fitting process that refines initial estimates to achieve improved accuracy in impedance and voltage profile estimation, as demonstrated in the contributed work.

TABLE III
7.5 kW IM Machine GBM Parameters (In Y-connections)

Parameter	Value	Parameter	Value	Parameter	Values
P (kW)	7.5 @ 50 Hz	N_r (r/min)	1460	$U_{a/Y}$ (V)	690
Inertia (Kg.m^2)	0.05	Q_s (stator slot)	36	*Phase*	3
$D_{s,i}$ (mm) (inner)	132	$D_{s,o}$ (mm) (outer)	220	Pole	4
Initial (analytical) parameters (before optimization)					
R_s (Ω)	0.68	R_r (Ω)	0.45	L_s (mH)	4.15
L_{mag} (μH)	0.15	L_r (mH)	4.15	R_T (kΩ)	2.7
C_{WG} (nF)	1.7	C_T (pF)	172	L_{DM} (mH)	28.8
C_{G1} (pF)	600	L_T (mH)	24	C_{CM} (nF)	1.8
C_{G2} (pF)	1100	L_{CM} (mH)	8.4	C_P (pF)	1200
R_{G1} (Ω)	1.34	L_{eq} (mH)	2.4	C_{DM} (pF)	799
R_{G2} (Ω)	300	L_c (μH)	0.13	C_B (pF)	218
R_E (kΩ)	6.6	C_{RG} (nF)	24.5	C_{WR} (nF)	1.8
Final optimized parameters					
R_s (Ω)	0.64	R_r (Ω)	0.46	L_s (mH)	4.21
L_{mag} (μH)	0.14	L_r (mH)	4.08	R_T (kΩ)	2.55
C_{WG} (nF)	1.64	C_T (pF)	165.37	L_{DM} (mH)	28.90
C_{G1} (pF)	590.03	L_T (mH)	23.35	C_{CM} (nF)	1.71
C_{G2} (pF)	1074.4	L_{CM} (mH)	8.21	C_P (pF)	1197.86
R_{G1} (Ω)	1.29	L_{eq} (mH)	2.38	C_{DM} (pF)	768.8
R_{G2} (Ω)	291.37	L_c (μH)	0.14	C_B (pF)	222.72
R_E (kΩ)	6.23	C_{RG} (nF)	25.83	C_{WR} (nF)	1.79

Using the GBM optimal fitting procedure, the mean error significantly decreases across all measurement representations compared with the initial model as shown in Figs. 17 and 22. The improvement is summarized by error-reduction index (ERI, %),

Authorized licensed use limited to: Tallinn University of Technology. Downloaded on July 07,2026 at 09:03:38 UTC from IEEE Xplore. Restrictions apply.

TABLE IV
CABLE GBM PARAMETERS PER UNIT LENGTH

Parameter	Value	Parameter	Value	Parameter	Value
Initial (analytical) parameters (before optimization)					
R_{s1} (mΩ)	5.4	C_{p1} (nF)	95	R_{s2} (mΩ)	40
L_{s1} (μH)	0.5	C_{p2} (nF)	20	R_{p1} (MΩ)	13
L_{s2} (μH)	7.8	R_{p2} (kΩ)	11.2	R_g (mΩ)	5.4
L_g (μH)	0.5	R_{gr1} (MΩ)	14	R_{gr2} (kΩ)	11.2
C_{gr1} (nF)	95	C_{gr2} (nF)	20		
Final optimal parameters					
R_{s1} (mΩ)	5.32	C_{p1} (nF)	91.08	R_{s2} (mΩ)	37.89
L_{s1} (μH)	0.47	C_{p2} (nF)	19.17	R_{p1} (MΩ)	13.26
L_{s2} (μH)	8.02	R_{p2} (kΩ)	11.69	R_g (mΩ)	5.47
L_g (μH)	0.48	R_{gr1} (MΩ)	14.34	R_{gr2} (kΩ)	10.55
C_{gr1} (nF)	100.4	C_{gr2} (nF)	21.09		

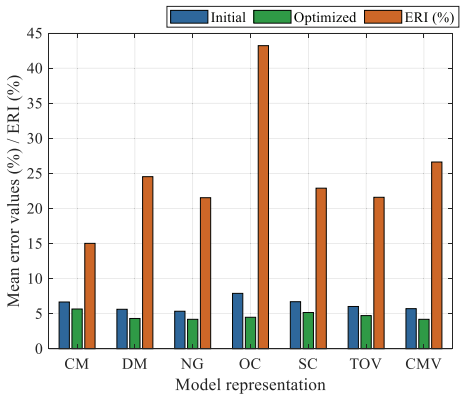


Fig. 25. Comparison of mean error values (%) across different models, highlighting the error reduction index (%) achieved through optimized parameter fitting using the GBM.

which quantifies the relative between the initial and optimized error as follows:

$$ERI\,(\%) = \frac{E_{init} - E_{opt}}{E_{init}} \times 100. \tag{15}$$

A higher ERI indicates a larger gain from the optimization step and more reliable voltage estimations over the evaluated band.

APPENDIX B

A. Calculation of the Common Mode Voltage of the Three-Phase IM Drive System [24]

$$V_{CM} = \frac{V_{aG} + V_{bG} + V_{cG}}{3} - \frac{V_{aN} + V_{bN} + V_{cN}}{3} \tag{16}$$

REFERENCES

[1] B. Asad, T. Vaimann, A. Belahcen, A. Kallaste, A. Rassõlkin, and M. N. Iqbal, "The cluster computation-based hybrid fem– Analytical model of induction motor for fault diagnostics," *Appl. Sci.*, vol. 10, no. 21, 2020, Art. no. 7572, doi: 10.3390/app10217572.

[2] J. E. Ruiz-Sarrio, J. A. Antonino-Daviu, A. Navarro-Navarro, and V. Biot-Monterde, "A review of broadband frequency techniques for insulation monitoring and diagnosis in rotating electrical machines," *IEEE Trans. Ind. Appl.*, vol. 60, no. 4, pp. 6092–6102, Jul./Aug. 2024, doi: 10.1109/TIA.2024.3384454.

[3] M. U. Sardar et al., "Inverter-fed motor drive system: A systematic analysis of condition monitoring and practical diagnostic techniques," *Energies*, vol. 16, no. 15, Jul. 2023, Art. no. 5628, doi: 10.3390/en16155628.

[4] X. Ju et al., "Voltage stress calculation and measurement for hairpin winding of EV traction machines driven by SiC MOSFET," *IEEE Trans. Ind. Electron.*, vol. 69, no. 9, pp. 8803–8814, Sep. 2022, doi: 10.1109/TIE.2021.3116577.

[5] M. U. Sardar, T. Vaimann, L. Kütt, B. Asad, A. Kallaste, and K. Kudelina, "Characterization of high-frequency impedance-based models for transient terminal overvoltage estimation in cable-fed motor drive systems," in *Proc. Int. Conf. Elect. Machines*, Sep. 2024, pp. 1–7, doi: 10.1109/ICEM60801.2024.10700495.

[6] O. Magdun and A. Binder, "High-frequency induction machine modeling for common mode current and bearing voltage calculation," *IEEE Trans. Ind. Appl.*, vol. 50, no. 3, pp. 1780–1790, May/Jun. 2014, doi: 10.1109/TIA.2013.2284301.

[7] V. Karakasl, F. Gross, T. Braun, H. De Gersem, and G. Griepentrog, "High-frequency modeling of delta-and star-connected induction motors," *IEEE Trans. Electromagn. Compat.*, vol. 64, no. 5, pp. 1533–1544, Oct. 2022, doi: 10.1109/TEMC.2022.3181337.

[8] M. S. Toulabi, L. Wang, L. Bieber, S. Filizadeh, and J. Jatskevich, "A universal high-frequency induction machine model and characterization method for arbitrary stator winding connections," *IEEE Trans. Energy Convers.*, vol. 34, no. 3, pp. 1164–1177, Sep. 2019, doi: 10.1109/TEC.2019.2891349.

[9] P. Xie, G. Vakil, and C. Gerada, "Electric drive systems with long feeder cables," *IET Electr. Power Appl.*, vol. 14, no. 1, pp. 16–30, 2020, doi: 10.1049/iet-epa.2018.5507.

[10] T. Plazenet, T. Boileau, C. Caironi, and B. Nahid-Mobarakeh, "A comprehensive study on shaft voltages and bearing currents in rotating machines," *IEEE Trans. Ind. Appl.*, vol. 54, no. 4, pp. 3749–3759, Jul./Aug. 2018, doi: 10.1109/TIA.2018.2818663.

[11] F. A. Kharanaq, A. Emadi, and B. Bilgin, "Modeling of conducted emissions for EMI analysis of power converters: State-of-the-art review," *IEEE Access*, vol. 8, pp. 189313–189325, 2020, doi: 10.1109/ACCESS.2020.3031693.

[12] B. Narayanasamy, A. S. Sathyanarayanan, F. Luo, and C. Chen, "Reflected wave phenomenon in SiC motor drives: Consequences, boundaries, and mitigation," *IEEE Trans. Power Electron.*, vol. 35, no. 10, pp. 10629–10642, Oct. 2020, doi: 10.1109/TPEL.2020.2975217.

[13] Y. Azadeh et al., "Cable and motor winding impedance interactions in motor drive systems and its impact on HF overvoltages," *IEEE Trans. Power Electron.*, vol. 39, no. 1, pp. 1244–1253, Jan. 2024, doi: 10.1109/TPEL.2023.3322639.

[14] H. Miloudi, M. Miloudi, A. Gourbi, M. H. Bermaki, A. Bendaoud, and A. Zeghoudi, "A high-frequency modeling of AC motor in a frequency range from 40 Hz to 110 MHz," *Elect. Eng. Electromechanics*, vol. 2022, no. 6, pp. 3–7, 2022, doi: 10.20998/2074-272X.2022.6.01.

[15] H. Dai, R. A. Torres, T. M. Jahns, and B. Sarlioglu, "Comparative study of conducted common-mode EMI in WBG-enabled DC-fed three-phase current-source inverter," *IEEE J. Emerg. Sel. Topics Power Electron.*, vol. 10, no. 6, pp. 7188–7204, Dec. 2022, doi: 10.1109/JESTPE.2022.3161422.

[16] M. U. Sardar, T. Vaimann, L. Kütt, B. Asad, A. Kallaste, and R. Land, "Wideband frequency response analysis for sensitive condition estimation of machine's turn insulation degradation faults," in *Proc. IEEE Workshop Elect. Machines Des., Control Diagnosis*, Apr. 2025, pp. 1–6, doi: 10.1109/WEMDCD61816.2025.11014207.

[17] J. Sun and L. Xing, "Parameterization of three-phase electric machine models for EMI simulation," *IEEE Trans. Power Electron.*, vol. 29, no. 1, pp. 36–41, Jan. 2014, doi: 10.1109/TPEL.2013.2264750.

[18] M. Keller, T. Petri, M. Waldhof, F. Schuller, M. Maier, and N. Parspour, "Modeling the dynamic voltage distribution in electric traction motor windings and its application on HV optimal winding design," *IEEE Trans. Ind. Appl.*, vol. 60, no. 3, pp. 3820–3829, May/Jun. 2024, doi: 10.1109/TIA.2024.3357053.

[19] H. Peng et al., "Voltage distribution modeling along stator windings in permanent magnet synchronous machines using coil-based grey box models," *IEEE Trans. Energy Convers.*, vol. 39, no. 3, pp. 1994–2007, Sep. 2024, doi: 10.1109/TEC.2024.3370800.

[20] A. Boglietti and E. Carpaneto, "An accurate induction motor high-frequency model for electromagnetic compatibility analysis," *Electric Power Compon. Syst.*, vol. 29, no. 3, pp. 191–209, 2001, doi: 10.1080/153250001300006626.

Authorized licensed use limited to: Tallinn University of Technology. Downloaded on July 07,2026 at 09:03:38 UTC from IEEE Xplore. Restrictions apply.

[21] H. Peng, Y. Yu, and K. Hameyer, "Conductor-based modeling of a single-tooth winding for EMI simulation," *IEEE Trans. Power Electron.*, vol. 39, no. 9, pp. 11099–11109, Sep. 2024, doi: 10.1109/TPEL.2024.3403669.
[22] P. C. Krause, O. Wasynczuk, and S. D. Sudhoff, *Analysis of Electric Machinery and Drive Systems*. Hoboken, NJ, USA: Wiley, 2010, doi: 10.1109/9780470544167.
[23] S. Zhu and B. Shi, "Modeling of PWM-induced iron losses with frequency-domain methods and low-frequency parameters," *IEEE Trans. Ind. Electron.*, vol. 69, no. 3, pp. 2402–2413, Mar. 2022, doi: 10.1109/TIE.2021.3065626.
[24] S. Baig, S. Ebrahimi, J. Jatskevich, L. Wang, and A. Fani, "Wide-band constant-parameter voltage-behind-reactance model of squirrel-cage induction machines," *IEEE Trans. Energy Convers.*, vol. 40, no. 1, pp. 185–196, Mar. 2025, doi: 10.1109/TEC.2024.3420897.
[25] A. S. Abdel-Khalik, S. Ahmed, A. A. Elserougi, and A. M. Massoud, "A voltage-behind-reactance model of five-phase induction machines considering the effect of magnetic saturation," *IEEE Trans. Energy Convers.*, vol. 28, no. 3, pp. 576–592, Sep. 2013, doi: 10.1109/TEC.2013.2258467.
[26] L. Wang, C. N. M. Ho, F. Canales, and J. Jatskevich, "High-frequency modeling of the long-cable-fed induction motor drive system using TLM approach for predicting overvoltage transients," *IEEE Trans. Power Electron.*, vol. 25, no. 10, pp. 2653–2664, Oct. 2010, doi: 10.1109/TPEL.2010.2047027.
[27] B. Mirafzal, G. L. Skibinski, R. M. Tallam, D. W. Schlegel, and R. A. Lukaszewski, "Universal induction motor model with low-to-high frequency-response characteristics," *IEEE Trans. Ind. Appl.*, vol. 43, no. 5, pp. 1233–1246, Sep./Oct. 2007, doi: 10.1109/TIA.2007.904401.
[28] G. Vidmar and D. Miljavec, "A universal high-frequency three-phase electric-motor model suitable for the delta- and star-winding connections," *IEEE Trans. Power Electron.*, vol. 30, no. 8, pp. 4365–4376, Aug. 2015, doi: 10.1109/TPEL.2014.2352452.
[29] H. Peng et al., "High-frequency modeling of permanent magnet synchronous machines using grey box models," *IEEE Trans. Transport. Electrific.*, vol. 10, no. 4, pp. 8150–8160, Dec. 2024, doi: 10.1109/TTE.2024.3363511.
[30] H. Liu, X. W. Zhang, and L. P. Tu, "A modified particle swarm optimization using adaptive strategy," *Expert Syst. Appl.*, vol. 152, 2020, Art. no. 113353, doi: 10.1016/j.eswa.2020.113353.



Muhammad Usman Sardar (Student Member, IEEE) was born in 1989 in Rahim Yar Khan, Pakistan. He received the B.Sc. and M.Sc. degrees in electrical power engineering from The Islamia University of Bahawalpur, Punjab, Pakistan. He is currently working toward the Ph.D. degree with Tallinn University of Technology, Tallinn, Estonia. His research interests include condition monitoring and fault diagnostics of electrical machines.



Toomas Vaimann (Senior Member, IEEE) was born in Pärnu, Estonia, in 1984. He received the B.Sc., M.Sc. and Ph.D. degrees in electrical engineering from the Tallinn University of Technology, Tallinn, Estonia, in 2007, 2009 and 2014 respectively. He is currently a Research Professor with the Department of Electrical Engineering, Tallinn University of Technology. Internationally, he has been a Postdoctoral Researcher with the Department of Electrical Engineering and Automation, Aalto University, Espoo, Finland. His main research focuses on the diagnostics of electrical machines.



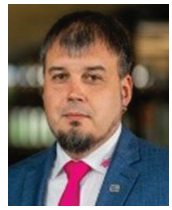
Lauri Kütt (Senior Member, IEEE) received the B.Sc. degree in computer and automation technology and the M.Sc. degree in electrical power engineering from the Tallinn University of Technology, Tallinn, Estonia, in 2002 and 2004, respectively, and the Ph.D. degree from the Department of Energy and Geotechnology, Tallinn University of Technology, in 2012. He is currently a Professor with the Department of Electrical Power Engineering and Mechatronics, Tallinn University of Technology. His current research interests include fast transients on electric power lines, diagnostics, power quality, and EMC.



Bilal Asad (Senior Member, IEEE) was born in 1986 in Pakistan. He received the B.Sc. degree in electronics engineering from The Islamia University of Bahawalpur, Bahawalpur, Pakistan and the M.Sc. degree in electrical engineering from the University of Engineering and Technology, Lahore, Pakistan and the Ph.D. degree from Tallinn University of Technology, Tallinn, Estonia and the Department of Electrical Engineering and Automation, Aalto University, Espoo Finland. His research interests include design, modeling, and fault diagnostics of electrical machines.



Ants Kallaste (Senior Member, IEEE) was born in Pärnu, Estonia in 1980. He received the B.Sc., M.Sc. and Ph.D. degrees in electrical engineering from the Tallinn University of Technology, Tallinn, Estonia, in 2004, 2006, and 2013, respectively. He is currently a Professor of electrical machines with the Department of Electrical Power Engineering and Mechatronics, Tallinn University of Technology. He is also the Head of Electrical Machines Research Group. He is also the member of Estonian Society of Moritz Hermann Jacobi.



Anton Rassõlkin (Senior Member, IEEE) born in Tallinn, Estonia, in 1985, holds a strong academic background in electric drives and power electronics. He received the B.Sc., M.Sc., and Ph.D. degrees from the Tallinn University of Technology, Tallinn, Estonia, in 2008, 2010, and 2014, respectively and the Dipl.-Ing. degree in automation from the University of Applied Science Giessen Friedberg, Giessen, Germany. He is currently a Tenure Track Professor in mechatronics with the Department of Electrical Power Engineering and Mechatronics, Tallinn University of Technology. His primary research interests include mechatronics and electrical drives, with a particular focus on applications in electric transportation and autonomous vehicles, including the development of their digital twins.

Authorized licensed use limited to: Tallinn University of Technology. Downloaded on July 07,2026 at 09:03:38 UTC from IEEE Xplore. Restrictions apply.

Appendix 4

Publication IV

M. U. Sardar, T. Vaimann, L. Kütt, B. Asad, A. Kallaste and H. A. Raja, "Wideband Frequency Diagnosis for High-Sensitivity Turn-Insulation Degradation Estimation in Inverter-Fed Machines," *2025 IEEE Symposium on Diagnostics for Electric Machines, Power Electronics and Drives (SDEMPED)*, Dallas, TX, USA, 2025, pp. 1-7, doi: 10.1109/SDEMPED53223.2025.11154298.

2025 IEEE Symposium on Diagnostics for Electric Machines, Power Electronics and Drives (SDEMPED) | 979-8-3503-8820-6/25/$31.00 ©2025 IEEE | DOI: 10.1109/SDEMPED53223.2025.11154298

Wideband Frequency Diagnosis for High-Sensitivity Turn-Insulation Degradation Estimation in Inverter-Fed Machines

Muhammad Usman Sardar
Department of Electrical Power Engineering and Mechatronics
Tallinn University of Technology
19086 Tallinn, Estonia
muhammad.sardar@taltech.ee

Toomas Vaimann
Department of Electrical Power Engineering and Mechatronics
Tallinn University of Technology
19086 Tallinn, Estonia
toomas.vaimann@taltech.ee

Lauri Kütt
Department of Electrical Power Engineering and Mechatronics
Tallinn University of Technology
19086 Tallinn, Estonia
lauri.kutt@taltech.ee

Bilal Asad
Department of Electrical Power Engineering and Mechatronics
Tallinn University of Technology
19086 Tallinn, Estonia
bilal.asad@taltech.ee

Ants Kallaste
Department of Electrical Power Engineering and Mechatronics
Tallinn University of Technology
19086 Tallinn, Estonia
ants.kallaste@taltech.ee

Hadi Ashraf Raja
Department of Electrical Power Engineering and Mechatronics
Tallinn University of Technology
19086 Tallinn, Estonia
hadi.raja@taltech.ee

***Abstract*— Stator turn insulation degradation is a critical failure mode in inverter-fed induction motors, often leading to unexpected shutdowns and safety hazards. Detecting this fault at an early stage remains difficult due to the weak high-frequency signatures it produces. This paper presents a grey-box modeling (GBM) approach for machines to identify their insulation-related parameters through optimal fitting using experimental impedance spectroscopy. High-frequency switching oscillation currents, captured under both healthy and degraded conditions, are analyzed in the fractional Fourier domain to enhance the sensitivity of fault representation. A resonance-centered optimal Mel filter bank (RMFB) is proposed to further improve the sensitivity of insulation degradation state estimation. Experimental validation on a 0.75 kW inverter-fed motor demonstrates that the proposed RMFB method achieves approximately seven times greater sensitivity in early fault estimations compared to the conventional FFT-based technique. The approach is lightweight, scalable, and suitable for real-time implementation in industrial motor drive systems, offering a robust solution for proactive insulation health monitoring.**

***Keywords*—Common mode impedance, Differential mode impedance, High-frequency machine modeling, Induction machine, Inverter drives.**

I. INTRODUCTION

Modern inverter-fed electric machines are essential in drive applications due to their energy efficiency and precise control. However, they are more susceptible to faults, necessitating effective condition monitoring [1], [2]. Modern power electronic device-based inverters generate high-frequency (HF) switching harmonics and reflected wave overvoltage (RWO) stresses on the machine's windings, accelerating insulation degradation and hence increasing the risk of failure. Implementing advanced monitoring techniques is crucial to detect early signs of deterioration of insulation and ensure reliable operation [3], [4]. Such faults can lead to catastrophic failures, causing unexpected downtime and high repair costs. Therefore, effective monitoring of insulation health is crucial for reliable operation [5]. Stator faults, particularly inter-turn insulation degradation, are a critical cause of failures in inverter-fed electric machine [6]. Traditional insulation monitoring methods, such as partial discharge (PD) and surge tests, often focus on ground-wall insulation, neglecting turn-to-turn degradation. Moreover, these methods are either destructive, require high impulse voltages, or are susceptible to inverter electromagnetic noise, making them less suitable for online monitoring in low-voltage machines [5], [7].

Wideband frequency response analysis (WFRA), which covers a high-frequency range particularly from 20 Hz to 100 MHz, has proven to be an effective diagnostic tool for identifying insulation degradation in inverter-fed machines. It provides high-resolution insights into turn-to-turn insulation faults across a wideband frequency spectrum [8], [9]. Analyzing changes in the machine's common mode (CM) and differential mode (DM) impedance and resonance characteristics across a wide frequency spectrum provides a reliable, non-invasive method for detecting early-stage insulation faults. However, developing a detailed machine model that accurately captures frequency behavior across a wide range of frequencies (wideband) and adapting signal processing techniques to represent its frequency spectrum remain significant challenges. For machine parametric identification, a grey-box model (GBM) of the machine, incorporating the effects of the cable and inverter, can be used with optimal fitting [10], [11]. Using the measured impedance-frequency profile and tracking the motor's resonance and anti-resonance behavior, insulation-related parameters can be identified, with turn capacitance being the key factor in determining the machine's insulation condition. WFRA utilizes HF switching oscillation currents generated during high switching operation, eliminating the need for external excitation sources [12], [13].

This research presents a proposed GBM of the induction motor (IM), explicitly incorporating the influence of both the inverter and cable to characterize machine behavior across a

Authorized licensed use limited to: Tallinn University of Technology. Downloaded on November 14,2025 at 17:03:11 UTC from IEEE Xplore. Restrictions apply.

wide frequency range accurately. The machine parameters are identified through optimal fitting of the measured impedance–frequency profile. This enables precise estimation of insulation-related characteristics, with turn capacitance established as a key indicator of insulation health. Subsequently, the research study employs an advanced signal processing technique, specifically the optimal FRFT combined with a resonance-centered Mel filter bank (RMFB). This RMFB methodology enhances time-frequency resolution, enabling the precise extraction of features associated with insulation degradation, particularly within resonance-sensitive frequency regions. The main contributions of this work are as follows:

- A GBM-based WFRA framework is proposed, combining IM parametric modeling and optimal FRFT with RMFB signal processing to extract insulation impedance features across a wideband frequency range.
- A new state estimation factor (SEF) metric is introduced to evaluate different levels of insulation degradation.
- Experimental validation on a 0.75 kW inverter-fed IM demonstrates the improvement of early-stage insulation fault estimation sensitivity by approximately sevenfold compared to conventional techniques.

The rest of the paper is structured as follows: Section II outlines the stator turn-insulation monitoring framework; Section III describes the measurement setup and impedance identification; Section IV presents the experimental results; Section V details the adapted methodology; Section VI discusses the performance evaluation; and Section VII concludes the paper.

II. Stator Turn Insulation Monitoring

A. Mechanism of Turn Insulation Degradation in Machines

Turn insulation degradation can lead to severe faults, like turn-to-turn short circuits, causing high currents and heat that compromise phase insulation. Rapid progression from minor faults to failure underscores the importance of early detection. One of the most indicative markers of this degradation is the change in turn-to-turn capacitance. As insulation deteriorates, especially in machines insulated with polyester-imide (PI) materials, the equivalent turn capacitance C_i tends to increase. Experimental studies have reported a 20% to 50% rise in C_i over the course of insulation aging or failure [11], [12]. This phenomenon is mathematically expressed by (1):

$$C_i = \varepsilon_o \varepsilon_r \frac{l_i l}{2 e_i} \tag{1}$$

Where ε_o and ε_r are the permittivity of free space and relative permittivity of the insulation material. l_i is the width of the turn, l is the length of the turn, and e_i is the insulation thickness. As insulation degrades, thinning or increased conductivity alters the effective dielectric properties, leading to a measurable rise in turn-to-turn capacitance C_i. Tracking this change offers a non-invasive, quantitative marker of aging [8].

In this research paper, changes in turn-insulation capacitance are simulated by adding additional capacitance $C_{T,\,Degraded}$ to the motor phase *a*. These variations serve as key degradation markers, underscoring the need for precise and sensitive diagnosis techniques.

B. Proposed Low-to-High Frequency Parametric IM GBM

The proposed IM model, depicted in Fig. 1, employs a grey-box modeling approach with detailed low to HF response parameters to analyze the motor's impedance behavior in conjunction with the cable and inverter. The proposed model of an IM includes key parameters: $R_{E,I}$ (iron-loss resistance), $L_{T,i}$, $R_{T,i}$ and $C_{T,i}$ (phase inter-turn branch elements) for HF behavior. R_S , $L_{S,i}$, and $M_{ab,i}$ are stator resistance, self and mutual inductance, while $R_{G,i}$ and $C_{G,i}$ represent the frame grounding resistance and capacitance. C_P and M_C account for phase-to-phase parasitic capacitance and mutual inductances representing at first turn and connections. Rotor parameters include R_r (resistance), L_r (leakage inductance), and L_{mag} (magnetizing inductance). The motor frame ground G serves as a common reference, and n, equal to ten, denotes the number of distributed segments for detailed analysis.

The proposed model parameters are optimized using the particle swarm optimization (PSO) algorithm to minimize errors between the simulated model response and measured experimental impedance and phase data. The initial IM parameters are computed from equations in [14], [15], with ±20% variation to aid optimization. A particle swarm optimization (PSO) algorithm then refines these parameters by minimizing the error between simulated and measured impedance and phase data.

The parameters of the proposed GBM precisely represent the resonance and anti-resonance frequencies of the machine's winding. CM impedance exhibits two natural resonance frequencies: series resonance/antiresonance (f_{AR}) and parallel resonance (f_R).

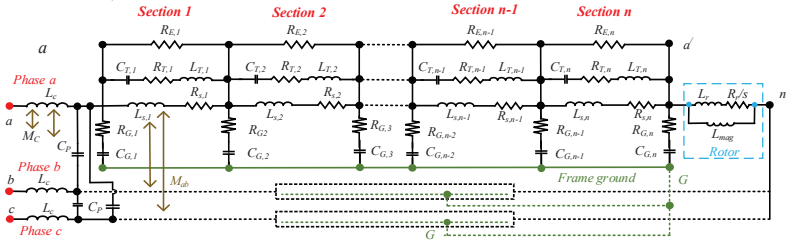


Fig. 1. Proposed low-to-high frequency parametric GBM of the IM.

Authorized licensed use limited to: Tallinn University of Technology. Downloaded on November 14,2025 at 17:03:11 UTC from IEEE Xplore. Restrictions apply.

C. Fractional Fourier Transform (FRFT) Method

FRFT generalizes the traditional FFT, transitioning from the time domain to an intermediate fractional domain [8]. FRFT method shows improved performance across varying $C_{T,Degraded}$ conditions. The FRFT of a signal $x(t)$ for a fractional order α is given by (2)-(3):

$$FRFT_{\alpha}(x(t)) = \int_{-\infty}^{\infty} x(t')K_{\alpha}(t,t')dt' \tag{2}$$

Where the Kernel function $K_{\alpha}(t,t')$is defined as use

$$K_{\alpha}(t,t') = \begin{cases} \sqrt{1-j\cot(\alpha)}e^{j\pi(t^2+t'^2)\cot(\alpha)-2jtt'\,\mathrm{cosec}(\alpha)}, & \alpha \neq n\pi \\ \delta(t-t'), & \alpha = 0 \\ \delta(t-t'), & \alpha = \pi \end{cases} \tag{3}$$

Where $\alpha = p\pi/2$ defines the angular displacement, where p is the order representing the rotation by the fractional multiplication by right angle (90^0) relative to the time axis, where t' denotes the fractional order frequency axis.

(a) Optimal FRFT with Proposed RMFB

The conventional Mel filter bank uses overlapping triangular filters that mimic the human ear's frequency perception. As defined in (4), these filters are distributed in the LF region and become progressively wider in the HF region, following the Mel scale's nonlinear characteristics [16], [17].

$$Mel(f) = 2595\log_{10}(1+\frac{f_0}{700}) \tag{4}$$

The frequency mapping of a customized MEL filter, RMFB, is defined in (5).

$$Mel_{centered}(f) = m.\arctan\left(\log_{10}\left(1+\frac{f}{f_0}\right)\right) + D \tag{5}$$

Where f_0 is the center frequency of the region under investigation, m is the scaling factor (set to two in this study), and D represents the frequency offset applied during the Mel filter bank design. The values are chosen based on the frequency band most sensitive to parallel resonance point (f_R).

III. Measurement Setup

A. HF Frequence Impedance Measurement

Fig. 2 shows the HF impedance measurement over the 20 Hz–120 MHz range, including the impedance analyzer and motor interface used to capture impedance magnitude and phase profiles.

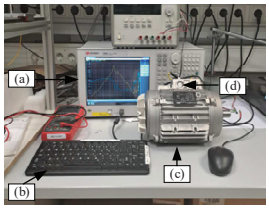


Fig. 2. Impedance measurement setup (a) impedance analyzer, (b) keyboard input interface, (c) IM, and (d) BNC input motor connection box.

B. Test Bench for Time Domain Analysis

Fig. 3 illustrates the experimental test bench setup consisting of a cable-fed inverter drive with a 5-meter power cable operating at a 10 kHz switching frequency. High-bandwidth probes (100 MHz) and an oscilloscope are employed to capture voltage and current waveforms. The IM operates at a 50 Hz fundamental frequency, and the acquired signals are recorded for post-processing and analysis.

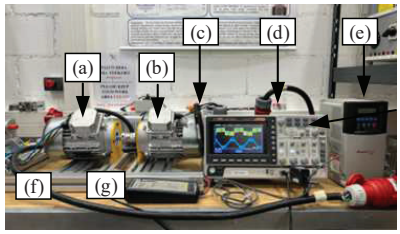


Fig. 3. Testbench setup: (a) load IM, (b) test IM, (c) HF current probe, (d) oscilloscope, (e) inverter, (f) 5 m power cable, (g) HF differential probe.

The average nominal stator turn-to-turn capacitance C_T of the IM winding was estimated as 368 pF by applying an optimal fitting procedure. To simulate insulation degradation, external capacitors ranging from 0.31 nF to 1.8 nF were connected across the IM stator's phase a winding.

IV. Experimental Results

A. Frequency Domain Validation

Fig. 4 (a) and (b) demonstrates the frequency domain validation by comparing the measured and modeled impedance profiles in DM and CM schematics. The top plot in part (a) shows the impedance magnitude, while the bottom plot in part (a) illustrates the phase response.

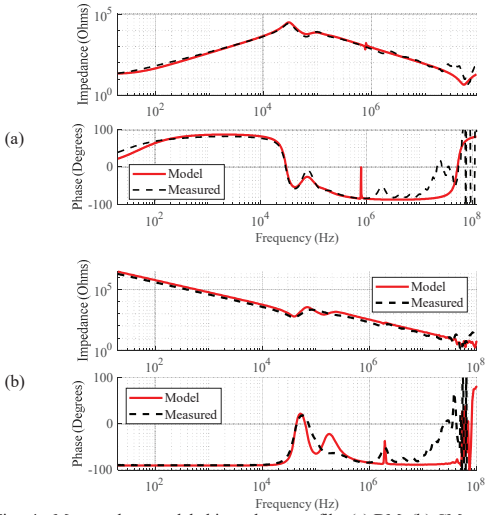


Fig. 4. Measured vs. modeled impedance profile: (a) DM, (b) CM.

Authorized licensed use limited to: Tallinn University of Technology. Downloaded on November 14,2025 at 17:03:11 UTC from IEEE Xplore. Restrictions apply.

B. Measured Signal Representation

The high switching voltage, V_{ab}, and oscillation current waveforms (I_a) waveforms during no-load IM operation are shown in Fig. 5. The phase current oscillation was used to analyze the insulation characteristics. Each switching oscillation spans 0.1 ms, as defined by the inverter's switching frequency.

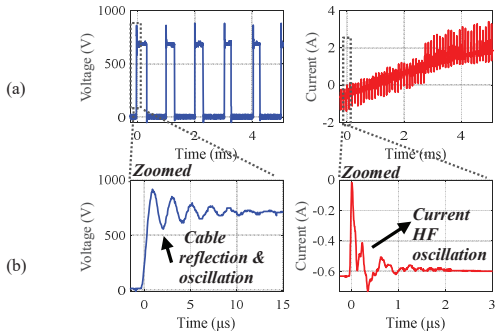


Fig. 5. Testbench signals: (a) V_{ab} and I_a; (b) zoomed high-time-domain view.

V. Methodology of Insulation State Estimation

The flowchart in Fig. 6 illustrates the complete workflow for insulation degradation analysis. It begins with experimental measurements and parameter identification using a GBM model, followed by optimal fitting through a cost function. The process then incorporates advanced signal processing techniques, including FFT, FRFT, and optimal FRFT with customized RMFB to extract sensitive features related to insulation faults.

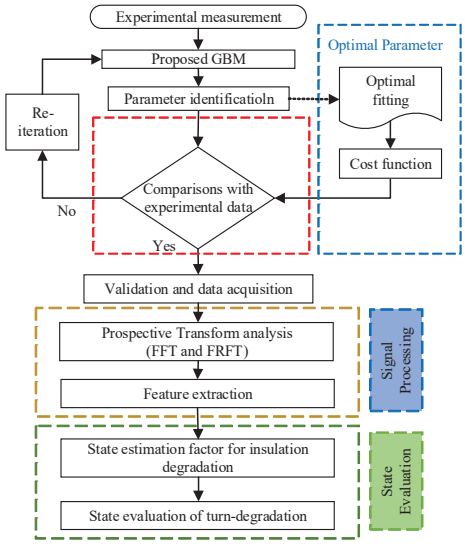


Fig. 6. Schematic of wideband frequency-based diagnosis for turn-insulation degradation.

The setup includes HF sensors (differential and current) (100 MHz) for capturing voltage and current signals in the high time domain. The signal acquisition was performed at a 100 mega-samples-per-second (MSps) rate, utilizing 100 single oscillation samples for post-processing.

A. Turn Insulation Degradation Fault Implementation

The insulation degradation fault is emulated in the motor's phase a by inserting external capacitors as the turn-to-turn capacitance $C_{T,\,Degraded}$, ranging from 0.31 nF to 1.80 nF. Every time, the motor's impedance response is recorded to analyze the cumulative effect of degradation. Fig. 7 presents the DM and CM impedance profile under health and various degraded cases. The resonance frequency f_R is observed to be 28 kHz, core frequency region (Δf_{OBS}) is from 10 kHz to 10 MHz.

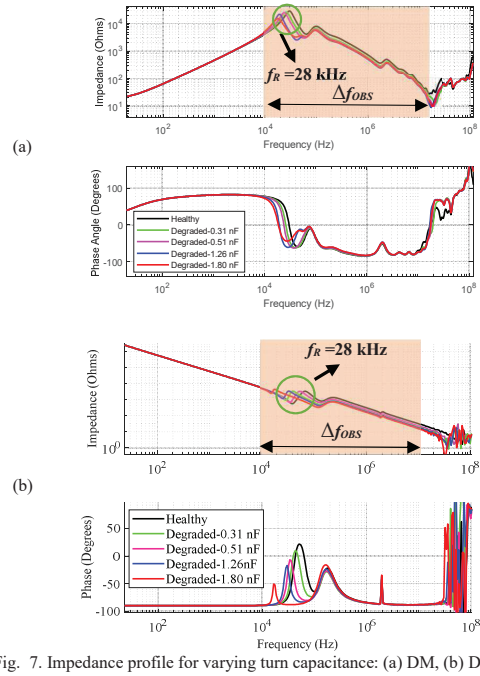


Fig. 7. Impedance profile for varying turn capacitance: (a) DM, (b) DM.

Table I outlines the degraded capacitance selections and their impact on the cumulative turn capacitance of the motor, as identified through re-iteration of optimal fitting procedure as stated in section II-(B). C'_T represents the turn capacitance changes, while $\Delta C'_T = C'_T - C_T$ indicates deviations from the healthy nominal value of C_T =368 pF.

TABLE I. Extracted Parameters of IM with Different $C_{T,\,Degraded}$.

$C_{T,\,Degraded}$ (nF)	$\Delta C'_T$ (pF)	Severity $\Delta C'_T / C_T$ (%)
0.31	11.2	3.04
0.51	34.8	9.46
1.26	53.7	14.59
1.80	93.5	25.40

Authorized licensed use limited to: Tallinn University of Technology. Downloaded on November 14,2025 at 17:03:11 UTC from IEEE Xplore. Restrictions apply.

VI. Performance Evaluation of RMFB

High-bandwidth current sensors capture the corresponding HF degraded currents, as illustrated in Fig. 8. Signal processing techniques such as FFT and FRFT are initially applied to analyze these oscillation patterns. These methods offer limited capability to isolate frequency components and detect variations in amplitude, dominant frequencies, and resonance behavior across different levels of degradation.

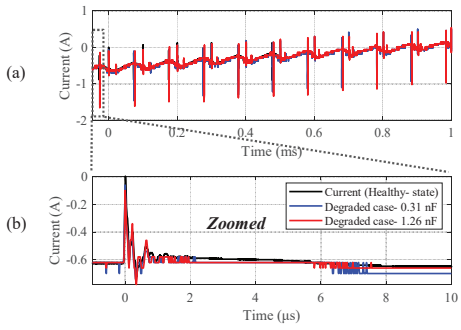


Fig. 8. Motor current (I_a): (a) time-domain signal, (b) zoomed view highlighting transients

A. Performance Evaluation for Tracing Degradation States

SEF is proposed for status evaluation based on the mean average error (MAE) between the healthy state and degraded current signal cases, as defined in (6)-(7).

$$MAE = \frac{1}{m}\sum_{i=1}^{m}\left|x_i^* - x_i\right| \tag{6}$$

$$SEF = \Delta MAE\% = \frac{MAE}{Mean\left(x_i^*\right)} \times 100\% \tag{7}$$

Where m resents the total samples, x_i^* denotes initial healthy case and x_i denotes multiple degradation cases. In these cases, $C_{T,Degraded}$ =0 nF or the healthy case was chosen as the benchmark reference

B. FFT Analysis of Current Oscillations

The time-domain signal of the motor line current (I_a) is analyzed for both healthy and degraded cases. Frequency-domain representation is essential for accurate analysis. The Fourier transform of the different current signals is computed and illustrated in Fig. 9.

C. FRFT Representation

In Fig. 10, the FRFT-processed signals display significantly enhanced waveform variations compared to the raw switching oscillation current, at the optimal order p=0.87. The fractional order (α) in the FRFT was empirically optimized to achieve maximum resolution and changes (MAE) between healthy and degraded signals, making it well-suited for detecting subtle variations. This was achieved through sensitivity analysis between the fractional order and MAE, with an optimal order of p=0.79 identified. Fig. 11 shows the FRFT spectrum of a single switching oscillation signal at varying fractional orders. The figure highlights that the FRFT spectrum reveals frequency-domain features sensitive to insulation changes.

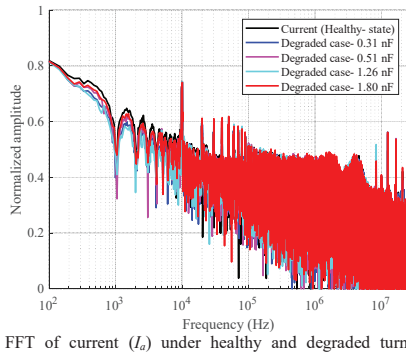


Fig. 9. FFT of current (I_a) under healthy and degraded turn-insulation conditions.

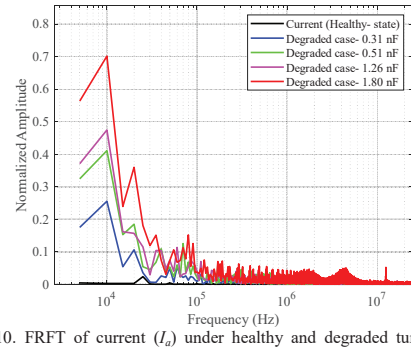


Fig. 10. FRFT of current (I_a) under healthy and degraded turn-insulation conditions.

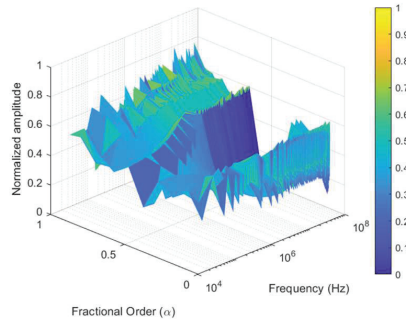


Fig. 11. FRFT spectrum of single switching oscillation current for 0.1 ms signal.

D. Proposed FRFT with RMFB Method

To further improve feature extraction, a customized Mel filter bank was integrated into the FRFT domain. The signal processing was implemented on MATLAB Simulink. The proposed customized Mel filter (RMFB) was explicitly designed to focus on the resonance-sensitive frequency region around 28 kHz, where degradation features are most prominent.

Authorized licensed use limited to: Tallinn University of Technology. Downloaded on November 14,2025 at 17:03:11 UTC from IEEE Xplore. Restrictions apply.

The filter enhances the amplitude of this core region (Δf_{OBS}) and suppresses irrelevant HF components, enabling more accurate detection.

The customized optimal FRFT-RMFB method, as defined in (5), is applied to the same dataset and demonstrates a substantial improvement in sensitivity.

Fig. 12 present the calculated MAE increases steadily with simulated degradation levels ($C_{T,Degraded}$), tracking turn insulation deterioration and performance of filtered algorithm.

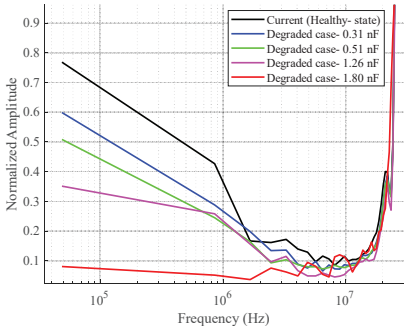


Fig. 12. Proposed RMFB of current (I_a) under healthy and degraded turn-insulation conditions.

Table II presents a comparative sensitivity analysis (SEF) among FFT, F, and FRFT-RMFB methods. The FRFT-RMFB method outperforms all others, especially at lower degradation levels (e.g., 310 pF), demonstrating its superiority in early-stage fault detection, as shown in Fig. 13.

As observed in the time-domain signal, directly identifying turn insulation degradation remains challenging. The FRFT method outperforms FFT by extracting richer features, enhancing the detection of turn insulation deterioration. However, the FRFT combined with the RMFB demonstrates higher sensitivity, offering a more accurate estimation of the insulation degradation state, especially in early fault conditions.

As listed, the SEF for FFT is only 6.33% at $C_{T,Degraded}$ = 1.8 nF. However, with RMFB implementation processing, this value rises to 44.40%, representing almost a significant sevenfold improvement over the conventional FFT method.

TABLE II. COMPARISON OF SEF (%) WITH DIFFERENT METHODS

$C_{T,Degraded}$ (nF)	FFT (%)	FRFT (%)	Proposed RMFB (%)
0.31	1.47	4.33	15.77
0.51	2.83	9.28	19.02
1.26	4.94	10.72	28.73
1.80	6.33	15.49	44.40

The SEF percentage change increases non-linearly with the proposed RMFB approach, particularly at lower capacitance values, demonstrating its superior effectiveness in detecting early-stage insulation degradation.

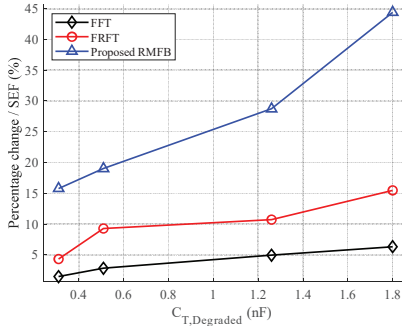


Fig. 13. SEF (%) comparison using different methods.

VII. CONCLUSION

Online monitoring of stator turn insulation conditions in inverter-fed machines is crucial for preventing sudden and catastrophic failures in safety-critical applications such as electric vehicles and high-speed railway traction systems. This research proposes a novel and robust framework to enhance the sensitivity and reliability of detecting stator turn insulation degradation. The approach integrates a low-to-HF GBM of motor impedance parameters, advanced signal processing using the optimal FRFT, and a customized RMFB designed around resonance-sensitive frequency regions. The validation was performed through detailed experimental studies, leading to the following key conclusions:

1. Proposed RMFB with optimal FRFT extracts subtle spectral features of insulation deterioration, offering superior detection sensitivity over FFT or other signal processing methods.
2. The novel RMFB filter, aligned with impedance resonance regions, enhances feature resolution while reducing computation.
3. The proposed method achieves nearly sevenfold improvement in early-stage insulation fault detection by tracking degradation capacitance variations.
4. This method provides a reliable platform for predictive maintenance in real-time applications like electric traction and industrial drives.

REFERENCES

[1] A. Abid, M. T. Khan, and J. Iqbal, "A review on fault detection and diagnosis techniques: basics and beyond," *Artif Intell Rev*, vol. 54, no. 5, 2021, doi: 10.1007/s10462-020-09934-2.

[2] B. Asad, T. Vaimann, A. Rassõlkin, A. Kallaste, and A. Belahcen, "Review of Electrical Machine Diagnostic Methods Applicability in the Perspective of Industry 4.0," *Electrical, Control and Communication Engineering*, vol. 14, no. 2, 2018, doi: 10.2478/ecce-2018-0013.

[3] D. Zheng, G. Lu, Y. Wu, Q. Zhang, and P. Zhang, "Online Detection and Classification of Interturn and Groundwall Insulation Aging Based on Broadband Common-Mode Impedance Spectrum," *IEEE Transactions on Industrial Electronics*, vol. 71, no. 3, 2024, doi: 10.1109/TIE.2023.3265024.

[4] J. Dittmann, M. England, and B. Ponick, "Design of hairpin windings considering the transient potential distribution," *Elektrotechnik und*

Authorized licensed use limited to: Tallinn University of Technology. Downloaded on November 14,2025 at 17:03:11 UTC from IEEE Xplore. Restrictions apply.

Informationstechnik, vol. 140, no. 2, 2023, doi: 10.1007/s00502-023-01129-1.

[5] J. E. Ruiz-Sarrio, J. A. Antonino-Daviu, A. Navarro-Navarro, and V. Biot-Monterde, "A Review of Broadband Frequency Techniques for Insulation Monitoring and Diagnosis in Rotating Electrical Machines," *IEEE Trans Ind Appl*, vol. 60, no. 4, pp. 6092–6102, 2024, doi: 10.1109/TIA.2024.3384454.

[6] D. Xiang, H. Li, H. Yan, Y. Zheng, N. Zhao, and B. Liu, "Online Monitoring of Incipient Turn Insulation Degradation for Inverter-Fed Machine Using Sensitive Tail Component in PWM Switching Oscillations," *IEEE Trans Power Electron*, vol. 36, no. 8, 2021, doi: 10.1109/TPEL.2021.3049809.

[7] D. Zheng and P. Zhang, "A Review of Fault Diagnosis and Online Condition Monitoring of Stator Insulation in AC Electrical Machine," 2019. doi: 10.13334/j.0258-8013.pcsee.182067.

[8] R. Fan, X. Lei, T. Jia, M. Qin, H. Li, and D. Xiang, "High-sensitive state perception method for inverter-fed machine turn insulation based on FrFT-Mel," *Global Energy Interconnection*, vol. 7, no. 2, pp. 155–165, Apr. 2024, doi: 10.1016/j.gloei.2024.04.004.

[9] D. Zheng, G. Lu, and P. Zhang, "An Improved Online Stator Insulation Monitoring Method Based on Common-Mode Impedance Spectrum Considering the Effect of Aging Position," *IEEE Trans Ind Appl*, vol. 58, no. 3, 2022, doi: 10.1109/TIA.2022.3160131.

[10] H. Peng, Z. Luo, Y. Yu, and K. Hameyer, "Modeling Voltage Distribution Along the Hairpin Windings of an Electrical Machine Using Impedance Fitting," in *2024 International Conference on Electrical Machines (ICEM)*, IEEE, Sep. 2024, pp. 1–7. doi: 10.1109/ICEM60801.2024.10700566.

[11] H. Peng, Y. Yu, and K. Hameyer, "Conductor-Based Modeling of a Single-Tooth Winding for EMI Simulation," *IEEE Trans Power Electron*, vol. 39, no. 9, pp. 11099–11109, 2024, doi: 10.1109/TPEL.2024.3403669.

[12] M. U. Sardar, T. Vaimann, L. Kütt, B. Asad, A. Kallaste, and R. Land, "Wideband Frequency Response Analysis for Sensitive Condition Estimation of Machine's Turn Insulation Degradation Faults," in *2025 IEEE Workshop on Electrical Machines Design, Control and Diagnosis (WEMDCD)*, IEEE, Apr. 2025, pp. 1–6. doi: 10.1109/WEMDCD61816.2025.11014207.

[13] H. Li, Y. Gu, D. Xiang, P. Zhang, P. P. Yue, and Y. Cui, "Online Condition Monitoring of Line-End Coil Insulation for Inverter-Fed Machine by Switching Oscillation Mode Decomposition," *IEEE Transactions on Industrial Electronics*, vol. 69, no. 11, 2022, doi: 10.1109/TIE.2021.3120491.

[14] J. Sun and L. Xing, "Parameterization of three-phase electric machine models for EMI simulation," *IEEE Trans Power Electron*, vol. 29, no. 1, 2014, doi: 10.1109/TPEL.2013.2264750.

[15] M. U. Sardar, T. Vaimann, L. Kütt, B. Asad, A. Kallaste, and K. Kudelina, "Characterization of High-Frequency Impedance-Based Models for Transient Terminal Overvoltage Estimation in Cable-Fed Motor Drive Systems," in *2024 International Conference on Electrical Machines (ICEM)*, IEEE, Sep. 2024, pp. 1–7. doi: 10.1109/ICEM60801.2024.10700495.

[16] Y. Chen, G. Peng, Z. Zhu, and S. Li, "A novel deep learning method based on attention mechanism for bearing remaining useful life prediction," *Applied Soft Computing Journal*, vol. 86, 2020, doi: 10.1016/j.asoc.2019.105919.

[17] Y. Wang, D. Sheng, H. Hu, K. Han, J. Zhou, and L. Hou, "A Novel Series Arc Fault Detection Method Based on Mel-Frequency Cepstral Coefficients and Fully Connected Neural Network," *IEEE Access*, vol. 10, 2022, doi: 10.1109/ACCESS.2022.3206547.

BIOGRAPHIES

Muhammad Usman Sardar was born in 1989 in Rahim Yar Khan, Pakistan. He obtained his B.Sc. and M.Sc. in Electrical Power Engineering from The Islamia University of Bahawalpur, Punjab, Pakistan, and is pursuing a Ph.D. at Tallinn University of Technology in Estonia. His research interests include condition monitoring and fault diagnostics of electrical machines.

Toomas Vaimann (S'11-M'14-SM'20) was born in Pärnu, Estonia, in 1984 and received his BSc, MSc and PhD degrees in electrical engineering from Tallinn University of Technology, Estonia, in 2007, 2009 and 2014 respectively. He is currently a research professor at Tallinn University of Technology, Department of Electrical Engineering. Internationally, he has been a postdoctoral researcher at the Department of Electrical Engineering and Automation, Aalto University, Espoo, Finland. His main research interest is the diagnostics of electrical machines.

Lauri Kütt (Senior Member, IEEE) received the B.Sc. degree in computer and automation technology and the M.Sc. degree in electrical power engineering from the Tallinn University of Technology, Tallinn, Estonia, in 2002 and 2004, respectively, and the Ph.D. degree from the Department of Energy and Geotechnology, Tallinn University of Technology, in 2012. He is currently a Professor and his current research interests include fast transients on electric power lines, power line diagnostics, power quality, and electromagnetic compatibility.

Bilal Asad was born in 1986 in Pakistan. He received his BSc in Electronics Engineering from The Islamia University of Bahawalpur and MSc in Electrical Engineering from University of Engineering and Technology (UET) Lahore, Pakistan and PhD from Tallinn University of Technology, Estonia and Department of Electrical Engineering and Automation, Aalto University, Espoo Finland. His area of interest includes design, modeling and fault diagnostics of electrical machines.

Ants Kallaste was born in Pärnu, Estonia in 1980 and received his BSc, MSc and PhD degrees in electrical engineering from Tallinn University of Technology, Estonia, in 2004, 2006 and 2013 respectively. He is currently a Professor of Electrical Machines at Tallinn University of Technology, Department of Electrical Power Engineering and Mechatronics. In addition, he holds the position of Head of Electrical Machines Research Group. He is the senior researcher of IEEE and member of Estonian Society of Moritz Hermann Jacobi.

Authorized licensed use limited to: Tallinn University of Technology. Downloaded on November 14,2025 at 17:03:11 UTC from IEEE Xplore. Restrictions apply.

Appendix 5

Publication V

M. U. Sardar, T. Vaimann, L. Kütt, B. Asad, and A. Kallaste, “Switching oscillation-based fractional-domain high-sensitive diagnosis of machine turn insulation degradation,” *Engineering Science and Technology, an International Journal*, vol. 72, Dec. 2025, doi: 10.1016/j.jestch.2025.102.

Engineering Science and Technology, an International Journal 72 (2025) 102224

Contents lists available at ScienceDirect

Engineering Science and Technology, an International Journal

journal homepage: www.elsevier.com/locate/jestch

Full Length Article

Switching oscillation-based fractional-domain high-sensitive diagnosis of machine turn insulation degradation

Muhammad Usman Sardar *, Toomas Vaimann, Lauri Kütt, Bilal Asad, Ants Kallaste

Department of Electrical Power Engineering and Mechatronics, Tallinn University of Technology, 19086 Tallinn, Estonia

ARTICLE INFO

Keywords:
Common mode impedance
High-frequency machine modeling
Induction machine
Turn insulation
Frequency transform analysis

ABSTRACT

Stator turn insulation degradation is a significant cause of failure in electric machines fed by high-frequency switching power electronic devices, making early-stage detection challenging due to weak fault characteristic signatures. This paper presents a novel non-invasive monitoring framework that integrates a proposed low-to-high-frequency parametric grey-box model (GBM) of the motor with advanced signal processing techniques. Key electrical parameters of the motor are extracted using optimal fitting with impedance spectroscopy, which represent frequency-dependent behaviors influenced by insulation degradation. To enhance detection sensitivity, the method employs an optimized fractional Fourier transform at the optimal order, coupled with a customized resonance-centred Mel filter bank (FRFT-RMFB). Experimental results on a 0.75 kW induction motor with controlled insulation degradation, implemented by parallel capacitive loading, show a higher improvement in early-stage fault sensitivity. The proposed FRFT-RMFB method enhances the sensitivity of turn insulation state estimation by nearly sevenfold compared with the conventional Fourier transform approach. The proposed framework is lightweight, generalized, and well-suited for real-time predictive maintenance, effectively minimizing false alarms in safety–critical applications such as industrial drives, electric vehicles, and high-speed rail systems. This work contributes to a new direction in frequency-domain diagnostics, combining accurate parametric modeling with high-resolution spectral feature extraction for early detection of insulation faults.

1. Introduction

The rapid growth of renewable energy and the widespread adoption of electric vehicles have heightened the focus on ensuring the reliability of electrical machine drive system [1,2]. By the application of advanced speed control strategies, the demand of high energy efficiency and modern inverter-fed machines is now extensively utilized across various applications [3,4]. Main occurring faults in electric machines are typically classified into three categories: stator-related (like winding insulation degradation and turn short circuit), rotor-related and bearing-related faults. Literature shows that stator faults comprise one-third of electric machine faults as demonstrated in the Fig. 1 [5,6]. The stator winding insulation is among the most failure-prone elements of a drive system, accounting for nearly 80% of stator electrical faults, most of which originate from localized inter-turn degradation [7,8].

In inverter-fed machines, insulation degradation is caused by various factors such as overvoltage stress, partial discharge, increased heating, high *dv/dt* transients, or mechanical vibrations [9]. A notable recent trend is the increasing adoption of high-switching power devices, which are progressively replacing conventional silicon-based power electronics. This shift results in higher switching frequencies and elevated operating voltages, placing greater stress on the insulation systems of electric machines.

Condition monitoring is essential for improving the reliability of electric machines. Insulation condition monitoring techniques are generally classified into offline and online methods [10]. Established offline testing techniques have laid the groundwork for the development of modern online monitoring approaches. Common offline tests include partial discharge (PD), insulation resistance, polarization index, and dissipation factor/capacitance (DF/C) tests [11,12],.

Online condition monitoring techniques are increasingly preferred because they enable real-time evaluation of dielectric health without interrupting machine operation. Methods such as impedance spectroscopy, surge testing, and leakage current monitoring [13] have been investigated for online insulation assessment. Nevertheless, most of these approaches primarily address groundwall insulation, while turn-to-turn degradation has received comparatively little attention. Currently, surge and partial discharge (PD) tests remain the

* Corresponding author.
E-mail address: muhammad.sardar@taltech.ee (M.U. Sardar).

https://doi.org/10.1016/j.jestch.2025.102224
Received 31 July 2025; Received in revised form 13 October 2025; Accepted 30 October 2025
Available online 10 November 2025
2215-0986/© 2025 The Author(s). Published by Elsevier B.V. on behalf of Karabuk University. This is an open access article under the CC BY license (http://creativecommons.org/licenses/by/4.0/).

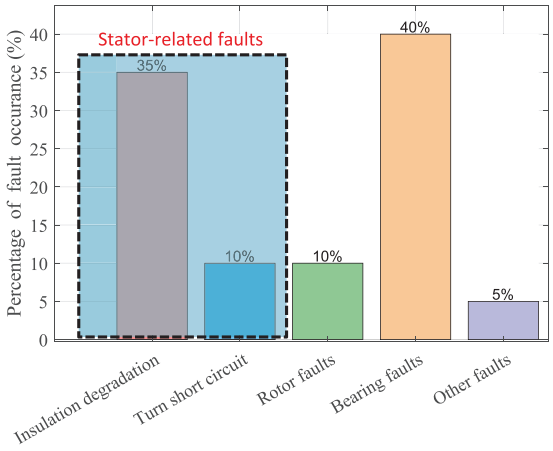


Fig. 1. Distribution of electric machine fault types.

predominant techniques for stator turn insulation evaluation. However, surge testing requires the application of high-voltage impulses, which may accelerate insulation deterioration, whereas online PD testing is highly vulnerable to inverter-induced electromagnetic interference and noise, limiting its practicality for low-voltage inverter-fed machines.

The current insulation diagnosis model provides limited study on the one-to-one link between ageing at specific locations (slot section, end winding, turn to turn) and the proposed indicator. In practice, capacitance and dissipation factor (C/DF) methods based on leakage current monitoring are established for mains-fed machines [14,15]. Real ageing studies report that insulation capacitance changes after degradation [16,17], and electrical stress can speed up this change [18]. Microstructural changes such as cracks, voids, polymer chain scission, and delamination modify the effective permittivity and field distribution, so parasitic capacitances shift: therefore, C/DF is a useful condition indicator [19]. Long-term overheating promotes oxidation and delamination, creating air-filled voids that usually reduce capacitance, while moisture or oil ingress and conductive contamination at the end windings can increase the measured capacitance: at high voltage, partial discharges in voids may also alter the apparent capacitance [20]. Overall, a 20 to 50 % variation in parasitic insulation capacitance is a practical marker of winding insulation degradation [21,22].

However, detecting changes in C/DF is challenging due to the high insulation impedance at low frequencies (LF), which necessitates the use of sensitive and expensive sensors. To enhance the responsiveness of online insulation monitoring, recent research has focused on exploiting the high-frequency (HF) characteristics of the drive system. These approaches fall into two main categories: the HF injection method and the inverter switching self-excitation method [23,24]. While the HF injection method requires an external excitation source that can interfere with machine operation, the self-excitation approach utilizes the inherent HF content generated by inverter switching, thereby eliminating the need for external stimuli and avoiding operational disruption.

In [25], HF behavior of the inverter was examined through the transient current response triggered by inverter switching, revealing that HF signatures can serve as effective indicators of turn insulation degradation. Furthermore, in [26], modeled the HF oscillation current generated during inverter switching as the resonant response of the stator winding's parasitic parameters, thereby enabling the detection of incipient turn insulation degradation via the switching transient frequency response. More recently, as in [27], the authors introduced and experimentally validated the tail component of the switching oscillation current as a reliable diagnostic feature for identifying turn insulation degradation in inverter-fed machines. In recent developments, the detailed parametric model, like grey-box models (GBMs), has gained prominence for representing the dynamic frequency behavior of machines with cables and inverters, where multiple low to HF machine parameters are identified through optimal fitting techniques. Compared to conventional lumped models, more generalized and section-wise representations provide improved accuracy in characterizing turn-to-turn insulation degradation phenomena [28,29]. These GBMs also provide valuable insight and a foundation for wideband frequency response analysis (WFRA) across low- to HF ranges by enabling the tracking of various existing machine parameters [30,31].

Despite the gradual deterioration of turn insulation, the resulting variations in HF switching oscillation current are subtle, which restricts the diagnostic resolution achievable in either the time or frequency domain. According to Heisenberg's uncertainty principle, it is fundamentally impossible to achieve optimal resolution in both domains simultaneously [32]. To address this limitation, the fractional Fourier transform (FRFT) can provide a powerful alternative, enabling flexible signal analysis within the fractional domain, where resolution can be enhanced by adjusting the fractional order [33]. The FRFT method has been broadly employed across various fields, including signal identification and radar communication systems [34].

In this work, the responsiveness of switching oscillation currents to insulation degradation is addressed using a design of experiment (DoE) by introducing external capacitors, and a high-sensitivity state estimation framework is proposed under HF supply or inverter excitation. Real-time thermal or chemical agent-based ageing D0E was not undertaken because it would irreversibly alter the test bench, pose contamination and safety risks, and preclude reuse of the machines for repeated trials and calibration. Instead, authors focused on a high-sensitivity state estimation framework validated under controlled electrical stresses that are compatible with safe, repeatable experimentation. In future work, it is planned to implement accelerated, real-time degradation (e.g., elevated heating and related stresses) and incorporate dedicated post-processing for analysis.

The proposed method employs a FRFT at the optimal order, coupled with a customized resonance-centred Mel filter bank (RMFB). This method first develops a comprehensive GBM of the machine, incorporating key frequency-dependent parameters to precisely quantify turn insulation capacitance. It supports the design of a customized optimal FRFT-RMFB filter to enhance detection sensitivity. The proposed filter is designed based on the machine common-mode (CM) impedance resonance frequency, further enhancing feature extraction. Additionally, the mean absolute error (MAE) or root mean square error (RMSE) is proposed as a quantitative evaluation metric for assessing the existing insulation condition.

The proposed method is experimentally applied to a 0.75 kW induction motor (IM), demonstrating substantial improvements in sensitivity for estimating incipient turn-to-turn insulation degradation. Compared to prior methods, this approach offers the following potential contributions:

- A WFRA-based framework, integrating a parametric GBM motor model (fitted via impedance spectroscopy across 20 Hz–100 MHz) with customized optimal FRFT-RMFB signal processing, for accurate tracking of frequency-dependent turn insulation degradation.
- A customized FRFT-RMFB filter bank, aligned with the machine's common-mode resonance, enhances the extraction of degradation-sensitive spectral features in the fractional domain.
- The proposed state estimation factor (SEF), derived from MAE, provides a robust quantitative index for assessing insulation degradation severity.
- Experimental validation on a 0.75 kW induction motor with controlled capacitive degradation ($C_{T,Degraded}$ = 0.31–1.80 nF) achieved a sevenfold improvement in early fault estimation sensitivity/SEF (76.06%) compared to FFT (9.39%).

The rest of the paper is organized as follows:

Section 2 outlines the overall framework for turn insulation degradation faults. Section 3 describes the diagnostic methodology in detail. Section 4 presents experimental measurement procedures and test bench setup. Section 5 evaluates the performance of the proposed approach using a HF supply configuration, while Section 6 assesses RMFB effectiveness with an inverter supply. Finally, Section 7 concludes the paper.

2. Turn insulation degradation faults in electric machine

2.1. Stator winding insulation ageing

Insulation degradation in stator windings is a critical reliability concern in inverter-fed electric machines, often leading to incipient turn-to-turn faults that can rapidly escalate into severe short circuits. These faults result in localized hot spots, excessive circulating currents, and potential breakdown of phase-to-phase or groundwall insulation. Owing to the short timescale in which minor degradation may evolve into catastrophic failure, early-stage estimation is imperative for predictive maintenance and fault prevention [35].

Thus, the fluctuation in turn capacitance (C_i), governed by the properties of the insulation material, especially in materials like polyester-imide (PI), can serve as a reliable indicator of insulation ageing. The value of C_i was calculated using Eq. (1), as referenced in [36].

$$C_i = \varepsilon_o \varepsilon_r \frac{l_i l}{2e_i} \tag{1}$$

where ε_o and ε_r are the permittivity of free space and relative permittivity of the insulation material. l_i is the width of the turn, l is the length of the turn, and e_i is the insulation thickness. This rise in capacitance provides a non-invasive and quantitative marker of insulation health, making it ideal for continuous monitoring strategies.

The external-capacitor emulation targets the capacitive branch of early turn-insulation drift; it does not fully capture resistive carbonization or PD channel formation. We therefore treat it as a controlled surrogate and corroborate its trends using stress-induced experiments. In this study, experimental tests typically use samples that replicate real insulation structures, including complete stators. Therefore, the outcomes of these studies can provide valuable insights into real ageing parameters and post-processing the fed-current signal for representing the diagnosis of machine turn insulation degradation. In the literature, a summary of relevant experimental results is presented in Table 1, highlighting observed changes in capacitance as a severity factor ($\Delta C'/C$) under various insulation ageing conditions. These studies consistently report capacitance increases ranging from 10% to higher, depending on the material type, temperature index, and oven exposure levels.

Table 1
Representation of accelerated ageing in the machine through capacitance variation.

Ref.	Ageing Sample	Machine/Coil model	Method and variation range	Severity $\Delta C'/C$ (%)
[27]	Full stator – accelerated aging	Coil/ conductor-based model	Capacitance degradation (0.1–4.7 nF)	2.11–22.40
[31]	Stator interturn and ground-wall-at multiple tapping	Mult-section winding model	Capacitance degradation (0.22–0.47 nF)	12–38.5
[37]	Localized stator-ground wall (turn 16th-48th)	Per turn lumped CM model	Capacitance degradation (1.70 nF)	13–22
[38]	Stator turn at phase *a*	Simple lumped parametric model	Capacitance degradation	2.11–22.40
[39]	Line-end coil insulation	HF π-lumped coil model	Capacitive degradation (0.025–0.68 nF)	0–20
Proposed FRFT-RMFB	**Stator turn at phase *a***	**Detailed parametric GBM**	**Capacitance degradation (0.3–1.8 nF)**	**3.04–25.40**

In this research paper, changes in turn-insulation capacitance are simulated by adding additional capacitance C_T, Degraded to the motor phase a-a' connections. These variations are key degradation markers, highlighting the need for precise and sensitive monitoring techniques.

2.2. Proposed low to HF machine's parametric GBM model

The proposed GBM IM model, depicted in Fig. 2, employs a grey-box modeling approach with detailed low-to-HF response parameters to analyze the motor's impedance behavior. The proposed model of an IM includes key parameters: $R_{E,i}$ (iron-loss resistance), $L_{T,i}$, $R_{T,i}$ and $C_{T,i}$ (phase inter-turn branch elements) for HF behavior. $R_{S,i}$, $L_{S,i}$, and $M_{ab,i}$ are stator resistance, self and mutual inductance, while $R_{G,i}$ and $C_{G,i}$ represent the frame grounding resistance and capacitance. C_P and M_C account for phase-to-phase parasitic capacitance and mutual inductances, representing the first turn and connections. Rotor parameters include R_r (resistance), L_r (leakage inductance), and L_{mag} (magnetizing inductance). The motor frame ground G serves as a common reference, and n, equal to ten, denotes the number of distributed segments for detailed analysis.

(a) Parameter Identification Methodology by Optimal Fitting

The initial guess of the IM parameters is numerically derived from analytical equations in [40,41], with a 20% variation applied to guide the optimization process. The parameters are then refined using a particle swarm optimization (PSO) algorithm, which minimizes the error between the simulated model response and the experimentally measured impedance profile. The resulting parameter set effectively represents the average behavior of the distributed winding characteristics over the analyzed frequency range. These finalized parameters form the foundation of the proposed low-to-HF GBM and are detailed in Appendix 1.

(b) Cost Function for Optimal Impedance Parameter

The cost functions evaluate how good a particular solution is based on the objective function (Obj_1 and Obj_2) as defined in Eq. (2)-(3). Fitness for both objective functions is typically based on minimizing the mean squared error (MSE) between practical and modeled impedances and phase angles.

$$Obj_1(Z_j) = \frac{1}{n}\sum_{i=1}^{n}\left[\,|Z_{ini}(f_i,x_j)| - |Z_{prac}(f_i,x_j)|\,\right]^2,\ and\ Obj_2(\theta_j)$$
$$= \frac{1}{n}\sum_{i=1}^{n}\left[\,|\theta_{ini}(f_i,x_j)| - |\theta_{prac}(f_i,x_j)|\,\right]^2 \tag{2}$$

$$Minimize Obj_1(Z_j)\ and\ Obj_2(\theta_j),\ subject\ to\ P_{varied} = (1 \pm 0.2)P_{initial} \tag{3}$$

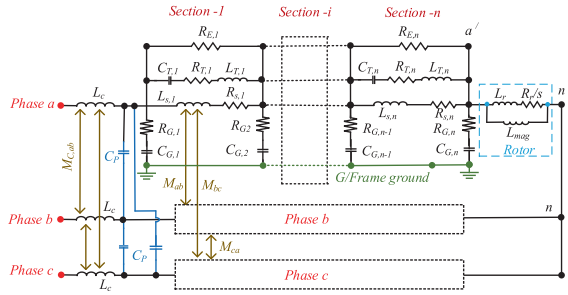


Fig. 2. Proposed low-to-HF parametric GBM model of IM.

where $P_{initial}$ represents the set of initial motor parameters proposed in GBM and P_{varied} denotes the corresponding parameter set after applying a ±20% variation. A lower MSE between model values and practical values indicates higher model fitness. Modified particle swarm optimization (MPSO) using the adaptive strategy as optimization algorithm (OA), inspired by bird flocking behavior, is used as an advanced OA to navigate complex, nonlinear, and multimodal solution spaces [42]. To prevent premature convergence and balance global exploration with local exploitation, MPSO uses a chaos-based nonlinear inertia weight, adaptive position updates, and terminal replacement, enhancing robustness for optimal solutions in complex problems. The initial parameter values extracted from the initial IM universal model and the finalised optimal values after optimal fitting are listed in Tables 13 and 14, respectively, and are added in Appendix 1.

3. Methodology for diagnosis of turn insulation degradation

3.1. FRFT method

FRFT extends the classical Fourier Transform or fast Fourier transform (FFT) by operating in an intermediate domain between time and frequency. This property makes it particularly effective for analyzing non-stationary or transient signals, such as those generated by HF switching in inverter-fed machines. Unlike conventional FFT and fixed-band filters, the FRFT can adaptively rotate the signal representation in the time–frequency plane to extract degradation-sensitive features [43]. The FRFT of a signal $x(t)$ for a fractional order α is given by Eq. (4):

The FRFT essentially performs a rotation of the signal representation by angle α in the time–frequency plane. When $\alpha = 0$, the FRFT reduces to the identity transform (time domain); when $\alpha = \pi/2$, it becomes the conventional Fourier transform (frequency domain).

$$FRFT_\alpha(x(t)) = \int_{-\infty}^{\infty} x(t')K_\alpha(t,t')dt' \tag{4}$$

Where the Kernel function $K_\alpha(t,t')$ is defined as in Eq. (5):

$$K_\alpha(t,t') = \begin{cases} \sqrt{1-j\cot(\alpha)}\, e^{j\pi(t^2+t'^2)\cot(\alpha)-2jtt'\mathrm{cosec}(\alpha)}, & \alpha \neq n\pi \\ \delta(t-t'), & \alpha = 0 \\ \delta(t-t'), & \alpha = \pi \end{cases} \tag{5}$$

This tunable transformation is critical for detecting subtle changes in waveform features that correlate with early-stage insulation degradation. As shown in the results section 5.1, an optimal fractional order (e.g., $p = 0.71$) maximizes sensitivity to fault-induced spectral shifts, forming the core of the developed algorithm [44].

3.2. Log-Gaussian filter bank (LGFB)

A set of logarithmically spaced Gaussian filters is applied to the FRFT spectrum to extract sensitive spectral features associated with turn insulation degradation [45]. The rationale for this approach stems from the fact that insulation degradation effects exhibit non-uniform frequency characteristics, with most of the energy concentrated near the system's parallel resonance frequency (F_P) and decaying gradually across adjacent frequency bands. This behavior is commonly observed in the common-mode and differential-mode impedance profiles of inverter-fed machines.

In contrast to triangular filters, which impose sharp boundaries and are less suited to modeling smooth spectral variations, Gaussian filters offer a continuous, smooth weighting function. This enables the LGFB to more effectively capture the distributed energy spread and resonance tails caused by evolving turn-to-turn capacitance and associated degradation. The implementation begins by defining a logarithmic frequency space spanning from 10 kHz to 10 MHz, covering the wide spectral window where insulation degradation signatures are most prominent. A total of $N = 10$ filters are positioned uniformly in this log-frequency space. The center frequencies μ_k of the filters are computed as in Eq. (6):

$$\mu_k = \log(f_k) \tag{6}$$

Each filter $G_k(f)$ is then defined by a Gaussian weighting function in the log-frequency domain in Eq. (7) [46]:

$$G_k(f) = \exp\frac{(-\log(f)-\mu_k)^2}{2\sigma^2} \tag{7}$$

here, σ controls the bandwidth of each filter in the log domain, enabling fine tuning of the spectral resolution and filter bank distribution is represented in Fig. 3.

3.3. Resonance-centered Mel filter bank (FRFT-RMFB)

In speech and audio signal processing, the Mel Filter Bank is a fundamental tool, most often used to compute Mel Frequency Cepstral Coefficients (MFCCs). It applies a series of triangular filters to the Mel-scaled frequency spectrum of the signal [47], as illustrated in Fig. 4.

Mel filter amplitudes increase much faster in the low-frequency range than in the mid- and high-frequency bands. The mapping of Mel frequency proceeds as Eq. (8) follows:

$$Mel(f) = 2595 \times \log_{10}(1+\frac{f_0}{700}) \tag{8}$$

Mel filter bank exhibits a non-linear distribution across the frequency axis. Filters are more densely concentrated in the LF region, offering finer resolution where human auditory sensitivity is highest. This mapping causes a steeper amplitude rise in the LF (0–4 kHz). range compared to the MF and HF regions.

While this mapping emphasizes the LF region, it is not well suited for insulation degradation, whose spectral effects concentrate near the machine's parallel resonance frequency at HF (near kHz to MHz). Extraction performance can be enhanced while reducing data volume by dynamically relocating the feature regions, beginning in the LF band, moving toward the resonance zone around F_R, and finally extending into the neighboring bands. The Mel-frequency mapping demonstrates the steepest slope near the characteristic frequency, indicating heightened spectral sensitivity in that region. Based on this observation, a novel resonance-centered Mel filter bank structure was designed, as illustrated in Fig. 5.

The customized resonance-centered Mel frequency (RMFB) mapping is distributed as Eq. (9) follows:

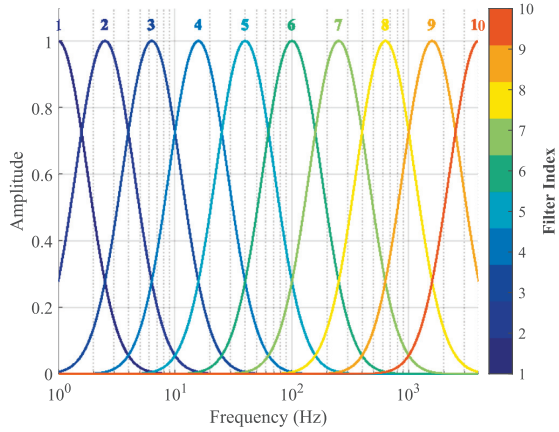


Fig. 3. Distribution of a conventional LGFB.

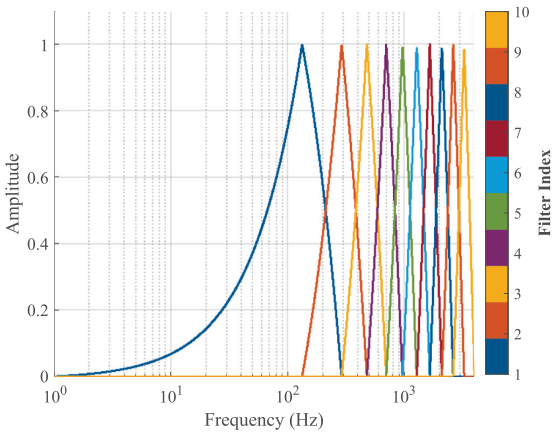


Fig. 4. Frequency distribution of filters in a standard Mel filter bank.

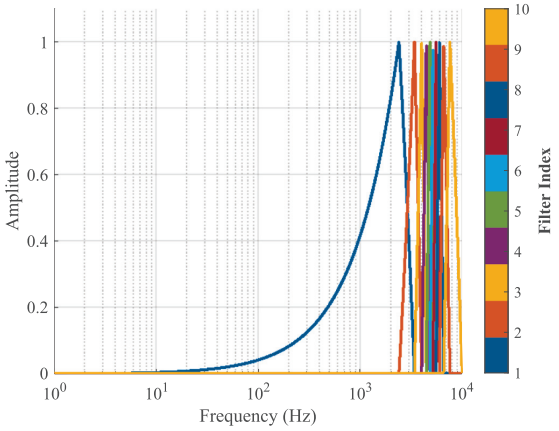


Fig. 5. Distribution of an adaptive RMFB.

$$Mel_{centered}(f) = m.\arctan\left(\log_{10}\left(1+\frac{f}{f_0}\right)\right)+D \tag{9}$$

where f_0, the center frequency of the mapping, was set to a higher kHz to align with higher resonance frequency (F_R) exhibited by machine's winding m, the scaling factor, was set to two to adjust the non-linear compression of the mapping and D, the offset, was set to 0 to ensure continuity at $f = f_0$. A core frequency region, denoted as Δf_{OBS}, around the reference F_R was defined within the range of 10 kHz-10 MHz to enhance the feature extraction [47]. Frequencies above 1 MHz were suppressed by setting filter weights to zero, reducing the influence of HF noise. The number of filters was set to 10, providing sufficient resolution across the sensitive bands. All post-processing was performed on a Core i7-1355U laptop with 16 GB RAM. The proposed FRFT-RMFB algorithm is band-limited to the switching-oscillation region and uses short-time records, minimizing both computational load and memory usage. Its core steps are FFT/FRFT transforms with complexity and a lightweight filter-bank projection over a limited frequency span, avoiding iterative solvers and large buffers. This design delivers low latency and modest resource demand, enabling real-time deployment on embedded CPUs without the need for dedicated accelerators.

3.4. State estimation and implementation Workflow

A step-by-step representation of the machine's turn insulation state estimation process by using a VFS supply or inverter-fed supply is illustrated in Fig. 6. The detailed methodology is outlined as follows:

i. Signal acquisition: wide-bandwidth current sensor is employed to capture the switching oscillation current generated by the supply. The recorded waveform is subsequently divided into individual oscillation cycles for detailed analysis.
ii. Signal processing: The segmented oscillation is processed using the optimal FRFT combined with resonance-centered Mel filtering (FRFT-RMFB) to extract time–frequency domain.
iii. Status evaluation: A uniform and identical MAE or RMSE is employed as the degradation index, quantifying the difference between healthy and degraded signal features. It is presented in Eq. (10)-(11) below.

$$MAE = \frac{1}{m}\sum_{i=1}^{m}\left|x_i^* - x_i\right| \tag{10}$$

$$RMSE = \sqrt{\frac{1}{m}\sum_{i=1}^{m}\left(x_i^* - x_i\right)^2} \tag{11}$$

where m represents the total sample count, x_i* denotes an initial or reference dataset case, and x_j denotes different degradation data representing an error data.

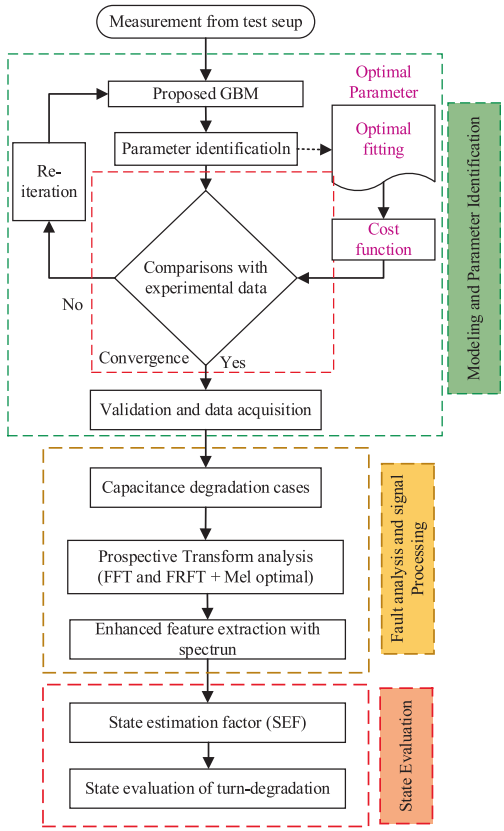


Fig. 6. Schematic diagram of the proposed optimal FRFT-RMFB framework.

4. Experimental study

4.1. Impedance measurement

Precise evaluation of stator turn insulation degradation relies on accurate measurement of the motor's HF impedance, which reflects parasitic and dielectric effects. In this work, standard connection schematics for both common mode (CM) and differential mode (DM) were used. The measurement setup with the schematics and practical measurement setup, shown in Fig. 7, employs a wideband impedance analyzer covering 20 Hz to 120 MHz.

4.2. Experimental test bench

To validate the feasibility and effectiveness of the proposed optimal FRFT-RMFB method, a series of experiments were designed and conducted. The configuration of the experimental setup is illustrated in Fig. 8. It includes the experimental setup and motor interface used to capture impedance and phase profiles. The study includes the experimental setup and motor interface used to capture impedance and phase profiles. A three-phase 0.75 kW induction motor served as the unit under test, designed to evaluate the behaviour and progression of turn insulation degradation under controlled laboratory conditions.

Initially, the motor was powered by a variable frequency supply (VFS) as depicted in Fig. 8. Subsequently, it was fed by an inverter to emulate real operational scenarios involving HF switching transients.

To capture the electrical response of the system current probe rated at 100 MHz was employed. These were connected to a digital storage oscilloscope (1 giga sample per second) for accurate recording of the switching oscillation waveforms. In addition to time-domain analysis, impedance characterization was performed using a wideband impedance/gain-phase analyzer (20 Hz–120 MHz), which provided frequency-dependent impedance and phase profiles of the stator winding and its parasitic elements.

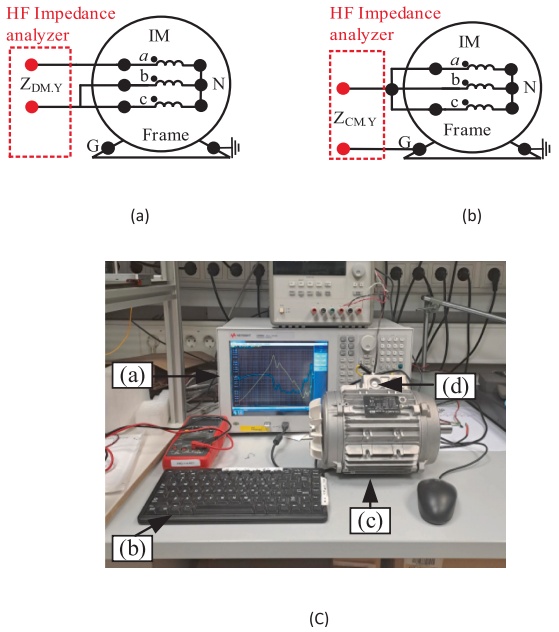


Fig. 7. Impedance measurement topologies for IM (a) DM, (b) CM, (c) Impedance measurement setup showing (a) analyzer (b) input interface (c) test motor (d) motor input interface.

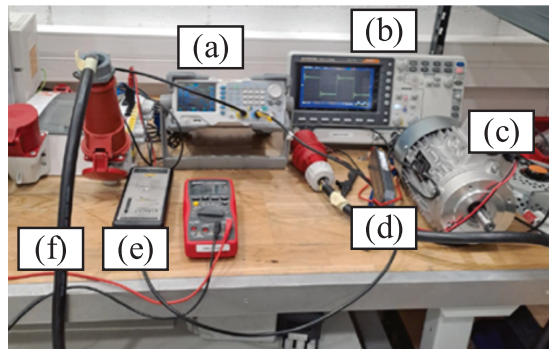


Fig. 8. VFS test setup: (a) VFS supply (initially at f_{sw} = 100 kHz), (b) oscilloscope, (c) motor, (d) current probe (100 MHz), (e) differential probe (100 MHz) (f) 5 m cable.

The test setup, in which the induction motor is fed by an inverter drive, is illustrated in Fig. 9. The key specifications of the induction motor used in the experiments are summarized in Table 2.

4.3. Frequency domain validation

Fig. 10 (a) and (b) demonstrate the frequency domain validation by comparing the measured and modeled impedance profiles through the conventional universal machine model [44] and the proposed GBM model in DM and CM schematics, respectively. The top plot in part (a) shows the impedance magnitude, while the bottom plot in part (a) illustrates the phase response. The parallel resonance frequency point f_R is identified at approximately 28 kHz. As described in Sections 2.2 (a) and 2.2 (b), the GBM is represented as an equivalent circuit composed of linear passive components, qualifying it as a linear time invariant (LTI) system. Consequently, for each measurement topology, the modeled impedance spectrum, defined in Eq. (12), is characterized by the frequency response analysis function $G_1(j \cdot \omega)$, where current is the input $I(j \cdot \omega)$ and voltage $U(j \cdot \omega)$ is the output in the frequency domain with $\omega = 2\pi f$ as angular frequency.

$$G_1(f) = \frac{U(j.\omega)}{I(j.\omega)} = G_1(j.\omega)\big|_{\omega=2\pi f} \tag{12}$$

Meanwhile, the measured impedance spectrum serves as the true realization of this WFRA, denoted as $G_1(f)$. For all measurement data set, $G_n(f)$, can be reconstructed from their respective spectra as defined in

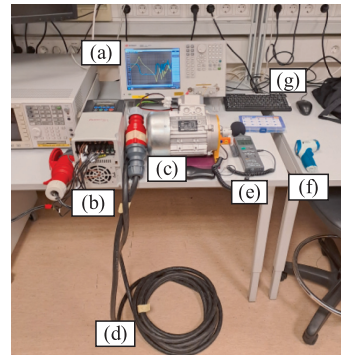


Fig. 9. Inverter-driven test setup (a) Impedance analyzer, (b) inverter at f_{sw} = 10 kHz), (c) test motor, (d) 5 m cable, (e) environment meter for humidity (f) thermometer (g) impedance anlyzer interface.

Table 2
Main parameter of the test bench motor.

Rated parameter	Value
Power (W)	0.75 kW
Voltage Δ/Y (V)	230/420 @ 50 Hz 265/460 @ 60 Hz
Current Δ/Y (I)	3.0/1.7 @ 50 Hz 2.6/1.5 @ 60 Hz
Speed (r/m)	1440 @ 50 Hz 1750 @ 60 Hz
Cos φ	0.76 @ 50 Hz 0.74 @ 50 Hz
Resistance phase a (Ω)	6.4

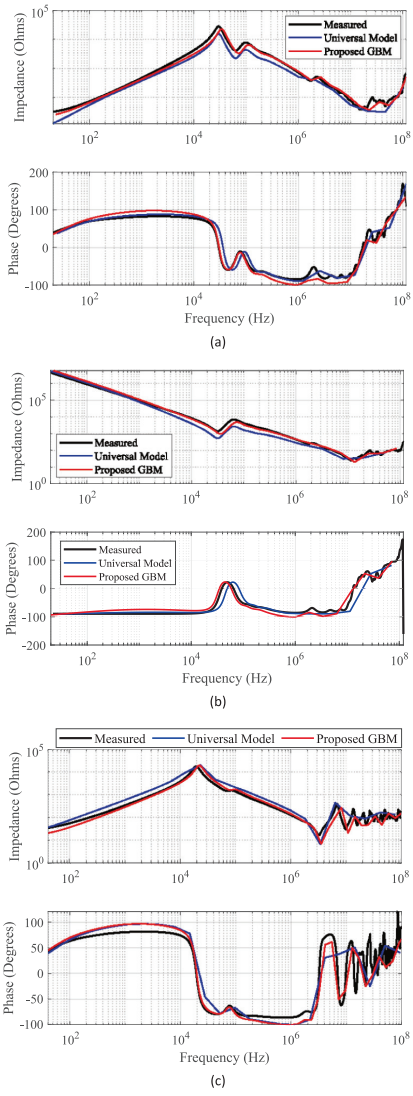


Fig. 10. Comparison of measured and proposed GBM modeled impedance profiles representing impedance magnitude and phase angle in (a) DM and (b) CM (c) 5 m cable with motor in DM.

the Eq. (13).

$$G_n(f) = Z_n(f_i) \cdot [(\cos\phi_n(f_i) + \sin\phi_n(f_i)] \quad (13)$$

Where by Z_n and ϕ_n are impedance amplitudes and impedance phase at frequency f_i, respectively.

4.4. Error interpretation in model validation

In this study, we introduce the magnitude of the mean average percent error (MAPE) by using the Eq. (14) to access the accuracy of the HF model's ability to replicate the frequency domain characteristics of the winding and cable-fed motor schematics by the proposed model compared to measured results.

$$\Delta Z_i = \frac{|x_i^* - x_i|}{x_i^*} \times 100 \ , \quad MAPE = \frac{1}{m}\sum_{i=1}^{m} \Delta Z_i \quad (14)$$

where m represents the total number of frequency sample, x_i* is the reference measurement (e.g., $|Z_{\text{measured}}(f_i)|$), and x_i is the corresponding model prediction (either the universal model or the proposed GBM model, e.g., $|Z_{\text{model}}(f_i)|$).

To achieve robust modeling, Fig. 11 presents error box plots of practical measurement in DM, CM, and cable-fed motor in DM compared with the initial/universal model as well as with the proposed/optimal model representations. Relative to the universal (initial) errors, the GBM-optimized models reduce the mean percentage error from 7.40% to 5.42% for DM, from 5.94% to 4.72% for CM, and from 7.34% to 4.98% for the cable-fed case. These changes correspond to relative reductions of 26.76%, 20.54%, and 32.15%, respectively. The interquartile ranges and whisker extents are also smaller after optimization, indicating lower dispersion and greater stability in the model response. Overall, the GBM improves fidelity to the measured impedance magnitude by reducing both bias (mean error) and variability across all operating conditions.

By utilizing the proposed GBM model with optimal fitting procedure, a significant reduction in mean error (%) is achieved across various measurement result representations, as shown in Fig. 11, compared to the initial model representations. The error reduction index (ERI %) quantifies the percentage improvement by calculating the relative difference between the initial/universal and proposed/optimized errors. Fig. 12 compares the percentage errors across the three model

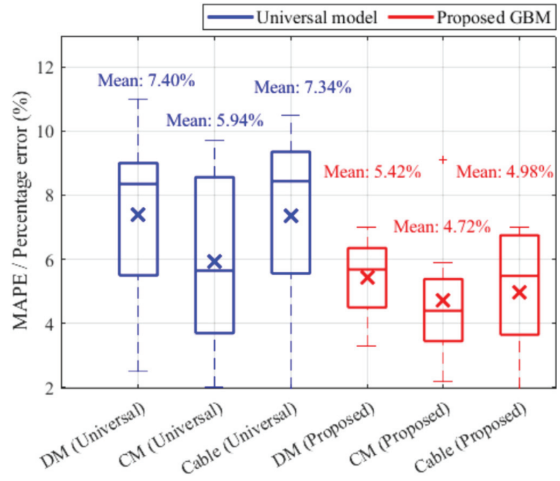


Fig. 11. Error boxplots for CM, DM, and cable + motor (DM); initial/universal model (blue, left) vs. proposed/optimized model (red, right) compared with impedance measurements.

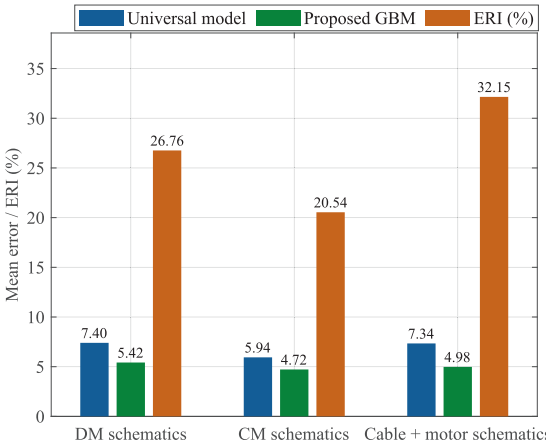


Fig. 12. Comparison of mean error (%) across different models, highlighting the error reduction index ERI (%) achieved through the proposed optimized parameter fitting process.

representations and highlights the error reduction index values of 26.76%, 20.54%, and 32.15% for DM, CM, and cable-plus-motor schematics, respectively, demonstrating the gains achieved through optimized GBM parameter identification.

4.5. Representation of the coefficient of coherence in modelling and measurements results

For better representation of validation error analysis and comparison of the datasets, the magnitude-squared coefficient of coherence (CoC/C_{GiGj}) [32], defined in Eq. (15), is used to assess the accuracy of the HF GBM's ability to replicate the frequency-domain characteristics of the windings and cable set.

$$C_{G_iG_j}(f) = \frac{|S_{G_iG_j}(f)|^2}{S_{G_iG_i}(f) \cdot S_{G_jG_j}(f)} \in [0,1] \tag{15}$$

Here, $S_{GiGj}(f)$ represents the cross-power spectral density between $G_i(f)$; and $G_j(f)$, calculated as follows in Eq. (16)-(18):

$$S_{G_iG_j}(f) = \frac{1}{N}\sum_{k=1}^{N} G_i(f_k) \cdot G_j^*(f_k) \tag{16}$$

$$S_{G_iG_i}(f) = \frac{1}{N}\sum_{k=1}^{N} |G_i(f_k)|^2 \tag{17}$$

$$S_{G_jG_j}(f) = \frac{1}{N}\sum_{k=1}^{N} |G_j(f_k)|^2 \tag{18}$$

where $G_j^*(f)$ represents the complex conjugate of $G_j(f)$. The coherence coefficient C_{GiGj} reveals the consistency of system responses $G_i(f)$ and $G_j(f)$ under identical input conditions. In this study, it is used as a metric for evaluating the effectiveness of HF parametric modeling in the frequency domain. Its values range from 0 to 1 as follows:

1. $C_{GiGj} = 1$ indicates perfect correlation between the modeled and real system frequency responses, demonstrating an ideal representation in the frequency domain.
2. $C_{GiGj} = 0$ indicates that the frequency responses of the model and the real system are completely uncorrelated or more-deviated.

For both GBM of cables and machines, the CoC/C_{GiGj} was calculated to quantify the agreement between the modeled and measured impedance spectra across the frequency range of 20 Hz to 120 MHz. The results are summarized in Table 3. In all topologies, a C_{GiGj} higher than 0.936 was achieved. For the IM GBM, the average CoC is 0.950, while for the cable fed with motor in the DM model, it is 0.949. These values, which are close to 1, indicate that both models can accurately capture the dynamic behavior and characteristics of the modeled subjects in the frequency domain.

The proposed model targets HF impedance parameters as well as switching-oscillation signatures and therefore does not fully capture (i) low-frequency dynamic response, resistive inter-turn parameters, (ii) deep-slot partial-discharge (PD) localization, or (iii) strict within-phase fault localization that lie outside the method's strongest sensitivity band. Its diagnostic fidelity can also degrade cable as well under large operating drifts (e.g., temperature, load) and unmodeled parasitics (cable routing, fixtures). Future work will couple the HF indicator with complementary LF/PD tests and multi-phase feature fusion to cover these regimes and improve localization.

4.6. Influence of the testbench environment

To investigate the influence of the test-bench environment, we measured impedance profiles for three connection schematics: common mode (CM), differential mode (DM), and cable-plus-motor DM under different test-bench environments. Measurements were performed under controlled environmental variations, including cable layout (unbent versus looped), ambient humidity levels, and motor temperature. The initial laboratory environment (specified humidity and temperature) was taken as the baseline. Resulting spectra under each condition were recorded and compared quantitatively by computing the CoC. It assesses agreement with the reference and quantifies the sensitivity of the proposed or initial method to environmental changes.

Fig. 13 illustrates the test-bench environment, comparing the unbent cable alignment in (a) with the looped structure in (b) and measurements were recorded with impedance anlyzer.

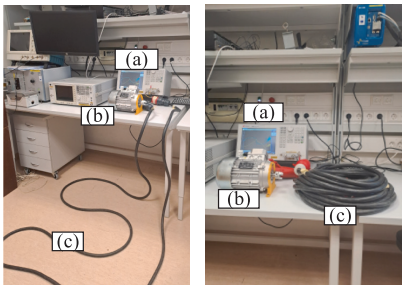
Fig. 14 shows the impedance profile of a 5 m cable feeding the motor in DM for unbent and looped layouts, allowing a direct assessment of layout effects. Additional DM measurements with the cable open circuit (DMOC) and shorted secondary (DMSC) were also recorded to evaluate layout-dependent variation in the results.

Table 4 shows uniformly high coherence between unbent and looped layouts across all schematics. The highest magnitude coherence is 0.992 for the cable + motor CM case, and the strongest phase coherence is 0.985 for the cable + motor DM case. Cable-only topologies remain consistent, with DMOC at 0.973 (magnitude) and 0.967 (phase), and DMSC at 0.983 (magnitude) and 0.957 (phase). Overall, the layout change has a negligible effect within 20–120 MHz.

Moreover, Tables 5 and 6 demonstrate that the method is repeatable under test bench conditions. CoC remains high and stable across the multiple tested environments. With temperature variation, motor CM reaches the strongest magnitude at 45.1 °C (0.961), while motor DM delivers the strongest phase at 60 °C (0.996); Cable + motor CM also preserves a high phase at 60 °C (0.981), whereas cable + motor DM

Table 3
CoC between the initial/universal and proposed optimal GBM model impedance profile.

Schematics	Model	Coefficient of coherence (CoC)	
		Impedance	Phase
Motor CM	Initial/universal model	0.941	0.931
	Proposed/optimal GBM	0.963	0.953
Motor DM	Initial/universal model	0.926	0.916
	Proposed/optimal GBM	0.946	0.936
Cable + Motor DM	Initial/universal model	0.927	0.912
	Proposed/ optimal GBM	0.955	0.943



(a) (b)

Fig. 13. Test bench layouts (a) unbent alignment (b) looped structure.

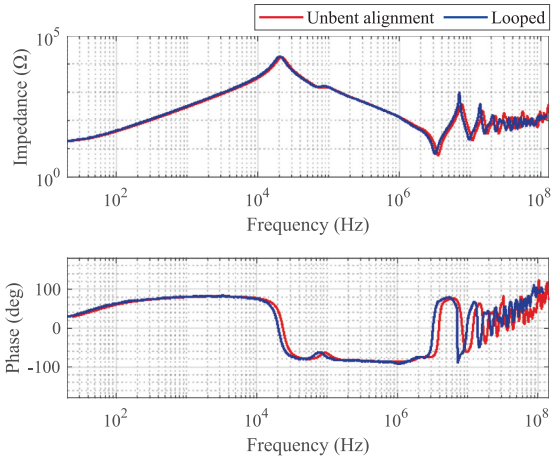


Fig. 14. Impedance of a 5-m cable fed along with the motor in DM under two different layouts.

Table 4
CoC between unbent and looped cable layouts under 20–120 MHz range.

Schematics	CoC between two layouts (Unbent and looped)	
	|z|	θ
Cable DMOC	0.973	0.967
Cable DMSC	0.983	0.957
Cable + motor CM	0.992	0.969
Cable + motor DM	0.989	0.985

Table 5
Temperature influence on the CoC relative to a 24.3 °C reference.

Schematics	CoC at 30.2 °C		CoC at 45.1 °C		CoC at 60 °C	
	|z|	θ	|z|	θ	|z|	θ
Motor CM	0.796	0.949	0.961	0.916	0.951	0.891
Motor DM	0.929	0.816	0.934	0.896	0.886	0.996
Cable + motor CM	0.928	0.926	0.827	0.937	0.817	0.981
Cable + motor DM	0.898	0.987	0.887	0.898	0.812	0.897

shows the largest thermal drop in magnitude to 0.812. Under humidity sweeps, cable + motor CM attains the top magnitude at 41.3% RH (0.986) and the top phase at 78.3% RH (0.987). Overall, the framework is robust to temperature and humidity, with notable sensitivity confined to the cable + motor DM configuration. The same schematic also achieves the top phase at 78.3% RH (0.987).

Table 6
Humidity influence on the CoC relative to a 42.8% RH reference.

Schematics	CoC at 41.3% RH (Indoor–humid)		CoC at 61.5% RH (Very–humid)		CoC at 78.3% RH (Near–saturated)	
	|z|	θ	|z|	θ	|z|	θ
Motor CM	0.971	0.948	0.985	0.899	0.961	0.941
Motor DM	0.913	0.958	0.926	0.948	0.946	0.926
Cable + motor CM	0.986	0.977	0.947	0.955	0.879	0.987
Cable + motor DM	0.873	0.862	0.817	0.937	0.827	0.917

4.7. Turn insulation degradation faults implementation

The electric machine utilizes polyesterimide (PI) as the primary insulation material, known for its thermal and dielectric stability. Progressive degradation of PI insulation has been shown to induce a relative increase in inter-turn capacitance, typically in the range of 20% to 50%, as in [48]. Turn insulation degradation was emulated in the stator winding (phase a) by externally connecting ceramic capacitors to simulate increased turn-to-turn capacitance ($C_{T,Degraded}$) as depicted in Fig. 15. The nominal capacitance of the stator turn (C_T) was estimated to be 368 pF, representing the mean value of the sectional turn capacities ($C_{T,i}$). To represent various levels of degradation, capacitors ranging from 0.31 nF (healthy) to 1.80 nF (severely degraded) were introduced.

For each degradation level, the motor's HF impedance response was measured to assess the progressive impact of insulation deterioration. As shown in Fig. 16, the impedance profile exhibited clear resonance shifts and amplitude variations with increasing fault severity. These changes reflect the cumulative effect of dielectric breakdown and parasitic alteration due to degradation. The measured spectra were subsequently processed using fractional-domain transformation and customized FRFT-RMFB filtering to enhance the extraction of degradation-related features, which serve as key indicators of insulation health.

Subsequently, the optimal fitting procedure outlined in Section 2.2 is re-applied to estimate the updated turn-to-turn capacitive parameters. These estimated values are then compared against the baseline (healthy) case to quantify the variation influenced by insulation degradation. Table 7 presents the variation in turn capacitance from the initial healthy baseline C_T across different emulated degradation cases. C'_T represents the new/updated average estimated turn capacitance under degraded conditions estimated through optimal fitting of the proposed GBM as well as calculated as lumped parameters as in [38]. While $\Delta C'_T = C'_T - C_T$ indicates deviations from baseline value of $C_T = 368$ pF. The corresponding percentage change ($\Delta C'_T/C_T$) quantifies the extent of degradation severity.

5. Experimental performance evaluation of proposed RMFB with HF VFS supply

Turn insulation degradation is characterized by subtle changes in the

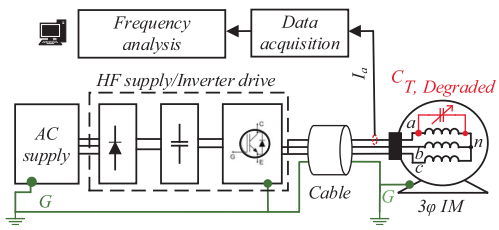


Fig. 15. Fault implementation layout.

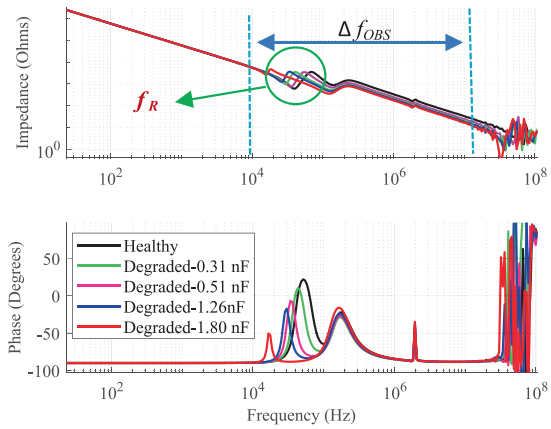


Fig. 16. Measured DM impedance profile under different turn degradation faults.

Table 7
Extracted parameters of the IM for varying external capacitances ($C_{T,Degraded}$).

$C_{T,Degraded}$ (nF) inserted	GBM Estimated $\Delta C'_T$ (pF)	Calculated $\Delta C'_T$ (pF)	Absolute Error (pF)	Severity $\Delta C'_T / C_T$ (%)
0 (healthy)	0.02	0.03	0.01	0
0.31	11.2	13.3	2.1	3.04
0.51	34.8	35.7	1.9	9.46
1.26	53.7	55.3	2.6	14.59
1.80	93.5	96.6	3.1	25.40

HF current waveform, with minor fluctuations serving as indicators of gradual insulation deterioration, as illustrated in Fig. 17. These variations result from multiple switching oscillations triggered by the supply switching frequency. Each switching cycle corresponds to a 10 μs time window, determined by a 100 kHz supply frequency. High-resolution signal acquisition is performed at a sampling rate of 100 mega-samples per second (MS/s), yielding 1000 data points per oscillation segment. For analysis and post-processing, one data-set sample consists of 100 consecutive segments.

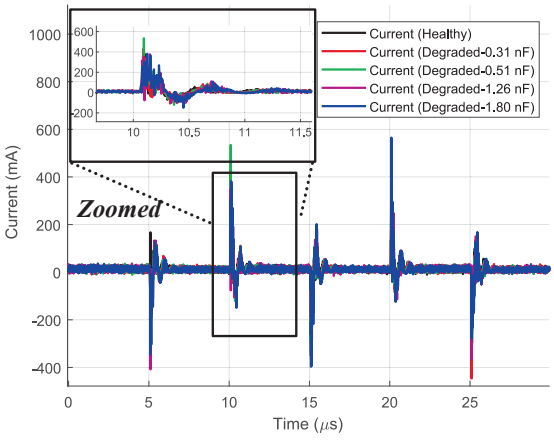


Fig. 17. Measured switching motor current (I_a) signal in the time domain.

5.1. Proposed FRFT with resonance centered Mel-Filter Banks (FRFT-RMFB)

This research study is implemented in MATLAB to analyze experimental data and post-processing. The FRFT spectrum in Fig. 18 reveals unique time–frequency features of a switching oscillation current sample that depend on the variation of the fractional order p. Therefore, finding the optimal value of p in order to maximize the sensitivity estimation of turn insulation degradation is critical. Another algorithm is defined to create the MAE values using the equation (10) with the healthy cases and the initial degraded current signals with 0.31 nF capacitance. It is observed that the different MAE values vary with the fractional order variations, and the highest MAE is considered to indicate a high resolution of the FRFT spectra. By considering it as an optimization problem, the Eq. (19) is utilized to get the optimal value of p.

$$Maximize\ \{MAE = \frac{1}{m}\sum_{i=1}^{m}|x_i^* - x_i|\ \}\ s.t.p_{varied} = [0,1] \tag{19}$$

where x_i* and x_i present the initial/healthy and 1st degraded impedance data set respectively, and m is the total number of counts. As illustrated by the sensitivity analysis in Fig. 19, MAE reaches its maximum at the optimal order $p = 0.71$, where the amplitude difference between the initial reference/healthy and 1st degraded state is highly observable. This optimal value enhances the resolution of degradation features, enabling a more precise assessment of insulation health.

To customize the optimal RMFB, we set its center frequency f_0 to 20 kHz, covering a frequency range of 10 kHz- 10 MHz. This range effectively captures the key features of turn-insulation state perception. The optimized filter design is shown in Fig. 20. After filtering the switching oscillation current signal, the results of Fig. 21. demonstrate a significant reduction in HF oscillations and a more precise definition of frequency band characteristics to acquire the turn insulation features.

To assess the effectiveness of the proposed FRFT-RMFB approach and other conventional methods, a dynamic variation metric, referred to as the SEF with MAE and RMSE, are defined in Eq. (20)-(21). The SEF quantifies the relative change in MAE and RMSE as a percentage of the reference healthy spectral value.

$$SEF_{MAE} = \Delta MAE\% = \frac{MAE}{MAE_{healthy}} \times 100\% \tag{20}$$

$$SEF_{RMSE} = \Delta RMSE\% = \frac{RMSE}{RMSE_{healthy}} \times 100\% \tag{21}$$

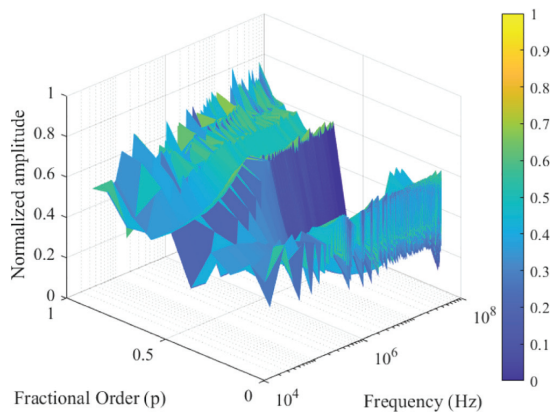


Fig. 18. FRFT spectrum of a single switching oscillation in the motor current (I_a).

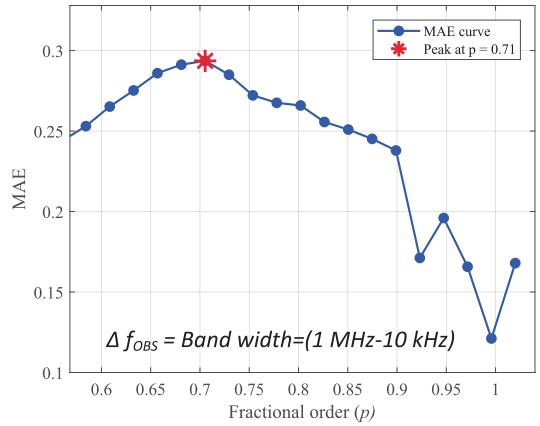


Fig. 19. Sensitivity analysis for the optimal fractional order extraction.

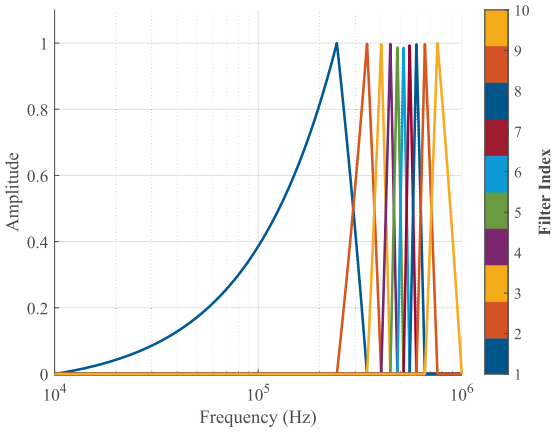


Fig. 20. Group distribution diagram of the proposed FRFT-RMFB.

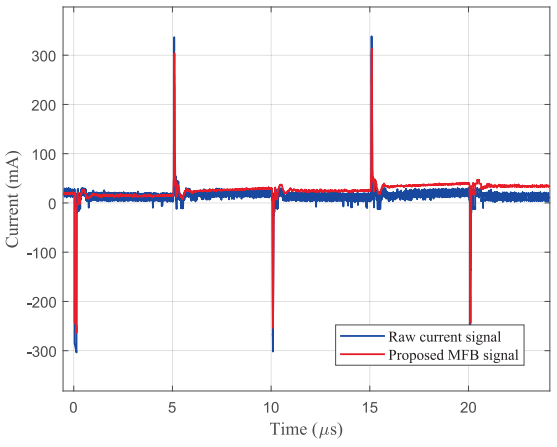


Fig. 21. Time domain representation of switching oscillation current with proposed FRFT-RMFB.

where x_i^* is the mean reference/baseline feature and x_i denotes the spectral amplitudes under diferent degraded conditions. Fig. 22 shows that the FRFT-RMFB processed results reveal more pronounced waveform changes in response to switching oscillation currents. This higher sensitivity enhances the estimation of turn insulation degradation, confirming that the RMFB approach offers improved insight into the progression of insulation aging.

To enable a comparative analysis, the spectral representations of signals processed using FFT and the Log-Gaussian Filter Bank (LGFB) are presented. As shown in Fig. 23(a), the FFT results exhibit only minor amplitude variations across different degradation levels, underscoring its limited effectiveness in capturing early-stage insulation deterioration. Although slight frequency shifts are observable, the FFT lacks the ability to detect localized transient features critical for identifying initial fault conditions. In contrast, the LGFB-processed spectra reveal subtle but discernible variations in normalized amplitude within the HF region as degradation progresses. These observations, also depicted in Fig. 23 ((b), demonstrate the LGFB method's superior sensitivity to insulation faults, particularly in the early stages.

The MAE values, evaluated using the Eq. (10), for various methods including FFT, Bandpass Filter, FRFT, LGFB, and the proposed FRFT-RMFB approach, are summarized in Tables 8 (MAE) and Table 9 (RMSE) to assess their performance in detecting turn insulation degradation.

Tables 10 (SEF_{MAE}) and Table 11 (SEF_{RMSE}) present the comparative frequency spectra obtained using different signal processing methods, including FFT, Bandpass filter, FRFT, LGFB, and the proposed FRFT-RMFB for the estimation of turn insulation degradation under varying degraded capacitance conditions. When $C_{T,Degraded} = 0.31$ nF, the SEF value for the FFT method is only 3.40%, whereas RMFB method yields a significantly higher value of 22.93%, representing an improvement of over seven times. Even at = 0.51 nF, the SEF for FFT reaches only 5.05%, which remains lower than the value achieved by the RMFB method at the lower degradation level of 0.31 pF, highlighting its superior sensitivity.

Fig. 24 visualizes the sharp incline in SEF_{MAE} for proposed FRFT-RMFB compared to other methods, emphasizing its superior sensitivity across all degradation levels. As degradation progress to higher values (e.g., $C_{T,Degraded} = 1.80$ nF), all methods show increased state estimation factor, with FFT at 9.39%, bandpass filter at 13.06%, FRFT at 33.32%, LGFT at 50.55%, and propose optimal FRFT-RMFB peaking at 76.06%. These results confirm that while traditional methods can track gross

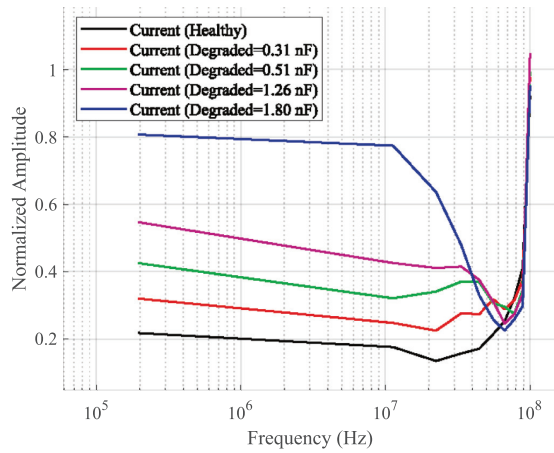


Fig. 22. Spectra of switching currents for different degraded states using proposed FRFT-RMFB.

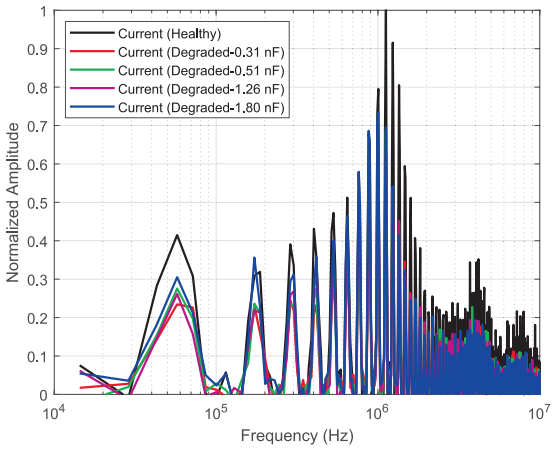


Fig. 23. Spectral representation using methods (a) FFT and (b) LGFB.

Table 8
MAE of Different Methods to Turn Insulation Degradation.

$C_{T,Degraded}$ (nF)	FFT	Bandpass Filter	FRFT	LGFB	Proposed FRFT-RMFB
0.31	0.0018	0.0218	0.0646	0.0226	0.0693
0.51	0.0029	0.0327	0.1383	0.0542	0.1091
1.26	0.0027	0.0480	0.1962	0.0781	0.1527
1.80	0.0047	0.1302	0.2865	0.1041	0.2295

degradation, they are insufficient for early-stage fault estimation, which is crucial for predictive maintenance.

To further clarify the proposed method, the influence of various contributing factors has been discussed in the preceding subsection.

5.2. *Effect of VFS switching frequency (f_{sw})*

The effect of VFS switching frequency on the proposed FRFT-RMFB diagnostic method was experimentally investigated. As shown in Fig. 25, the turn insulation sensitivity SEF_{MAE} remains the same consistently with capacitance across different switching frequencies (5 kHz, 10 kHz, 50 kHz, and 100 kHz), exhibiting minimal deviation. This confirms the method's robustness and frequency-agnostic nature, making it highly suitable for insulation degradation monitoring in systems with variable switching conditions.

Table 9
RMSE of Different Methods to Turn Insulation Degradation.

$C_{T,Degraded}$ (nF)	FFT	Bandpass Filter	FRFT	LGFB	Proposed FRFT-RMFB
0.31	0.0065	0.0781	0.2315	0.0896	0.081
0.51	0.0058	0.0655	0.2772	0.1512	0.133
1.26	0.0061	0.1081	0.4418	0.1911	0.314
1.80	0.0096	0.2664	0.5862	0.2382	0.414

Table 10
Comparison of the percentage sensitivity (SEF_{MAE}) of Different Methods to Turn Insulation Degradation.

$C_{T,Degraded}$ (nF)	FFT (%)	Bandpass Filter (%)	FRFT (%)	LGFB (%)	Proposed RMFB (%)
0.31	3.40	3.94	7.71	19.27	22.93
0.51	5.05	6.45	16.57	24.53	35.12
1.26	6.36	7.59	23.39	34.24	50.37
1.80	9.39	13.06	33.32	50.55	76.06

Table 11
Comparison of the percentage sensitivity (SEF_{RMSE}) of Different Methods to Turn Insulation Degradation.

$C_{T,Degraded}$ (nF)	FFT (%)	Bandpass Filter (%)	FRFT (%)	LGFB (%)	Proposed RMFB (%)
0.31	4.19	4.83	9.46	28.01	22.93
0.51	6.24	7.96	20.48	35.40	36.12
1.26	8.96	10.69	32.98	44.77	76.06
1.80	10.81	15.03	39.37	55.79	89.33

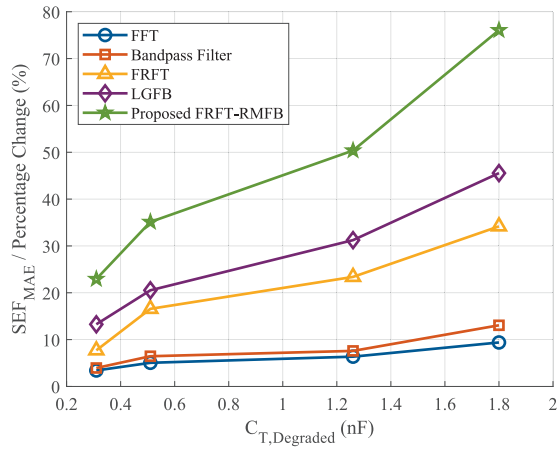


Fig. 24. Sensitivity comparison results (SEF) with MAE across different methods.

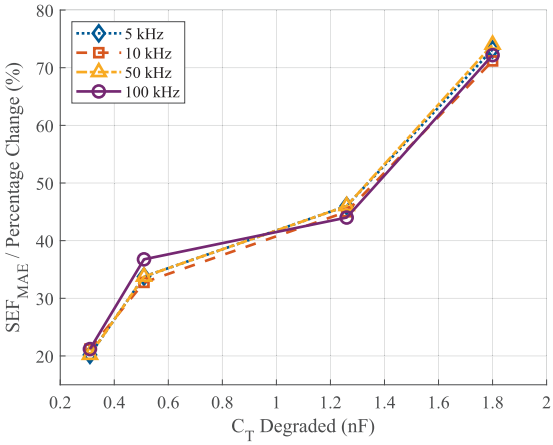


Fig. 25. Sensitivity comparison results (SEF) across different switching frequencies f_{sw}.

5.3. Effect of data acquisition sampling rate and low-bandwidth sensors

With the experimental setup, a low sampling frequency is preferable for implementing the FRFT-based CM method. Since the sensitive oscillation components lie in the several kHz range, a sampling frequency in the order of 10 MHz is more than sufficient to capture key features for insulation degradation analysis.

As demonstrated in Fig. 26, the SEF_{MAE} results at 100 MHz, 20 MHz, and 10 MHz exhibit negligible variation, confirming that lower sampling rates can still accurately identify degraded insulation phases.

5.4. Degraded phase identification

To detect the faulty phase, HF current sensors were placed on all three motor phases while degradation was emulated on phase *a* using added capacitance. As shown in Fig. 27, only phase a exhibited a significant rise in SEF, while phases b and c remained stable. This confirms the method's ability to accurately identify the degraded phase using sensitive current analysis. For general diagnosis without phase localization, a single current sensor around all three cables is sufficient.

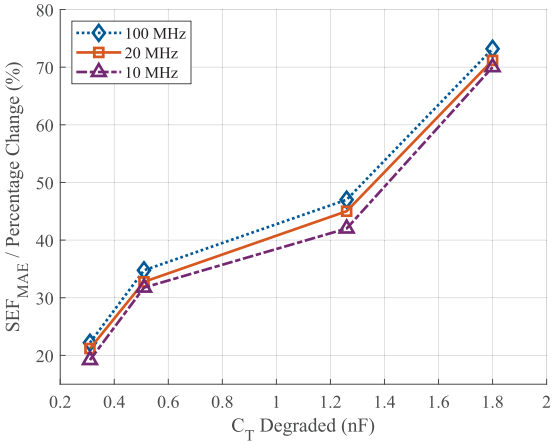


Fig. 26. Sensitivity comparison results (SEF) across different sampling data rates.

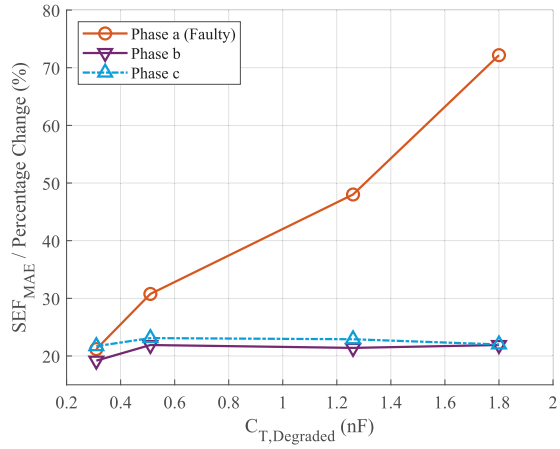


Fig. 27. Sensitivity comparison results (SEF) across different machine phases.

6. Experimental performance evaluation of the proposed FRFT-RMFB with inverter-fed supply

6.1. Performance evaluation of the proposed FRFT-RMFB

Fig. 28 presents the PWM voltage waveform together with the associated switching oscillation current during the normal operation of the inverter-fed machine.

The inverter's switching frequency was set to 10 kHz, and the data acquisition was performed at a corresponding high sampling rate of 100 MS/s to ensure accurate capture of HF transients. To evaluate the sensitivity of the stator turn insulation degradation, varying capacitance values $C_{T,Degraded}$ are used to represent different stages of insulation deterioration in phase *a* coil. Similarly, high-bandwidth current sensors (100 MHz) capture the corresponding oscillation currents, as demonstrated in Fig. 29.

As illustrated earlier in Fig. 18, the FRFT spectrum of the switching oscillation current reveals distinct characteristics that depend on the fractional order p. Identifying the optimal p is essential to enhance sensitivity to insulation degradation using the procedure in Section 5.1, we re-optimized the fractional order p by maximizing the MAE between healthy and degraded spectra. The highest MAE value at $p = 0.79$ yields the strongest response to degradation. At this optimal order, the spectral amplitude differences between healthy and degraded conditions are most pronounced, enabling more effective estimation and clearer differentiation of turn insulation fault severity levels. Fig. 30 (a) presents the spectra obtained using the standard FRFT, which exhibits relatively subtle waveform changes across different insulation states. In contrast, Fig. 30 (b), shows the proposed optimal FRFT-RMFB processed spectra, revealing more pronounced variations. This demonstrates that the optimal FRFT-RMFB method offers enhanced sensitivity and faster estimation capability for identifying turn insulation degradation.

6.2. Evaluation of fault sensitivity with the state-of-the-art transforms

The current signals from the healthy case and each degraded case are analyzed using the continuous wavelet transform (CWT) to capture their joint time–frequency behavior, as demonstrated in Fig. 31. To enable quantitative comparison, multiple signal statistics (root-mean-square as RMS amplitude, peak-to-peak range, skewness, and kurtosis) together with scalogram features, including the spectral centroid, spectral bandwidth, and total band-limited energy, were computed. The statistical values for each degraded case are compared against the healthy baseline; in particular, the RMS metric is reported as a percentage

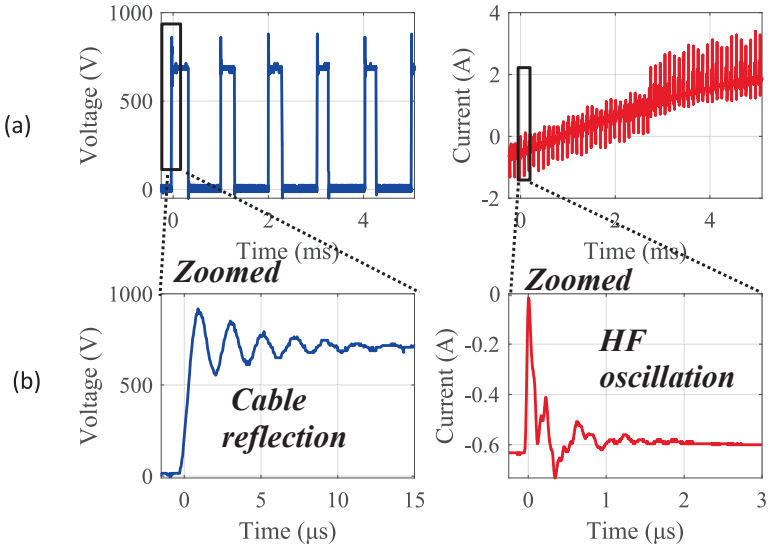


Fig. 28. IM Testbench signal representation: (a) Measured voltage and current waveforms; (b) Zoomed-in view highlighting HF components in the time domain.

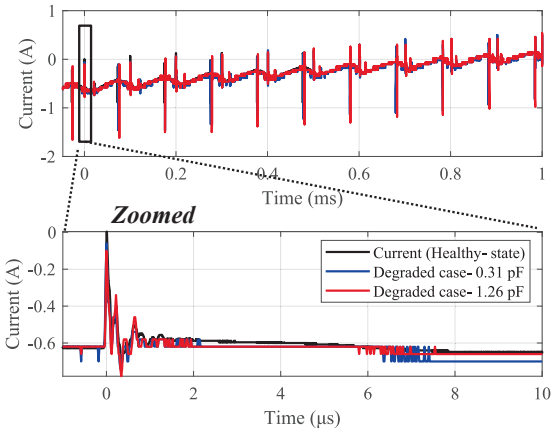


Fig. 29. Measured inverter-fed motor current signal in the time domain with a zoomed-in view highlighting transient features.

change relative to the healthy condition, as defined in Eq. (22) to quantify the degree of degradation.

$$RMS = \sqrt{\frac{1}{N}\sum_{n=1}^{N-1} x[n]^2} \tag{22}$$

where $x[n]$ is the nth discrete sample current signal (healthy or degraded), n is the sample index ($0 \le n \le N-1$), N is is the number of samples in the analysis window, and the sampling frequency is f_s with sampling interval $\Delta t = 1/f_s$ and sample times $t_n = n\,\Delta t$.

Also, the current signals from the healthy and each degraded case are analyzed using the empirical mode decomposition (EMD) followed by the Hilbert transform to obtain their joint time–frequency representation. For quantitative comparison, signal-level statistics (root-mean-square amplitude as RMS, peak-to-peak range, skewness, and kurtosis) were extracted. Then, Hilbert–Huang features from the IMFs, including the marginal-spectrum centroid (energy-weighted mean instantaneous frequency), and total band-limited Hilbert energy over the analysis band, as demonstrated in Fig. 32, were computed. For statistical analysis, the intrinsic mode functions (IMFs) were used for case-to-case comparison. Here $A_1^{(H)}$ and $A_1^{(F)}$ denote the instantaneous amplitudes of the first IMF (via the Hilbert transform) for the healthy and faulty cases, respectively. The percentage deviation is defined in Eq. (23), and for each faulty case, it presents the mean percentage deviation relative to the healthy baseline.

$$D[n] = \frac{|A_1^{(F)}[n] - A_1^{(H)}[n]|}{A_1^{(H)}[n]} \times 100 \quad , \; n \in I \tag{23}$$

Moreover, the current signals (healthy and degraded) are analyzed with spectral kurtosis (SK) to localize impulsive/non-Gaussian behavior in frequency, which is demonstrated in Fig. 33. For each signal, we computed the short-time Fourier transform (STFT) and form the second and fourth moments of the complex spectrum magnitude across time and $M_4(f) = \mathbb{E}_t\{|S(f,t)|^4\}$. STFT uses a 256-sample window, 128-sample overlap, and $N_{\mathrm{FFT}} = 512$. We restricted the analysis to 100 kHz $\le f \le$ 10 MHz and compared each degraded case to the healthy baseline by the band-wise percentage change as defined in Eq. (24), from which the mean over the band is quantified as a key indicator of degradation severity.

$$\Delta_{SK}(f) = \frac{|SK_F(f) - SK_H(f)|}{SK_F(f)} \times 100 \tag{24}$$

Accurately estimating turn insulation degradation in the time domain is highly challenging, as incipient fault signatures are typically weak in amplitude and often overlap with other signal components, obscuring reliable detection. The proposed FRFT-RMFB method overcomes this limitation by isolating degradation-sensitive features more effectively than the conventional FFT approach. This advantage is quantitatively tabulated in Table 12 with a comparison of corresponding SEF values, used as the key sensitivity metric.

Specifically, at $C_{T,Degraded} = 0.31$ nF, the FFT method yields a SEF of only 1.47%, whereas the FRFT-RMFB method achieves 15.77%, representing an enhancement of over sevenfold as demonstrated by Fig. 34. Remarkably, even at a higher degradation level ($C_{T,Degraded} = 0.51$ nF),

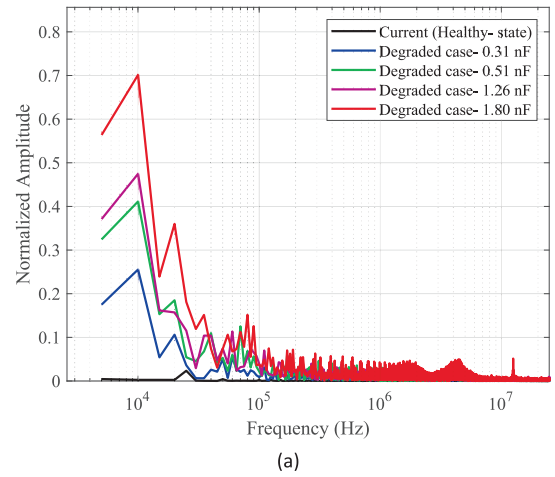


Fig. 30. Comparative representation of spectra by utilizing (a) FRFT (b) proposed FRFT-RMFB.

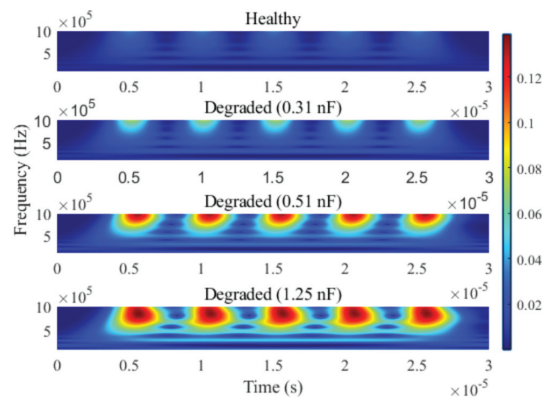


Fig. 31. Continuous wavelet transform of the current for the healthy case and the degraded cases, showing time–frequency energy distributions.

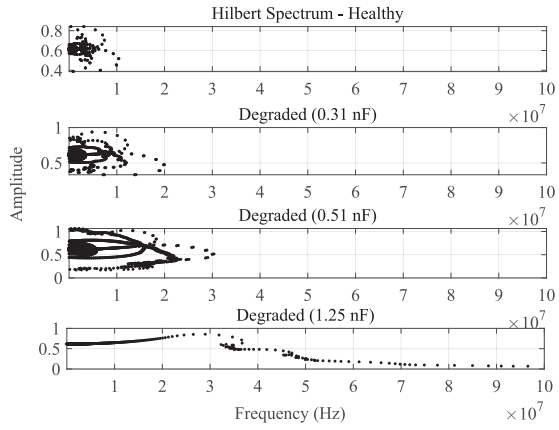


Fig. 32. Hilbert-Huang transform (HHT) of the current for the healthy case and the degraded cases, showing time–frequency energy distributions.

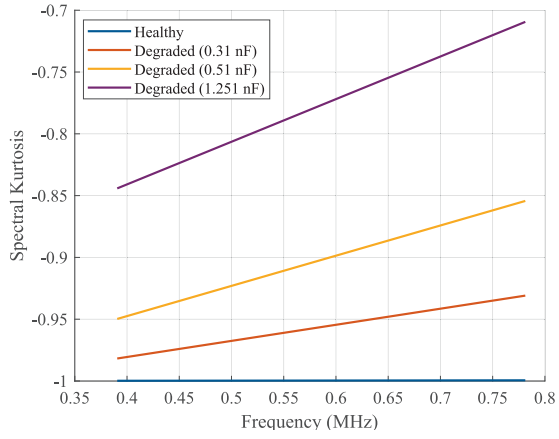


Fig. 33. Spectral Kurtosis representation of current signals under healthy and degraded cases.

Table 12
Comparison of the SEF_{MAE} as a percentage sensitivity of different methods to turn insulation degradation.

$C_{T,Degraded}$ (nF)	FFT (%)	FRFT (%)	SK (%)	HHT (%)	CWT (%)	Proposed FRFT-RMFB (%)
0.31	1.47	4.33	2.17	2.24	0.21	15.77
0.51	2.83	9.28	4.32	5.44	1.81	19.02
1.26	4.94	10.72	9.76	7.82	5.07	28.73
1.80	6.33	15.49	22.29	12.38	15.56	44.40

Table 13
0.75 kW IM universal model HF impedance parameters.

Parameter	Value	Parameter	Value
R_s (Ω)	5.91	C_T (pF)	368
L_s (mH)	39.2	L_T (mH)	242.53
C_{WG} (pF)	843	C_P (pF)	300
R_T (kΩ)	2.71	L_c (μH)	10.69
C_{G1} (pF)	268	R_E (kΩ)	17.72
C_{G2} (pF)	890	R_{G2} (Ω)	310
R_{G1} (Ω)	2.98		

Table 14
GBM Optimal 0.75 kW IM low-to-HF impedance parameters identified through an optimal fitting process.

Parameter	Value	Parameter	Value
Section 1 ***(Out of 10 total sections)***			
R_s (Ω)	0.64	L_s (mΩ)	0.65
R_r (Ω)	0.63	L_r (mH)	0.62
L_{mag} (mH)	4.50	M_{ab} (mH)	3.23
M_{bc} (mH)	3.19	M_{ab} (mH)	3.33
M_C (μH)	0.04	C_T (pF)	36.98
C_{WG} (nF)	0.98	L_T (mH)	24.25
R_T (kΩ)	0.37	C_P (pF)	30.90
C_{G1} (pF)	33.37	L_{eq} (μH)	239
C_{G2} (pF)	89.64	L_c (μH)	1.98
R_{G1} (Ω)	0.29	R_E (kΩ)	1.8
R_{G2} (Ω)	31.99		

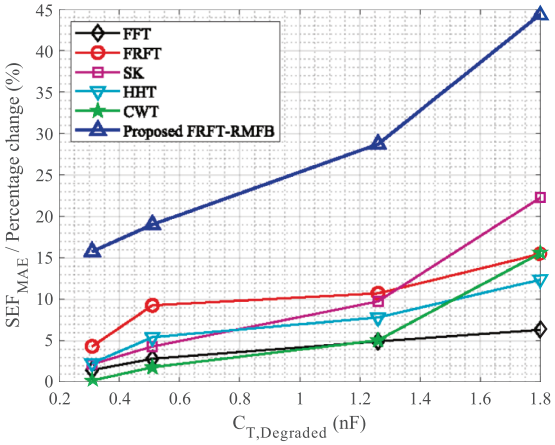


Fig. 34. Evaluation of sensitivity performance across various techniques.

the FFT-derived SEF value (2.83%) still falls short of the FRFT-RMFB result at 0.31 nF, highlighting the method's superior responsiveness to estimate early-stage insulation faults. These findings firmly demonstrate the robustness of the FRFT-RMFB method in extracting weak degradation indicators and its effectiveness in advancing early fault estimation beyond the capabilities of traditional spectral analysis techniques.

Compared with FFT, band-pass filters, and separate FRFT or LGFB methods, as well as SK, HHT, and CWT, the spectral response of the optimal FRFT-RMFB method offers significantly enhanced sensitivity across varying stages of capacitance degradation. This advantage is most evident during early-stage insulation degradation, where traditional methods typically miss subtle spectral changes. The integration of a tailored RMFB filter within the fractional domain enhances resonance-sensitive features, enabling more accurate fault estimation. These results confirm the method's diagnostic robustness and its potential for real-time monitoring in safety–critical applications.

7. Conclusion and outlook

To enhance the reliability of inverter-fed machines, an advanced signal processing technique utilizing the FRFT-RMFB method is proposed for diagnosing high-risk phase turn insulation. The key conclusions derived from the experimental investigations are as follows:

- FRFT enables the extraction of fine, non-stationary features associated with turn insulation degradation in IM, significantly improving estimation sensitivity.
- A custom optimal FRFT-RMFB filter was designed based on the machine's intrinsic CM impedance resonance, enhancing feature extraction while minimizing computational cost.
- By utilizing this methodology, experimental results confirm nearly a seven-fold improvement in early-stage estimation sensitivity compared to traditional methods.
- This method also offers the benefit of reducing sensor bandwidth requirements while supporting low-volume data processing by utilizing the FRFT-RMFB framework.

This framework holds strong potential for deployment in real-time condition monitoring of critical applications such as electric vehicles and high-speed rail systems. Future developments will target the automation of applied diagnosis and explore the integration of deep learning algorithms to further boost diagnostic accuracy and computational efficiency, enabling scalable and intelligent insulation monitoring solutions.

CRediT authorship contribution statement

Muhammad Usman Sardar: Validation, Software, Methodology, Investigation, Formal analysis, Conceptualization. **Toomas Vaimann:** Visualization, Supervision, Resources, Project administration, Methodology, Data curation, Conceptualization. **Lauri Kütt:** Formal analysis, Data curation, Conceptualization. **Bilal Asad:** Supervision, Software, Resources, Project administration, Methodology, Investigation, Data curation, Conceptualization. **Ants Kallaste:** Validation, Supervision, Resources, Project administration.

Declaration of competing interest

The authors declare that they have no known competing financial interests or personal relationships that could have appeared to influence the work reported in this paper.

Appendix 1

Machine Low-to-HF Parameters Extraction by optimal fitting.

In the low-to-HF distributed-parameter proposed GBM model, the machine parameters were identified through an optimal fitting procedure. The initial guesses were based on numerically calculated values as presented in Table 13 by the universal IM model, and a bounded percentage variation was applied to explore the parameter space. The final values for the proposed low-to-HF machine GBM were determined by minimizing the error between the measured and modeled impedance profile in the entire frequency range (20 Hz−120 MHz), ensuring the accurate extraction of key parameters listed in Table 14 (of section 1) without requiring direct inductance measurements.

References

[1] Z. Lu, H. Li, Y. Qiao, Morphological evolution of power systems with high share of renewable energy generations from the perspective of flexibility balance, Quanqiu Nengyuan Hulianwang 4 (2021), https://doi.org/10.19705/j.cnki.issn2096-5125.2021.01.003.
[2] W. Qiu, X. Jiang, Z. Lin, L. Li, Y. Pei, Y. Tao, A. Contract-Based, Decentralized and privacy-preserving computation scheme of evaluation indices of shared energy storage market for renewable energy accommodation, IEEE Trans. Ind. Appl. 59 (2023), https://doi.org/10.1109/TIA.2022.3225783.
[3] V. Thomas, S. Kumaravel, S. Ashok, Fuzzy controller-based self-adaptive virtual synchronous machine for microgrid application, IEEE Trans. Energy Convers. 36 (2021), https://doi.org/10.1109/TEC.2021.3057487.
[4] J. Li, Y. Chen, S. Li, Early warning of inter-turn short circuit fault in excitation windings of synchronous generator based on deep belief network, Dianli Zidonghua Shebei/electric Power Automation Equipment 41 (2021), https://doi.org/10.16081/j.epae.202011033.
[5] B. Asad, T. Vaimann, A. Belahcen, A. Kallaste, Broken rotor bar fault diagnostic of inverter fed induction motor using FFT, Hilbert and Park's Vector approach, in: Proceedings – 2018 23rd International Conference on Electrical Machines, ICEM 2018, (2018). https://doi.org/10.1109/ICELMACH.2018.8506957.

[6] M.U. Sardar, T. Vaimann, L. Kütt, A. Kallaste, B. Asad, S. Akbar, K. Kudelina, Inverter-fed motor drive system: a systematic analysis of condition monitoring and practical diagnostic techniques, Energies (basel) 16 (2023) 5628, https://doi.org/10.3390/en16155628.
[7] P. Castro Palavicino, B. Sarlioglu, Estimation of Position and Shorted Turns Percentage of an Inter-Turn Short Circuit in Interior Permanent Magnet Synchronous Machines Based on a Current Observer and Stationary Reference Frame Tracking, in: IEEE Trans Ind Appl, (2023). https://doi.org/10.1109/TIA.2023.3268996.
[8] O. Alshorman, A. Alshorman, A review of intelligent methods for condition monitoring and fault diagnosis of stator and rotor faults of induction machines, Int. J. Electr. Comp. Eng. 11 (2021), https://doi.org/10.11591/ijece.v11i4.pp2820-2829.
[9] C. Park, H. Lee, M.O. Zapico, S. Bin Lee, D.D. Reigosa, F.B. Del Blanco, G.C. Stone, Automated testing for early identification of PD in the stator insulation of low voltage VFD motors, IEEE Trans. Ind. Appl. 59 (2023), https://doi.org/10.1109/TIA.2023.3258430.
[10] G. Niu, X. Dong, Y. Chen, Motor fault diagnostics based on current signatures: a review, IEEE Trans. Instrum. Meas. 72 (2023), https://doi.org/10.1109/TIM.2023.3285999.
[11] G.C. Stone, H.G. Sedding, C. Chan, Experience with Online partial-discharge measurement in high-voltage inverter-fed motors, IEEE Trans. Ind. Appl. (2018), https://doi.org/10.1109/TIA.2017.2740280.
[12] W.R. Jensen, E.G. Strangas, S.N. Foster, A method for online stator insulation prognosis for inverter-driven machines, IEEE Trans. Ind. Appl. 54 (2018), https://doi.org/10.1109/TIA.2018.2854408.
[13] I. Oliveira Zaparoli, M. Tulio Alves Evo, H. De Paula, Reliability of Industrial Drive Systems: A Review on InterTurn ShortCircuit Detection in DTC Driven Motors, in: Conference Record – IAS Annual Meeting (IEEE Industry Applications Society), (2021). https://doi.org/10.1109/IAS48185.2021.9677314.
[14] F. Perisse, D. Mercier, E. Lefevre, D. Roger, Robust diagnostics of stator insulation based on high frequency resonances measurements, IEEE Trans. Dielectr. Electr. Insul. 16 (2009), https://doi.org/10.1109/TDEI.2009.5293965.
[15] P. Neti, S. Grubic, Online broadband insulation spectroscopy of induction machines using signal injection, IEEE Trans. Ind. Appl. 53 (2017), https://doi.org/10.1109/TIA.2016.2639014.
[16] G. Zanuso, L. Peretti, Evaluation of high-frequency current ringing measurements for insulation health monitoring in electrical machines, IEEE Trans. Energy Convers. 37 (2022), https://doi.org/10.1109/TEC.2022.3182364.
[17] J.E. Ruiz-Sarrio, J.A. Antonino-Daviu, A. Navarro-Navarro, V. Biot-Monterde, A review of broadband frequency techniques for insulation monitoring and diagnosis in rotating electrical machines, IEEE Trans. Ind. Appl. 60 (2024) 6092–6102, https://doi.org/10.1109/TIA.2024.3384454.
[18] R. Leuzzi, V.G. Monopoli, L. Rovere, F. Cupertino, P. Zanchetta, Analysis and detection of electrical aging effects on high-speed motor insulation, IEEE Trans. Ind. Appl. 55 (2019), https://doi.org/10.1109/TIA.2019.2929013.
[19] D. Zheng, P. Zhang, A Novel Method of Monitoring and Locating Stator Winding Insulation Ageing for Inverter-fed Machine based on Switching Harmonics, in: ECCE 2020 - IEEE Energy Conversion Congress and Exposition, (2020). https://doi.org/10.1109/ECCE44975.2020.9235834.
[20] K.N. Gyftakis, M. Sumislawska, D.F. Kavanagh, D.A. Howey, M.D. McCulloch, Dielectric characteristics of electric vehicle traction motor winding insulation under thermal aging, IEEE Trans. Ind. Appl. 52 (2016), https://doi.org/10.1109/TIA.2015.2495296.
[21] M. Sumislawska, K.N. Gyftakis, D.F. Kavanagh, M.D. McCulloch, K.J. Burnham, D. A. Howey, The impact of thermal degradation on properties of electrical machine winding insulation material, IEEE Trans. Ind. Appl. 52 (2016), https://doi.org/10.1109/TIA.2016.2544745.
[22] I. Tsyokhla, A. Griffo, J. Wang, Online condition monitoring for diagnosis and prognosis of insulation degradation of inverter-fed machines, IEEE Trans. Ind. Electron. 66 (2019), https://doi.org/10.1109/TIE.2018.2885740.
[23] S. Cao, F. Niu, X. Huang, S. Huang, Y. Wang, K. Li, Y. Fang, Time-frequency characteristics research of common mode current in PWM motor system, IEEE Trans. Power Electron. 35 (2020), https://doi.org/10.1109/TPEL.2019.2916686.
[24] M.A. Vogelsberger, C. Zoeller, H. Ertl, T.M. Wolbank, Insulation health state monitoring of traction machines based on online switching transient exploitation, in; PCIM Europe 2017 – International Exhibition and Conference for Power Electronics, Intelligent Motion, Renewable Energy and Energy Management, (2017). https://doi.org/10.1109/SBMicro.2017.7990858.
[25] P. Nussbaumer, M.A. Vogelsberger, T.M. Wolbank, Induction machine insulation health state monitoring based on online switching transient exploitation, IEEE Trans. Ind. Electron. 62 (2015), https://doi.org/10.1109/TIE.2014.2361114.
[26] H. Li, M. Zhao, D. Xiang, H. Yan, On-line monitoring of incipient turn insulation deterioration of servo motor using switching transient frequency response, Zhongguo Dianji Gongcheng Xuebao/Proc. Chinese Soc. Electr. Eng. 40 (2020), https://doi.org/10.13334/j.0258-8013.pcsee.190809.
[27] D. Xiang, H. Li, H. Yan, Y. Zheng, N. Zhao, B. Liu, Online monitoring of incipient turn insulation degradation for inverter-fed machine using sensitive tail component in PWM switching oscillations, IEEE Trans. Power Electron. 36 (2021), https://doi.org/10.1109/TPEL.2021.3049809.
[28] H. Peng, S. Stevic, Z. Luo, N. Driendl, D. Butterweck, L. Sharifian, Y. Firouz, K. Hameyer, Voltage distribution modeling along stator windings in permanent magnet synchronous machines using coil-based grey box models, IEEE Trans. Energy Convers. 39 (2024), https://doi.org/10.1109/TEC.2024.3370800.
[29] H. Peng, N. Driendl, S. Stevic, D. Butterweck, Y. Firouz, L. Sharifian, K. Hameyer, High-frequency modeling of permanent magnet synchronous machines using grey box models, IEEE Trans. Transp. Electrif. (2024), https://doi.org/10.1109/TTE.2024.3363511.
[30] M.U. Sardar, T. Vaimann, L. Kütt, B. Asad, A. Kallaste, R. Land, Wideband Frequency Response Analysis for Sensitive Condition Estimation of Machine's Turn Insulation Degradation Faults, in: 2025 IEEE Workshop on Electrical Machines Design, Control and Diagnosis (WEMDCD), IEEE, (2025), pp. 1–6. https://doi.org/10.1109/WEMDCD61816.2025.11014207.
[31] D. Zheng, G. Lu, P. Zhang, A noninvasive interturn insulation condition monitoring method based on the common-mode impedance spectrum of inverter-fed machines, IEEE Trans. Ind. Appl. 57 (2021), https://doi.org/10.1109/TIA.2021.3094176.
[32] S. He, W. Tian, J. Zhang, K. Li, M. Zhang, R. Zhu, A high efficient approach for power disturbance waveform compression in the view of heisenberg uncertainty, IEEE Trans. Industr. Inform. 15 (2019), https://doi.org/10.1109/TII.2018.2868732.
[33] F. Sahinuc, A. Koc, Fractional fourier transform meets transformer encoder, IEEE Signal Process Lett. 29 (2022), https://doi.org/10.1109/LSP.2022.3217975.
[34] X. Cunxiang, Z. Limin, Z. Zhaogen, Quasi-LFM radar waveform recognition based on fractional Fourier transform and time-frequency analysis, J. Syst. Eng. Electron. 32 (2021), https://doi.org/10.23919/JSEE.2021.000097.
[35] A. Gandhi, T. Corrigan, L. Parsa, Recent advances in modeling and online detection of stator interturn faults in electrical motors, IEEE Trans. Ind. Electron. 58 (2011), https://doi.org/10.1109/TIE.2010.2089937.
[36] F. Perisse, P. Werynski, D. Roger, A new method for AC machine turn insulation diagnostic based on high frequency resonances, IEEE Trans. Dielectr. Electr. Insul. 14 (2007), https://doi.org/10.1109/TDEI.2007.4339494.
[37] D. Zheng, G. Lu, P. Zhang, An improved online stator insulation monitoring method based on common-mode impedance spectrum considering the effect of aging position, IEEE Trans. Ind. Appl. 58 (2022), https://doi.org/10.1109/TIA.2022.3160131.
[38] R. Fan, X. Lei, T. Jia, M. Qin, H. Li, D. Xiang, High-sensitive state perception method for inverter-fed machine turn insulation based on FrFT-Mel, Global Energy Interconnect. 7 (2024) 155–165, https://doi.org/10.1016/j.gloei.2024.04.004.
[39] H. Li, Y. Gu, D. Xiang, P. Zhang, P.P. Yue, Y. Cui, Online condition monitoring of line-end coil insulation for inverter-fed machine by switching oscillation mode decomposition, IEEE Trans. Ind. Electron. 69 (2022), https://doi.org/10.1109/TIE.2021.3120491.
[40] J. Sun, L. Xing, Parameterization of three-phase electric machine models for EMI simulation, IEEE Trans. Power Electron. 29 (2014), https://doi.org/10.1109/TPEL.2013.2264750.
[41] M.U. Sardar, T. Vaimann, L. Kütt, B. Asad, A. Kallaste, K. Kudelina, Characterization of high-frequency impedance-based models for transient terminal overvoltage estimation in cable-fed motor drive systems, in: 2024 International Conference on Electrical Machines (ICEM), 2024, pp. 1–7, https://doi.org/10.1109/ICEM60801.2024.10700495.
[42] H. Liu, X.W. Zhang, L.P. Tu, A modified particle swarm optimization using adaptive strategy, Expert Syst. Appl. 152 (2020), https://doi.org/10.1016/j.eswa.2020.113353.
[43] Z. Li, X. Zhang, Q. Yang, Y. Xiao, H. An, H. Yang, J. Wu, J. Yang, Hybrid SAR-ISAR image formation via joint FrFT-WVD processing for BFSAR ship target high-resolution imaging, IEEE Trans. Geosci. Remote Sens. 60 (2022), https://doi.org/10.1109/TGRS.2021.3117280.
[44] X. Bi, S. Guo, Y. Yang, Q. Shu, Adaptive target extraction method in sea clutter based on fractional fourier filtering, IEEE Trans. Geosci. Remote Sens. 60 (2022), https://doi.org/10.1109/TGRS.2022.3192893.
[45] T. Sibanda, Synchronous median instantaneous power spectrum-gram (SM-IPSgram): a filter banks decomposition for identifying informative frequency band and a weighting function, Mech. Syst. Signal Process. 211 (2024), https://doi.org/10.1016/j.ymssp.2024.111214.
[46] N. Goel, J. Singh, Analysis of Kaiser and Gaussian window functions in the fractional fourier transform domain and its application, Iran. J. Sci. Technol. – Trans. Electr. Eng. 43 (2019), https://doi.org/10.1007/s40998-018-0100-6.
[47] R. Muralishankar, D. Ghosh, S. Gurugopinath, A novel modified Mel-DCT filter bank structure with application to voice activity detection, IEEE Signal Process Lett. 27 (2020), https://doi.org/10.1109/LSP.2020.3006447.
[48] H. Li, D. Xiang, X. Yang, X. Zhang, Compressed sensing method for IGBT high-speed switching time on-line monitoring, IEEE Trans. Ind. Electron. 66 (2019), https://doi.org/10.1109/TIE.2018.2847647.

Appendix 6

Publication VI

M. U. Sardar et al., "High-Frequency Impedance Parametric Modeling and Partial Discharge Validation for RUL Estimation of Thermally Aged Stator Insulation," *2026 International Conference on Electrical Machines (ICEM)*, Funchal (Madeira), Portugal, 2026, pp. 1-7, doi: 10.1109/ICEM68283.2026.11757493.

High-Frequency Impedance Parametric Modeling and Partial Discharge Validation for RUL Estimation of Thermally Aged Stator Insulation

Muhammad Usman Sardar, Toomas Vaimann, Lauri Kütt, Bilal Asad, Ants Kallaste
Department of Electrical Power Engineering and Mechatronics, Tallinn University of Technology
19086 Tallinn, Estonia
muhammad.sardar@taltech.ee

Hujun Peng, Simon Steentjes
Institute of Electrical Machines (IEM), RWTH Aachen University
52062 Aachen, Germany
hujun.peng@iem.rwth-aachen.de

2026 International Conference on Electrical Machines (ICEM) | 979-8-3315-6232-8/26/$31.00 ©2026 IEEE | DOI: 10.1109/ICEM68283.2026.11757493

***Abstract*—The degradation of stator winding insulation is a primary contributor to failures in inverter-fed machines. This study proposed a comprehensive condition-monitoring framework for stator winding subjected to a controlled, accelerated thermal ageing cycle. A high-frequency (HF) frequency response analysis (FRA) based on the proposed machine model was mapped with partial discharge (PD) to evaluate multiple degradation levels. The proposed machine model enabled accurate tracking of turn-to-turn and phase-to-ground capacitance variations, which are critical dielectric markers. Furthermore, PD analysis using inception voltage (PDIV) and PD charge was evaluated as a complementary discharge-based indicator. An Arrhenius–Miner thermal ageing model quantified cumulative insulation damage, with each ageing cycle contributing approximately 2.4 % to the total life consumption. The remaining useful life (RUL) decreased monotonically from 100% (healthy state) to 74 %, validating the enhanced early-stage sensitivity of FRA compared with conventional indicators. The validated model-based framework exhibited superior sensitivity to early-stage insulation degradation, thereby facilitating predictive maintenance strategies and providing a robust physics-based foundation for machine learning–assisted, model-driven prognostics.**

Keywords—Condition monitoring, Grey-box modeling impedance spectroscopy, Inverter-fed machines, Partial discharges.

I. INTRODUCTION

Inverter-Fed motors (IFMs) have been widely used in wind power generation, rail transportation, ship electric propulsion, and other important fields, and their reliability is crucial to the safe operation of the whole system [1], [2]. The insulation system of motors is continuously subjected to various ageing stresses and gradually ages during operation, especially with the popularity of wide-bandgap devices in inverters. The higher *dv/dt* and switching frequency greatly accelerate this process. Stator insulation faults account for 30 %–40 % of low-voltage (LV) motor failures and 60 %–70 % of high-voltage motor failures [3], [4]. A localized interturn short-circuit fault can generate a large circulating short-circuit current, producing significant heat that can damage the insulation between adjacent windings. This rapid deterioration can quickly escalate to a phase-to-phase (PP) or ground-wall (GW) insulation failure [1]. Abrupt motor failure will lead to significant downtime and economic losses [5]. Therefore, it is necessary to develop reliable methods for monitoring motor insulation conditions to provide early warning of potential failures and support preventive maintenance.

Consequently, considerable research has focused on PD-free machine design to strengthen insulation robustness under inverter-induced electrical stress [6], [7]. Several inverter-based offline insulation condition monitoring and diagnostic techniques have been reported using indicators such as partial discharge (PD), insulation capacitance (IC), dissipation factor (DF), and insulation resistance (IR) [8], [9]. High *dv/dt* inverter pulse voltages are widely used to excite PD activity for early detection of interturn, PP, and GW insulation defects. Certainly, the Partial Discharge Inception Voltage (PDIV) could decrease due to thermal stress, i.e., a lower voltage may be sufficient to initiate PD activity in thermally aged insulation systems. Hence, although the electric machine may be PD-free at the beginning of its life, it may develop PD during its service life [10], [11]. In addition, IC and DF extracted from inverter-induced non-zero common-mode leakage currents and switching transient responses (STR) have been applied to evaluate insulation ageing trends [9], [12]. However, these offline methods remain sensitive to pulse characteristics, tuning requirements, and electromagnetic interference, limiting robustness and repeatability [13]. Periodic monitoring of the winding's health can help prevent unexpected machine failures [6]. Two widely deployed testing and inspection methods are impedance spectroscopy and PD analysis (e.g., PDIV measurements). The non-destructive nature of both techniques makes them good candidates for health condition assessments [14], [15].

Frequency response analysis (FRA) over a wide frequency range (20 kHz–100 MHz), spanning from low-frequency (LF) to high-frequency (HF) regions, has demonstrated strong capability as a diagnostic tool for detecting insulation degradation in inverter-fed machines. FRA is more suitable than IR or DF for inverter-fed machines because it captures the distributed winding capacitance and HF effects excited by WBG switching transients. [16], [17]. For machine parametric identification, a grey-box model (GBM) of the induction machine (IM) incorporating the effects of the cable and inverter can be used for optimal fitting [18], [19]. Using the measured impedance-frequency profile and tracking the motor's resonance and anti-resonance behavior, insulation-related parameters can be identified, with turn-to-turn capacitance being the key factor in determining the machine's insulation condition. Thermal ageing of electrical insulation is commonly described using Arrhenius kinetics, which correlates insulation lifetime with temperature-dependent chemical degradation mechanisms. For variable- or cyclic-thermal degradation level (TDL), Miner's linear damage accumulation rule is widely used in combination with the Arrhenius model to estimate cumulative life consumption.

Authorized licensed use limited to: Tallinn University of Technology. Downloaded on November 16,2026 at 14:36:27 UTC from IEEE Xplore. Restrictions apply.

This combined Arrhenius–Miner framework has been extensively adopted for accelerated ageing assessment of inverter-fed machine windings [20], [21]. The literature review indicates some significant limitations: insensitivity to early degradation, limited physical interpretation of diagnostic features, weak integration of impedance analysis and PD analysis, and a lack of a unified framework for life prediction.

To overcome these gaps, this paper proposes a physics-consistent HF insulation monitoring framework that combines parametric impedance modeling with partial discharge-based indices, thereby improving condition assessment and quantitative estimation of remaining life. The main contribution of this paper is summarized below:

- Precise parameter identification from the proposed HF GBM of the IM for frequency response–based insulation characterization.
- Representation of degradation-sensitive GBM parameters with partial discharge (PDIV and PD charge) measurements to establish unified dielectric health markers.
- Integration of an Arrhenius–Miner thermal ageing life-cycle model to map cumulative damage and RUL evolution, and multi-domain condition monitoring parameters.

The rest of the paper is structured as follows: Section II outlines the stator insulation ageing framework; Section III describes the measurement setup and methodology; Section IV presents the measurement results; Section V analyzes the extracted health-monitoring markers; and Section VI concludes the paper.

II. Stator Insulation Ageing and Condition Monitoring

This section describes the accelerated thermal ageing process of stator winding insulation and presents techniques based on HF impedance and partial discharge for condition monitoring.

A. Sample under Thermal Degradation Cycle

The test sample was a three-phase IM stator winding, selected to monitor insulation ageing. Thermal ageing cycles were conducted by placing the stator assembly in a calibrated electric oven to ensure uniform and precise temperature control, in accordance with the thermal endurance principles specified in IEC 60034. Progressive thermal degradation of insulation changes its dielectric properties, causing measurable changes in the winding impedance and related HF response parameters.

Similar to the temperature-cycling life prediction framework proposed for LV transportation electric machine windings [22], this work adopts an accelerated ageing–based lifetime modeling approach to quantify insulation degradation under temperature profile (TP). Building on experimentally calibrated lifetime models, the proposed methodology links measured ageing indicators to equivalent life consumption and RUL estimation.

As insulation deteriorates, the equivalent turn-to-turn capacitance Ci may vary due to changes in dielectric permittivity and insulation geometry. Depending on the dominant ageing mechanism (e.g., thinning, delamination, or micro-cracking), C_i can either increase or decrease [4]. This relationship is described by (1):

$$C_i = \varepsilon_o \varepsilon_r \frac{l_i l}{2e_i} \tag{1}$$

Where ε_o and ε_r are the permittivity of free space and the relative permittivity of the insulation material. l_i is the width of the turn, l is the length of the turn, and e_i is the insulation thickness. As insulation degrades, thinning or increased conductivity alters the effective dielectric properties, leading to a measurable change in turn-to-turn capacitance C_i. Tracking this change offers a non-invasive, quantitative marker of ageing [16].

B. Proposed Low-to-High Frequency Parametric IM GBM

The proposed IM model, shown in Fig. 1, adopts a GBM framework previously developed by the authors in their earlier work [4]. The GBM includes key parameters: $R_{E,i}$ (iron-loss resistance), $L_{T,i}$, $R_{T,i}$ and $C_{T,i}$ (phase inter-turn branch elements) for HF behavior. R_S , $L_{S,i}$, and $M_{ab,i}$ are stator resistance, self and mutual inductance, while $R_{G,i}$ and $C_{G,i}$ represent the frame grounding resistance and capacitance. C_{ph} and M_C account for phase-to-phase parasitic capacitance and mutual inductances.

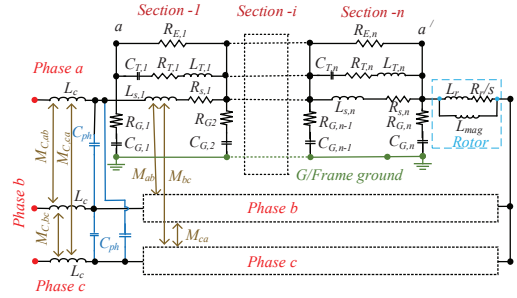


Fig. 1. Low-to-HF parametric GBM of IM.

Rotor parameters include R_r (resistance), L_r (leakage inductance), and L_{mag} (magnetizing inductance). The motor frame ground G serves as a common reference, and n, equal to ten, denotes the number of distributed segments for detailed analysis.

C. Parameter Identifications of the Proposed GBM of IM

The study employs an RLC-based parametric impedance model of the IM, where the initial parameters are derived from the analytical formulations presented in [23], [24]. The explanation for identifying the parameter is detailed in section IV-A, where the equations are applied to the measured results to formulate the model.

A refined set of model parameters is obtained through an optimal fitting procedure using a numerical optimization algorithm. Specifically, a particle swarm optimization (PSO) technique is employed to minimize the deviation between the simulated and experimentally measured impedance magnitude and phase responses across the investigated frequency range.

Authorized licensed use limited to: Tallinn University of Technology. Downloaded on November 16,2026 at 14:36:27 UTC from IEEE Xplore. Restrictions apply.

III. Measurement Set-up and Methodology

The framework proposed in this paper (Fig. 2) combines accelerated thermal ageing testing of motor stators with a unified insulation condition monitoring platform utilizing both FRA and PD analysis. Age-sensitive GBM dielectric parameters and PD functions are extracted and systematically correlated to construct physically meaningful insulation condition indicators. The Arrhenius-Miner cumulative damage model is then used to map these correlated indicators, allowing the construction of quantitative condition indicators and the evaluation of the remaining life (RUL) evolution.

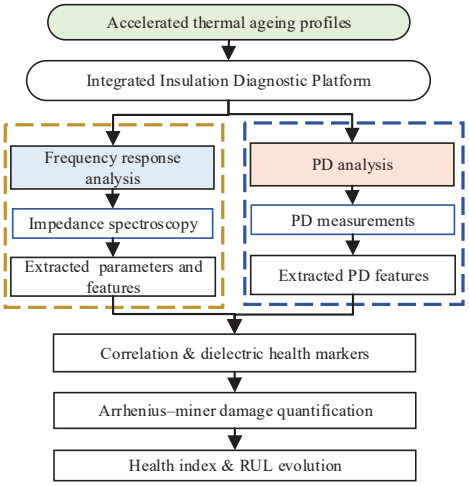


Fig. 2. Thermal ageing and insulation condition monitoring framework.

A. Accelerated thermal ageing set-up and procedure

Fig. 3 shows the experimental setup used to measure thermal degradation and HF impedance over a frequency range of 20 Hz to 120 MHz. The system includes a calibrated heating chamber, a temperature monitoring device, and a test motor. As shown in Fig 4, the HF impedance analyzer (Keysight, E4990A) and its measurement interface are used to record the amplitude and phase distribution of the DM and CM impedances over multiple degradation cycles. Each cycle represents a thermal degradation level (TDL), ranging from the normal/healthy state (TDL-0) to severe state TDL-20.

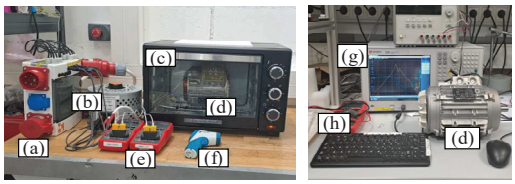


Fig. 3. Test setup for thermal degradation and impedance measurements (a) supply, (b) autotransformer, (c) heating chamber, (d) test motor (e) thermocouple units (f) infrared thermometer (g) impedance analyzer and (h) analyzer interface.

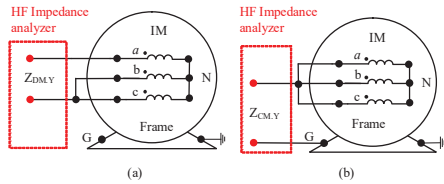


Fig. 4. Measurement schematics of winding impedance in (a) DM (b) CM

B. PDIV measurement set-up and procedure

Fig. 5 presents the laboratory PD test setup, including the HV ac source, coupling components, and the test motor arrangement. Fig. 6 shows the corresponding schematic diagram of the partial discharge (PD) measurement configuration for the IM under high-voltage excitation.

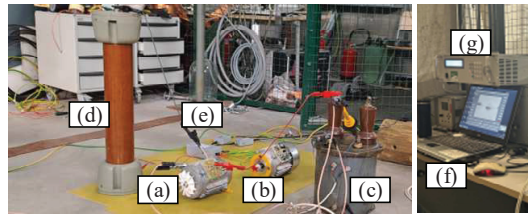


Fig. 5. Partial-discharge measurement setup (a) test sample (b) healthy motor (c) HV transformer (d) coupling capacitor (e) PD measuring unit, (f) PC for data acquisition (g) oscilloscope and (h) AC supply control unit.

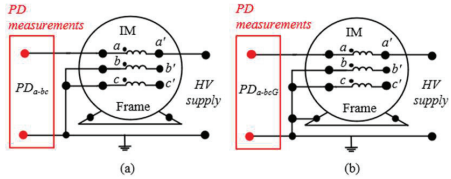


Fig. 6. Test schematics for PD measurement (a) phase-to-phase (b) ground-wall.

The partial discharge measurement setup consisted of PD measurement equipment from PDS (Power Diagnostix System). Phase-to-phase and ground-wall PDIV were measured following the connections described in IEC 60034-27-1 [28].

C. Arrhenius–Miner Thermal Ageing Model and RUL estimation

The Arrhenius model is widely used to describe the thermal ageing behaviour of electrical insulation under constant-temperature conditions. The insulation lifetime ($L(t)$) at temperature T is expressed as

$$L(T) = A\, e^{B/T} \quad . \tag{2}$$

where A and B are material-dependent constants obtained from accelerated thermal ageing tests, and T denotes the absolute temperature in Kelvin. The ageing acceleration factor (AAF), which quantifies the relative ageing rate at temperature $T(t)$ with respect to T_{ref}, is given by

$$AAF(t) = \frac{L(T_{ref})}{L(T(t))} = e^{B\left(\frac{1}{T_{ref}} - \frac{1}{T(t)}\right)} \tag{3}$$

Authorized licensed use limited to: Tallinn University of Technology. Downloaded on November 16,2026 at 14:36:27 UTC from IEEE Xplore. Restrictions apply.

The incremental Miner insulation damage is defined as

$$dD(t) = \frac{AAF(t)}{L_{ref}}\, dt\ . \tag{4}$$

where L_{ref} denotes the nominal insulation lifetime at the reference temperature T_{ref} . For discretely sampled temperature data T_i with corresponding time intervals Δt_i that define the TP, the cumulative insulation damage (D) is evaluated as

$$D = \frac{1}{L_{ref}} \sum_{i=1}^{N} AAF_i\, \Delta t_i\ . \tag{5}$$

Finally, the remaining useful life (RUL) expressed in percentage is calculated as

$$RUL\ (\%) = (1 - D) \times 100\ . \tag{6}$$

The tested IM employs a LV, class-F, type-I random-wound insulation system characterized by Arrhenius parameters A=2.36×10^{-10} and B=15359, consistent with IEC 60034-18. A reference hot-spot temperature of T_{ref} of 155 °C (428 K) is selected, with a nominal insulation lifetime (L_{ref}) of 15 years (approx. 131,000 h). As depicted IN Fig. 7, for an accelerated ageing TP of 200 °C (473 K), the AAF calculated from (3) is approximately 30. indicating that degradation progresses about thirty times faster than at the reference condition or

$$1\ hour\ at\ 200°C\ \approx\ 30\ hours\ at\ 155°C\ .$$

For an initial thermal exposure of (200 ^{0}C) for 50 h (ten 5 h cycles), the equivalent life consumption at 155°Cbecomes $30 \times 50 = 1500$ h. The corresponding D is therefore

$$D = \frac{30\times 50}{131000} = 0.012\ \ or\ 1.2\%\ \ \text{and}\ \ RUL = 98.8\ \%.$$

Similarly, at an accelerated temperature of 250 °C, for 50 hours, the equivalent life consumption at 155°C becomes $677 \times 50 = 1500$ h. The corresponding D is therefore

$$D = \frac{677\times 50}{131000} = 0.26\ \ or\ 26\%\ \text{and}\ RUL = 74\ \%.$$

IV. Measurements Results

This section presents the measured impedance characteristics of the motor under progressive thermal ageing.

A. Temperature profile (TP)

Fig. 7 presents the time-temperature profile of the sample during thermal degradation in the oven. The specimen was subjected to repeated heating cycles, where each cycle consisted of 5 h of heating followed by cooling and measurement intervals.

B. Impedance Spectroscopy During the Degradation Cycle

Fig. 8 shows the practically measured CM and DM impedance spectra at different degradation levels. As ageing progresses, the resonance frequencies (f_s, f_p) shifts toward higher frequencies and noticeable changes appear in the impedance magnitude, particularly around and above the resonance region. These trends suggest alterations in the effective capacitances and dielectric behavior of the interturn and ground-wall insulation, confirming that impedance spectroscopy can effectively capture variations in degradation-related parameters.

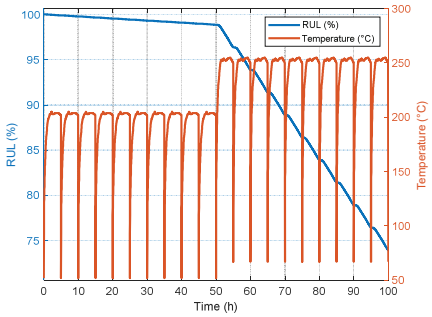


Fig. 7. Time evolution of RUL with the sample's TP.

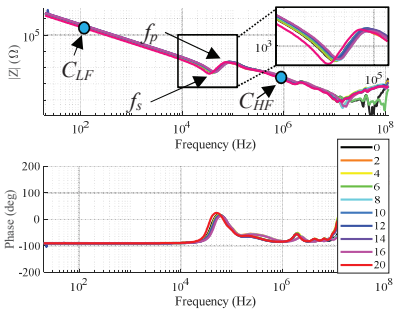


Fig. 8. Measured impedance profile for every degradation cycle.

C. GBM Parameter Identification Through Optimal Fitting

Based on impedance measurements, the HF insulation-related parameters are initially calculated according to (7)-(11). Subsequently, a more refined set of parameters is obtained through optimal-fitting procedures, in which the model response is iteratively adjusted to minimize the error between the simulated and experimentally measured responses.

$$C_{HF} = \frac{1}{2\pi f_{HF} Z_{HF.CM}}\ ,\ C_{LF} = \frac{1}{2\pi f_{LF} Z_{LF.CM}} \tag{7}$$

$$C_{G1} = \frac{1}{3} C_{HF},\quad C_{G2} = \frac{1}{3}(C_{LF} - C_{HF}) \tag{8}$$

$$R_E = \frac{2}{3}|Z_r| \tag{9}$$

$$f_p = \frac{1}{2\pi\sqrt{L_s(C_T + C_{G2})}} \tag{10}$$

$$f_s = \frac{1}{2\pi\sqrt{L_s\left(C_T + \frac{C_{G1}C_{G2}}{C_{G1}+C_{G2}}\right)}} \tag{11}$$

$$\tan\delta = \frac{1}{2\pi f_{LF} R_P C_P} \tag{12}$$

Where R_p and C_p represent the parallel resistive and capacitive common-mode dielectric parameters (CMDP),

Authorized licensed use limited to: Tallinn University of Technology. Downloaded on November 16,2026 at 14:36:27 UTC from IEEE Xplore. Restrictions apply.

respectively, obtained from common-mode impedance measurements.

GBM more closely follows the measured impedance response in the high-frequency region, where conventional models begin to deviate, as shown in Fig. 9.

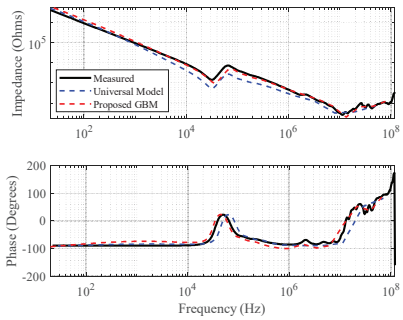


Fig. 9. Comparison of measured impedance profile with GBM.

During the PSO optimization, inductive parameters were fixed as thermal ageing primarily impacts the dielectric permittivity and insulation geometry, thus predominantly affecting capacitive and resistive branches.

D. Choice of GBM parameter to characterize the insulation

Once the frequency-related parameters were identified with their percentage variations, the resistive and capacitive parameters were found to be more dominant and more sensitive to thermal degradation, hence their values showed a clearer change with ageing. In contrast, the inductive parameters presented only minimal change, indicating that they are less affected by insulation deterioration. Section V presents the insulation markers based on GBM parameters and CMDP, which are used to represent insulation health.

E. PD analysis

Fig. 10 presents the evolution of phase-to-phase and ground-wall PD characteristics during thermal ageing at 200 °C. A consistent reduction in PDIV is observed with increasing degradation level, where phase-to-phase PDIV decreases from 658 V (TDL-0) to 590 V (TDL-20), and ground-wall PDIV drops from 634 V to 550 V, corresponding to reductions of approximately 10 % and 13 %, respectively.

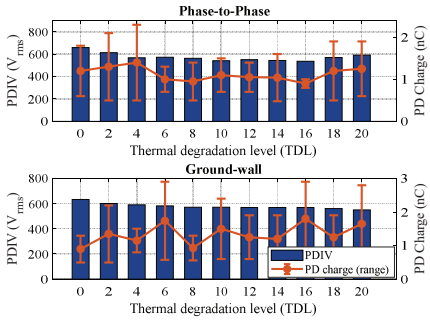


Fig. 10. Experimental PD measurement results with degradation cycle.

The progressive PDIV reduction aligns with the decline in RUL from 100% to 74 %, confirming that PD parameters provide quantitative and statistically consistent indicators of insulation deterioration under thermal ageing conditions.

V. Analysis of Health Monitoring Markers

For every degradation case, the absolute change is first calculated as

$$\Delta x = x_{case} - x_{base} \ . \tag{13}$$

where x_{base} corresponds to the initial healthy (TDL-0) value. The relative percentage variation (Δ%) represents the change from the TDL-0 baseline as

$$\Delta\% \, x = \frac{x_{case} - x_{base}}{x_{base}} \times 100 \ . \tag{14}$$

By referencing each parameter to its healthy baseline (TDL-0), the progression of degradation severity can be directly quantified.

Fig. 11 and Fig. 12 demonstrate the variation trends in the FRA-based GBM parameters with thermal degradation from TDL-0 to TDL-20. The impedance magnitude ΔZ_{CM} and ΔR_P initially increase at a lower temperature level and then decreases at the final degradation stage. The capacitive parameters show an initial decreasing trend, although under severe thermal stress, they exhibit an increasing variation of up to 25%.

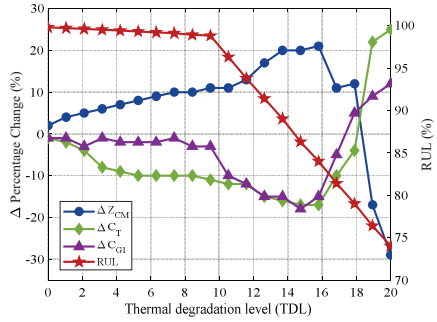


Fig. 11. Evolution of FRA-based GBM health markers.

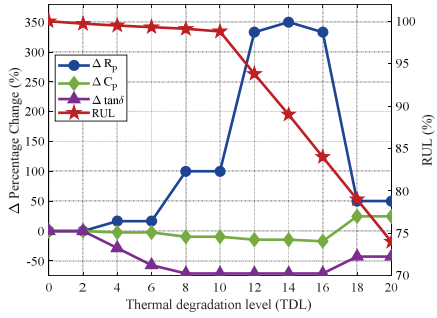


Fig. 12. Evolution of CMDP health markers during thermal ageing.

Fig. 13 shows PDIV's greater sensitivity to early-stage insulation degradation. The phase–phase PDIV initially decreases by approximately 10 %, clearly indicating insulation weakening. The ground–wall PDIV shows a similar trend but is less pronounced. However, PD-charge values

Authorized licensed use limited to: Tallinn University of Technology. Downloaded on November 16,2026 at 14:36:27 UTC from IEEE Xplore. Restrictions apply.

exhibit noticeable fluctuations and do not exhibit strict monotonicity. Compared with FRA markers, PDIV provides stronger early-detection capability, whereas PD charge serves as a complementary but more variable indicator of severity.

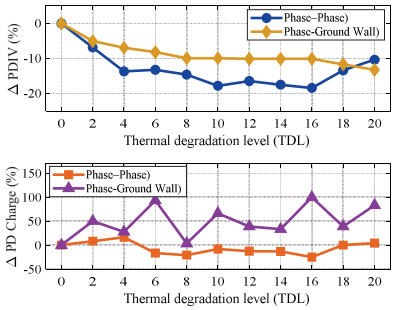


Fig. 13. Evolution of PD parameters during thermal ageing.

VI. Conclusion

Implementation of a robust stator insulation condition-monitoring framework is crucial for ensuring the reliability of power electronics-based industrial and transportation systems. Degradation-sensitive GBM parameters were physically correlated with PDIV and PD charge to establish unified and interpretable dielectric health markers. PD charge serves as a more effective pre-failure indicator, whereas the proposed FRA framework demonstrates higher sensitivity to early-stage insulation ageing. Specifically, an Arrhenius–Miner thermal ageing framework, driven by measured TPs, was integrated to quantify cumulative damage and the subsequent evolution of the remaining useful life. Furthermore, GBM provides a framework for the generation of synthetic degradation data under controlled ageing scenarios. This supports the development of robust machine-learning–based condition monitoring and prognostics while preserving physical interpretability and engineering relevance.

References

[1] S. Huang, A. Aggarwal, E. G. Strangas, B. Khoshoo, K. Li, and F. Niu, "Mitigation of Interturn Short-Circuits in IPMSM by Using MTPCC Control Adaptive to Fault Severity," *IEEE Trans. Power Electron.*, vol. 37, no. 4, 2022, doi: 10.1109/TPEL.2021.3127538.

[2] B. Asad, T. Vaimann, A. Rassõlkin, A. Kallaste, and A. Belahcen, "Review of Electrical Machine Diagnostic Methods Applicability in the Perspective of Industry 4.0," *Electrical, Control and Communication Engineering*, vol. 14, no. 2, 2018, doi: 10.2478/ecce-2018-0013.

[3] W. Zhou, M. DIab, and X. Yuan, "Impact of Parasitic and Load Current on the Attenuation of Motor Terminal Overvoltage in SiC-Based Drives," *IEEE Trans. Ind. Appl.*, vol. 58, no. 2, 2022, doi: 10.1109/TIA.2022.3141703.

[4] M. U. Sardar, T. Vaimann, L. Kütt, B. Asad, and A. Kallaste, "Switching oscillation-based fractional-domain high-sensitive diagnosis of machine turn insulation degradation," *Engineering Science and Technology, an International Journal*, vol. 72, Dec. 2025, doi: 10.1016/j.jestch.2025.102224.

[5] S. Huang, A. Aggarwal, E. G. Strangas, K. Li, F. Niu, and X. Huang, "Robust Stator Winding Fault Detection in PMSMs with Respect to Current Controller Bandwidth," *IEEE Trans. Power Electron.*, vol. 36, no. 5, 2021, doi: 10.1109/TPEL.2020.3030036.

[6] L. Lusuardi, A. Cavallini, V. Madonna, P. Giangrande, and M. Galea, "Unconventional accelerated thermal ageing test for traction electric motors in vehicles," in *2020 IEEE Electrical Insulation Conference, EIC 2020*, 2020. doi: 10.1109/EIC47619.2020.9158744.

[7] L. Elorza Azpiazu, G. Almandoz, A. Egea, G. Ugalde, and X. Badiola, "Study of Partial Discharge Inception Voltage in Inverter Fed Electric Motor Insulation Systems," *Applied Sciences (Switzerland)*, vol. 13, no. 4, 2023, doi: 10.3390/app13042417.

[8] H. Lee, H. Kim, J. Jeong, K. Lee, S. Bin Lee, and G. Stone, "Inverter-Embedded Partial Discharge Testing for Reliability Enhancement of Stator Winding Insulation in Low Voltage Machines," *IEEE Trans. Ind. Appl.*, vol. 58, no. 2, 2022, doi: 10.1109/TIA.2022.3142712.

[9] M. F. Shaikh, H. Lee, B. Battulga, S. Bin Lee, and G. C. Stone, "Detection of Severe Ground Insulation Deterioration Before Failure in VFD-Fed Motors Using Off-Line Common-Mode Voltage," *IEEE Trans. Ind. Appl.*, vol. 60, no. 1, 2024, doi: 10.1109/TIA.2023.3307344.

[10] C. Park *et al.*, "Automated Testing for Early Identification of PD in the Stator Insulation of Low Voltage VFD Motors," *IEEE Trans. Ind. Appl.*, vol. 59, no. 4, 2023, doi: 10.1109/TIA.2023.3258430.

[11] P. Wang, S. Ma, S. Akram, K. Zhou, Y. Chen, and M. T. Nazir, "Design of Archimedes Spiral Antenna to Optimize for Partial Discharge Detection of Inverter Fed Motor Insulation," *IEEE Access*, vol. 8, 2020, doi: 10.1109/ACCESS.2020.3033300.

[12] D. Zheng, G. Lu, G. Li, M. Yao, and P. Zhang, "Quasi-Online Technique for Health Monitoring of Stator Winding Insulation in Inverter-Fed Motor Using Switching Transient Voltage Response," in *2023 26th International Conference on Electrical Machines and Systems, ICEMS 2023*, 2023. doi: 10.1109/ICEMS59686.2023.10344804.

[13] J. E. Ruiz-Sarrio, J. A. Antonino-Daviu, A. Navarro-Navarro, and V. Biot-Monterde, "Broadband Technique Analysis for Insulation Fault Detection and Condition Monitoring in Rotating Electrical Machines," in *Proceedings of the 2023 IEEE 14th International Symposium on Diagnostics for Electrical Machines, Power Electronics and Drives, SDEMPED 2023*, 2023. doi: 10.1109/SDEMPED54949.2023.10271498.

[14] S. Xiang *et al*., "Life Prediction of Ground-Wall Insulation Material in Electric Motors Based on Accelerated Degradation Test under Different Failure Mechanisms," in *IEEE Journal of Emerging and Selected Topics in Industrial Electronics*, vol. 6, no. 2, pp. 654-663, April 2025, doi: 10.1109/JESTIE.2024.3522001.

[15] J. E. Ruiz-Sarrio, J. A. Antonino-Daviu, A. Navarro-Navarro, and V. Biot-Monterde, "A Review of Broadband Frequency Techniques for Insulation Monitoring and Diagnosis in Rotating Electrical Machines," *IEEE Trans. Ind. Appl.*, vol. 60, no. 4, pp. 6092–6102, 2024, doi: 10.1109/TIA.2024.3384454.

[16] R. Fan, X. Lei, T. Jia, M. Qin, H. Li, and D. Xiang, "High-sensitive state perception method for inverter-fed machine turn insulation based on FrFT-Mel," *Global Energy Interconnection*, vol. 7, no. 2, pp. 155–165, Apr. 2024, doi: 10.1016/j.gloei.2024.04.004.

[17] D. Zheng, G. Lu, and P. Zhang, "An Improved Online Stator Insulation Monitoring Method Based on Common-Mode Impedance Spectrum Considering the Effect of Aging Position," *IEEE Trans. Ind. Appl.*, vol. 58, no. 3, 2022, doi: 10.1109/TIA.2022.3160131.

[18] M. U. Sardar, T. Vaimann, L. Kutt, B. Asad, A. Kallaste, and A. Rassõlkin, "Modeling Cable-Fed Induction Motor Drives with Optimized Impedance Characterization Across a Low to High-Frequency Spectrum," *IEEE Transactions on Energy Conversion*, 2025, doi: 10.1109/TEC.2025.3630465.

[19] H. Peng *et al.*, "High-frequency Modeling of Permanent Magnet Synchronous Machines using Grey Box Models," *IEEE Transactions on Transportation Electrification*, 2024, doi: 10.1109/TTE.2024.3363511.

[20] M. U. Sardar, T. Vaimann, L. Kütt, B. Asad, A. Kallaste, and R. Land, "Wideband Frequency Response Analysis for Sensitive Condition Estimation of Machine's Turn Insulation Degradation Faults," in *2025 IEEE Workshop on Electrical Machines Design, Control and Diagnosis (WEMDCD)*, IEEE, Apr. 2025, pp. 1–6. doi: 10.1109/WEMDCD61816.2025.11014207.

[21] H. Li, Y. Gu, D. Xiang, P. Zhang, P. P. Yue, and Y. Cui, "Online Condition Monitoring of Line-End Coil Insulation for Inverter-Fed Machine by Switching Oscillation Mode Decomposition," *IEEE Transactions on Industrial Electronics*, vol. 69, no. 11, 2022, doi: 10.1109/TIE.2021.3120491.

[22] Z. Jian, Z. Qin, H. Xiaoyan, F. Youtong, and T. Jie, "Motor Insulation Remaining Useful Life Prediction Method Based on Accelerating

Authorized licensed use limited to: Tallinn University of Technology. Downloaded on November 16,2026 at 14:36:27 UTC from IEEE Xplore. Restrictions apply.

Degradation Data and Field Degradation Data," *Diangong Jishu Xuebao/Transactions of China Electrotechnical Society*, vol. 38, no. 3, 2023, doi: 10.19595/j.cnki.1000-6753.tces.221227.

[23] J. Zhang *et al.*, "A Review of Reliability Assessment and Lifetime Prediction Methods for Electrical Machine Insulation Under Thermal Aging," 2025. doi: 10.3390/en18030576.

[24] P. Nussbaumer, M. A. Vogelsberger, and T. M. Wolbank, "Induction machine insulation health state monitoring based on online switching transient exploitation," *IEEE Transactions on Industrial Electronics*, vol. 62, no. 3, 2015, doi: 10.1109/TIE.2014.2361114.

[25] X. Zhou, Y. Ji, P. Giangrande, W. Zhao, and M. Galea, "Temperature Cycling Life Prediction of Low-Voltage Transportation Electric Machines Winding: From Lifetime Model Proposal to Applications," *IEEE Transactions on Transportation Electrification*, 2025, doi: 10.1109/TTE.2025.3648430.

[26] J. Sun and L. Xing, "Parameterization of three-phase electric machine models for EMI simulation," *IEEE Trans. Power Electron.*, vol. 29, no. 1, 2014, doi: 10.1109/TPEL.2013.2264750.

[27] M. U. Sardar, T. Vaimann, L. Kütt, B. Asad, A. Kallaste, and K. Kudelina, "Characterization of High-Frequency Impedance-Based Models for Transient Terminal Overvoltage Estimation in Cable-Fed Motor Drive Systems," in *2024 International Conference on Electrical Machines (ICEM)*, IEEE, Sep. 2024, pp. 1–7. doi: 10.1109/ICEM60801.2024.10700495.

[28] IEC, Rotating electrical machines – Part 27-1: Off-line partial discharge measurements on the stator winding insulation of rotating electrical machines, EVS-EN IEC 60034-27-1:2018, 2018.

BIOGRAPHIES

Muhammad Usman Sardar was born in 1989 in Rahim Yar Khan, Pakistan. He obtained his B.Sc. and M.Sc. in Electrical Power Engineering from The Islamia University of Bahawalpur, Punjab, Pakistan, and is pursuing a Ph.D. at Tallinn University of Technology in Estonia. His research interests include condition monitoring and fault diagnostics of electrical machines.

Toomas Vaimann was born in Pärnu, Estonia, in 1984 and received his BSc, MSc and PhD degrees in electrical engineering from Tallinn University of Technology, Estonia, in 2007, 2009 and 2014 respectively. He is currently a research professor at Tallinn University of Technology, Department of Electrical Engineering. Internationally, he has been a postdoctoral researcher at the Department of Electrical Engineering and Automation, Aalto University, Espoo, Finland. His main research interest is the diagnostics of electrical machines.

Lauri Kütt received the B.Sc. degree in computer and automation technology and the M.Sc. degree in electrical power engineering from the Tallinn University of Technology, Tallinn, Estonia, in 2002 and 2004, respectively, and the Ph.D. degree from the Department of Energy and Geotechnology, Tallinn University of Technology, in 2012. He is currently a Professor and his current research interests include fast transients on electric power lines, power line diagnostics, power quality, and electromagnetic compatibility.

Bilal Asad was born in 1986 in Pakistan. He received his BSc in Electronics Engineering from The Islamia University of Bahawalpur and MSc in Electrical Engineering from University of Engineering and Technology (UET) Lahore, Pakistan and PhD from Tallinn University of Technology, Estonia and Department of Electrical Engineering and Automation, Aalto University, Espoo Finland. His area of interest includes design, modeling and fault diagnostics of electrical machines.

Ants Kallaste was born in Pärnu, Estonia in 1980 and received his BSc, MSc and PhD degrees in electrical engineering from Tallinn University of Technology, Estonia, in 2004, 2006 and 2013 respectively. He is currently a Professor of Electrical Machines at Tallinn University of Technology, Department of Electrical Power Engineering and Mechatronics. His research interests encompass electrical machine design, additive manufacturing of electrical machines, and related aspects of electrical drive systems.

Hujun Peng received the B.Sc. degree in electrical engineering from Zhejiang University, Hangzhou, China, in 2013, the M.Sc. degree from Dresden University of Technology, Dresden, Germany, in 2017, and the Ph.D. degree from RWTH Aachen University, Aachen, Germany, in 2023. Since February 2023, he has been a Postdoctoral Researcher with the Institute of Electrical Machines. His research interests include high-frequency modeling of electrical machines. He also works on characterization of insulation systems in electrical machines.

Simon Steentjes received the Diploma and Dr.-Ing. degrees in electrical engineering and information technology from RWTH Aachen University, Aachen, Germany. From 2011 to 2018, he was a Research Associate and Group Leader with the Institute of Electrical Machines (IEM). He subsequently held expert and management positions in electric machine development at Audi AG and Hilti Entwicklungsgesellschaft mbH. In October 2024, he was appointed Full Professor with the Chair of Electrical Machines and Drives and Director of IEM at RWTH Aachen University, with research interests in magnetic and winding material modeling, multiphysical simulation, and inverter–machine interactions.

Authorized licensed use limited to: Tallinn University of Technology. Downloaded on November 16,2026 at 14:36:27 UTC from IEEE Xplore. Restrictions apply.

Curriculum Vitae

Personal data

Name: Muhammad Usman Sardar
Date of birth: 15/01/1989
Place of birth: Punjab, Pakistan
Citizenship: Pakistan

Contact data

E-mail: muhammad.sardar@taltech.ee, engr.usman.ee@gmail.com

Education

2023–2026	Ph.D. Electrical Power Engineering and Mechatronics, Tallinn University of Technology, Estonia
2012–2015	M.Sc. Electrical (Power) Engineering, The Islamia University of Bahawalpur, Pakistan
2008–2012	B.Sc. Electrical (Power) Engineering, The Islamia University of Bahawalpur, Pakistan
2006–2008	B.Sc. (Mathematics & Physics), The Islamia University of Bahawalpur, Pakistan

Language competence

English	Fluent
Urdu	Native
Punjabi	Native
Estonian	Beginner
Chinese	Beginner

Professional employment

2023-2026	Early Stage Researcher (1.00) Department of Electrical Power Engineering and Mechatronics, Tallinn University of Technology, Estonia
2017-2023	Lecturer Khwaja Fareed University of Engineering and Information Technology, Rahim Yar Khan, Pakistan
2015-2017	Lecturer Riphah International University (Lahore Campus), Pakistan

Projects

- LEEEE21116 “Development of risk and condition-based asset management principles” (01.01.2025–31.12.2026), Principal Investigator: Toomas Vaimann, Tallinn University of Technology, School of Engineering, Department of Electrical Power Engineering and Mechatronics. Funder: European Commission
- VERT24056 (101177220) “Enhancing Capacity in Condition-based Maintenance of Wind Energy” (01.01.2023−04.11.2025), Principal Investigator: Jako Kilter, Tallinn University of Technology, School of Engineering, Department of Electrical Power Engineering and Mechatronics. Funder: Elering AS, Estonian Transmission System Operator

Elulookirjeldus

Isikuandmed

Nimi: Muhammad Usman Sardar
Sünniaeg: 15/01/1989
Sünnikoht: Punjab, Pakistan
Kodakondsus: Pakistan

Kontaktandmed

E-post: muhammad.sardar@taltech.ee, engr.usman.ee@gmail.com

Hariduskäik

2023–2026	Ph.D. Elektroenergeetika ja mehhatroonika, Tallinna Tehnikaülikool
2012–2015	M.Sc. Electrical (Power) Engineering, The Islamia University of Bahawalpur, Pakistan
2008–2012	B.Sc. Electrical (Power) Engineering, The Islamia University of Bahawalpur, Pakistan
2006–2008	B.Sc. (Mathematics & Physics), The Islamia University of Bahawalpur, Pakistan

Keelteoskus

Inglise keel	kõrgtase
Urdu	Emakeel
Pandžabi	Emakeel
Eesti	Algaja
Hiina	Algaja

Teenistuskäik

2023-2026	Nooremteadur (1.00) Department of Electrical Power Engineering and Mechatronics, Tallinn University of Technology, Estonia
2017-2023	Lektor Khwaja Fareed University of Engineering and Information Technology, Rahim Yar Khan, Pakistan
2015-2017	Lektor Riphah International University (Lahore Campus), Pakistan

Projektid

- LEEEE21116 “Development of risk and condition-based asset management principles” (01.01.2025–31.12.2026), Principal Investigator: Toomas Vaimann, Tallinn University of Technology, School of Engineering, Department of Electrical Power Engineering and Mechatronics. Funder: European Commission
- VERT24056 (101177220) “Enhancing Capacity in Condition-based Maintenance of Wind Energy” (01.01.2023−04.11.2025), Principal Investigator: Jako Kilter, Tallinn University of Technology, School of Engineering, Department of Electrical Power Engineering and Mechatronics. Funder: Elering AS, Estonian Transmission System Operator

ISSN 2585-6901
ISBN 978-9916-80-609-8